The Royal Institution of Great Britain
Davy-Faraday Research Laboratory

Department of Geological Sciences

University College London

University of London

Title:

Computational study of doped ~~AlPO frameworks~~ ALUMINO PHOSPHATE CATALYSTS

Thesis submitted for the degree of Doctor of Philosophy

By

Iman Saadoune

2004

UMI Number: U602744

All rights reserved

INFORMATION TO ALL USERS
The quality of this reproduction is dependent upon the quality of the copy submitted.

In the unlikely event that the author did not send a complete manuscript
and there are missing pages, these will be noted. Also, if material had to be removed,
a note will indicate the deletion.

UMI U602744
Published by ProQuest LLC 2014. Copyright in the Dissertation held by the Author.
Microform Edition © ProQuest LLC.
All rights reserved. This work is protected against
unauthorized copying under Title 17, United States Code.

ProQuest LLC
789 East Eisenhower Parkway
P.O. Box 1346
Ann Arbor, MI 48106-1346

Abstract

In this thesis, a combination of computational techniques, namely periodic *ab-initio* QM methods, and interatomic potentials (IP) have been applied to study metal substituted aluminophosphate (MeAlPOs) catalysts. This computational study has focused on the following topics:

(1) The structural, electronic, acid and redox properties of substitutional dopants in AlPO frameworks:

The heteroatoms investigated include Mg^{2+}, B^{3+}, $Cr^{2+/3+}$, $Mn^{2+/3+}$,$Fe^{2+/3+}$, $Co^{2+/3+}$, Ni^{2+}, Ca^{2+}, Ga^{2+}, and Sr^{2+}. Structural data for the defect centres are in agreement with the available experimental data obtained by *in situ* EXAFS studies. The calculated energetic results, which include the substitutional and redox energies of the dopant ions, are able to rationalise the experimental evidence concerning the framework instability at high metal loading, and the redox activity during catalytic cycles. Results suggest that among the transition metal ions investigated, Fe is the most stable in the 3+ oxidation state, while Mn is the most stable as the 2+ ion. The acid strength is due to a complex combination of the structural and electronic features of the dopant ion, and does not show appreciable correlation with the local environment or electronic properties of the metal dopant in the framework.

(2) Site ordering of trivalent substitutional ions in AlPOs:

Results show that the size of 3+ metal dopants has a major influence upon their site ordering in AlPO frameworks. Bigger metal dopants prefer to substitute 'free' Al sites, located in unconstrained regions of the framework, whereas small metal dopants are energetically stable when replacing Al sites situated in smaller cages. This site preference increases on increasing the size difference between host ion (Al^{3+}) and dopant, and is explained via the topological features of the host AlPO framework.

(3) Hydration in MeAlPO-34 catalysts

Upon hydration, the presence of a metal dopant in the AlPO framework activates the framework towards hydration. Substitutional Me^{3+} ion interacts preferentially with water molecules; the adsorbed water is energetically stable when coordinated to the heteroatom rather than the framework Al species. This indicates that the Me^{3+} dopant is a better Lewis acid than framework aluminium.

In divalent metal doped AlPO-34 framework, the dopant is screened by the acid OH group from direct interaction with the adsorbed water. The water-dopant Lewis interaction is from the region behind the Brønsted acid site. The stable adsorption site in the Me^{2+} doped AlPO-34 is the acid proton, which forms a strong hydrogen bond with the water oxygen. The Me^{2+}-OH substitutional defect activates the framework Al ions towards hydration, in particular the Al ion located opposite to the Me^{2+} dopant and in the same cage containing the defect. The latter result is important to explain the low resistance of AlPOs and MeAlPOs to steaming and chemical treatment at high temperature, which may limit their applicability in heterogeneous catalysis compared to zeolites.

Table of contents

List of Figures

List of Tables

Copyright

The copyright of this thesis rests with the author and no quotation from it or information derived from it may be published without the prior written consent of the author,©Iman.Saadoune.)

Acknowledgments

First, I would like to thank my supervisor Dr Furio Corà, whose advice and ideas were invaluable. I would also like to thank him for the great interest he took in my progress, his encouragements, his exceptional generosity and his enormous help and guidance during the writing of my thesis.

I am also indebted to my supervisor Professor Richard Catlow for his support, encouragements, and for the useful discussions and involvement throughout these three years. Thanks also to my supervisor at UCL Professor David Price for his genuine help, Dr Maria Alfredson for her encouragements, support and help with my molecular calculations.

I must also thank Dr Gopinathan Sankar, Dr Scott Woodley for the useful discussions, and the EPSRC for funding.

I would like to thank these special people at the RI: Manisha Mistry, Christianna Zenonos, Alexandra Simperler, Maria Alfredson, Ilona Franklin, Dinah Parker, Said Hamad Gomes, Naseem Ramsahye, and David Plant for their friendliness (and making me look forward to the coffee breaks).

Many thanks to mum, dad, brothers and sisters for their love, support and encouragements.

Finally I would like to thank my husband Mustafa and daughter Insaf: "*without your love, understanding and tolerance I would never have done this*".

I shall dedicate this thesis to:
Mum, dad, Mustafa, Insaf and my new baby Adam.

"The important thing in science is not so much to obtain new facts as to discover new ways of thinking about them"

By Sir William Bragg

Introduction and aim

Understanding the chemistry of complex systems, be they solids or molecules, requires an accurate knowledge of their structures at the atomic level. The past two decades have seen a remarkable increase in the range and availability of computer modelling techniques, due to the rapid development in computational power, but also to the wider recognition of computational techniques as vital tools in the study of structural and electronic properties of complex materials. Computational techniques are routinely applied in the study of proteins, pharmaceuticals and in the conformational analysis of organic molecules. Such techniques have a similar rôle in the study of inorganic materials, including those with complex structures such as microporous catalysts or superconducting oxides, which are the current focus of attention in solid state inorganic chemistry, due to their important applications in modern technologies, from heterogeneous catalysis to microelectronics.

Aims of this thesis: The broad aim of the present work is to apply a combination of computational techniques to advance our understanding of the chemistry and catalytic properties of metal-substituted aluminophosphate microporous materials (MeAlPO).

Aluminophosphate molecular sieves (AlPOs) are closely related to the well known aluminosilicate and silicate zeolites. The choice of AlPOs as materials to study is due to the richness of their polymorphic structures, coupled with their ability to accommodate a wide range of metal dopants. The latter property confers on these materials either redox and/or acid catalytic activity, which can be used in heterogeneous catalysis.

Why computational techniques? The choice of computational techniques as the main tool in this thesis to study metal substituted AlPO catalysts, is because they allow to a great extent the control of those parameters that are not as easily controlled in experiments. Properties such as solid composition, oxidation state, size of dopants, level of doping, and dopant location in the solid, can be mastered directly by computational techniques. Although these methods provide solutions that can be ideal, nevertheless they give detailed atomic level information on the local environment of the metal dopants and their oxidation state, as well as an accurate description of the long range structure of the host AlPO framework. The acid strength associated with different metal dopants, for instance, can be calculated and predicted also for dopants that have not yet been introduced experimentally in the framework through synthesis. The substitutional energy of the dopants and the redox potential of transition metal dopants in AlPO catalysts, the mode of interaction of water with possible adsorption sites in the host framework are indeed properties that are not easily controlled in experimental techniques, and therefore results of the calculations complement experimental information, and are of interest to experimentalists. The information that we aim to achieve through this computational study will be valuable in terms of providing a better understanding of metal substituted catalysts and rationalising their catalytic activity.

Computational methods applied: In general terms, we have applied two types of computational methodologies: first, *ab-initio* quantum mechanical (QM) methods, and secondly, methods based on interatomic potentials. *Ab-initio* is a latin expression that means "from the beginning": computation of electronic structures and other physical properties of materials are derived from the laws of Quantum Mechanics alone, and do not require a prior experimental knowledge of the system under investigation. Such methods attempt to solve, at some level of approximation, the Schrödinger's equation of the system under study; in these methods the electronic, as well as structural properties are taken into account. In the study of doped AlPO frameworks, in particular, the structural properties of the dopants can be predicted together with their electronic properties, such as the spin state of transition metal dopants and the bonding in the framework.

Methods based on interatomic potentials (IP), instead, use simpler descriptions of forces: the electrons are not treated explicitly but their effects are subsumed into interatomic potential functions, which describe the changes in the energy of the system as a function of nuclear coordinates only. Such methods are used here mainly to provide us with information on the structural strain caused by introducing dopants with different ionic size and/or charge, and the effect of the dopant size upon its site ordering in AlPO frameworks.

Plan of the thesis: The thesis is divided into eight main chapters. The first three serve as an introduction to materials and methods; chapter 1 provides background information on microporous aluminophosphates, and reviews the available experimental and computational studies on these materials; chapter 2 explains the theory behind the most common computational techniques available to study

crystalline solids; chapter 3 explains the methodology applied in this work. Results of our computational work are described in the following chapters. Chapters 4-6 present results on Me^{2+} and Me^{3+} doped AlPOs, focussing first on their structural and then on their catalytic properties. Chapter 7 reports results on hydration of doped AlPO frameworks. In chapter 8 we summarise the main results and conclusions of the thesis.

"The important thing in science is not so much to obtain new facts as to discover new ways of thinking about them"

By Sir William Bragg

Introduction and aim

Understanding the chemistry of complex systems, be they solids or molecules, requires an accurate knowledge of their structures at the atomic level. The past two decades have seen a remarkable increase in the range and availability of computer modelling techniques, due to the rapid development in computational power, but also to the wider recognition of computational techniques as vital tools in the study of structural and electronic properties of complex materials. Computational techniques are routinely applied in the study of proteins, pharmaceuticals and in the conformational analysis of organic molecules. Such techniques have a similar rôle in the study of inorganic materials, including those with complex structures such as microporous catalysts or superconducting oxides, which are the current focus of attention in solid state inorganic chemistry, due to their important applications in modern technologies, from heterogeneous catalysis to microelectronics.

Aims of this thesis: The broad aim of the present work is to apply a combination of computational techniques to advance our understanding of the chemistry and catalytic properties of metal-substituted aluminophosphate microporous materials (MeAlPO).

Aluminophosphate molecular sieves (AlPOs) are closely related to the well known aluminosilicate and silicate zeolites. The choice of AlPOs as materials to study is due to the richness of their polymorphic structures, coupled with their ability to accommodate a wide range of metal dopants. The latter property confers on these materials either redox and/or acid catalytic activity, which can be used in heterogeneous catalysis.

Why computational techniques? The choice of computational techniques as the main tool in this thesis to study metal substituted AlPO catalysts, is because they allow to a great extent the control of those parameters that are not as easily controlled in experiments. Properties such as solid composition, oxidation state, size of dopants, level of doping, and dopant location in the solid, can be mastered directly by computational techniques. Although these methods provide solutions that can be ideal, nevertheless they give detailed atomic level information on the local environment of the metal dopants and their oxidation state, as well as an accurate description of the long range structure of the host AlPO framework. The acid strength associated with different metal dopants, for instance, can be calculated and predicted also for dopants that have not yet been introduced experimentally in the framework through synthesis. The substitutional energy of the dopants and the redox potential of transition metal dopants in AlPO catalysts, the mode of interaction of water with possible adsorption sites in the host framework are indeed properties that are not easily controlled in experimental techniques, and therefore results of the calculations complement experimental information, and are of interest to experimentalists. The information that we aim to achieve through this computational study will be valuable in terms of providing a better understanding of metal substituted catalysts and rationalising their catalytic activity.

Computational methods applied: In general terms, we have applied two types of computational methodologies: first, *ab-initio* quantum mechanical (QM) methods, and secondly, methods based on interatomic potentials. *Ab-initio* is a latin expression that means "from the beginning": computation of electronic structures and other physical properties of materials are derived from the laws of Quantum Mechanics alone, and do not require a prior experimental knowledge of the system under investigation. Such methods attempt to solve, at some level of approximation, the Schrödinger's equation of the system under study; in these methods the electronic, as well as structural properties are taken into account. In the study of doped AlPO frameworks, in particular, the structural properties of the dopants can be predicted together with their electronic properties, such as the spin state of transition metal dopants and the bonding in the framework.

Methods based on interatomic potentials (IP), instead, use simpler descriptions of forces: the electrons are not treated explicitly but their effects are subsumed into interatomic potential functions, which describe the changes in the energy of the system as a function of nuclear coordinates only. Such methods are used here mainly to provide us with information on the structural strain caused by introducing dopants with different ionic size and/or charge, and the effect of the dopant size upon its site ordering in AlPO frameworks.

Plan of the thesis: The thesis is divided into eight main chapters. The first three serve as an introduction to materials and methods; chapter 1 provides background information on microporous aluminophosphates, and reviews the available experimental and computational studies on these materials; chapter 2 explains the theory behind the most common computational techniques available to study

crystalline solids; chapter 3 explains the methodology applied in this work. Results of our computational work are described in the following chapters. Chapters 4-6 present results on Me^{2+} and Me^{3+} doped AlPOs, focussing first on their structural and then on their catalytic properties. Chapter 7 reports results on hydration of doped AlPO frameworks. In chapter 8 we summarise the main results and conclusions of the thesis.

Chapter 1 Microporous aluminophosphate catalysts

In this chapter, we first introduce the structural features of aluminophosphate molecular sieves (AlPOs), and of their-metal substituted derivatives (MeAlPOs). We also introduce the commonly accepted nomenclature and terminology with which these materials are designated, and that will be used in the thesis. We then highlight the chemical and catalytic properties of MeAlPOs that make them of interest for the synthesis chemistry industry, and summarise the current experimental and theoretical knowledge on these materials.

1.1 Introduction

Solid aluminophosphates (AlPOs), of overall chemical composition $AlPO_4$, have a rich polymorphic chemistry, which includes several microporous modifications. Microporous materials are a class of crystalline solids whose structure contains pores and internal cavities of size comparable to that of common organic molecules; these typically range from ~ 3Å to over 10Å. Depending on the pore dimensions, some molecules are allowed to diffuse into the channels and cavities of the solid, while other molecules can be refused on the basis of their larger molecular size. The ability of differentiating the behaviour of molecular species depending on their size and shape is termed *molecular sieving*,[1] and is at the basis of applications in the fields of liquid and gas separation, and heterogeneous catalysis.[2]

The best known example of microporous oxide materials is represented by the silica-based zeolites, of which a representative example, faujasite is shown in Figure 1.1.

We employ Figure 1.1 to introduce the nomenclature used to describe zeolites and the other microporous oxides.

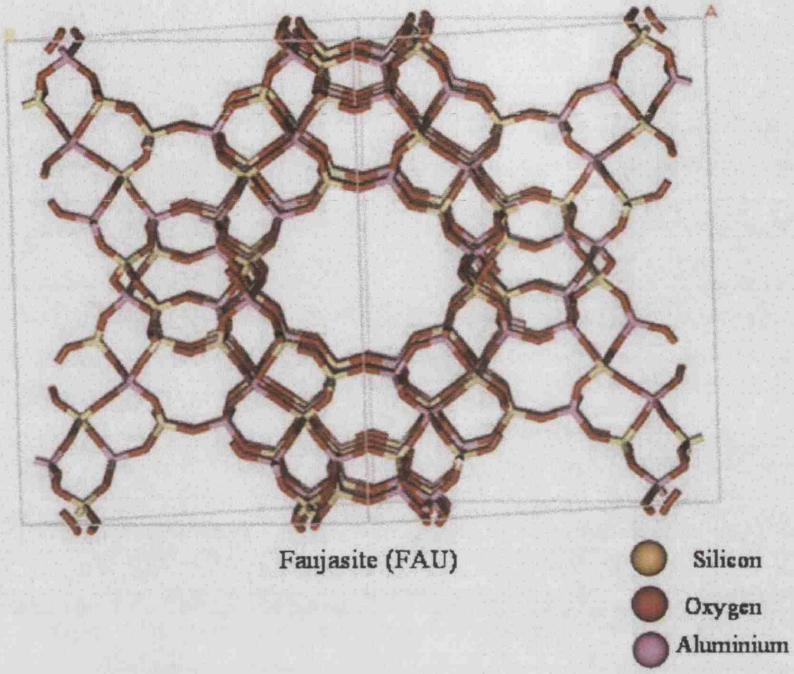

Figure 1.1: *Faujasite framework, given as an example of microporous zeolite structure.*

We can clearly recognise from Figure 1.1 the regular void structure, separated by solid walls. In the nomenclature of microporous solids, the atoms composing the solid walls are indicated collectively as *framework*. The framework is in turn built of corner sharing tetrahedra, which connect into closed rings, cages and channels. The cation at the centre of each tetrahedron is generically indicated as a T site, while rings present in the structure are denoted by the number of T sites of which they are composed. An *n*-ring is therefore a subunit of the framework formed by *n* TO_4 tetrahedra. Common values of *n* are 4, 5, 6 and 8. The size of the void space inside an *n*-ring increases with the value of *n*; the highest number of *n* currently achieved in stable microporous structures is 14.

Since the TO_4 tetrahedra composing the framework are corner sharing an oxygen atom, the latter is often referred to as *bridging* oxygen.

Apart from the framework atoms, microporous materials may contain other structural units, such as cations and/or neutral molecules hosted in the voids. These are called *extra framework* cations and *sorbed* molecules, respectively.

Several cationic species are stable in tetrahedral coordination, and can enter the T sites of the microporous framework. In the case of zeolites, the T ions are Si^{4+} and Al^{3+}. In fact, the general composition of a zeolite is $M^{m+}{}_{x/m} \cdot [(Si_{1-x}\ Al_x\ O_2)]^{x-} \cdot n\ H_2O$ where M^{m+} are non framework cations, $[(Si_{1-x}\ Al_x\ O_2)]^{x-}$ is the framework and $n\ H_2O$ are the sorbed species, in this case water molecules. The framework of aluminosilicate zeolites is anionic in nature; in the as-synthesised materials, positively charged organic template molecules act as charge compensating species. After post-synthetic treatments of these materials, *i.e.* calcination and removal of the template molecules, non-framework cations are then used for charge compensation. The framework can also be compensated by a proton bonded to one bridging oxygen atom, as illustrated in Figure 1.2. This proton confers Brønsted acidity to the material.

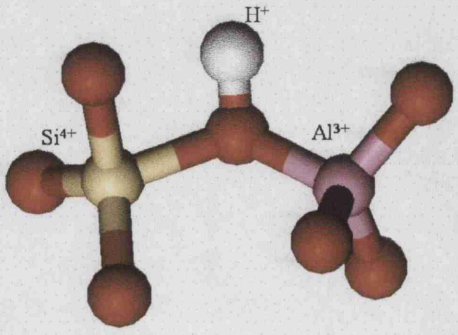

Figure 1.2: *Charge compensating proton, bonded to the bridging oxygen between the aluminium and the silicon atoms of the zeolitic framework*

The charge compensating cations in zeolites often have high mobility, which facilitates the exchange between these cations and others. This feature gives rise to the ion exchange property of zeolites, which is exploited for water softening in detergents, nuclear effluent treatment, waste treatment and soil nutrition.[2] The natural aluminosilicate zeolites clinoptilolite and mordenite are commonly applied.[3]

Furthermore, substitution of hetero-atoms in place of aluminium or/and silicon in aluminosilicate zeolites, yields materials with exciting catalytic activity.

The original family of crystalline aluminosilicates and silica-based zeolites, has been extended to include new chemical building blocks, such as aluminophosphates (AlPOs),[4] gallophosphates (GaPOs),[5] beryllophosphate (BePOs),[4] low-dimensional transition metal phosphates, as well as mesoporous silicates, aluminosilicates[6] and transition metal oxides.[7,8] All these materials constitute a new and large family of microporous oxides, collectively named as *zeotypes*.

The success in the discovery of new chemical blocks has been achieved by a progress made in understanding the synthesis procedure, a field which has more recently benefited from the increasing involvement of rational computational approaches in the search for new catalysts. Modelling can now provide atomic level details on possible structures and active sites. [9,10,11] Table 1.1 gives a summary of the major discoveries and advances in microporous oxides during the last fifty years.

Table 1.1: *Developments of microporous oxides (from reference 3).*

Time of initial discovery	Composition
Late 40's to early 50's	Low Si/Al ratio zeolites
Mid 50's to late 60's	High Si/Al ratio zeolites
Early 70's	SiO_2 microporous silicates
Late 70's	$AlPO_4$ aluminophosphates-metallo-silicates, aluminosilicates
Late 70's to early 80's	SAPO and MeAlPO
Early to Mid 80's	$AlPO_4$ -based frameworks*
Early to Mid 90's	metallophosphates mesoporous molecular sieves octahedral- tetrahedral frameworks

* Includes pure AlPO frameworks and metal substituted AlPOs.

1.1.1 Aluminophosphates: structure and properties

Let us now consider the materials of interest to this thesis: the microporous aluminophosphate molecular sieves (AlPOs). Their structure consists of corner-shared AlO_4 and PO_4 tetrahedra, which build up a three-dimensional framework with channels and pores of molecular dimensions. The AlO_4 and PO_4 tetrahedra are strictly alternated; hence, AlPO frameworks are composed only of *n* rings with an even number of T sites.

AlPOs have been first discovered by Wilson *et al*[4] in the early 1980's. Since then, many novel AlPO frameworks have been synthesised, some of which are structurally analogous to known aluminosilicate polymorphs. For instance, AlPO-34 has the chabasite structure (CHA), AlPO-37 the Faujasite (FAU), and AlPO-20 the Sodalite structure (SOD). Some aluminophosphates, however, have unique structures with no zeolite counterparts, *e.g.* AlPO-5 (AFI), AlPO-11(AEL) and VPI-5. The three letter code accompanying the name of each of the AlPO framework listed above, *i.e.* CHA or AFI, is used here to define the framework *type* of these materials. These codes have been assigned to confirmed framework types by the Structure Commission of

the International Zeolites Association; these are normally derived from the name of the zeotype or the material type. Information about the framework types of AlPOs and other zeotypes and their nomenclature, are described in reference 12. In Figure 1.3 we show the structure of AlPO-5 (AFI); it consists of *4*-ring, *6*-ring, and *12*-ring that form a 1D channel structure. The main *12*-ring channels are nearly circular and have a diameter of 7.3 Å.

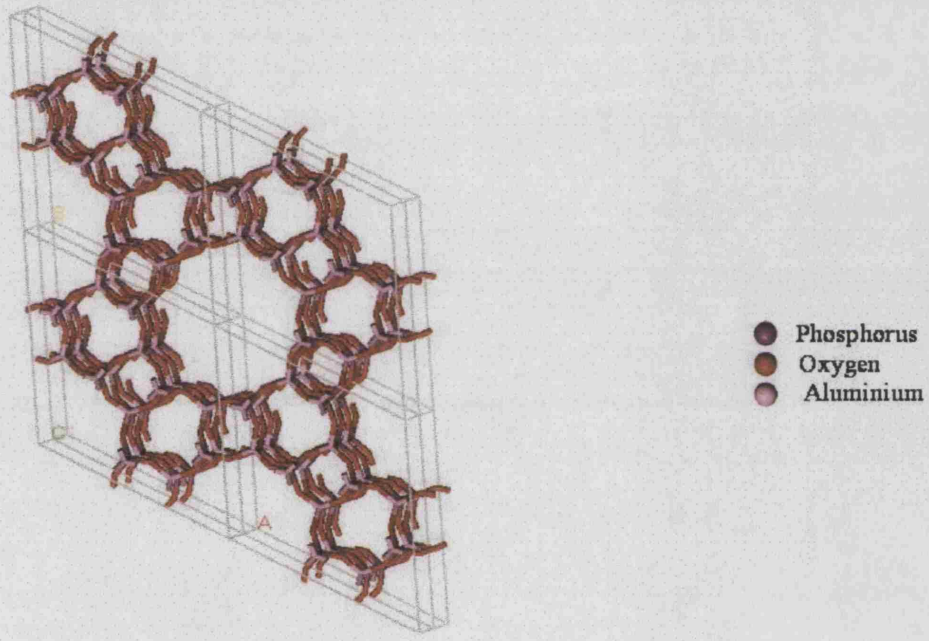

Figure 1.3: *3 Dimensional structure of AlPO-5*

AlPO frameworks are hydrophilic in nature, a feature which distinguishes them from the hydrophobic pure-silica and aluminosilicate zeolites with high Si/Al ratio. On exposure to wet atmosphere, the framework aluminium ion can expand its coordination number from four to five or six. Dehydration of AlPO frameworks can be accomplished without the complete collapse of the structure, thus a reversible change of the coordination sphere of aluminium is conceivable in AlPO frameworks.[13,14]

In some AlPO frameworks, such as JDF-20, the adsorption of water can further result in the hydrolysis of some of the Al-O-P bonds, with the formation of hydroxyl groups. Thus, interrupted AlPO frameworks, with no strict alternation of AlO_4 and PO_4 tetrahedra, and in which Al-O-P bonds are systematically missing can be formed; these materials are termed $AlPO_4$ hydroxides.[15]

The hydrophilic nature of AlPO materials was first explained by Wilson *et al* [4] to be due to the difference in electronegativity between aluminium and phosphorus atoms, which creates a dipole moment that attracts the dipole of the adsorbed water molecules.

1.1.2 Defect Chemistry of AlPOs

Like purely siliceous zeolites, in principle, "defect free" AlPO frameworks are chemically inert, as in the pure $AlPO_4$ composition with invariant Al_2O_3/P_2O_5 ratio they possess a balanced framework charge. Defect free frameworks display neither ion exchange capacity nor framework acidity. AlPO frameworks can be chemically activated by doping; AlPO frameworks, in particular, show a greater flexibility towards chemical substitutions than silica zeolites. The formal charge of dopants successfully introduced in the framework of AlPOs varies between +2 to +5.[15,16]

The metal dopants incorporated include *alkali earth* and *transition metals*. Their substitution can be described via two mechanisms, identified as SM I, and SM II.[15] These are schematically described in Figure 1.4. The substitution mechanism SM I consists of a replacement of an aluminium ion by an element with +1(Ia) valence (there is no evidence yet for this substitution), +2 (Ib) or +3 (Ic), while SM II involves the substitution of a phosphorus by an element with a +4 (IIa) or +5 (IIb) valence.

Other types of substitution are less likely to take place, as they lead to either a positively charged framework, or a too high negative charge density. In the case of Si^{4+} dopants (the material is indicated as SAPO), the substitution can take place simultaneously in the place of neighbour aluminium and phosphorus atoms, leading to a so called silicon cluster or island.[3,15,17]

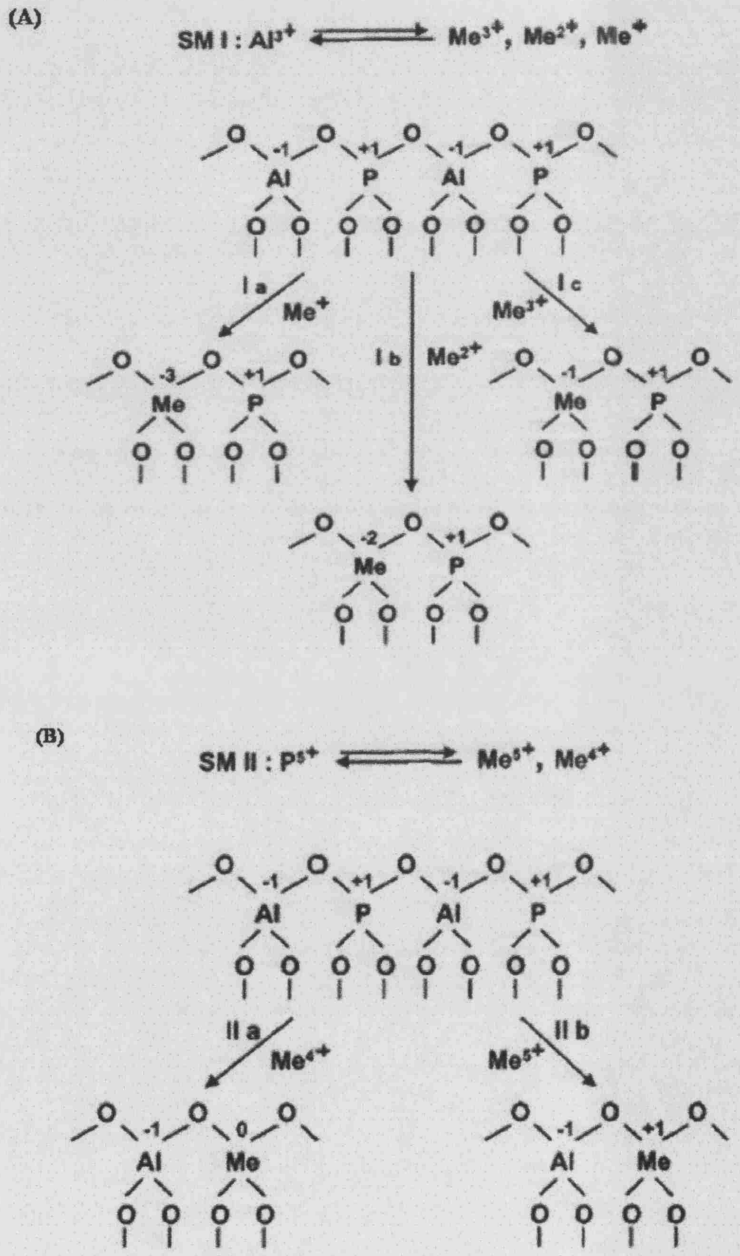

Figure 1.4: *Metal dopant substitution mechanisms SM I (A) and SM II (B) in AlPO frameworks (after reference 15)*

It is apparent from Figure 1.4 that substitution mechanisms SM Ia, Ib and IIa lead to a negative framework; this is compensated for by a positively charged species, such as extra-framework cations or protons. In the former case the materials exhibit cation exchange capacity, while in the latter the modified AlPO framework has Brønsted acidity. On the other hand, substitution mechanisms SM Ic and IIb yield, in principle, neutral frameworks, hence no charge balancing species are involved.

Among the elements that can be successfully incorporated into AlPO frameworks, we find several transition metal ions; if these ions are capable of changing their oxidation state reversibly, the framework can also act as redox catalyst.[15,16,18] One of many examples is provided by CoAlPOs, in which cobalt has been shown to be stable in both Co^{2+} and Co^{3+} forms, and whose properties as both acid and redox catalyst have been extensively investigated.[19]

1.1.3 Catalytic activity of MeAlPOs

In order to be considered for industrial applications, a solid catalyst must show high activity. A useful definition of activity is the *turnover frequency*, *i.e.* the number of times that the overall catalytic reaction of interest takes place per *catalytic site* and per unit of time, for a fixed set of reaction conditions. [20] Additional requirements are long term stability, including the framework phase stability, and shape selectivity; the latter is the reaction specificity arising from the presence of a sterically confined environment in which the molecules are converted. Shape selectivity involves matching the size and shape of reactants, transition states and products with the size and shape of the microporous framework of the solid catalyst.[3,21] There are three categories of shape selectivity, namely *reactant*, *product* and *transition state* selectivity [1] (see Figure 1.5).

- **Reactant shape selectivity:** in this case the microporous framework of the solid catalyst behaves as a typical molecular sieve and discriminates certain molecules according to their molecular size and structure from entering the pores of the solid, while other smaller molecules are allowed to enter.
- **Product shape selectivity:** this is due to the difference of diffusivity between different reaction products in the pores of the solid; only molecules that are able to leave the catalyst channels are found in the product mixture.
- **Transition state shape selectivity:** this occurs when the spatial configuration around a reaction intermediate, located in the internal pores of the solid, is such that only certain configurations are possible. In this way, only the required transition state is formed in the solid cavities.

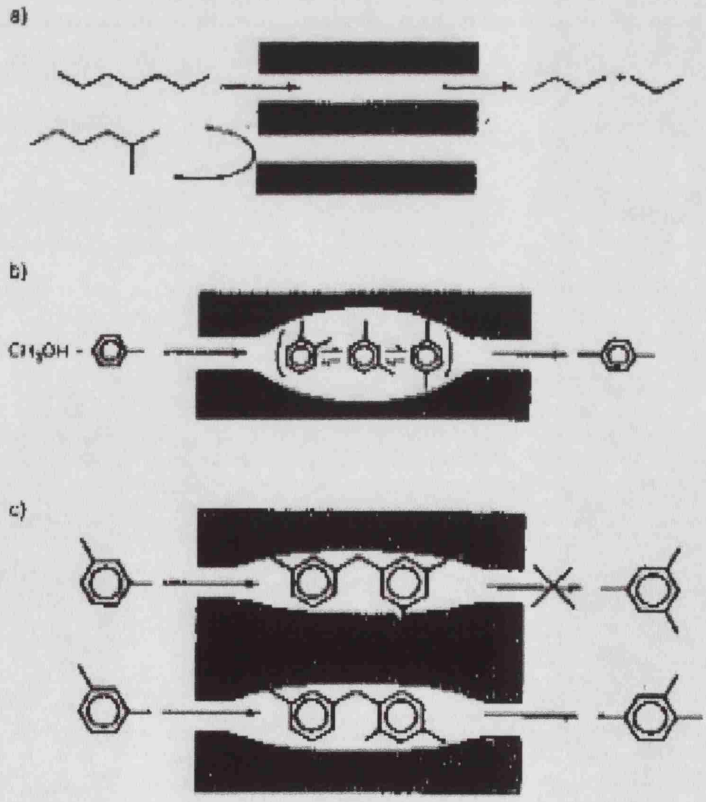

Figure 1.5: *The three main categories of shape selectivity: (a) Reactant selectivity (b) Product selectivity and (c) Transition state selectivity (from reference 21).*

The catalytic activity of MeAlPOs is related to their defect chemistry. Given the shape selectivity character of MeAlPOs, combined with the presence of the acid and/or redox centres within the channels, one can view the materials as micro-reactors, in which the reaction products formed are controlled by the size and shape of the pore and cage openings.

1.1.3.1 Acidity of MeAlPOs

Acid catalysed reactions are the backbone of the modern chemical industry. [2,3,22] Among these reactions three processes are of particular interest in the catalytic applications of MeAlPOs, namely:

(1) The methanol to olefin (MTO) process, which accomplishes the conversion of methanol to light olefins, such as ethylene, propene, and butene; these chemicals are the centre-piece in the production of synthetic fibres, plastics and petrochemicals.

(2) The skeletal isomerization of butene to isobutene, a starting material for the production of methyl tert-butyl ether (MTBE), used as an oxygenated octane additive in the reformulated gasolines, and

(3) the catalytic cracking of hydrocarbons in the oil refining industry.

All these reactions are activated by acid catalysts, which enable us to speed up the processes, and give better yields and selectivity. Acid catalysts are responsible for producing more than 108 million tons per year of products.[2,3]

The first acid catalysts used included liquid homogeneous catalysts such as HF, H_2SO_4, $HClO_4$, and H_3PO_4.[23] Since the 1940's the acid catalysis field moved towards replacing liquid acids with solid acid catalysts, which show many advantages over liquid acids, such as the ease of handling, catalyst regeneration, decreasing corrosion problems, and environmentally safe disposals.[18]

Solid acid heterogeneous catalysis is based on the same principle as homogenous acid catalysis. Acids are characterised by their ability to donate a proton (H^+); when a reactant receives a proton from the acid, it is chemically activated, and forms a reactive intermediate. The latter may change shape and/or configuration, or undergo other chemical rearrangements before returning the proton to the catalyst. In the former case the catalytic reaction leads to the formation of an isomer – a compound with the same chemical composition but different molecular structure; in the latter, the catalytic reaction leads to the formation of a new molecule.

Microporous oxides, including zeolites and MeAlPOs, are among microporous materials that have potential application as solid acid catalysts. Small-pore AlPO frameworks, such as SAPO-34, SAPO-18, and SAPO-17 (the structure of the latter frameworks is closely related to SAPO-34, but crystallographically distinct) have shown high selectivity for methanol conversion into light olefins, principally ethene, propene, and butene in the MTO-process.[24] In addition, doping small-pore SAPO or AlPO frameworks with divalent metal dopants, including transition metals, has shown to enhance the catalytic performance of these materials; the performance of MeAPSO-34 and MeAlPO-18 frameworks have been tested by several groups.[25,26,27,28] Inui *et al*[25] and Thomas *et al*[26] reported independently that the nickel-containing SAPO-34 is one of the best catalysts for methanol conversion into olefins. Also Co and Zn-AlPO-18 materials showed good catalytic performance.[26]

The origin of the Brønsted acidity of MeAlPOs, is linked to the presence of a loosely bonded proton which charge compensates the low valent metal dopants in the AlPO framework. The catalytic activity of these materials is connected to the concentration and strength of the acid sites in the molecular sieve structure, which in turn depends upon the type and concentration of metal dopants incorporated.[29] For example, on

reducing the concentration of acid sites in MeAlPOs catalysts, the conversion of olefins to paraffins decreases,[30,31] while moderate acid sites are more selective in the skeletal isomerisation of alkenes.[32]

Apart from the bridging hydroxyl groups of the framework, responsible for the Brønsted acidity, MeAlPOs exhibit Lewis acidity. Experimental temperature programmed desorption (TPD) and calorimetric data probing the interaction of Lewis basic molecules, such as ammonia or acetonitrile, with metal doped AlPO frameworks,[32] showed that the adsorption of probe molecules increases in transition metal doped AlPO frameworks. Therefore, these metals can act as potential Lewis acid centres. [33]

The flexibility of AlPO frameworks to accommodate a wide range of dopants, which depending on the *type* of metal incorporated can confer to the material an acidity of variable strength, combined with the high shape-selectivity of AlPO frameworks, make MeAlPOs important solid acid catalysts, which are open to further development and tailoring. These features motivate the growing interest in discovering new MeAlPO catalysts, with improved catalytic activity and selectivity.

1.1.3.2 Redox activity of MeAlPOs

Selective oxidation reactions are applied throughout the chemical industry to produce chemicals, ranging form bulk scale oxygenates to pharmaceuticals, and fine chemicals.[34,35] Traditionally, oxidation has been achieved via the use of sacrificial oxidants, such as peroxides (R-O=O-R), or aggressive agents such as chromates ($Cr_2O_7^{2-}$) or permanganates (MnO_4^-), which are both expensive to produce and potentially harmful for the environment. For obvious economical and environmental reasons, tremendous efforts have therefore been directed in the last decades towards

improving the performance of the redox catalysts so that they exhibit better selectivity, activity and environmental friendliness. However, designing redox catalysts that combine all these characteristics is a challenging task.

The first transition metal-doped microporous oxide synthesised is Titanium silicate-1 (TS-1),[36] a silicate that has the MFI structure with a small fraction of silicon atoms substituted by titanium. TS-1 was found to be an environmentally friendly redox catalyst, that catalyses a broad range of selective oxidations with hydrogen peroxides.[21,24] Given the industrial importance of redox catalysis,[37] the synthesis of other microporous structures that incorporate transition metal ions has attracted much attention. Experimental work has now shown that AlPO frameworks are better as hosts for transition metal dopants than zeolites. Dopants with charge that can vary between 2+ and 5+, have been successfully introduced in AlPO frameworks.[15,16] The incorporation of transition metal dopants such as, Cr, Mn, Fe, Co, V and Ti, yields potential heterogeneous redox catalysts for oxidation reactions. For instance, CoAlPO molecular sieves have been shown to be active for the oxidation of hydrocarbons using O_2.[38] Sheldon and co-workers examined the catalytic properties of doped AlPO-5 systems, and found CrAlPO-5 to be excellent recyclable catalyst for the oxidation of secondary alcohols to the corresponding ketones, using *tert*-Butyl hydroperoxide (TBHP) and O_2 as oxidants.[39] Dai *et al* have also demonstrated that MeAlPOs have significant catalytic activity for the hydroxylation of phenol with hydrogen peroxide; FeAlPOs showed comparable performance to TS-1 for these reactions.[40] Raja *et al* showed that Mn- and Co- containing AlPO-36 catalysts are active for epoxidation of alkenes.[41]

With the continuous efforts made to improve MeAlPO catalysts, these materials currently show promising activity and selectivity for two of the most challenging and

industrially important oxidation reactions, namely the selective oxidation of terminal methyl groups of linear alkanes, of interest as potential feedstocks for the chemical and pharmaceutical industries, and the oxidation of cyclohexane to cyclohexanol and cyclohexanone, the centre piece for the production of Nylon-6 and Nylon-6,6.[18,34] Co- and Mn-doped AlPO-18 materials have higher selectivity for the former reaction, while FeAlPO-5 and VPI-structured CrAlPOs are better catalysts for the oxidation of cyclohexane. [18,42]

The redox activity in MeAlPOs is achieved when the transition metal dopants in the framework, such as Cr, Mn, Fe, or Co, can reversibly change their oxidation state. A major advantage of these catalysts is their ability to use molecular oxygen as an oxidising agent, which is a clean alternative to 'sacrificial' oxidants such as hydrogen peroxides and alkyl-peroxides, which are themselves the products of oxidation reactions. The ability of using molecular oxygen as oxidant gives MeAlPOs a prominent rôle to play in selective oxidation reactions of hydrocarbons, and raises the prospect of their application for industrial oxidation processes.

1.1.4 Hydrophilicity of MeAlPOs

Another important characteristic of MeAlPO frameworks is the increased hydrophilicity of these materials upon doping.[43,44] This feature has been recently revealed experimentally, and is directly linked to the presence of the dopant ions in the framework: trivalent metal dopants such as Fe, Mn and Cr, when incorporated in the AlPO framework, have been found to increase their coordination number in presence of water.[45]

Water plays a central rôle in the applications of metal doped AlPOs in catalysis. Even when operating in a perfectly dry atmosphere and using anhydrous reagents,

water is often one of the products generated *in situ* during the catalytic cycle. One example is provided by the methanol conversion to hydrocarbons:[31]

$$2CH_3OH \underset{+H_2O}{\overset{-H_2O}{\rightleftharpoons}} CH_3OCH_3 \xrightarrow{-H_2O} \text{Light olefins} \quad (1.1)$$

The presence of basic molecules such as water inside the microporous structure can modify the framework acidity and redox chemistry.

1.1.5 Summary

It is apparent that MeAlPO show interesting chemical flexibility and promising catalytic activity, which depends crucially upon the chemistry and the local environment of the metal dopant. Understanding the structural, electronic, Brønsted and Lewis acid, and redox properties associated with different metal ions in AlPOs, and the way in which polar molecules such as water may interact with the metal or the acid site, is therefore a crucial step towards rationalising the catalytic behaviour of these heterogeneous catalysts, and maximising their selectivity and catalytic efficiency.

In the following section, we shall review the available experimental and theoretical studies on AlPOs. First we highlight the characterisation methods used on AlPO systems, and the information gained from these experiments, then we review previous computational works performed on AlPO systems, which have been scarce. Additional information regarding the results available in the literature on AlPOs and zeolites will be given and discussed further in chapters 4-7, as appropriate for the topic of each section.

1.2 Experimental studies on MeAlPOs

Different MeAlPO materials have been characterised via a broad range of experimental techniques. Among these it is important to mention Infra-Red (IR), Nuclear Magnetic Resonance (NMR), Electron Spin Resonance (ESR) and X-ray Absorption (EXAFS and XANES) spectroscopies; X-ray Diffraction (XRD), Temperature Programmed Desorption (TPD), and Thermo-Gravimetric Analysis (TGA).

X-ray diffraction (XRD) is mainly used for phase identification, crystallinity and phase purity of a newly synthesised MeAlPO material. Laboratory X-ray diffractometers can be very useful in solving structures, although synchrotron radiation (SR) X-rays (with higher resolution and better-defined peaks) are favoured for structure solution and refinement, particularly for powder samples, such as that of AlPO and other zeolite materials.[3] Lattice parameters and coordinates of the constituents atoms are obtained for AlPO and zeolites structures, and are compiled in the database of the *International Zeolites Association* (IZA), which is also available online.[46]

Generally, XRD provides little information on the dopant ions, because metal dopants are usually present at low concentration, and are distributed in a disordered fashion in the solid.[47,48] The characterisation of the *local* environment of metal-dopants in MeAlPOs can be performed via X-ray absorption spectroscopy (XAS) which includes X-ray Adsorption Near Edge Structure (XANES) and Extended X-ray Absorption Fine Structure (EXAFS) spectroscopies. The former provides information on the electronic structure and the chemical environment of the metal dopant, while the latter gives the structural properties, *i.e.* the bond distances

between the metal dopant and its neighbouring atoms, with a typical error bar of ± 0.02Å.

The combined application of XRD and XAS techniques yields a reliable description of the short range environment of the metal dopants, and a long range structure of the AlPO frameworks. Such techniques have been extensively used to fully characterise metal doped AlPO catalysts.[19,33,49,50] One of their advantages is that they can be carried out *in situ*, to give information about the state of the catalyst under operating conditions. Among the main limitations of XAS techniques, however, is that they provide only the average bond length between the metal dopant and its nearest neighbour oxygens over the entire structure of the solid, regardless as to whether the dopants are located in different environments or have different oxidation states. In addition, such techniques rely on crystallographically well-characterised model systems that represent the typical coordination geometry of the dopant ions. If such a model is not available, it will be difficult to associate the structure derived from XAS with an electronic state of the metal ions, hence crucial information on the metal dopant will remain unresolved.

ESR is a powerful technique to study paramagnetic transition metal ions, and in general all open shell defect centres, in MeAlPO frameworks.[15,16,51,52] Coordination number, oxidation and spin state of the open-shell ions can be deduced from the ESR spectrum. ESR studies have been useful for providing direct evidence on the presence of transition metals, and if these metals are present as extra-framework ions or incorporated directly into the AlPO framework sites.[16,53]

NMR techniques have been extensively used to probe the composition, and the chemical environment of framework aluminium and phosphorus atoms in the pure and metal doped AlPO frameworks.[54,55] Such techniques have been shown to provide

valuable evidence on the incorporation of metal dopants in the place of aluminium or phosphorus atoms; for instance analysis of ^{31}P NMR spectra showed that the incorporation of metal dopants into the lattice sites distorts the symmetry of the latter, hence altering the appearance of the chemical shifts corresponding to the ^{31}P atoms that are (next) nearest neighbour to the metal dopants. The change in the chemical environment of phosphorus in MeAlPOs correlates with the number of dopant atoms incorporated.[56]

Similarly, ^{1}H NMR methods have been applied to probe acid proton sites, [57]and to identify adsorbed chemical species such as water or methanol in AlPO systems, and the interaction of these adsorbed molecules with the acid sites.[58,59]

IR spectroscopy is widely used to study admolecules on the microporous frameworks, but also the properties of framework OH groups, [3] including the Brønsted acid site discussed in section 1.1. This technique provides the whole phonon spectra of the materials under investigation, including the stretching frequencies of the bridging hydroxyl group, which is an *indirect* measure of the acidity of the material. Identifying the stretching frequencies of the hydroxyl group situated in the vicinity of each metal dopant in MeAlPO frameworks is proven, however, to be difficult to achieve. This is due to the broadening of the OH Brønsted acid vibration bands, as acid protons can be present in different chemical environments in the solid.[60] The acidity of MeAlPOs is therefore *directly* studied by examining the interaction of basic probe molecules, such as acetonitrile, ammonia or water, with the acid sites (Brønsted and/or Lewis) of the solid. For instance, acetonitrile is used to probe Lewis acid sites, [19] while other smaller molecules such as ammonia and CO are used to probe the acid protons and determine their concentration in the solid. Small probe molecules can access most of the acid protons in the solid, allowing them to probe

the maximum concentration of Brønsted acid sites that may be involved in catalytic reactions, while larger molecules are more selective.[3] Not only vibrational spectroscopies, but also Thermo-Gravimetric Analysis (TGA), and Temperature Programmed Desorption (TPD) provide useful data in this respect. IR spectroscopy yields the vibration bands corresponding to the adsorbed probe molecules while TGA and TPD analysis give information on the coverage level of these probe molecules, and their interaction energy with the acid sites in the AlPO framework.

Results from these experimental techniques, as a whole, give us valuable information on the composition of the MeAlPO materials, including their structure, the oxidation state of the transition metal dopants, the type and strength of acid sites present in these materials. However, experimental techniques lack atomic level detail on the local environment of the metal dopants, especially when the latter are bonded to oxygen atoms in different chemical environments, and also on the mode of interaction between the acid site or transition metal dopant and the adsorbed molecules. This atomic level information, which is needed to understand the catalytic properties of these materials, is achievable by computer modelling.

1.3 Theoretical studies on AlPO systems

During the last decade, in the field of microporous solids, computer modelling techniques have been mainly applied to study zeolites. Modelling of these materials has been a particularly active field, owing both to the complexity and diversity of their structures, and to the interest in their physico-chemical properties.

Although AlPOs share many characteristics and properties of zeolites (see section 1.1), it is only during the mid 1990's that atomistic modelling of their structures has

begun to attract attention. Earlier modelling works on AlPO systems[17,61,62] have been performed by methods based on interatomic potentials (IP). Accurate potentials have been derived for AlPO systems, such as the shell model potentials developed by Gale and Henson,[63] and Sauer and Schröder.[64] Earlier studies have been reported by several authors; for instance Ruiz-Salvador *et al*[62] used lattice energy minimisation techniques to refine the structure of AlPO-5. This study highlighted the rôle of lattice simulation techniques in assisting experiment with refining complex structures. Sastre *et al*[17] investigated silicon substitution in SAPO-5 and SAPO-34. The authors of this work confirmed the stability of clusters comprising Si-O-Si bridges within the two systems under investigation, and found that the acidity correlates with silicon island sizes.

Early quantum mechanical (QM) *ab-initio* studies on pure AlPO systems were based on cluster models. Márquez and co-workers reported a joint experimental-theoretical study on amorphous alminophosphate-like catalysts. They found that the Hartree-Fock (HF) method reproduces the experimental structural data well.[65] Corà and Catlow,[66] later applied periodic *ab-initio* QM techniques to investigate the structural and bonding properties, and the stability of a number of AlPO polymorphs. Results of this work agreed with the above study, as they also showed that the HF level of theory is sufficient in terms of describing AlPO framework structures, as it gives results in good agreement with experiment. The authors have also discovered that the tetrahedral backbone of AlPOs is very different from that of pure silica-zeolites; the former is made up by discrete Al^{3+} and PO_4^{3-} molecular ionic units, whereas the SiO_2 backbone of zeolites is made up from a continuous network of covalent Si-O-Si bonds, see Figure 1.6. The ionic character of the bonding between Al^{3+} and the PO_4^{3-} unit is responsible for the overall hydrophilicity of AlPO frameworks. Poulet *et al*,[67]

used Density Functional Theory (DFT) calculations to investigate the hydration of AlPO-34, and highlighted the hydrophilic character of this material.

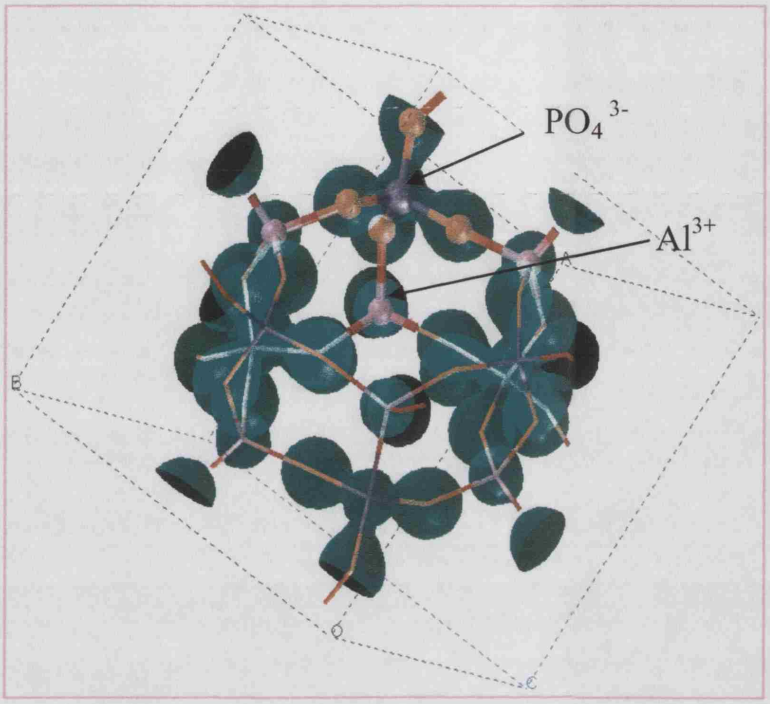

Figure 1.6: *Three-dimensional isodensity plot (ρ = 0.05|e|Å^{-3}) of the electronic density in the unit cell of AlPO-34 (CHA), calculated with DMOL3*[68]*. Note the natural separation of the structure into discrete Al^{3+} and PO_4^{3-} (From reference 66)*

Computational studies on metal incorporation, be they alkali earth or transition metals, in AlPO frameworks have been scarce, and only few publications have been reported. Among these studies, Gonzales *et al* [69,70] studied the incorporation of iron in the place of framework aluminium using IP methods. The other study is reported by Henson *et al*, who applied cluster models and DFT to study the incorporation of cobalt in AlPO frameworks, and the interaction of this metal with base molecules, such as acetonitrile. [71] Another study based on DFT cluster models was reported for vanadium-substituted AlPO systems, and showed that the incorporation of this metal

in the place of either phosphorus or aluminium framework sites is not feasible.[72] Corà *et al* used DFT periodic ab-initio calculations to investigate the cobalt incorporation in AlPO-34 and calculate the redox potentials of the Co^{2+}/Co^{3+} pair;[73] later Corà *et al* published a joint theoretical–experimental investigation of manganese,[74] and iron[43] incorporation in AlPO frameworks. In these studies, the authors highlighted the role of high level QM periodic calculations in assisting experiment, with accurately determining the local environment and oxidation state of transition metal dopants in AlPO frameworks.

Finally, it is worth mentioning the QM *ab-initio* calculations performed on silicon doped AlPO frameworks (SAPOs). For instance, Jeanvoine *et al* [75] studied the structure of Brønsted acid sites and the effect of silicon substitution in the SAPO-34 framework. Termath *et al* [76] and Jeanvoine *et al*[77] have investigated, with DFT calculations, the interaction of water molecules with Brønsted acid sites in these materials. Results of these studies will be discussed later in Chapter 7.

It is apparent from the above discussion that the characterisation of metal doped AlPOs with computational techniques is far from complete. Important features of the metal dopants, including their structural and electronic properties, and their influence on the catalytic properties is still missing. This thesis work aims to bridge this gap and contribute to a better understanding of the chemistry that follows the introduction of metal dopants in AlPO frameworks, by carrying out an extensive computational study on these materials. The objectives of this thesis are given in the following section.

1.4 Objectives of the thesis

The main objectives of this thesis are:

- To provide structural details on the incorporation of a range of di-valent and tri-valent metal dopants in AlPO frameworks.
- To determine the energetics of introducing dopants into the AlPO frameworks, and factors that affect such substitution, including the site ordering of dopants in the microporous framework.
- To characterise the electronic and chemical properties of the dopants, and correlate such properties with the acid strength, and with the redox potential of the dopants in the framework
- To study the hydration of doped AlPO frameworks, and its effects on the catalytic properties of the material.

This information will provide accurate atomic detail for the description of doped AlPO frameworks, and therefore will give an insight into the catalytic behaviour of these materials, which is beneficial in order to tailor their catalytic properties.

References

1 J.W.McBain, *The sorption of gases and vapours by solids*. **1932**, London: Rutledge and Sons.

2 A. Dyer. *An Introduction to Zeolite Molecular Sieves*, **1988**, John Wiley and Sons, Chichester.

3 H. Van Bekkum, E. M. Fanigen, P. A. Jacobs, J. C. Jansen, *Introduction to Zeolites Science and Practice*, **2001**, Elsevier, Amesterdam

4 S. T. Wilson, B. M. Lock, C.A. Messina, T. R. Cannan, E. M. Flanigen, *J. Am. Chem. Soc.*, **1982**, *104*, 1146

5 J. A. Martens, P. A. Jacobs, J. Weitkamp and L. Puppe (Eds), *Catalysis and Zeolites Fundamentals and Applications,* **1999,** Springer-Verlag, Berlin

6 C. T. Kresge, M.E. Leonowicz, W. J. Roth, J. C. Vautuli, J. S. Beck, *Nature*, **1999**, *359*, 710

7 J. S. Beck, J. C. Vartuli, *Curr, Opin. Solid state. Mater. Sci.*, **1996**, *1*, 4

8 Y. Ma, W. Tong, H. Zhou, S. L. Suib, *Micropor. Mesopor. Mater.* **2000**, *37*, 2303

9 D. W. Lewis, G. Sankar, J. K. Wyles, J. M. Thomas, C. R. A. Catlow and D. J. Willock, *Angew. Chemie- Int.* **1997**, *36*, 2675.

10 C. R. A. Catlow, L. Ackermann, R. G. Bell, F. Corà, D. H. Gay, M. A. Nygren, J. C. Pereira, G. Sastre, B. Slater, P. E. Sinclair, *Faraday Discuss*, **1997**, *106*, 1

11 C. M. Draznieks, J. M. Newsam, A. M. Gorman, C. M. Freeman, G. Ferey, *Angew. Chem. Int. Ed.*, **2000**, *39*, 2770.

12 Ch. Baerlocher, W.M. Meier, D.H. Olson, *Atlas of zeolite framework types, 5th ed.*, Elsevier, Amsterdam, 2001.

13 M. P. J. Peeters, J. W. De Hann, L. J. M. Van de Ven, J. H. C. Van Hoof, *J. Phys. Chem.* **1993**, *97*, 5363.

14 M. P. J. Peeters, L. J. M. Van de Ven, J. H.C. Van Hoof, *J. Phys. Chem.* **1993**, *97*, 8254.

15 B. M. Weckhuysen, R. R. Rao, J. A. Marten, R. A. Schoonheydt, *Eur. J. Inorg. Chem.* **1999**, 565.

16 M. Hartmann, L. Kevan, *Chem. Rev.* **1999**, *99*, 635.

17 G. Sastre, D. W. Lewis, and C.R.A. Catlow, *J. Phys. Chem. B*, **1997**, *101*, 5249

18 J.M.Thomas, *Angew. Chem. Int. Engl*, **1994**, *33*, 913

19 P. A. Barrett, G. Sankar, C.R.A. Catlow, J. M. Thomas, *J.Phys. Chem.* **1996**, *100* 227

20 J. M. Thomas, W. J. Thomas, *Principles and Practice of Heterogeneous Catalysis*, **1996**, VCH, Weinheim. PP. 27

21 I. W. C. E. Arends, R. A. Sheldon, M. Wallau, U. Schuchardt, *Angew. Chem. Int. Ed. Eng.* **1997**, *36*, 1144

22 A. Corma, H. Garcia, *Catal. Tod*, **1997**, *38*, 257

23 A. Corma, *Currt. Opin. Sol. Stat. Mater. Sci,* **1997**, *2*, 63

24 J. Chen, P. A. Wright, J. M. Thomas, S. Natarajan, L. Marchese, S. M. Bradley, G. Sankar, C. R. A. Catlow, P. L. Gai-Boyes, R. A. Townsend, C. M. Lok, *J. Phys. Chem.* **1994**, *98*, 10216.

25 T. Inui, S. Phatanasri, H. Matsuda, *J. Chem. Soc, Chem. Commun.* **1990**, 205.

26 J. M. Thomas, Y. Xu, C. R. A. Catlow, J. W. Couves, *Chem. Mater.* **1991**, *3*, 667

27 S. Hočevar, J. Levec. *J. Catal.* **1992**, *135*, 518

28 J. Chen, J. M. T. Thomas, *J. Chem. Soc. Chem. Commun.* **1994**, 603.

29 S. Hočevar, J. Batista, V. Kaučič, *J. Catal*, **1993**, *139*, 351

30 G. F. Froment, W. J. H. Dehertog, A. J. Marchi, *Catalysis*, **1992**, *9*, 1.

31 M. Stöcker, *Microp. Mesop. Mater*, **1999**, *29*, 3.

32 G. Lischke, B. Parlitz, U. Lohse, E. Schreier, R. Fricke., *App. Catal. A. General*, **1998**, *166*, 351

33 P. A. Barrett, G. Sankar, R. H. Jones, C. R. A.Catlow, J. M. Thomas, *J. Phys. Chem. B*, **1997**, *101*, 9555

34 R. A. Sheldon, J. K. Kochi, *Metal-Catalysed Oxidation of organic Compounds*, Academic Press, New York, **1981**

35 U. Schuchardt, D. Cardoso, R. Sercheli, R. Pereira, R. S. da Cruz, M. C. Guerreiro, D. Mandelli, E. V. Spinace, E. M. Pires, *App. Catal. A.* **2001**, *211*, 1

36 M. Taramasso, G. Perego, B. Notari, *U. S. Patent*, **1983**, *4*, 410.

37 R. A. Sheldon, M. Wallau, I. W. C. E. Arends, U. Schuchardt, *Acc. Chem. Res*, **1998**, *31*, 485

38 B. Kraushaar-Czarnetzki, W. G. M. Hoogervorst, R. R. Andrea, C. A. Emeis, W. H. Stork, *In Zeolites Chemistry and Catalysis*. P. A. Jacobs, N. I. Jager, L. Kubelkova, B. Wichterlova, Eds, Elsevier: Amesterdam, **1991**, *69*, 231.

39 J. D. Chen, J. Dakka, E. Neelman, R. A. Sheldon, *J. Chem. Soc. Chem. Commun,* **1993**, 1379

40 P. S. E. Dai, R. H. Petty, C. W. Ingram, R. Szostak, *App. Catal. A.*, **1996**, *143*, 101.

41 R. Raja, G. Sankar, J. M. Thomas, *Chem. Commun*, **1999**, 829.

[42] F. J. Luna, S. E. Ukawa, M. Wallau, U. Schuchardt, *J. Mol. Catal. A: Chem* **1997**, *117*, 405

43 C. Zenonos, G. Sankar, F. Corà, D. W. Lewis, Q. A. Pankhurst, C. R. A. Catlow and J. M. Thomas, *Phys. Chem. Chem. Phys*, **2002**, *4*, 5421

44 J. D. Chen, R. A. Sheldon, *J. Catal.* **1995**, *153*, 1

45 P. S. Singh, P. N. Joshi, S. P. Mirajkar, B. S. Rao, and V. P. Shiralkar, *J. Phys. Chem. B*, **1999**, *103*, 5338.

46 http://www.iza-structure.org/databases

47 J. M. Thomas, R. Raja, G. Sankar, and R.G. Bell, *Nature*, **1999**, *398*, 227

48 G. Sankar, J. M. Thomas, *Topics in Catalysis*, **1999**, *8*, 1

49 F. Corà, G. Sankar, C. R. A. Catlow, J. M. Thomas, *Chem. Commun*, **2002**, 734

50 G. Sankar, D. Gleeson, J. M. Thomas and A. D. Smith, *J. Syn Rad*, **2001**, *8*, 625

51 A. M. Prakash, M. Hartmann, Z. Zhu, L. Kevan, *J.Phys. Chem. B*, **2000**, *104*, 1610.

52 Z. Zhu, T. Wasowicz, L. Kevan, *J. Phys. Chem B*, **1997**, *101*, 10763

53 D. Arieli, A. Delabie, D. E. W. Vaughan, K. G. Strohmaier, D. Coldfarb, *J. Phys. Chem. B*, **2002**, *106*, 7509.

54 N. N. Tušar, A. Tuel, I. Arčon, A. Kodre, V. Kaučič, *Prog. Zeolites. Microp. Mater*, **1997**, *105*, 501.

55 A. Tuel, I. Arčon, N. N. Tušar, A. Meden, V. Kaučič, *Micro. Mater*, **1996**, *7*, 271

56 A. Philippo, F.Salehiard, D.P. Luigi, M. W. Anderson, *J. Phys.Chem. B*, **1998**, *102*, 8974

57 A. Buchholz, W. Wang, A.Arnold, M. Xu, M. Hunger, *Micro.Meso. Mater*, **2002**, *56*, 267

58 A. Buchholz, W. Wang, A.Arnold, M. Xu, M. Hunger, *Micro.Meso. Mater*, **2003**, *57*, 157

59 F. Salehirad, M. W. Anderson, *J. Catal.* **1998**, *177*, 189.

60 L. Frunza, J. Pelgrims, H. Leeman, P. V. D. Voort, E. F. Vansant, R. A. Schoonheydt, B. M. Weckhuysen, *J. Phys. Chem, B*, **2001**, *105*, 2677

61 N. J. Henson, A. K. Cheetham and J.D.Gale, *Chem. Mater*,**1996**, *8*, 664

62 R. Ruiz-Salvador, G. Sastre, D. W. Lewis and C. R. A. Catlow, *J. Mater. Chem.*, **1996**, *6* , 1837

63 J. D. Gale and N. J. Henson. *J. Chem. Soc., Faraday Trans*,**1994**, *90*, 3175

64 J. Sauer, K. Schröder. *Collect. Czech. Commun*, **1998**, 63

65 A. M. Márquez, J. Oviedo, J. Fernández-Sanz, J. J. Benitez, J. A. Odriozola, *J. Phys. Chem. B*, **1997**, *101*, 9510

66 F. Corà, C. R. A. Catlow, *J. Phys. Chem B*, **2001**, *105*, 10278

67 G. Poulet, P. Sautet, A. Tuel, *J. Phys. Chem B*, **2002**, *106*, 8599

68 Dmol User Guide, Semptember 1997. Molecular Simulations Inc., San Diego, **1997**

69 J. G. González, J. de la Cruz Alcaz, A. R. Ruiz-Salvador, A. Cómez, A. Dago, Carlos de las Pozas, *Micro. Meso. Mater*, **1999**, *29*, 361

70 J. G. González, C. de las Pozas, *Chem. Mater*, **2002**, *14*, 2817

71 N. J. Henson, P. J. Hay, A. Redondo, *J. Phys. Chem. A* , **2000**, *104*, 2423

72 H. Y. Cheng, E. Yang, C. J. Lai, K. J. Chao, A. C. Wei, J. F. Lee, *J. Phys. Chem. B*, **2000**, *104*, 4195

73 F. Corà, C. R. A.Catlow, A. D'Ercole. *J.Mol.Catal A.* **2001**, *166*, 87

74 F. Corà, G. Sankar, C. R. A. Catlow, J. M. Thomas, *Chem. Commun*, **2002**, 734

75 Y. Jeanvoine, J. G. Ángyán, G. Kresse and J. Hafner. *J. Phys.Chem. B*, **1998**, *102*, 5573

76 V. Termath, F. Haase, J. Sauer, J. Hutter, and M. Parrinello, *J. Am. Chem. Soc*, **1998**, *120*, 8512

77 Y. Jeanvoine, J. G. Ángyán, G. Kresse and J. Hafner. *J. Phys.Chem. B*,**1998**, *102*, 7307

Chapter 2 Computational techniques

The aim of this chapter is to introduce the basic concepts underlying computational methods, in particular those that have been applied during this thesis work. Both *ab initio* quantum mechanical (QM) techniques, and methods based on interatomic potentials (IP) will be surveyed.

2.1 *Ab-initio* QM techniques

Ab-initio QM methods exploit the laws of quantum mechanics to obtain information about the system under study. Although computationally demanding, these techniques allow us to perform accurate calculations on the structural and electronic properties of a wide range of materials. The absence of phenomenological parameters, in fact, makes these methods generally applicable, also to systems that are difficult to study experimentally and on which experimental information is sparse.

The laws of quantum mechanics state that the electronic and structural properties of a given material, with M nuclei and N electrons, can -in principle- be calculated by solving Schrödinger's equation, which is expressed as follows:

$$\hat{H}\Psi = E\Psi \qquad (2.1)$$

where $\hat{H}$ is the Hamiltonian, a differential operator representing the total energy of the system, E is the energy of the state, and Ψ is the wavefunction. The latter depends on all degrees of freedom, *i.e.* the coordinates of all particles in the system.

The square of the wave function, $|\Psi|^2$, is interpreted as the probability distribution of the particles within the system. The Hamiltonian operator $\hat{H}$ is defined as the sum of the kinetic and potential operators of all particles of the system (electrons and nuclei):

$$\hat{H} = \hat{T} + \hat{V}. \qquad (2.2)$$

The Schrödinger's equation, however, can only be solved exactly for hydrogen atoms and one-electron systems like He^+; for systems with two or more electrons, and solids obviously fall in this category, approximations are needed.

The Born-Oppenheimer approximation[1] exploits the fact that electrons are lighter than nuclei, and therefore move more quickly. For instance, calculations show that the average speed of an electron in the hydrogen molecule is approximately 1000 times the average speed of a proton.[2] Therefore electrons are assumed to adjust instantly to any changes in the position of the nuclei. This approximation separates the motion of the electrons from that of the nuclei, and allows the Schrödinger's equation to be solved only for the electrons in a field of fixed nuclei:

$$\hat{H}_e(R)\,\Psi_e(r, R) = E^{eff}(R)\,\Psi_e(r, R), \qquad (2.3)$$

where the electronic Hamiltonian operator is written as a sum of the kinetic energy of the electrons, electrostatic forces between all charged particles, and exchange forces between the electrons

$$\hat{H}_e = \hat{T}_e(r) + \hat{V}_{ne}(r, R) + \hat{V}_{ee}(r) + \hat{V}_{nn}(R), \qquad (2.4)$$

In equation 2.4, T_e is the kinetic energy of the electrons, V_{ne} is the external potential term, and accounts for the classical electrostatic attraction forces between electrons and nuclei, V_{ee} is the electron–electron repulsion potential, and V_{nn} is the nuclear-nuclear repulsion; the latter does not depend on electron coordinates, and is constant for a given nuclear geometry, R.

Solving equation 2.3 for the electronic wavefunction will produce the effective nuclear potential function E^{eff} (R), which is used as the potential for the nuclear Hamiltonian.

$$H_n(R) = T_n(R) + E^{eff}(R) \qquad (2.5)$$

The Hamiltonian of equation 2.5 is used for studying the nuclear motion, describing the vibrational, rotational, and translational states of the nuclei, as well as the relative energy of different configurations; for instance, if another set of nuclear positions is chosen, this will lead to a new electronic wavefunction and a new total energy. The relative energies between different structures are obtained in this way; the stable structure will have the lowest total energy. This nuclear configuration is also indicated as equilibrium structure of the system studied.

Two major approaches based on the QM formulation are widely applied in solids, namely Hartree Fock (HF) and Density Functional Theory (DFT). The most apparent difference between the two theories lies in the fact that HF is a wavefunction-based theory, whereas DFT is an electronic density approach. In the next two sections, we shall describe both theories and highlight their differences.

2.2 Hartree Fock theory

The Hartree Fock theory uses the original many-electron wavefunction of equation 2.3 and adopts a further approximation, which is based on the separation of the many-electron wavefunction into a set of one-electron wavefunctions. In the process of achieving this separation, the wave function is first expressed as a product of one-

electron wave functions Φ_i, each of which depends on the coordinate and spin of a single electron:

$$\Psi_e(1, 2, \ldots..N) = \Phi_1(1) \cdot \Phi_2(2) \ldots.. \Phi_N(N) \qquad \textbf{(2.6)}$$

The wavefunction of equation 2.6 does not satisfy the Fermi-Dirac statistics, which states that the wave function of fermions (*e.g.* electrons) must be antisymmetric with respect to the exchange of two particles (*i.e.* it must change sign when the coordinates of two electrons are exchanged).

The antisymmetric requirement of the many electron wave function is obtained when the latter is written as an antisymmetric product of the one-electron wave functions Φ_i, *i.e.* of functions Ψ_e, of the same type as equation 2.6. Slater determinants are used to create a linear combination of products with alternating signs corresponding to all possible exchanges of electron coordinates:

$$\Psi_e(1, 2, \ldots..N) = 1/\sqrt{N!}\ \det[\Phi_1(1) \cdot \Phi_2(2) \ldots.. \Phi_N(N)] \qquad \textbf{(2.7)}$$

The energy corresponding to the wavefunction Ψ_e (hereafter simply indicated as Ψ) is obtained by integration:

$$\mathbf{E} = \frac{\langle \Psi | \hat{H} | \Psi \rangle}{\langle \Psi | \Psi \rangle} = \frac{\int \Psi^* \hat{H} \Psi d\tau}{\int \Psi^* \Psi d\tau} \qquad \textbf{(2.8)}$$

The variational principle is then used to find equations that allow the actual determination of the one-electron wave functions. The latter states that for any trial wave function, the expectation value of the energy can never be less that the true ground state energy E_0, and is always an upper estimate to the exact total energy.

$$\mathbf{E_0 \leq} \frac{\int \Psi^* \hat{H} \Psi d\tau}{\int \Psi^* \Psi d\tau} \qquad \textbf{(2.9)}$$

Therefore, given approximate many-electron wave functions, the solution to the Schrödinger's equation can be calculated by varying each one-electron wave function in such a way that it minimises the total energy:

$$\frac{\partial E}{\partial \Phi_i} = 0. \qquad (2.10)$$

In this way, one finds conditions for each wave function in the form of one electron wavefunctions, known as Hartree Fock equations:

$$\hat{F}\Phi_i = \left[-\frac{1}{2}\nabla^2 + V_c + \mu_x^i \right]\Phi_i = \varepsilon_i \Phi_i . \qquad (2.11)$$

The Hartree Fock equation resembles the Schrödinger equation, in a way that the former is also an eigenvalue problem, but the operator in the left hand of equation 2.11, is not the Hamiltonian operator, as previously described for the Schrödinger's equation, but it is the Fock operator, $\hat{F}$. The latter describes the effect of all particles, including the other N-1electrons, on the solution of one-electron of the system. The expression for the Fock operator consists of the one electron kinetic energy term $(-\frac{1}{2}\nabla^2)$, a Coulomb potential term (V_c), which describes the electrostatic potential generated by all charged particles in the system, *i.e.* electrons and nuclei, and the exact-exchange operator μ_x^i, which is *non local.* The effects of the exchange operator μ_x^i are first the effective reduction of the electrostatic repulsion between electrons of equal spin, and second the cancellation of a self Coulomb interaction of electrons, which means that one electron does not interact with itself.[3]

The Hartree Fock approximation describes the motion of one electron in the average field created by all other electrons of the system. This approximation neglects the direct correlation in the motion between electrons, especially those of opposite spin,

which leads to an overestimation of the electron repulsion potential, and a systematic overestimation of the total energy. The missing correlation effect represents the main limitation of the HF theory.

In principle, the HF approach can be improved, by accounting for correlation. This is usually achieved through the so-called post-HF methods, such as the Configuration Interaction (CI) and the Møller-Plesset (MP) schemes[5], or by estimating the correlation energy using one of the correlation-only functionals available in the Density Functional Theory, applied to the HF equilibrium electronic density. The latter scheme is also called correlation a posteriori (HF +correlation).[3] Post-HF methods, such as MP and CI, have been developed for molecular systems; their application for the study of solids, however, is still in an early stage of development, which makes them unavailable for the study of solids.

2.2.1 Solving Hartree Fock equations for molecular systems

Let us now go back to the solution of the Hartree Fock equations:

$$\hat{F}\Phi_i = \varepsilon_i \Phi_i, \qquad \textbf{(2.12)}$$

in which $\hat{F}$ is the Fock operator, as described in equation 2.10. Solving this equation requires finding the eigenvalues ε_i, and eigenstates Φ_i for each electron in the system, including its spin dependence. Given the complexity of this problem, finding all the information was only made possible by Roothaan in 1951.[4] He suggested that the one-electron wave function can be expanded in a set of fixed basis functions (Linear Combination of Atomic Orbitals):

$$\Phi_i(r) = \sum_j^{Nb} \chi_j(r) c_{ij}, \qquad \textbf{(2. 13)}$$

where the basis set functions $\chi_j(r)$ as well as their number N_b have been chosen in advance, the index j categorizes different functions used, therefore only the expansion coefficient c_{ij} are varied. The energy of a given molecular system is then obtained by applying the variational principle

$$\frac{\partial E}{\partial c_{ij}} = 0. \qquad (2.14)$$

The algebraic expression for this variational principle is provided by the so-called Roothan-Hartree Fock equations:

$$FC=SCE, \qquad (2.15)$$

where F is the representation of the Fock operator $\hat{F}$ (see equation 2.12), S is the overlap matrix, which contains the overlap elements between basis functions, and C is the matrix of the c_{ij} coefficients.

$$F_{jk} = \langle \chi_j | F | \chi_k \rangle \qquad (2.16)$$

$$S_{jk} = \langle \chi_j | \chi_k \rangle \qquad (2.17)$$

The indices j and k refer to two basis functions.

2.2.2 Solving Hartree Fock equations for periodic systems

When dealing with infinite systems such as solids, the solution of the Roothan-Hartree Fock equations becomes impossible, since the dimension of the representative matrices coincides with the number of basis functions employed, which increases linearly with the number of atoms in the system. A solution is possible for crystalline solids, in which the structure can be described via the periodic translation in the three dimensions of a limited set of atoms, known as a unit cell. The electronic wavefunction must have the same 3D translational symmetry as the crystal structure.

To construct basis functions which satisfy the periodicity of solids, the Bloch theorem is applied. This theorem introduces new functions which are defined as

$$\Phi_k(r) = U_k(r)e^{ikr}, \qquad (2.18)$$

where the function $U_k(r)$ has the three-dimensional periodicity of the crystal lattice, and k is known as a wave vector.

$$U_k(r+a_n) = U_k(r), \qquad (2.19)$$

where a_n is a vector, the latter may be expressed in terms of three primitive translation vectors a_1, a_2, a_3 as follows:

$$a_n = n_1a_1 + n_2a_2 + n_3a_3. \qquad (2.20)$$

The type of basis functions employed in equation 2.18 will be discussed in section 2.2.4

The matrix representation of the Roothan–HF equation (2.15) for a crystalline solid will have the same dimension as the number of basis functions in the primitive unit cell and equation 2.15 is solved separately for each value of the wave vector k.

$$\mathbf{F(k)C(k)= S(k)C(k)E(k)} \qquad (2.21)$$

2.2.3 Application of the Hartree Fock theory to open shell systems

The *Restricted Hartree Fock (RHF)* theory describes systems with even number of electrons, in a way that each spatial orbital is restricted to have two electrons, one with α (up, +1/2) and one with β (down, -1/2) spin. The one-electron wavefunction expansion in equation 2.12 is then employed together with the variational method (equation 2.13) to derive the optimal values of the coefficients.

Open shell systems, such as molecules with odd number of electrons, radicals, ferromagnetic and antiferromagenetic solids, contain unpaired electrons. These systems are treated in the HF theory via two approaches, called UHF and ROHF.

In the *Unrestricted Hartree Fock (UHF)* approach two sets of molecular orbitals are used: one for electrons of α spin and the other for electrons of β spin:

$$\Phi^{\alpha}_{i}(r) = \sum_{j}^{Nb} \chi_{j}(r) c^{\alpha}_{ij} \qquad (2.22)$$

$$\Phi^{\beta}_{i}(r) = \sum_{j}^{Nb} \chi_{j}(r) c^{\beta}_{ij} \qquad (2.23)$$

The variational principle is then applied to obtain the optimal coefficients for α and β orbitals separately. Therefore, UHF is twice as expensive as the RHF approach.

An alternative solution is given by the *Restricted Open Shell Hartree Fock (ROHF)* theory. The latter uses the same set of spatial orbitals to describe both α and β electrons. These orbitals can be populated either by paired electrons (with α and β spin), or by only one electron. This approach is less commonly used compared to RHF and UHF as it gives less accurate energies, due to the constraints posed on the solution by the choice of having $C^{\alpha}_{ij}=C^{\beta}_{ij}$. Figure 2.1 illustrates RHF singlet, and ROHF and UHF doublet states.

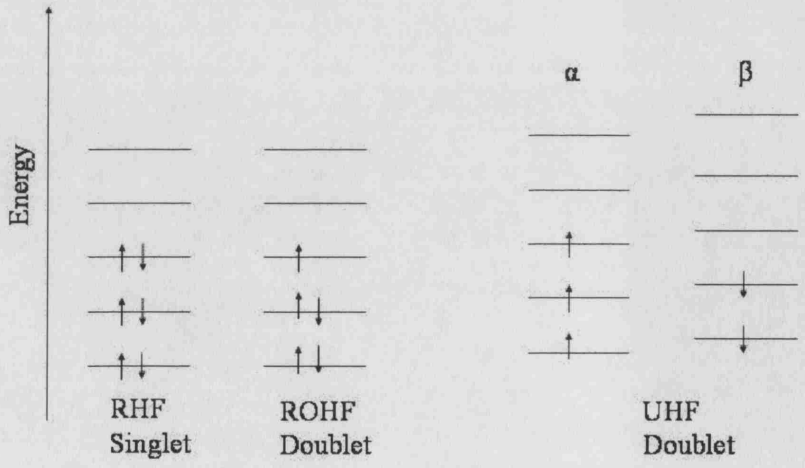

Figure 2.1: *Illustration of RHF singlet, and ROHF and UHF doublet states. (Adapted from reference 5)*

2.2.4 Basis set

Let us now go back to the Roothaan HF equations (2.12), where the one-electron wave function is expressed as a linear combination of basis functions χ_j. In order to describe accurately the solution, a large number of basis functions are required, and in principle the "exact" solution is achieved for a complete (infinite) basis set. However, including more basis functions also increases the computational cost. Hence, the right balance between the accuracy and cost depends on the right choice of the representative basis set.

Basis sets are classified into two broad categories: *localised* and *delocalised* functions. Examples of the first category include the Slater-type orbitals (STO) and Gaussian basis sets (GTO), whereas planewave basis sets are the most commonly used for the second category. Mixed basis sets of localised and delocalised basis functions are also possible; these are applied in computational schemes that divide the space into atomic spheres, within which localised basis sets are employed, and interstitial regions where the electron density is represented by plane wave functions.

Localised basis sets are associated with an atomic centre, and are expressed in terms of a radial and an angular-dependent part; the latter is a spherical harmonic, which is the exact angular solution for the one-electron problem in a spherically symmetric potential. The radial function depends on the spherical part of the potential.[5] This is approximated by localised basis sets using the assumption that around each atomic centre in a molecule the electronic wave function resembles that of an isolated atom. Although such an assumption is not entirely true, as the wave function is likely to change when atoms are in a molecule or in solids, it represents a suitable reference for the basis set. The disadvantages of choosing localised basis sets, however, are the

complexity in calculating matrix elements (see equations 2.15 and 2.16), and the non orthogonality of the basis set.

The second type of basis set is formed by *delocalised* basis functions. Their formulation is based on a completely different approach. Plane-wave functions have three dimensional periodicity, and therefore such basis functions are especially appropriate for 3D solid systems. Their use leads to a simpler algebra compared to localised basis set; however they are defined over the entire unit cell, and no longer associated with a particular atom. The number of plane waves needed for an accurate description of the electronic density depends on the size of the unit cell and not on the number of the constituent atoms; it is in general very large because plane-wave functions bear no resemblance to the shape of the electronic density in chemical systems. This is particularly true for core electrons, that are extremely well localised around the nucleus of the atom to which they belong.

In order to reduce the computational cost, delocalised basis sets use the so-called *pseudopotential approximation* to describe core states. The latter exploits the fact that most physical properties are determined only by the valence electrons. The pseudopotential removes the core electrons and replaces them with a smooth effective potential acting on the valence electrons.

Plane wave basis sets are more suited to describe metallic systems, where electrons are delocalised.

2.3 Density Functional Methods

In this section we shall underline the basic concepts of density functional theory (DFT). Although in our calculations we have used mainly the HF theory, DFT

techniques are widely applied in the study of solids, which is the main area of work of this thesis.

Density Functional theory is based on two theorems, proved by Hohenberg and Kohn in 1964[6], and a computational scheme proposed by Kohn and Sham in the following year.[7]

The first theorem states that *the electron density ρ(r) determines the external potential.*[6] Since the Hamiltonian in equation 2.4 is specified by the external potential and depends on the number of electrons N (N can be obtained from the density by integration over all space), this implies that the ground state wavefunction Ψ, and energy can be obtained from the electron density. The Hohenberg and Kohn theory, therefore means that there is a 1:1 correspondence between the electronic density of a system and its wavefunction, and we can write the energy of the Schrödinger's equation as a functional of the electron density. For convenience the functional is decomposed into three terms:

$$E[\rho] = T[\rho]+V_{ext}[\rho]+V_{ee}[\rho] \qquad \textbf{(2.24)}$$

The nuclear-nuclear repulsion is constant according to the Born-Oppenheiner approximation. V_{ee} [ρ] is the functional describing the electron-electron interaction. The variational theorem of Hohenberg and Kohn, The latter states that for any trial density $\rho_t(r)$ that satisfies the constraint of:

$$\int \rho_t(r)\, dr = N \qquad \textbf{(2.25)}$$

then

$$E[\rho_t] \geq E_0 \qquad \textbf{(2.26)}$$

where E_0 is the exact energy of the system investigated. The Kohn and Sham formulation of DFT attempted to approximate the kinetic energy of equation 2.23,

and electron-electron functionals.[7] They introduced a new fictitious system of N non-interacting electrons described by a single determinant of N one–electron wavefunctions Φ_i (as the Slater determinant in the HF theory). In this system the kinetic energy and the electron density are known from the one–electron wave function:

$$T_s[\rho] = -\frac{1}{2}\sum_i^N \left\langle \Phi_i \middle| \nabla^2 \middle| \Phi_i \right\rangle . \qquad \textbf{(2. 27)}$$

In the equation above, the suffix **s** means that this is not the true kinetic energy, but that of a system of non interacting electrons, whose corresponding one-electron wavefunction $\Phi_i(r)$ generates the exact density:

$$\rho(r) = \sum_i^N \left\langle \Phi_i \middle| \Phi_i \right\rangle . \qquad \textbf{(2. 28)}$$

In real systems the electrons are interacting, hence $T_s[\rho]$ does not provide the total kinetic energy. The remaining kinetic energy can be expressed as:

$$T_r[\rho] = (T[\rho] - T_s[\rho]) \qquad \textbf{(2. 29)}$$

The energy functional in equation 2.24 is rearranged as:

$$E[\rho] = T_s[\rho] + V_{ext}[\rho] + J[\rho] + E_{xc}[\rho], \qquad \textbf{(2. 30)}$$

where J is the classical Coulomb interaction between two charge distributions:

$$J[\rho] = \frac{1}{2}\iint \frac{\rho(r)\rho(r')}{|r - r'|} dr dr', \qquad \textbf{(2. 31)}$$

and the 4th term in equation 2.30 is the exchange-correlation energy, $E_{xc}[\rho]$. It accounts for the errors made in using a non-interacting kinetic energy and treating the electron-electron interaction classically:

$$E_{xc}[\rho] = (T[\rho]-T_s[\rho]) + (V_{ee}- J[\rho]) \qquad (2.32)$$

E_{xc} is called exchange-correlation energy because it accounts for exchange energy and the correlation in the motion of the individual electrons (the missing part in the HF theory). E_{xc} also accounts for the effects arising from the kinetic energy of a system of non-interacting electrons.

The solution of the Kohn-Sham (KS) equation is, in principle, exact; however, the expression for the exchange-correlation functional $E_{xc}[\rho]$ is unknown. If such an approximate expression is found, one can apply the variational principle of the Kohn-Sham theory. Since the electron density is expressed in terms of one-particle wave functions (see equation 2.26), one can find a set of one-particle wavefunctions that minimise the energy, and satisfy the Kohn-Sham equations:

$$\left[-\frac{1}{2}\nabla^2 + V_{ext}(r) + \int \frac{\rho(r')}{|r-r'|}dr' + V_{xc}(r)\right] \Phi_i(r) = \varepsilon_i \Phi_i(r) \qquad (2.33)$$

The Kohn-Sham equations have the same formal structure as the Hartree-Fock equations (see equation 2.11), however the theories are very different. The Kohn-Sham approach tries to achieve an exact correspondence of the one electron density and ground state energy with the many body system described by the Shrödinger's' equation, providing that the exact functional of $E_{xc}[\rho]$ is found. The HF theory seeks an approximation to the many electron wave functions, by using a single determinant, and ignores correlation effects.

The usefulness of DFT theory relies entirely on the approximations used to construct a working formulation for the exchange-correlation functionals $E_{xc}[\rho]$, and many different functionals are currently available. In the following sections, we shall highlight the most commonly used.

2.3.1 Local Density Approximation (LDA)

The first approximation of the exchange-correlation functional is based on the local density approximation (LDA)[8,9].It refers to the uniform electron gas, in which the local exchange-correlation energy per electron depends on the local charge density only:

$$E_{xc}[\rho] = \int dr \varepsilon_{xc}(\rho)\rho(r) , \qquad (2.34)$$

where $\varepsilon_{xc}(\rho)$ represents the exchange–correlation energy per particle for a uniform electron gas of density ρ. The latter can be calculated exactly for the homogenous electron gas, and is expressed as a sum of the correlation and exchange contributions

$$\varepsilon_{xc}(\rho) = \varepsilon_x(\rho) + \varepsilon_c(\rho). \qquad (2.35)$$

Parameterisations of the correlation functional, $\varepsilon_c(\rho)$ have been proposed by Perdew-Zunger, [10] and Vosko-Wilk-Nusair.[11] The exchange term is calculated by Dirac.[12]

The LDA approximation has performed well for systems where the electronic density is more homogenous, and does not rapidly change with space, for instance systems with delocalised electrons such as metals. LDA, however, showed weaknesses in terms of describing systems with localised electrons, either molecules or insulating solids. It often gives too short bond lengths and overestimates the binding energies.[13,14] Such weaknesses arise from two characters of the LDA: first, the formulation of the exchange correlation energy depends on the electron density in one point of space, which means LDA does not describe accurately the electronic rearrangement in bonds. Therefore LDA can be unreliable in terms of describing the nature of bonding in molecules and solids. Second, the electron-electron Coulomb interaction energy in equation 2.31 includes the contribution arising from the

interaction of each electron with itself (self interaction). This is cancelled in the HF method by the self-exchange term, but not in DFT.

2.3.2 Generalised Gradient Approximation Functionals

The local description of the exchange-correlation term in LDA is improved by accounting for the non uniformity of the electronic distribution in chemical systems. The local character of the E_{xc} term in the LDA is corrected by the inclusion of terms that depend upon the gradient of the density, and not only on its value, at each point of space: $E_{xc} = E_{xc}[\rho,\nabla\rho]$. This formulation is called Generalised Gradient Approximation (GGA). Several approaches have been made to find expressions for the exchange-correlation functional $E_{xc}[\rho,\nabla\rho]$, for example those of Becke-Lee-Yang-Parr (B-LYP)[15,16], Hampercht-Cohen-Tozer-Handy (HCTH),[17] Perdew-Wang (PWGGA) [18,19], Perdew 86 (P86)[20], Perdew-Burke-Ernzerhof (PBE).[21] Expressions for the exchange-correlation functional are obtained via analytical functions, whose parameters are obtained either by fitting to experimental data, [15-17]or derived from the principles of quantum mechanics.[18-21] GGA methods provide a more flexible description for the electronic distribution in chemical systems; therefore GGA improves on the LDA description of bonds lengths and binding energies of molecular systems. However, as in LDA, GGA does not solve the self–interaction problem, which arises from the original KS formalism of DFT. Hence this argument can be applied to all DFT methods that employ a functional of the total electronic density ρ. The flexibility of GGA can be further increased in a generation of functionals that depend on the second derivative of the density, referred to as Meta-GGA,[22,23,24] which are typically represented as:

$$E_{xc} = \int \rho(r)\, \varepsilon_{xc}(\rho, \nabla\rho, \nabla^2\rho)\, dr. \qquad \textbf{(2. 36)}$$

2.3.3 Hybrid Exchange Functionals:

One of the latest developments in DFT is the use of so-called hybrid functionals, in which the HF and DFT formulation of exchange forces is mixed. The exchange-correlation energy E_{xc} in hybrid functionals is written as a linear combination of its density functional and Hartree-Fock theory expressions:

$$E_{xc}^{hybrid} = \alpha (E_x^{HF} - E_x^{DFT}) + E_{xc}^{DFT} \qquad (2.37)$$

where the value of the mixing parameter α is treated as empirical parameter, and can range between 0 and 1.

The most popular hybrid functional has been proposed by Becke, the so-called B3LYP scheme[25], in which the value of α has been obtained by fitting experimental data for molecular systems. Such a derivation provides the optimal value of $\alpha = 0.20$. The inclusion of some degree of exact HF exchange to the GGA and LDA functionals enables the resulting hybrid-functionals to account for the self interaction problem, as well as for the non uniformity of the electron density in solid and molecular systems. Corà *et al*[26] have examined the performance of hybrid (HF-DFT) exchange functionals within Density Functional Theory in describing the properties of crystalline solids. In this work they have allowed the value of α to vary systematically from 0 to 1 for each system examined. They have concluded that the best fraction of HF exchange to be included in the functionals varies according to a combination of system and property under investigation. For solid systems a value of α which is higher than that proposed by Becke of 0.2 is required. This requirement is associated with the Madelung field, which creates a strong localising field in the crystal that is not present in molecules.

Although *ab-initio* QM techniques are being applied increasingly for solids, one should keep in mind that these methods are computationally very expensive, and are still limited to few tens or perhaps hundreds of atoms. For more complex structures, such as large pores zeolites and AlPOs, QM calculations can be extremely expensive and very much time consuming, especially for units cells with little or no symmetry. To be feasible on a routine scale, the study of systems involving hundreds or thousands of atoms requires a simplified description of forces, such as the one achieved in the semiclassical methods, based on interatomic potentials. These methods are described in the next section.

2.4 Semi-classical methods

Unlike the quantum mechanical methods described above, techniques based on interatomic potentials (IP) omit the explicit treatment of electrons. The total energy of the system is instead expressed as a function of the nuclear coordinates only, and depends on bond distances and angles in the structure examined via a numerical or analytical relationship. IP-based techniques have been applied successfully to a wide range of chemical problems, ranging from the solid state[27,28] to large organic molecules.[29] Different mathematical expressions are usually adopted for the construction of the potential model, which depend on the nature of bonding in the system under study.

2.4.1 Interatomic Potential functions

Interatomic potentials describe, in analytical or numerical form, the forces between atoms. By evaluating these forces, it is possibly to calculate the total energy with respect to the nuclear coordinates.

In the case of crystalline solids, the potential energy function U (r_1, r_2, ..., r_N) describes the cohesive energy as a function of the nuclear coordinates of the component atoms (r_1 , r_2 , ...r_N).

$$U = \sum_{i}^{N}\sum_{j}^{N}\Phi_{ij}(r_i, r_j) + \sum_{i}^{N}\sum_{j}^{N}\sum_{K}^{N}\Phi_{ijk}(r_i, r_j, r_k) + \ldots \quad (2.38)$$

The potential energy function is expanded in terms of two-body terms, which depend only on the relative position of pairs of atoms, three-body terms that depend on the position of three atoms, etc. For molecules and molecular solid systems, the expansion could be extended to include higher four body terms that describe the dihedral angle between four atoms. For inorganic crystalline solids, however, the expansion to higher body terms is not commonly included. For ionic solids, the potential energy Φ_{ij} is often expressed by including only the two-body term; this includes both Coulombic (long range effects) and non-Coulombic terms (short range).

$$\Phi_{ij}(r_i, r_j) = \frac{q_i q_j}{r_{ij}} + V_{ij}(r_i, r_j), \qquad (2.39)$$

where q_i is the net charge on the ion i. The Coulombic terms, with their $\frac{1}{r}$ dependence, are long-ranged in nature, which makes the summation of equation (2.39) difficult to converge in real space. The method of Ewald[30,31] provides a solution to this problem, and is currently used in most modern simulation codes, including QM programs. This technique divides the electrostatic sum into two parts: the first (at short distance) is summed in real space, while the second (at longer distance) is computed in reciprocal space. On the other hand, the non-Coulombic term, which is of short range nature, converges rapidly, and a cut off distance can be employed to further minimise the computational time.

The non-Coulombic terms combine repulsive and attractive forces acting between ion pairs. The repulsive interactions arise from the short-range repulsion between the neighbouring closed shell electron configurations. The attractive forces result instead from dispersion forces and the formation of instantaneous dipoles (the Van der Waals interaction) and the covalency of the system.

For ionic and semi-ionic solids[32], the short range forces are often described by the following analytical function, known as the Buckingham potential:[33]

$$V_{ij}= A_{ij} \exp (-r_{ij} / \rho_{ij}) - (C_{ij} / r^{6}_{ij}), \qquad \textbf{(2. 40)}$$

in which the exponential expression represents the hardness of the ion, while the r^{-6} term represents the Van der Waals interactions.

For a description of interactions between ions bonded by a partly covalent bond, a Morse potential is sometimes preferable:

$$V_{ij}= D_{ij} [1-\exp[-\alpha_{ij}(r_{ij}-r_e)]], \qquad \textbf{(2. 41)}$$

where D_{ij} is the dissociation energy of the bond between the two ions i and j, r_e is the equilibrium bond length, and α_{ij} is a constant related to the stretching force constant k_{ij}, and can be determined from spectroscopic data

$$\alpha_{ij} = \sqrt{\frac{k_{ij}}{2D_{ij}}} . \qquad \textbf{(2. 42)}$$

To describe rare-gas and molecular crystals, the Lennard-Jonnes potential is commonly used. The latter has the following expression:

$$V_{ij}= A_{ij} r_{ij}^{-12} - B_{ij} r_{ij}^{-6} \qquad \textbf{(2. 43)}$$

The inclusion of many–body effects is sometimes necessary to model systems with directional covalent bonding, such as zeolite frameworks and molecular solids. This is usually accomplished via a three-body angular term, which describes the energy required for bending an angle formed by three atoms. It is usually expanded as a Taylor series around the equilibrium bond angle, and terminated at the second order, giving rise to an angle bending potential[34] of the following form:

$$E(\Theta) = \frac{1}{2} k_b(\Theta - \Theta_0)^2, \qquad (2.44)$$

where Θ is the angle between the three atoms and Θ_0 is its equilibrium value; k_b is the appropriate force constant. For more accuracy, higher orders of Taylor expansion can also be included.

2.4.2 Shell model

The effect of ion polarisability in ionic and semi-ionic solids described via interatomic potentials can be incorporated by the use of the shell model, originally developed by Dick and Overhauser[35]. The ions are modelled as a massive core charged q_{core}, which bears the mass of the ion, linked by a harmonic spring constant k to a massless shell charged q_{shell}. This simple mechanical treatment of the polarisability is illustrated in Figure 2.2.

The free atom polarisability α, is given by $\alpha = \frac{q^2}{k}$, where q is the total charge on the ion.

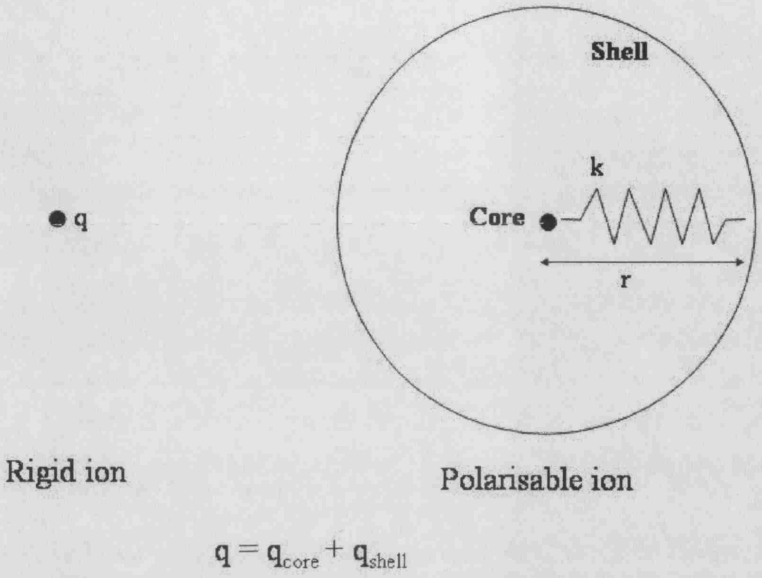

Figure 2.2: *Illustration of the shell model of ionic polarisability*

2.4.3 Energy minimisation techniques

We have seen in previous sections that different Hamiltonians can be applied to calculate the energy of a particular system; the energy is a function of all nuclear coordinates and is used to describe the potential energy surface of a given system.

When modelling chemical systems, be they molecules or solids, we are interested in knowing the structures that have minimum energy. Any movement away from the minimum leads to structures with higher energy. The potential energy surface is very complex as it is a multidimensional function of the coordinates of the system under investigation, and can contain several maxima and minima; the latter can be either local or global (see Figure 2.3).

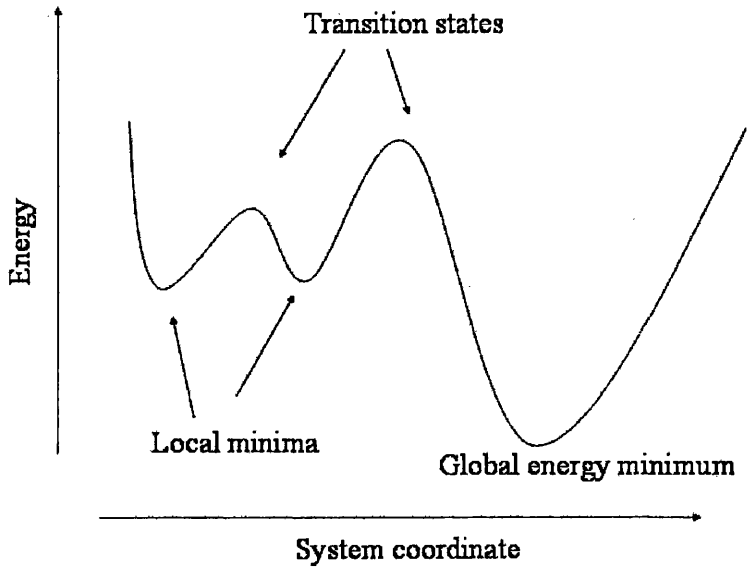

Figure 2.3: *A simplified (1D) representation of the potential energy surface with different types of minima and transition states.*

The minimum points on the potential energy surface can be located using energy minimisation techniques; these search for the points on the potential energy surface where the gradient of the energy with respect to all nuclear coordinates function is zero:

$$\frac{\partial U}{\partial r_i} = 0, \qquad \textbf{(2. 45)}$$

Energy minimisation techniques may employ first and in some cases also second derivatives of the energy, in order to facilitate the search for the points with zero gradient, *i.e.* maxima and minima. Commonly used energy minimisation alghorithms include Steepest Descent, Conjugate Gradients, and Newton Raphson Methods. The reader is directed to references[2,4,5] for more details about energy minimisation techniques.

2.4.4 Parametrisation

All the parameters of the potential functions need to be fitted to reproduce available reference data.

The availability and the accuracy of suitable interatomic potentials is vital to the simulation of atomistic properties of materials. Different approaches can be followed for the derivation of such parameters, which can be classified as empirical and non-empirical, according to the way the reference data are obtained. Non–empirical parameterisation procedures seek to determine the parameters by attempting to fit data from high level calculations, such as *ab-initio* QM methods; usually the reference data are the equilibrium geometry and the energy surface corresponding to structural distortions. Empirical methods, in contrast, attempt to derive the interatomic potential parameters by fitting to known experimental data of the system studied. Observables such as equilibrium structure, lattice energy, dielectric and elastic constants, when available, can be used. The parameters of the interatomic potentials are adjusted in an iterative way in order to achieve a best fit to the experimental or theoretical properties.

The interatomic potentials are in general applied to the study of structures that have not been included in the fitting database. The transferability requirement, however, is not guaranteed when applying any of the methods outlined above; therefore, care should always be taken when using the interatomic potentials outside the range of geometries represented in the reference data.

References

1 M. Born and J. R. Oppenheimer, *Ann .Phys,* **1927**, *84*, 457

2 D.O. Hayward, *Quantum Mechanics for chemists*, Royal Society of Chemistry, 2002, p 140.

3 C. Pisani, R. Dovesi, C. Roetti, *Quantum Mechanical Calculations of the Properties of Crystalline Materials*, Lecture Notes in Chemistry, Vol. 67, Springer **1996**.

4 A. R. Leach, *Molecular Modelling, Principles and Applications*, Harlow, Addison Wesley Longman ltd, **1996**.

5 F. Jensen, *Introduction to Computational Chemistry*, Denmark, John Wiley and Sons, **1999**.

6 P. Hohenberg and W. Kohn, *Phys. Rev.* **1964**, *B864*, 136

7 W. Kohn, L. J. Sham, *Phys. Rev.* **1965**, *A1133*, 140

8 R.G. Parr and W.Yang, *Density Functional Theory of Atoms and Molecules*, Oxford University Press, New York, **1989**

9 P. Hohenberg and W.Kohn, *Phys. Rev.* **1964**, *B864*, 136

10 J. P. Perdew, A. Zunger, *Phys. Rev.* **1981**, *B23*, 5048.

11 S.H.Vosko, L. Wilk and M. Nusair, *Can. J. Phys.* **1980**, *58*, 1200

12 P. M. A. Dirac, *Proc. Camb. Phil. Soc.* **1930**, *26*, 376.

13 M. Weinert, E. Wimmer, A. J. Freeman, *Phys. Rev.* **1982**, *B26*, 4571

14 C. R. A. Catlow, A. Cheetham, *New Trends in Materials chemistry*, NATO ASI Series, Kluwer Academic Publishers, Series C: Mathematical and Physical Sciences, **1995**,*498*, 209

15 A. D. Becke, *Phys Rev A*, **1988**, *38*, 3098

16 C. Lee, W. Yang, R. G. Parr, *Phys. Rev.* **1988**, B37, 785

17 F. A. Hamprecht, A.J. Cohen, D. J. Tozer, N. C. Handy, *J. Chem. Phys*, **1998**, 109, 6264.

18 J. P. Perdew, Y. Wang, *Phys. Rev.*, **1986**, *B33*, 8800,

19 J. P. Perdew, Y. Wang, *Phys. Rev*, **1992**, *B45*, 13244

20 J. P. Perdew, *Phys. Rev.*, **1986**, *B33*, 8822

21 J. P. Perdew, K. Burke, M. Ernzerhof, *Phys. Rev*, **1996**, *77*, 3865.

22 V. Tschinke, T. Zieglar, *Can. J. Chem*, **1989**, *67*, 460

23 R. Neumann, N. C. Handy, *Chem. Phys. Lett*, **1997**, *16*, 266

24 J. P. Perdew, S.Kurth, A. Zupan, P. Blaha, *Phys. Rev. Lett.* **1999**, *82*, 2544,

25 A. D. Becke, *J. Chem. Phys.* **1993**, *98*, 548.

26 F. Corà, M. Alfredsson, G. Mallia, D. S. Middlemiss, W. C. Mackrodt, R. Dovesi, R. Orlando, *The Performance of hybrid density functionals in solid state chemistry*, in J. McGrady and N. Kaltsoyannis (Ed), Density Functional Theory in Inorganic Chemistry, Springer-Verlag, Heidelberg, *Vol. 113*, 2004, *pp 171-232.*

27 C. R. A. Catlow, L. Ackermann, R. G. Bell, F. Corà, D. H. Gay, M. A. Nygren, J. C. Perieira, G.Sastre, B. Slater and P. E. Sinclair, *Faraday Discuss.*, **1997**, *106*, 1-40

28 C. R. A. Catlow, Ed, *Modelling the structure and reactivity in Zeolites*, First edition, Academic Press, London, **1992**

29 N. L. Allinger, *J. Am.Chem.Soc.*, **1977**, *99*, 8127

30 P. P. Ewald, *Ann.Physik*, **1921**, *64*, 253

31 M.P. Tosi, *Solid State Physics*, eds. F. Seitze and K. Turbill, Vol. 16, New York, academic Press, **1964**, p.1.

32 A. M. Stoneham and J. H. Harding, *Ann. Rev. Phys. Chem.*, **1986**, *37*, 35

33 R. A. Buckingham, *Proc. Royal. Soc,* London, **1936**, *A 168*, 264

34 M. J. Saunders, M. Leslie, C. R. A. Catlow, *J. Chem. Soc. Chem. Comm*, **1984**, 1271.

35 B. G. Dick, A. W. Overhauser, *Phys. Rev*, **1958**, *112*, 90

Chapter 3 Methodology

The goal of this thesis work is to study computationally the properties of metal doped AlPO frameworks. In particular we shall concentrate on two topics: first the chemistry that follows doping of AlPO frameworks with a wide range of di- and tri-valent ions; namely Mg^{2+}, B^{3+}, Ca^{2+}, Sr^{2+}, $Cr^{2+/3+}$, $Mn^{2+/3+}$, $Fe^{2+/3+}$, $Co^{2+/3+}$, Ni^{2+}, Ga^{3+} and Zn^{2+} in the Al framework site. Second the hydration of doped AlPO frameworks.

In this chapter we shall describe the models available to study *defects* in solids, and the methodologies applied in our work.

3.1 Defect models for AlPOs

When dopants are introduced in the structure of AlPOs, the framework substitution breaks the 3D periodicity of the host system; such a feature happens whenever a point defect occurs in a crystalline (periodic) system. There are three different models that are available to study point defects in crystals, in this case the metal substitution in AlPO frameworks:

- Isolated cluster approach
- Embedded cluster approach
- Supercell approach

The qualitative features of each model are described separately in the following sections.

3.1.1 Isolated cluster approach

This model of the defect involves taking a small molecular fragment (a cluster), which includes the dopant ion and its close crystalline environment, out of the crystalline material; if the creation of the cluster from the crystalline structure requires the cleaving of chemical bonds between border atoms in cluster and environment, the resulting dangling bonds are saturated by a proton or a hydroxyl group. When using the cluster model, we assume that the molecular fragment generated represents the crystalline material in a close neighbourhood of the dopant ion.

The isolated cluster approach has been widely applied to study problems concerning zeolites; these include structural properties, acidity, [1,2,3,4] reactivity of heteroatoms in zeolites, and reaction mechanisms of industrially important chemical reactions, such as the epoxidation of alkenes on titanosilicates.[5,6,7]

In principle, the larger the size of the cluster, the more accurate the description of the local environment of the dopant atom. In zeolites, for instance, the size of the cluster is measured in terms of the number of tetrahedral T sites in the cluster (see Figure 3.1). The use of a cluster model is convenient, as it is computationally inexpensive when compared with periodic models; the finite cluster size allows the use of high quality basis sets, and permits the inclusion of correlation effects by using methods based on DFT and post-HF Hamiltonians.

Cluster models can be sufficient in providing useful insight into the material under investigation; however, this method has two main limitations. The first concerns the boundary effects due to the saturation of dangling bonds: atoms at the edge of the cluster, including those having saturated dangling bonds, are in a different environment than those in the crystal. The second limitation is related to the finite

size of the cluster, which does not account properly for the long-range electrostatic (Couloumb) forces that are present in crystalline solids. Madelung potential and electric field gradient, which are characteristic properties of ionic and partially ionic solids are therefore neglected or misrepresented. These two properties have shown to be important for obtaining quantitative understanding on the mechanism of chemical processes that occur at the active sites in zeolites.[8]

Most of early computational studies of defects in zeolites have been based on the isolated cluster model. Although this approach has been applied to study also small number of AlPO systems,[9, 10,11] it has been shown that the extension of using the cluster approach from zeolites to model AlPOs is not as easy as it could be imagined from their structural analogy[12]. The problem is related to the fact that the framework charges of the Al and P ions are different; therefore, if the cluster is not accurately selected, it may become either charged or affected by an intense Coulomb field gradient across the structure, as represented in Figure 3.1. Neither situation reflects the crystalline environment of aluminophosphate frameworks: in the real material, the long-range ordered alternance of Al and P ions balances their different charges, and gives rise to a smooth Madelung field in the interstitial regions. The above limitations may substantially affect the reliability of cluster-model calculations in simulating the local environment of dopants and the chemical reactions occurring in AlPOs. Henson *et al* reported lack in consistency of results obtained with clusters of different sizes, and that larger clusters give poorer agreement with EXAFS data concerning equilibrium bond distances. [10] Therefore, cluster model calculations are not in general adequate for representing AlPO frameworks. The inclusion of the long range effects and of the Madelung potential can, in principle, be achieved by applying the embedded cluster approach, described in the following section.

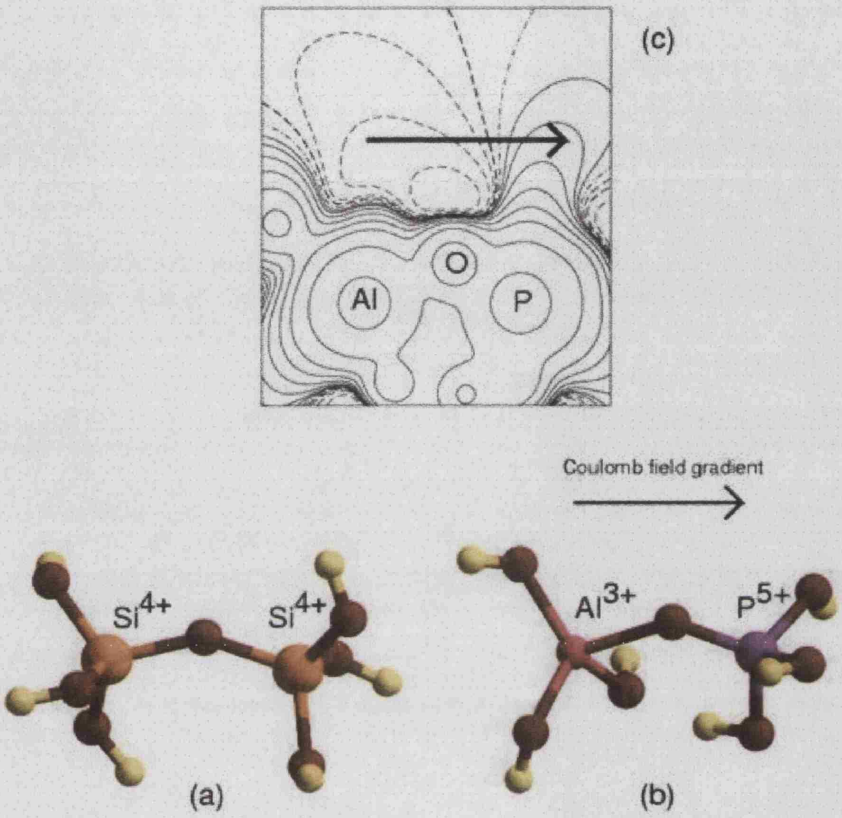

Figure 3.1: *Structure of 2-T sites clusters representing microporous frameworks of composition SiO_2 (a) and $AlPO_4$ (b). Electrostatic potential generated by the AlPO fragment (c). The Figure is taken from reference 12.*

3.1.2 Embedded-cluster approach

The central idea of the embedded-cluster models[13,14,15] is to divide the crystal into two different regions, described with decreasing accuracy while moving away from the central region of interest: the core region is a small cluster where the defect element occurs, and is the same as described for the isolated cluster model. This core

region is usually described at a quantum mechanical level of theory. The outer region is not neglected, as for the isolated cluster, but is instead described by simpler methods, for instance by using interatomic potentials or even only point charges. Inclusion of the outer region enables us to account for the Coulomb field generated by the rest of the solid in the defect zone.

The embedded cluster approach has shown to give better results for many studies on adsorption and reactions at the Brønsted acid sites of zeolites.[14,16,17]

Other types of embedded cluster approaches can be defined, for instance those based on full quantum embedded clusters, where both the core, and the outer region are treated quantum mechanically.[8,18] In the study of doped AlPOs, embedded cluster approaches have been applied, so far, only to the study of SAPO systems, and not for alkali earth- and transition metal-doped frameworks.

3.1.3 Supercell model

While the isolated and embedded cluster models apply techniques derived from molecular quantum chemistry, another possibility to describe point defects arises from solid-state techniques; this is the supercell model. In the latter approach, a unit cell of the host material with a point defect is selected and repeated in three dimensional space; the unit cell chosen is a multiple of the undoped host system. In this way the doped material is treated as a perfect crystal using standard crystalline methods based on periodic boundary conditions. For the supercell approach to be reliable, the distance between the neighbouring point defects generated by translational symmetry should be large, to minimise or eliminate the interactions that may occur between defects. (See Figure 3.2)

Although supercell methods are computationally expensive, as they describe with the same accuracy both the active site and the rest of the solid, they provide a correct

description of the crystalline environment, including the Madelung field and the structural strain caused by the crystalline matrix on the substitutional defect.

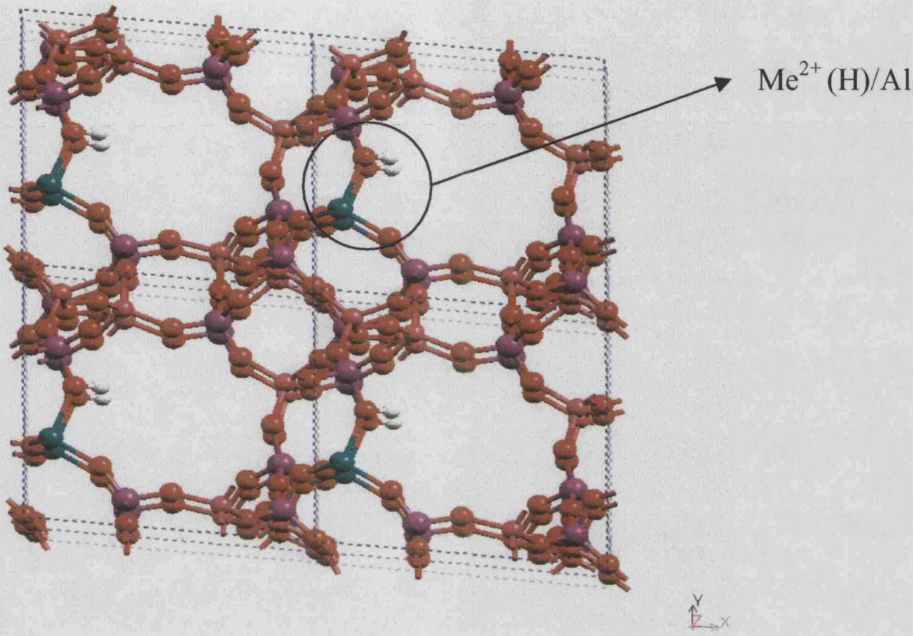

Figure 3.2: *Representation of a Me^{2+} substitutional ion, charge–compensated by an acidic proton, in the AlPO-34 framework described with a supercell model*

3.2 The computational tools:

There are a number of computational codes that enable us to apply one or more of the models described earlier to study problems concerning metal doped AlPOs. In this thesis work, we have used three codes; these are CRYSTAL, Gaussian 98 (G98) and GULP (General Utility Lattice Program). They are based on different Hamiltonian models, and the purpose of using each code is influenced by the type of the problem that we want to solve in order to calculate the properties of interest. We therefore, describe the main features of each code applied.

3.2.1 CRYSTAL Program [19]

This code enables the application of the supercell model, and permits the QM calculation of both periodic and molecular systems; it includes both Hartree-Fock and Density Functional theories. The crystalline or molecular orbitals are described with a Linear Combination of Atomic Orbitals (LCAO) approximation. The basis set is in turn expressed as a linear combination of Gaussian type functions (see section 2.2.4).

Amongst the new important features that have been included in this program during the past years is the implementation of the analytical gradient;[20] which facilitates the determination of equilibrium geometries of the systems under investigation.

During this thesis work, we have used a privately released version of the CRYSTAL program, provided to us by the authors. Our work is among the first employing the analytical gradient routines, which have been vital to properly relax complex host systems such as microporous AlPOs. All the periodic QM calculations of this work have been performed using CRYSTAL.

3.2.2 Gaussian 98 (G98) [21]

This program is originally designed to perform *ab-initio* QM calculations on molecular systems. As in the CRYSTAL code, G98 uses the MO-LCAO approximation, where the basis sets are also expressed as a linear combination of Gaussian type functions.

The G98 program has been used for our preliminary calculations on molecular systems, as will be described in section 5.2.1.

3.2.3 General Utility Lattice Program (GULP)[22]

This code applies methods based on interatomic potentials; it was originally developed for the treatment of periodic systems and has been later extended to study surfaces. We have used GULP to relax the bulk structures of MeAlPO systems, in order to account for the structural strain in the AlPO framework caused by the introduction of dopants, and to systematically examine the replacement of a framework Al site with dopant ions of different sizes.

3.3 Computational details for defect calculations on Me-AlPOs

Our initial goal was to optimise the bulk structure of MeAlPOs using QM methods. However, the CRYSTAL program provides only the gradient for internal coordinates, while the analytical gradient for optimising cell parameters is still under development. Therefore, for practical reasons, our calculations on the metal doped AlPO frameworks have been performed using a two step procedure: first we relax the AlPO framework around the dopant with methods based on interatomic potentials (IP), using the GULP code; the latter allows the optimisation of both unit cell parameters and internal coordinates of the system under study. In this way we obtain the change occurring in the volume of the unit cell needed to accommodate the steric strain caused by the dopant ions, which have different size from the host Al they replace. Subsequently, and keeping the cell parameters fixed at the values obtained from the IP method, we refine the resulting structure with QM periodic calculations.

In order to use this approach, we need to ensure that the IP available for AlPOs are reliable, which we discuss in the following section.

3.3.1 Comparison of interatomic potentials available for ALPOs

Several IPs have been derived to describe the structures of AlPO systems, for instance those proposed by Gale and Henson[23], Van Beest *et al*,[24] Sauer and Schröder,[25] and Demontis *et al.*[26] In the following discussion we shall refer to them as IP1 [23], IP2 [24], IP3 [25] and IP4 [26], respectively. In order to choose a suitable pair potential for AlPO frameworks, we have tested these four potentials, and we consider the calculated properties for four AlPO polymorphs, namely α-Berlinite, AlPO-34 (Chabasite), AlPO-20 (Sodalite) and AlPO-5 (AFI), all shown in Figure 3.3. These structures have unique framework topologies, and are unrelated to each other, which allows us to sample the structural diversity of AlPOs; in addition, these systems have been studied by experimental means, and their crystallographic structures are well characterised.[27,28,29,30,31,32] In the case of α-Berlinite, experimental data on elastic and dielectric constants, as well as the phonon spectrum, are also known.[33,34]

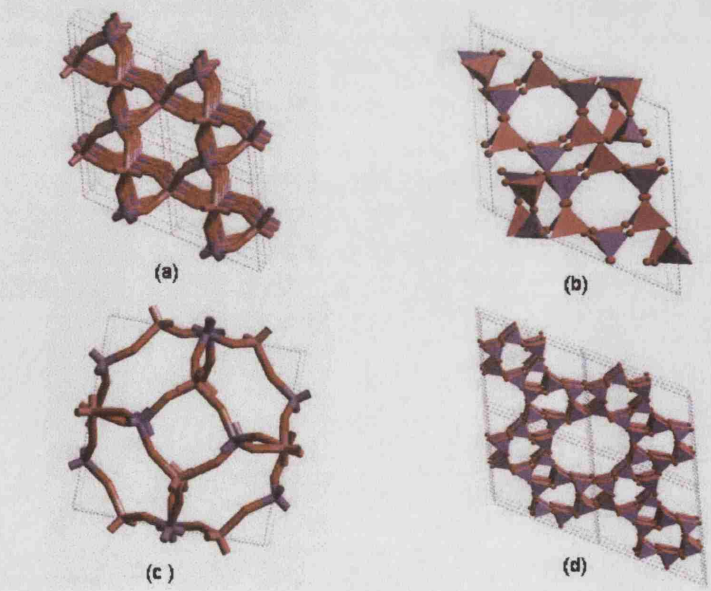

Figure 3.3: *The structure of the four AlPO polymorphs investigated (a): α-Berlinite, (b): AlPO-34 (CHA), (c): AlPO-20 (SOD) and (d): AlPO-5 (AFI)*

The main features of the four different IP parameterisations of examined are listed in Tables 3.1 and 3.2.

Table 3.1: *A brief description of the AlPOs interatomic potentials, and the methods by which they have been derived:*

Potential	Name	Description
IP1	Gale and Henson [23]	Shell model potential. Parameters fitted empirically to the structure and properties of Berlinite.
IP2	Van Beest *et al* [24]	Rigid ion potential. Parameters first fitted to Hartree-Fock calculations on $Si(OH)_4$, $Al(OH)^-_4$, and $P(OH)^+_4$ fragments, refitted to reproduce the α-Quartz and Berlinite structures.
IP3	Sauer and Schröder [25]	Shell model potential. Parameters derived from DFT-B3LYP calculations on 4-ring models of AlPOs and SAPOs.
IP4	Demontis *et al* [26]	Effective harmonic potential, developed for molecular dynamics simulations of AlPOs.

Table 3.2: *Summary of the main features of the four interatomic potentials examined.*

Potential	T— O T(P, Al)	Polarisable oxygen ion	Charges	Three Body Terms
IP1	Buckingham+ Couloumb	Included	Formal	Included
IP2	Buckingham+ Couloumb	Not included	Partial	Included
IP3	Buckingham+ Couloumb	Included	Formal	Included
IP4	Harmonic (n.n +n.n.n)	Not included	No charge	Not Included

The structures of the four AlPO polymorphs have been energy minimized, using the four potentials. Three sets of calculated observables are then compared to experimental results; these are listed below:

1. The equilibrium structure, represented by cell volume and the internal (T-O) bond distances, whose values are summarized in Table 3.3
2. The properties for Berlinite; these include elastic, dielectric and piezoelectric constants, and are reported in Table 3.4
3. The relative stability for the four polymorphs, listed in Table 3.5

The initial structures for the optimization of the four AlPO polymorphs were taken from crystallographic data.[27-32] All the structural parameters, *i.e.* cell dimensions and atomic coordinates, were optimized under constant pressure conditions, where both internal degrees of freedom and cell parameters are allowed to relax, using the Broyden-Fletcher-Goldfarb-Shanno (BFGS) algorithm, [35] with a convergence criterion of 0.001eV/Å in the gradient. The BFGS minimization algorithm generally leads to rapid convergence within a few optimisation cycles for AlPO-20, AlPO-34 and Berlinite systems. For the AlPO-5 structure, we have used the RFO optimisation algorithm instead, [36] to remove the imaginary vibrational frequencies that appeared in the lattice phonon calculations. The RFO algorithm conditions the second derivative matrix to be of the correct form, forcing the convergence of the AlPO-5 structure to a true minimum.

In Table 3.3 we report the average calculated values of the T-O bond distances within each TO_4 tetrahedral unit. The structures modelled have only one crystallographic unique Al and P site, and thus the geometry of that single TO_4 unit can be employed to characterise the entire structure

Table 3.3: *Comparison of the calculated and experimental average T-O bond distances (r, in Å), cell volumes (V in Å^3), and Al-O-P angles (in degrees) in α-Berlinite, AlPO-34, AlPO-20 and AlPO-5.*

α-Berlinite					
	Exp [28]	**IP1**	**IP2**	**IP3**	**IP4**
V	231.5	228.8	242.9	244.9	247.9
r(Al-O)	1.736	1.735	1.741	1.732	1.719
r(P-O)	1.522	1.521	1.508	1.551	1.516
Al-O-P	142.3	141.1	149.35	145.65	152.2
AlPO-34					
	Exp [27]	**IP1**	**IP2**	**IP3**	**IP4**
V	2390.2	2377.1	2561.8	2501.5	2432.6
r(Al-O)	1.723	1.724	1.751	1.726	1.720
r(P-O)	1.510	1.517	1.510	1.549	1.516
Al-O-P	148.6	147.2	154.5	148.7	149.5
AlPO-20					
	Exp [32]	**IP1**	**IP2**	**IP3**	**IP4**
V	702.6	698.4	757.7	736.5	633.7
r(Al-O)	1.743	1.715	1.748	1.716	1.722
r(P-O)	1.515	1.513	1.510	1.544	1.548
Al-O-P	138.7	152.6	163.1	156.6	136.3
AlPO-5					
	Exp[30,37]	**IP1**	**IP2**	**IP3**	**IP4**
V	1384.3	1375.8	1436.3	1461.3	1457.2
r (Al-O)	1.709	1.723	1.744	1.724	1.720
r (P-O)	1.486	1.516	1.509	1.547	1.531
Al-O-P	156.9	147.9	160.7	152.5	159.4

Bond distances are among the observables that we want to reproduce correctly in the modelling work on MeAlPOs, as they are relevant in the comparison with available experimental data. The IP employed must therefore be able to reproduce structural details within 0.01 Å. In this respect, we see from the data of Table 3.3 that only the shell-model potential derived by Gale and Henson (labelled IP1) describes correctly both the Al-O and P-O bond distances derived from experimental X-ray diffraction on α-Berlinite. Also, for the Al-O-P angle, the IP1 potential gives a good reproduction of the experimental value; the only drawback is a small underestimation, by approximately 1%, of the equilibrium volume. As explained by Gale *et al*,[23] this underestimation is likely to be attributed to thermal expansion effects: while the calculations are performed at a temperature of 0K, and do not include vibrational contributions, the experimental values include thermal effects.

The DFT-parameterized potential of Sauer and Schröder (IP3) predicts P-O bond distances that are too long. This trend is related to the quantum mechanical cluster calculations, from which the potentials has been derived, which themselves predicted long P-O distances. It is also of interest to compare the Al-O-P bond angles calculated with the potentials IP1, IP2 and IP3. While the IP1 and IP3 account for the polarisability of the oxygen ions via a shell model description, the IP2 potential describes oxygen as a rigid ion. Partial covalence in the bonding is introduced in IP2 via partial charges. From the data of Table 3.3, we see that the model potentials of Gale and Henson (IP1) and Sauer and Schröder (IP3) are superior in describing the angles in these systems. In contrast, the rigid ion model of Van Beest (IP2) predicts systematically higher values for the Al-O-P angles, when compared with the experimental ones. This comparison suggests that the oxygen ions are polarised in the AlPO structures; omission of such property gives rise to inaccurate geometries, in

which the oxygen migrates towards the line joining neighbouring Al and P ions, *i.e.* the region of the solid where the electrostatic potential is most favourable for an anionic species.[38] This attempt by the oxygen ions to screen the Al-P Coulomb repulsion causes the observed overestimation of the Al-O-P angles. The negative charge of the oxygen ion, therefore, has a screening effect on the electrostatic repulsion between Al and P ions, which requires a description of the oxygen polarisabilty to be correctly included in the computational model.

To investigate how well the available interatomic potentials reproduce the known properties of α-Berlinite other than the structure, we have calculated the elastic, dielectric and piezoelectric constants, and in Table 3.4 we compare them with the experimental values. We would like to stress here that such a comprehensive comparison of calculated and experimental properties can only be performed for the Berlinite structure. The latter is the stable crystalline form of AlPOs, analogous to the α-Quartz polymorph of silica, and it has been widely investigated experimentally. The microporous polymorphs AlPO-34, AlPO-20 and AlPO-5, instead, are usually synthesised as fine powdered systems, which makes a study of their physical properties by experimental means rather challenging.

With the only exception of IP4, the values of the elastic constants calculated using the different potentials, are more similar to each other and generally in satisfactory agreement with experiment (see Table 3.4). The Gale and Henson parametrisation however, appears superior in reproducing the static dielectric properties (ε^0) for Berlinite. Values calculated by the Demontis potential (IP4) are far outside the experimental range, and since the potential does not consider charges, no estimate can be made on the dielectric constants.

Table 3. 4: *Observed and calculated properties of α-Berlinite: elastic constants C, static dielectric constants ε^0, piezoelectric stress constants d, and Piezoelectric strain constants e.*

	Exp [33]	IP1	IP2	IP3	IP4
$C_{11}/10^{11}$dyn cm-2	6.34	8.18	8.58	8.25	10.24
C_{12}	0.23	1.59	1.03	1.31	-2.63
C_{13}	0.58	2.22	1.91	2.08	-4.29
C_{14}	-1.21	-1.08	-1.33	-1.21	4.34
C_{33}	5.58	10.70	10.4	9.85	5.94
C_{44}	4.32	4.40	4.78	4.24	2.20
C_{66}	3.06	3.29	3.78	3.47	6.43
ε^0_{11}	5.47	5.25	1.91	1.22	-
ε^0_{33}	5.37	5.42	1.93	4.43	-
$d_{11}/10^{12}CN^{-1}$	-3.30	-2.30	-1.57	-2.43	-
$d_{14}/10^{12}CN^{-1}$	1.62	1.09	0.24	0.66	-
e_{11}/Cm^{-2}	-0.22	-0.34	-0.24	-0.36	-
e_{14}/Cm^{-2}	0.15	0.08	0.17	0.05	-

The large diagonal terms of the elastic tensor, C_{11} and C_{33}, are not reproduced accurately by any of the calculations. There is still uncertainty in the experimental values; Chang,[34] for instance, measured $8.58.10^{11}$ dyn cm^{-2} for C_{33}, much closer to the values predicted, as opposed to $5.58.10^{11}$ dyn cm^{-2} given by reference 33. Since the elastic constants C_{11} and C_{33} were included among the empirical data to which IP1 has been fitted, the discrepancy between calculated and experimental values of C_{33} must be attributed to the simplified expression of forces in methods based on interatomic potentials, which cannot reproduce all details of the structural distortion corresponding to C_{33}.

The calculated piezoelectric stress constants, d_{11} and d_{44}, are underestimated by all three potentials, though again the Gale and Henson potential performs better. For the calculated piezoelectric strain constant, **e**, the rigid ion model of Van Beest seems to give very good agreement with experiment and is significantly better than the two shell model potentials IP1 and IP3.

In the previous discussion we have investigated the performance of the interatomic potentials available for AlPOs in terms of describing equilibrium geometries and the properties of Berlinite. We now want to compare the accuracy of the potentials also to describe the energetics of AlPO systems. To this aim, we have compared the calculated relative stabilities of the four AlPO polymorphs with the experimental ones, whose values are reported in Table 3.5.

Table 3. 5: *Relative stability of AlPOs polymorphs (kJ/mol)*

	Exp[39]	IP1	IP2	IP3	IP4
α-Berlinite	0.00	0.00	0.00	0.00	0.00
AlPO-5	11-17	8.79	99.45	1.63	-1.74
AlPO-20	11-17	14.32	66.73	2.15	39.98
AlPO-34	11-17	17.17	88.75	6.95	-1.61

The sets of parameters labelled as IP1-3, as well as the QM calculations, predict the α-Berlinite phase as the stable AlPO polymorph, in agreement with experiment. This is not the case, however for the parameters derived by Demontis (IP4). The latter already showed severe limitations in the calculated geometry and physical properties of Berlinite. In our opinion, the absence of charges in the description of AlPOs with IP4 is a severe approximation to guarantee the reliability of results, and we consider that this parameterisation of AlPOs should be disregarded from further applications other than the molecular dynamics studies for which it has been derived.

The shell model potential of Gale and Henson predicts correctly the experimental range of relative stability of the four AlPO polymorphs, and the order of their stability as being E(Berlinite-α)<E(AlPO-5)<E(AlPO-20)<E(AlPO-34) in agreement with the results of QM calculations. The Sauer and Schröder potential estimated a similar order of stabilty, but underestimated the energy differences by more than 70%.

Our results, therefore, show that the ionic shell model potentials are better in terms of describing the geometry of such systems, particularly when it comes into describing the angles of the systems investigated. The pair potential which best describes the properties of all the systems studied is that proposed by Gale and Henson (IP1). We shall therefore use this pair potential for all our IP calculations.

In the Gale and Henson potential, the parameters of which are reported in Table 3.6, the interaction between two ions is expressed through the Buckingham potential, combined with the electrostatic potential energy. The interactions between three ions are described by a harmonic angle-bending three body potential, and Oxygen ions are modelled by the shell model of Dick and Overhauser.[40] (See section 2.3.2 for the description of IP terms).

Table 3.6: *Parameters of the Gale and Henson potential.*[23]

Buckingham Potentials	**A/ eV**	**ρ/Å**	**C/eV Å^6**
Al^{3+}-O^{2-}	1460.3	0.2991	0.0
P^{5+}-O^{2-}	877.34	0.3594	0.0
O^{2-}-O^{2-}	22764.00	0.1490	27.88
Three-body potential	**K/eV rad^{-1}**		**θ_0/degrees**
O-T-O*	2.09724		109.47

* T= Al or P

Core-shell-potential			k/eV Å^2	
O^{2-}			74.92	
Coulombic Charges	P^{5+}	Al^{3+}	O^{2-}(core)	O^{2-}(shell)
	5+	3+	0.86902	-2. 86902

3.3.2 Computational details of IP calculations

To describe the structures of MeAlPO systems with IP methods, we need first to model correctly the interaction parameters between the different dopant ions, and their neighbouring oxygen atoms (Me-O); hence, we have applied the following procedure:

Each metal dopant studied in this work has different ionic radius (size), compared to the original Al framework site. A summary of data available from the literature (reference 41) for the ionic radius of the dopants studied in this work is given in Table 3.7.

Table 3.7: *Ionic radius (r, in Å) of different 2+ and 3+ metal ions, from Reference 41*

Me^{2+}	r	Me^{3+}	r
Mg^{2+}	0.65	B^{3+}	0.20
Ca^{2+}	0.99	Ga^{3+}	0.62
Cr^{2+}	0.89	Cr^{3+}	0.63
Mn^{2+}	0.8	Mn^{3+}	0.66
Fe^{2+}	0.75	Fe^{3+}	0.64
Co^{2+}	0.72	Co^{3+}	0.63
Ni^{2+}	0.69		
Zn^{2+}	0.74		
Sr^{2+}	1.12		

The ionic size can be controlled in computational methods that employ interatomic potentials of the Buckingham form. The two body term of the energy is given by equation (3.1)

$$E_{ij}= A_{ij} \exp(-r_{ij} /\rho_{ij}) + C_{ij}/r_{ij}^{6} + q_iq_j/r_{ij} \qquad \textbf{(3.1)}$$

The bond distance is related to the value of the parameters *A* and *ρ*. Assuming a Huggins-Mayer relationship, if r_o is the equilibrium interatomic separation, then

$$A=\exp [r_o/\rho] \qquad \textbf{(3.2)}$$

If r_o varies by an amount Δr due to a change in size of the metal dopant, the pre-exponential factor A is modified as follows

$$A'=A\cdot\exp [\Delta r/\rho] \qquad \textbf{(3.3)}$$

Vice-versa, a change in A will modify the ionic radius of the ion according to

$$\Delta r= \rho \ln [A'/A]. \qquad \textbf{(3.4)}$$

By applying equation (3.4) the pre-exponential factor A' of the Buckingham potential for each metal dopant studied can be obtained from the value of the Al-O Buckingham potential of the Gale and Hesson IP. Thus, the interaction parameters between each metal dopant and its neighbouring oxygen atoms can be approximated. Furthermore, by varying continuously the pre-exponential factor, the size of the dopant ion can be varied systematically. We shall apply the latter procedure in the study of the site ordering of dopants in AlPO-41 (AFO) and DAF-1 (DFO), which is described in section 5.3.

3.3.3 Computational details of the *ab-initio* QM calculations

The QM calculations on the doped AlPO frameworks are performed at the (Unrestricted) Hartree-Fock (HF) level of theory, as implemented in the latest version of the program CRYSTAL.[19] The electronic distribution of the system is described as a linear combination of atomic orbitals, and the basis functions are expressed analytically as a contraction of Gaussian–type orbitals. The basis set employed to describe the host AlPO framework has been optimised by Corà *et al*;[42] it is of a double-zeta plus polarisation quality, which allows for a good description of the electronic distribution on the metal sites. The basis sets used for the di- and tri-valent dopants are taken from the CRYSTAL code on-line library.[43] For Mg^{2+}, Ca^{2+} and Ni^{2+} ions 8-511d1G, 86-511d3G, and 86-411d31G basis sets are used respectively; for Ga^{3+} and B^{3+} metal ions we used 86-4111d4G (derived for GaAs and GaN structures), and 6-21d1G basis sets (derived for BN and BP), while all the other transition metal dopants are described by a 86-4111d41G basis set. The basis set used for Sr^{2+} is previously unpublished.[44] For completeness, all the basis sets employed are listed in the appendix 1.

We have chosen to use the HF Hamiltonian in our work, because it includes the exact expression for the exchange forces, which are expected to be important for the description of the spin state of open-shell transition metal ions. The HF calculations on the undoped framework yielded an equilibrium structure in very close agreement with experiment;[42, 45] the results of HF calculations on the doped systems are expected therefore to provide a reliable description of the local environment of the metal ions, that can be usefully compared with experimental data, for instance from X-ray absorption spectroscopy.[46]

The Coulomb and exchange contributions are truncated in the CRYSTAL program by selecting a series of overlap 'cut-offs' referred to as integral tolerances (ITOL): the values of (5,5,5,5,11) have been used; the first and second values refer to the overlap and penetration threshold for the Couloumb integrals respectively, the third is the overlap threshold for the exchange integrals, while the fourth and the fifth values correspond to pseudo-overlaps of the exchange series. The selection for such thresholds is performed according to overlap-like criteria: when the overlap between two atomic orbitals is smaller than 10^{-ITOL}, integrals are disregarded or evaluated by Ewald summations. A full account for the computational technique to evaluate Coulomb and exchange contributions is described in references. [47,48] The sampling of reciprocal space has been performed in a regular array of 2x2x2 k-points, which for wide band-gap insulators such as AlPOs is sufficient to converge results.

In our QM calculations on doped AlPOs we have chosen the AlPO-34 (CHA) framework shown in Figure 3.4, which is iso-structural to the aluminosilicate zeolite Chabasite, as representative of the class of microporous AlPO catalysts. This choice is due first to the relevance of AlPO-34 in catalysis; MeAlPO-34 systems have been found to be highly selective for a number of industrially important reactions such as the methanol conversion into light olefins,[49] and the selective oxidation of alkanes[50] (see section 1.1.3). Second, the AlPO-34 framework has a relatively small unit cell, containing 36 ions, which makes our periodic QM calculations feasible on a routine scale.

Our goal is to predict and compare the properties of different dopants incorporated in AlPO frameworks. Experimental evidence shows that the same metal dopant behaves very similarly in different AlPO frameworks:[51] its electronic properties and the local

environment are only marginally affected by framework topology. Despite the rich polymorphism shown by AlPOs, in fact, each structure contains only tetrahedrally coordinated cations; the local environment of the substitutional dopant will be differentiated only by the second or further neighbours of the dopant. Therefore, we shall expect the results of our calculations using the AlPO-34 framework to be a valid representation of properties and behaviour of the same dopant in other AlPO frameworks, and provide a good ground for comparing the general properties of different dopants in AlPO frameworks.

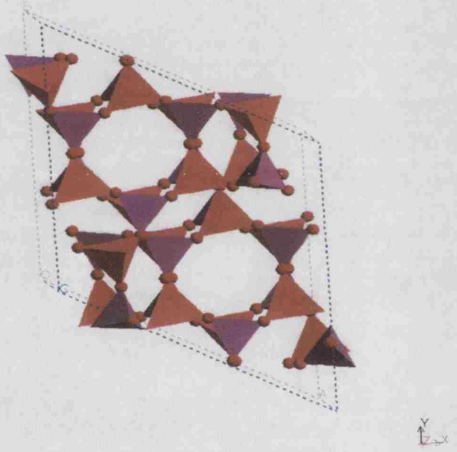

Figure 3.4: *Structure of AlPO-34 (CHA)*

We have applied the supercell approach to describe the doped framework of MeAlPO-34. The level of doping chosen in our calculations is of one dopant ion per unit cell of AlPO-34, the same as illustrated in Figure 3.2. Although the concentration of heteroatoms in the computational work is higher than achievable experimentally (the incorporation of metal ions into the framework sites of AlPOs only occurs at low concentration of ~ 1-5 atomic percent), by choosing this level of doping the unit cell dimension is kept to the same size for Me-AlPO-34 as it was in the pure AlPO-34 framework, *i.e.* 36 ions. This number of ions, with the absence of

symmetry elements that can reduce the computational expense, is already demanding for accurate *ab-initio* QM calculations. Even with this unit cell, each calculation performed requires the optimisation of (36x3-3)=105 independent degrees of freedom. In the case when compensating ions or adsorbed molecules are present, the number of independent degrees of freedom will increase even further. This level of doping, however, is already sufficient to guarantee that there is no interaction between defects, as metal dopants are separated by a distances, equal to the unit cell dimension of the host framework (approximately 10Å).

In the case of divalent doped AlPO-34, we have charge-compensated the negative framework by protonating one of the four oxygen ions that are nearest neighbour of the metal dopant: the metal dopant has four crystallographically different oxygen atoms, labeled as O_1, O_2, O_3 and O_4 as illustrated in Figure 3.5. We have chosen in this work to charge compensate the oxygen O_1, following evidence from earlier QM calculations on H-SAPO-34 system, which showed that protonating O_1 yields the most stable configuration.[25,52,53,54]

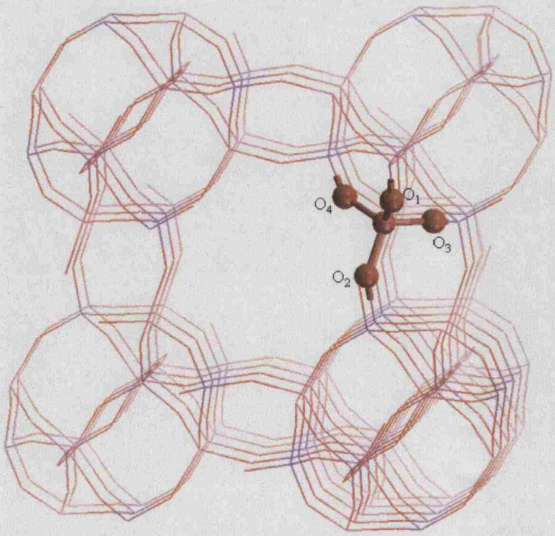

Figure 3.5: *Crystallographic position of the four framework oxygens O_1, O_2, O_3 and O_4 in the AlPO-34 framework*

No constraint has been imposed onto the electronic configuration of the metal dopants under investigation, except for their spin multiplicity. All the possible spin states compatible with the number of *d* electrons for the dopant ions with open shell electronic configuration, namely Cr^{2+} ($3d^4$), Cr^{3+} ($3d^3$) Mn^{2+} ($3d^5$), Mn^{3+}($3d^4$), Fe^{2+} ($3d^6$), Fe^{3+}($3d^5$), Co^{2+} ($3d^7$), Co^{3+} ($3d^6$) and Ni^{2+} ($3d^8$) have been investigated. The relative stability of the different spin states has been compared by calculating their energy in the geometry generated by the IP calculation; results are reported in Table 3.8.

Table 3. 8: *Relative stability of different spin states of transition metal dopants in AlPO frameworks, calculated as ($E_{MS/LS}$-E_{HS}), and given in eV.*

	High Spin (HS)	Medium Spin (MS)	Low Spin (LS)
Cr^{2+}	0	2.28	4.49
Cr^{3+}	0	-	1.87
Mn^{2+}	0	3.27	5.77
Mn^{3+}	0	2.38	3.78
Fe^{2+}	0	2.45	5.01
Fe^{3+}	0	3.60	5.43
Co^{2+}	0	-	2.23
Co^{3+}	0	2.44	4.82

Our calculations suggest that the high spin state is stable for all the metal ions studied. This result agrees with EPR studies performed on transition metal dopants incorporated in AlPO frameworks.[55] The stability of the high spin state can be attributed to the low crystal field splitting of the *d* levels on the dopant ion in the AlPO framework: the tetrahedral coordination by partly covalent oxygen ligands, in fact, is not sufficient to stabilise low spin states. All the HF calculations reported in chapters 4-7 are therefore based on transition metal ions in a high spin configuration.

All calculations have been performed with a ferromagnetic order, in which all the transition metal ions have parallel spin, as this minimises the computational cost.

For each dopant examined, a full geometry optimisation at the QM level has been performed. These calculations included all the internal coordinates, but not the lattice parameters, which have been kept fixed at their value optimised in the IP study. All the calculations have been performed using P1 symmetry. The geometry optimisations have been considered as converged when the following conditions are satisfied: (1) the maximum gradient component is less than 4.5 x 10^{-4} atomic units (Eh/bohr, a.u.), (2) the mean gradient is less than 3.0 x 10^{-4} a.u, (3) the maximum atomic displacement is less than 1.8 x 10^{-3} bohr, (4) the mean atomic displacement is less than 1.2x10^{-3} bohr. Under these conditions the energy change in the final geometry optimisation steps is of the order of 0.001 eV or smaller.

Once the equilibrium structure has been obtained for the divalent metal doped AlPO-34 frameworks, the dynamical matrix at the Γ point of reciprocal space has been calculated numerically. Diagonalisation of the dynamical matrix yields the phonon spectrum of the system, in the harmonic approximation, from which the OH stretching frequencies discussed in section 6.1.1 have been derived.

References

1 J. Sauer, P. Ugliengo, E. Garrone, V. R. Saunders, *Chem. Rev.* **1994**, *94*, 2095

2 J. Sauer, *Chem. Rev.* **1989**, *89*, 199

3 J. Limtrakul, P. Chuichay, S. Nokbin, *J. Mol. Stuct*, **2001**, *560*, 169

4 R. A. Van Santen, G. J. Karmer, *Chem. Rev.* **1995**, *95*, 637

5 P. E. Sinclair, C. R. A. Catlow, *J. Phys. Chem B.* **1999**, *103*, 1084

6 P. E. Sinclair, A. De Vries, P. Sherwood, C. R. A. Catlow, R. A. Van Santen, *J. Chem. Soc., Faraday Trans.* **1998**, *94*, 3401

7 C. M. Barker, Ph. D. Thesis, University of London, 2001.

8 P. Treesukol, J. P. Lewis, J. Limtrakul, T. N. Truong, *Chem. Phys. Lett.* **2001**, *350*, 128.

9 A. M. Márquez, J. Oviedo, J. Fernández-Sanz, J. J. Benitez, J. A. Odriozola, *J. Phys. Chem. B.* **1997**, *101*, 9510

10 N. J. Henson, P. J. Hay, A. Redondo, *J. Phys. Chem. A* , **2000**, *104*, 2423

11 Y. Cheng, E. Yang, C. J. Lai, K. J. Chao, A. C. Wei, J. F. Lee, *J. Phys. Chem. B* **2000**, *104*, 4195

12 F. Corà, C. R. A. Catlow, A. D'Ercole. *J. Mol. Catal A*, **2001**, *166*, 87

13 M. Sierka, J. Sauer, *J. Phys. Chem. B.* **2001**, *105*, 1603

14 P. Sherwood, A.H de Vries, S. J. Collins, S. P. Greatbanks, N. A. Burton, M. A. Vincent, I. H. Hiller, *Faraday Dis.* **1998**, *106*, 79

15 G. Ricchiardi, A. de Man, J. Sauer, *Phys. Chem. Chem. Phys*, **2002**, *2*, 2195

16 S. P. Greatbanks, P. Sherwood, I. H. Hillier, R. J. Hall, N. A. Burton, I. R. Gould, *Chem. Phys. Lett*, **1995**, *234*, 367

17 M. Brändle, J. Sauer, R. Dovesi, N. M. Harrison, *J. Chem. Phys*, **1998**, *109 (23)*, 10379.

18 C. Pisani, U. B. Birkenheuer, *Int. J. Quantum. Chem*, **1995**, *29*, 221.

19 V. R.Saunders, R. Dovesi, C. Roetti, M. Causà, N. M.Harrison, R. Orlando, C. M. Zicovich-Wilson, K. Doll, B. Civalleri, *CRYSTAL 2003 User's Manual*, University of Torino, **2003**

20 K. Doll, *Comp. Phys. Comm.* **2001**, *137*, 74.

21 M. J. Frisch, G. W. Trucks, H. B. Schlegel, G. E. Scuseria, M. A. Robb, J. R. Cheeseman, V. G. Zakrzewski, J. A. Montgomery, Jr., R. E. Stratmann, J. C. Burant, S. Dapprich, J. M. Millam, A. D. Daniels, K. N. Kudin, M. C. Strain, O. Farkas, J. Tomasi, V. Barone, M. Cossi, R. Cammi, B. Mennucci, C. Pomelli, C. Adamo, S. Clifford, J. Ochterski, G. A. Petersson, P. Y. Ayala, Q. Cui, K. Morokuma, D. K. Malick, A. D. Rabuck, K. Raghavachari, J. B. Foresman, J. Cioslowski, J. V. Ortiz, A. G. Baboul, B. B. Stefanov, G. Liu, A. Liashenko, P. Piskorz, I. Komaromi, R. Gomperts, R. L. Martin, D. J. Fox, T. Keith, M. A. Al-Laham, C. Y. Peng, A. Nanayakkara, M. Challacombe, P. M. W. Gill, B. Johnson, W. Chen, M. W. Wong, J. L. Andres, C. Gonzalez, M. Head-Gordon, E. S. Replogle, and J. A. Pople, Gaussian, Inc., Pittsburgh PA, 1998.GAUSSIAN 98 (Revision A, 6), **1998**

22 J. D. Gale, *J. Chem. Soc. Faraday. Trans.*, **1997**, *93 (4)*, 629

23 J. D. Gale and N. J. Henson, *J. Chem. Soc., Faraday Trans.*,**1994**, *90*, 3175

24 B. W. H. van Beest, G. J. Kramer and R. A. van Santen, *Phys. Rev. Lett.*, **1990**, *64*, 1995

25 J. Sauer, K. Schröder. *Collect. Czech. Commun.*, **1998**, *63*

26 P. Demontis, J. Gulin Gronzalez, G. B. Suffritti, A. Tilocca, C. de las Pozas, *Micro. Meso. Mate. A.*, **2001**, *42*, 103

27 M.M. Harding, B.M. Kariuki, *Acta Crystallogr.*, **1994**, *C50*, 852

28 N. Thong, D. Schwarzenbach, *Acta Crystallogr*, Sect. A. **1979**, *35*, 658

29 S. Qiu, Q. Pang, H. Kessler and J. L. Guth, *Zeolites*, **1989**, *8*, 440

30 J. W. Richardson, J. Pluth and J. V. Smith, *Acta Crystalogr*, Sect. C, **1987**, *43*, 1469

31 J. M. Bennett, J. P. Cohen, E. M. Flanigen, J.J. Pluth, J.V. Smith, In ACS Symp. Ser.; *Am. Chem. Soc:* Washington, **1983**, *218*, 109

32 P. Behrens, G. Van de Goor, M. Wiebcke, C. Braunbarth, A. M. Schneider, J. Felsche, G. Engelhardth, P. Fischer, K. Futterer, W. Depmeier, *Proceedings of the 8th International Symposium On Molecular Recognition and Inclusion*, **1994**.

33 H. Wang, B. Xu, X. Liu, J. Han, S. Shan and H. Li, *J. Crystal Growth*, **1986**, *79*, 227

34 Z. P. Chang, IEEE Trans. Sonics Ultrasonics, **1976**, *23*, 127

35 D. F. Shanno, *Math. Comp*, **1970**, *93*, 629

36 J. Simons, P. Jørgernson, H. Taylor and J. Ozment, *J. Phys. Chem.*, **1983**, *87*, 2745.

37 N. J. Henson, A. K. Cheetham and J.D.Gale, *Chem. Mater.*,**1996**, *8*, 664

38 A.R. Ruiz-Salvador, G. Sastre, D. W. Lewis and C. R. A. Catlow, *J. Mater. Chem.*, **1996**, *6 (11)*, 1837

39 Y. Hu, and A. Navrotsky, C.Y. Chen and M.E. Davis., *Chem. Mater.*,**1995**, *7*,1816

40 B. G. Dick, A. W. Overhauser, *Phys. Rev.*, **1958**, *112*, 90.

41 R.C. Weast, *CRC Handbook of Chemistry and Physics 59th ed.*, CRC Press, Palm Beach, **1978**.

42 F. Corà, C. R. A. Catlow, *J. Phys Chem B*, **2001**, *105,* 10278.

43 www.chimifm.unito.it/teorica/crystal/Basis_Sets/mendel.html.

44 R. Dovesi, Private communication.

45 F. Corà, C. R. A. Catlow, A. D'Ercole. *J.Mol.Catal A*, **2001**, *166*, 87.

46 G. Sankar, J. M. Thomas, *Top. Catal*, **1999**, *8*, 1

47 R. Dovesi, C. Pisani, C. Roetti, V. R. Saunders, *Phys. Rev.* **1983**, *B 28*, 5781

48 V. R. Saunders, C. Freyria-Fava, R. Dovesi, L. Salasco, C. Roetti, *Mol. Phys.* **1992**, *77*, 629

49 J. Chen, P. A. Wright, J. M. Thomas, S. Natarajan, L. Marchese, S. M. Bradley, G. Sankar, C. R. A. Catlow, P. L. Gai-Boyes, R. A. Townsend, C. M. Lok, *J. Phys. Chem.* **1994**, *98*, 10216.

50 J.M. Thomas, *Angew. Chem. Int. Eng*, **1994**, *33*, 913

51 S. Hočevar, J. Batista, V. Kaučič, *J. Catal*, **1993**, *139*, 351

52 F. Corà, C. R. A. Catlow, B. Civalleri, and R. Orlando, *J. Phys. Chem B.* **2003**, *107*, 11866

53 R. Shah, J. D. Gale, M. C. Payne, *Chem. Commun*, **1997**, *131.*

54 Y. Jeanvoine, J. G. Ángyán, G. Kresse and J. Hafner. *J. Phys.Chem. B*, **1998**, *102*, 5573

55 M. Hartmann, L. Kevan, *Chem. Rev.* **1999**, *99*, 635

Chapter 4 Defect chemistry of MeAlPO-34 catalysts

As we have seen in Chapter 2, doped AlPOs are of particular interest for heterogeneous catalysis. The catalytic activity of the material depends in a crucial way upon the *type* and *local environment* of the metal dopant[1]. Hence, acquiring atomic level detail on the local structure and electronic properties of active metal dopants in AlPOs is a requisite for rationalising the catalytic properties and the behaviour shown by these materials.

In this chapter, we shall discuss the calculated structural and electronic properties of a wide range of divalent and trivalent metal dopants; these include metals that are known experimentally to replace the Al framework sites in AlPO frameworks, such as Mg^{2+}, $Cr^{2+/3+}$, $Mn^{2+/3+}$, $Fe^{2+/3+}$, $Co^{2+/3+}$, Ni^{2+}, and Zn^{2+}. Other metal dopants such as B^{3+}, Ca^{2+}, and Sr^{2+} have not been yet successfully incorporated into the Al framework positions. The structural and electronic properties of these dopants have been predicted, and are included here for comparison with the other metal dopants.

4.1 Local environment of the metal dopants

The results from the periodic QM calculations on the MeAlPO-34 frameworks (the methods applied are described in section 3.3.3) provide us with parameters that fully characterise these materials, *i.e.* the local environment of each metal dopant and the long range structure of the doped framework. In this section, we focus on the local environment of the metal dopants.

The parameters that describe the local environment of the active metal centres are the four Me-O bond distances, R(Me-O_n) between the Me dopant and its four nearest

neighbour oxygens; the average Me-O bond distance, <R>; and the Me-O-P angles around the oxygens that are nearest neighbours of the metal.

In the following sections, we shall examine first the results concerning the bond distances around the 2+ and 3+ dopants, and then the changes occurring to the T-O-P angles in the presence of metal dopants.

4.1.1 Me-O bond distances of dopants in AlPO-34 catalysts

The calculated (Me-O) bond distances for di- and tri-valent metal dopants are reported in Tables 4.1 and 4.2 respectively. For frameworks doped with divalent metals, one oxygen is protonated for charge balance; the following labelling of the four oxygens that are nearest neighbours to the dopant will be used: O_H is the protonated oxygen, while O_{1-3} are the three unprotonated species, in order of increasing distance from Me^{2+}. For trivalent metal dopants, no proton is present and we label the four oxygens as O_{1-4}, in order of increasing distance from Me^{3+}.

Table 4.1: *Me-O bond distances R, in Å, for divalent metal dopants in the MeAlPO-34 frameworks examined. The column indicated as <R> reports the average Me-O bond distance. The Al-O bond distances in the undoped AlPO-34 framework are also reported, for comparison. Experimental EXAFS or crystallographic data from the literature, where available, are included.*

Me	R (Me-O_1)	R(Me-O_2)	R(Me-O_3)	R(Me-O_H)	<R>	Exp ±0.02Å
Mg	1.85	1.87	1.91	2.08	1.93	1.94[2]
Ca	2.17	2.19	2.24	2.41	2.25	-
Cr	1.99	2.03	2.04	2.36	2.11	-
Mn	2.01	2.02	2.04	2.26	2.08	2.02[3]
Fe	1.97	1.98	1.99	2.19	2.01	-
Co	1.94	1.94	1.95	2.14	1.99	1.94[4]
Ni	1.89	1.89	1.90	2.19	1.97	1.94[5]
Zn	1.90	1.90	1.91	2.19	1.97	1.96[6]
Sr	2.36	2.42	2.45	2.55	2.44	-
Al	1.72	1.72	1.73	1.73	1.73	1.73[7]

Before comparing the local environment of the different divalent metal dopants reported in Table 4.1, we shall first examine in detail the local environment of one of the divalent metal dopants investigated. We have chosen Mg^{2+}, which is a closed shell ion and is the smallest divalent metal dopants investigated, with an ionic radius of 0.65 Å.[8] The ionic radius of the original framework Al^{3+} ion is of 0.5 Å.[8] The local environment of Mg^{2+} is illustrated in Figure 4.1, where the four Mg-O bond distances are also reported.

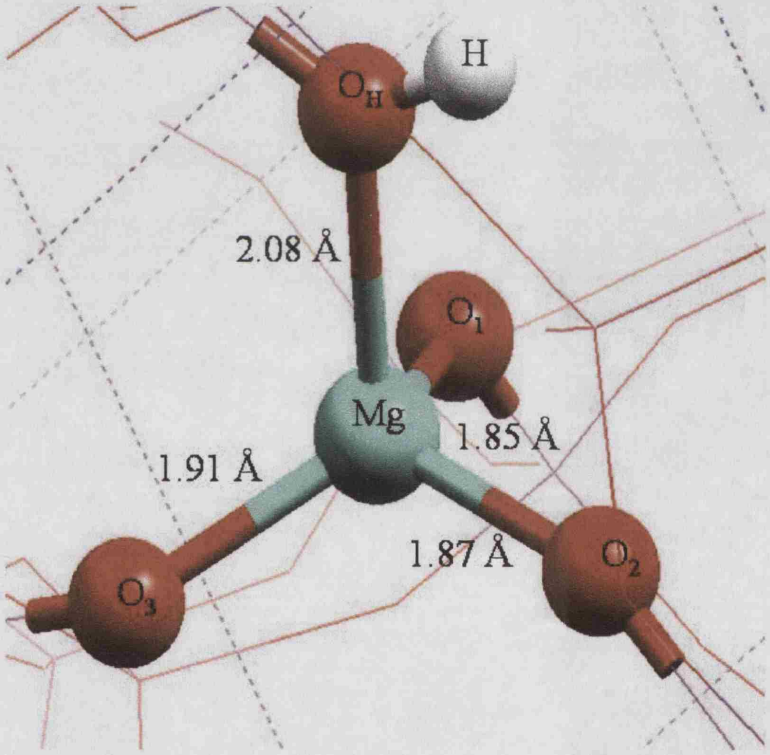

Figure 4.1: *Local environment of Mg^{2+} in the AlPO-34 framework.*

We see in Figure 4.1, that the local environment of Mg is a distorted tetrahedron, the longest bond distance is R(Mg-O_H) between the Mg ion and the protonated oxygen O_H. The latter is up to 0.23 Å longer than the other Mg-O bond distances. The distortion of the local environment of the Mg ion is clearly caused by the chemical

inequivalence of its four nearest-neighbour oxygens, owing to the presence of the acid proton bonded to one oxygen.

The average bond distance between the Mg and the four neighbouring oxygens <R> is 0.2 Å longer than that of the original Al^{3+} ion, as expected, given the larger ionic size of Mg^{2+} indicated earlier. The correlation between tabled ionic sizes and bond distances in the AlPO framework is pronounced for each dopant, as shown in Figure 4.2, where we plot the average Me-O bond distance as a function of the ionic radius of the dopants. As it is expected, we see in Figure 4.2, that the larger the metal dopant, the larger the difference between Me-O and Al-O bond distances; for instance the average Sr-O bond distance is 0.74 Å longer than the Al-O. This result indicates that the incorporation of divalent metal dopants causes a structural strain in the doped region of the host AlPO framework.

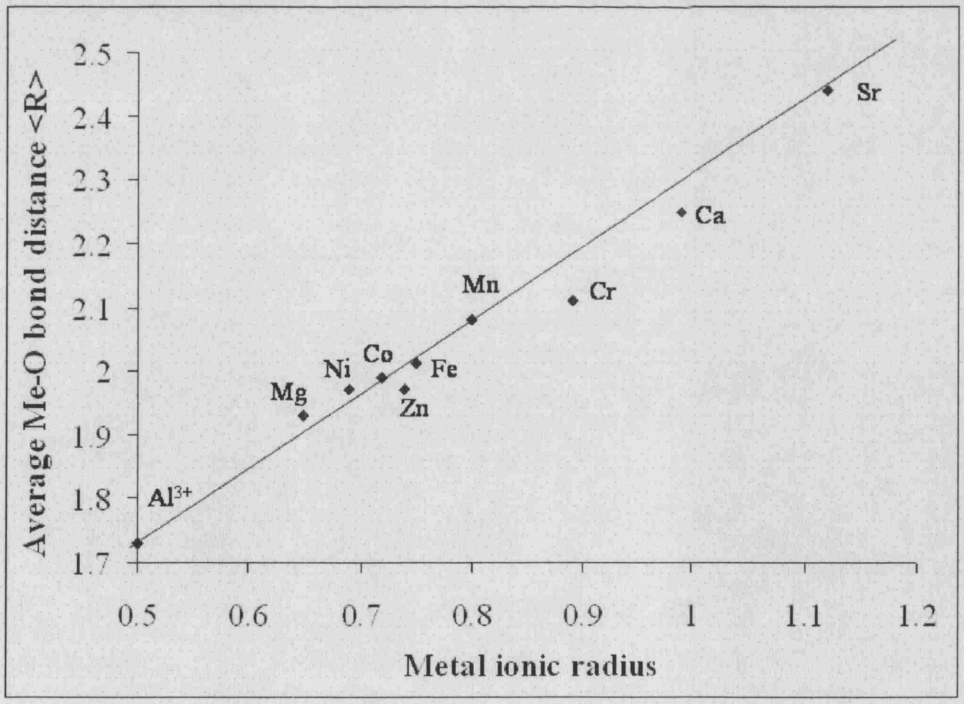

Figure 4.2: *Calculated average Me-O bond distance <R> (in Å) as a function of the ionic radius of the metal dopant (in Å).*

From Table 4.1, we see that the local environment of both close- and open-shell dopants investigated is structurally distorted, as was the case for the Mg ion. Jahn-Teller type distortions, when present in transition metal dopants, play only a minor rôle compared to the structural relaxation around the acid OH group. The local distortion around divalent metal dopants is dictated by the chemical inequivalence of the four oxygens that are nearest neighbour to the metal dopant. This result is consistent with the Al^{3+}/Si^{4+} defect in aluminosilicate zeolites, where several computational studies have shown that the Al-O_H bond distance to the protonated oxygen is considerably longer than the three Al-O bond distances to the unprotonated species. [9,10]

The situation is different in the case of trivalent metal dopants, where no charge compensation is required. Results are listed in Table 4.2.

Table 4.2: *Calculated Me-O bond distances (in Å) for trivalent metal centers in MeAlPO-34 catalysts. Experimental EXAFS or crystallographic data, where available, are also reported.*

Me	R(Me-O_1)	R(Me-O_2)	R(Me-O_3)	R(Me-O_4)	<R>	Exp ±0.02Å
B	1.46	1.48	1.53	1.55	1.50	-
Ga	1.80	1.81	1.81	1.82	1.81	1.82[11]
Cr	1.88	1.88	1.89	1.91	1.89	-
Mn	1.86	1.87	1.91	1.91	1.88	1.85[12]
Fe	1.86	1.86	1.87	1.88	1.86	1.86[13]
Co	1.83	1.84	1.85	1.86	1.84	1.89[4]
Al	1.72	1.72	1.73	1.73	1.73	1.73[7]

We note from the Table that the tetrahedral coordination environment of Ga^{3+} and Fe^{3+} ions shows only minor differences (less than 0.02 Å) in the four Me-O bond lengths. Fe^{3+} is a high spin d^5 open shell ion, which is not subject to Jahn-Teller distortions; its electronic configuration of *d* orbitals allows a symmetrical tetrahedral

coordination. The coordination of the other open shell ions such as Cr^{3+}, Co^{3+} and especially Mn^{3+}, however, is much more distorted owing to Jahn-Teller effects. While in divalent doped AlPOs, the closed-shell dopants such as Mg, Ca, and Sr have distorted environment (see Table 4.1), closed-shell +3 ions such as Ga occupy instead a much more regular crystalline position (see Table 4.2). The only exception is B^{3+}, whose local environment is much more distorted, with two short and two long B-O bonds. The average B-O bond distance is 1.50 Å which is 0.23 Å smaller than the original Al-O average bond distance. The distortion seen in the local environment of the B^{3+} ion is therefore due to its smaller size compared to the original Al framework ion; the B dopant is in fact too small to retain the undistorted tetrahedral coordination of Al sites in AlPOs. Corà *el al*[14] found that B^{3+} in the silica framework of Chabasite is stable in a trigonal coordination, in which the B-OH bond is effectively broken; the local environment is not the same for B^{3+} in AlPOs, where the coordination of B^{3+} is still tetrahedral. This feature is illustrated in Figure 4.3, where the four B-O bond distances are also reported.

With the exception of the B^{3+} dopant, the calculated Me–O bond distances of the other Me^{3+} ions examined are considerably longer than the Al-O in the host AlPO framework, in a similar manner to that described for divalent metal dopants. The isomorphous substitution of trivalent metals in the place of the Al^{3+} in the AlPO framework also introduces a structural strain. The size factor of divalent and trivalent metal dopant may contribute to limiting the maximum level of doping achievable experimentally to a low value or a few atomic percent.

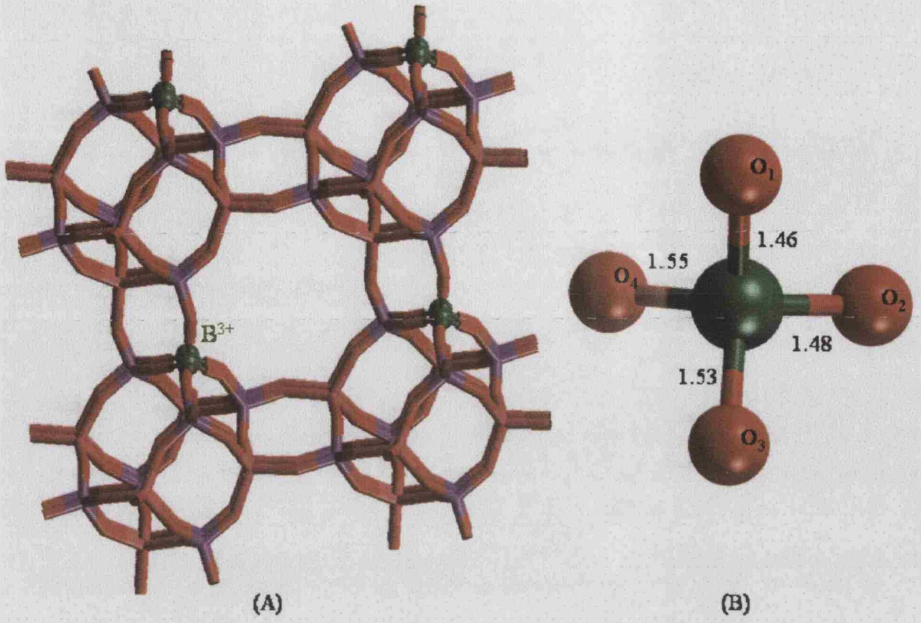

Figure 4.3: *Local coordination of a B^{3+} dopant in AlPO-34 frameworks. (A) shows the BAlPO-34 framework, and (B) reports the four (B-O) bond distances, in Å.*

When comparing the calculated Me-O bond distances with available EXAFS experimental results (see section 1.2) we notice that the error is not uniform; the calculated Me-O distance for Mg^{2+}, Ni^{2+}, and Zn^{2+} ions, which are stable only in the 2+ oxidation state, is within the experimental error of ±0.02 Å associated with the EXAFS technique employed. The calculated bond distances for Mn and Co ions, that are known experimentally to exist in both +2 and +3 oxidation states in the AlPO framework, instead, show a much larger difference from the experimental results, of up to 0.06 Å for Mn.

It is noticeable that the calculated values are always greater than experiment. Our calculations correspond to an ideal form of the MeAlPO framework, in which no template molecule is present in the structure, and all the dopants are in the reduced 2+ oxidation state. The experimental measurements concerning the reduced form of

the MeAlPO catalyst are often performed on the as-synthesised material (see section 1.1); calcinations to remove the organic templates can in fact oxidise, at least partially, the metal dopants. The overestimation of the calculated, compared to the experimental, bond distance of Mn^{2+} and Co^{2+} ions, suggests that in the as-synthesised MeAlPO structure some of the dopant ions may be present in 3+ oxidation state, so that a mixture of Me^{2+} and Me^{2+} is present in framework.

Let us now consider the trivalent metal dopants (see Table 4.2). The calculated bond distances for Al, Ga, Fe and Mn ions are in good agreement with the experimental values; the calculated bond distance for Co is underestimated by 0.05Å. Our calculations correspond in this case to a fully oxidised form of the CoAlPO framework, in which only Co^{3+} ions are present. The underestimation of the calculated Co-O bond distance, compared to the experimental one, suggests that in the experimental CoAlPO sample some of the Co ions are reduced, and that a mixture of Co^{2+} and Co^{3+} is present in the framework.

Since the XAS data are element-specific, but cannot differentiate its oxidation state,[3] Sankar and co-workers[4, 12,13] reported that the experimental EXAFS results represent an average of the properties of all the Me dopants present in the solid. A fraction of Me ions in 3+ oxidation state will cause a decrease of the Me-O bond distances observed experimentally, proportional to the fraction of Me ions oxidised in the real material, while a fraction of Me ions in 2+ oxidation state will cause an increase of the experimental Me-O bond distances. Results of our calculations on transition metal dopants can effectively help to determine the average oxidation state of transition metal dopants in MeAlPO-34 and other MeAlPO catalysts.

The Me-O bond distance obtained from EXAFS for each MeAlPO catalyst has been rationalised as being the average between Me^{2+}-O and Me^{3+}-O distances. Using the

average Me-O values <R> obtained from the theoretical and experimental work, the fraction of metal dopants Me^{3+} and Me^{2+} that are present in AlPO catalysts can be estimated using the following relationship[4]:

$$R_{EXAFS} = x\, R_{Me}^{3+} + (1-x)\, R_{Me}^{2+}, \qquad (4.1)$$

where R_{Me}^{3+} and R_{Me}^{2+} are the average bond distances calculated for the Me^{3+}-O and Me^{2+}-O respectively. Corà *et al* reported a detailed study in which results from *ab-initio* calculations on the Mn doped AlPO-34 framework have been used to determine the average oxidation state of Mn dopants in AlPO catalysts.[12]

4.1.2 Local environment of metal dopants as described by Me-O-P bond angles

In this section we shall describe the changes that take place in the T-O-P framework angles in the doped MeAlPO frameworks.

From the calculated value of the Me-O-P and T-O-P angles (T can be either the metal dopant or the framework Al ion) information can be obtained on the structural distortion around the metal dopant which is complementary to the Me-O bond distances examined above. The deviation of the calculated T-O-P angles between the doped and the undoped AlPO structure, in fact, provides a straight forward way to estimate the range of the structural distortion around the metal dopant. A graphical representation of the relaxation around the dopant is provided in Figure 4.4.

Let us first imagine that, upon inclusion in the AlPO framework of the Me^{2+} dopant, only its nearest neighbour oxygens are allowed to relax around the metal dopant, while the next-nearest neighbour phosphorus ions and the rest of the structure are

kept fixed (see Figure 4.4 (b)). The larger the size of the metal dopant, the more its nearest neighbour oxygens will relax away from it. This relaxation movement causes a decrease of the Me-O-P angles compared to the original Al-O-P; the bigger the structural relaxation upon doping, the larger the change of the Me-O-P angle. In addition to the presence of the large metal dopant, we have seen in the previous discussion that the Me-O_H bond of the dopant to the protonated oxygen is longer than the other Me-O bonds. Therefore we expect the Me-O_H-P angle centred on the bridging hydroxyl group to be particularly small.

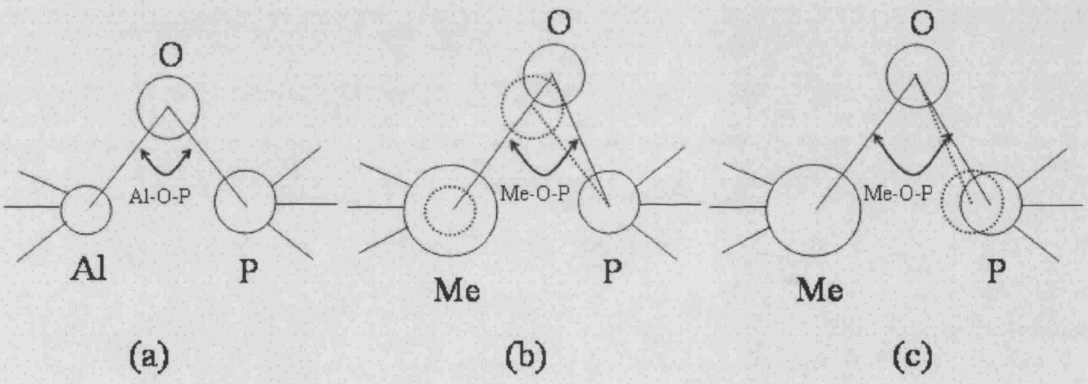

Figure 4.4: *Graphical representation of the relaxation around the metal dopant, and its effects on the Me-O-P angles.*

In the real solid, the structural relaxation extends beyond the first shell of neighbours around the metal dopant. A radial relaxation of the next-nearest neighbour phosphorus ions away from the metal centre, following the relaxation of the nearest neighbour oxygens, will cause the Me-O-P angle to increase (see Figure 4.4 (c)). As the relaxation extends to further shells of ions in the structure, also the P-O-Al angles centred on oxygens further away from the dopant will vary. However, since the

crystalline matrix exerts a steric constraint on the metal dopant, the extent of structural relaxation decays when moving away from the dopant ion. The change in the bond angles between undoped and doped materials provides a numerical way to estimate the range of this structural relaxation: monitoring the change in the calculated T-O-P bond angles for subsequent shells of neighbours, will enable us to estimate readily the region of the solid that is structurally affected by the dopant. Furthermore, it has been shown that the ^{31}P NMR chemical shift, *i.e.* a measurable observable, correlates with the average T-O-P bond angle in AlPOs.[15] Understanding the correlation between the properties of the metal dopant, such as charge and ionic radius, with the local and long-ranged structural relaxation in a simple polymorph (AlPO-34), and in an idealised situation of non-interacting defect centres, will therefore provide a valuable reference against which to compare and rationalise the experimental information obtained for real MeAlPO catalysts.

Results concerning the calculated value of T-O-P angles (T=Me, Al) in divalent and trivalent metal doped AlPO-34 frameworks are reported in Tables 4.3 and 4.4 respectively. We shall first discuss the results concerning divalent metal doped AlPO-34, and subsequently describe results for trivalent metal dopants.

Table 4.3: *Calculated value of the T-O-P angles (in degrees) in the Me^{2+}-(H)-AlPO-34 frameworks. The symbol Me-O_H-P indicates the angle around the bridging hydroxyl group, Me-O_{nn}-P is the average of the four angles on the oxygens that are nearest neighbour to the dopant, while the column T-O-P indicates the values of the angle averaged over the whole structure. The column Al-O-P refers to the angle around all oxygen ions in the structure, that are not nearest neighbour to the dopant.*

Me	Me-O_H-P	Me-O_{nn} -P	T-O-P	Al-O-P
Mg	132.41	138.69	147.17	148.86
Ca	126.05	127.84	142.61	144.96
Cr	127.50	124.89	143.92	147.72
Mn	127.81	130.91	145.06	147.89
Fe	128.97	131.93	145.77	148.54
Co	129.34	133.79	146.06	148.51
Ni	126.44	135.56	146.41	148.58
Zn	131.30	132.47	145.73	148.38
Sr	116.20	118.14	140.49	144.96
Al	-	148.59	148.59	148.59

The distortion from the undoped material is particularly pronounced around the protonated oxygen (column Me-O_H-P), whose angle with the framework ions changes by as much as 30° for the large Sr^{2+} ion. The difference from the undoped framework is important for all the four nearest-neighbour oxygens of the dopant (column Me-O_{nn}-P), as expected from the description given in Figure 4.4. The local distortion causes a decrease of the T-O-P angle averaged over the whole structure, a value which can be measured experimentally by ^{31}P NMR.[15] When we limit our attention to the oxygens that are not nearest neighbour of the dopant (column Al-O-P in Table 4.3), however, we notice only minor changes (of less than 1°) from the undoped AlPO-34 framework structure. This result suggests that the structural distortion caused by the dopant is "local", and affects its nearest neighbour ions, but does not propagate to the undoped regions of the framework. The only exceptions to

the above result are Ca and Sr, *i.e.* the largest dopant ions examined (see the Me-O bond distances in Table 4.1). The optimised value of the Al-O-P bond angles away from the Ca and Sr dopants are lower than the value of the Al-O-P angle in the undoped AlPO-34, which indicates that the structural strain caused by the biggest dopant ions is long-ranged, and propagates towards the undoped regions of the host framework. In Figure 4.5 we plot the calculated value of the T-O-P angle as a function of the ionic radius of the dopant. These two observables show a good linear correlation, clearly indicating that the structural distortion correlates with the steric hindrance of the large divalent ions when they are isomorphously introduced in the AlPO framework.

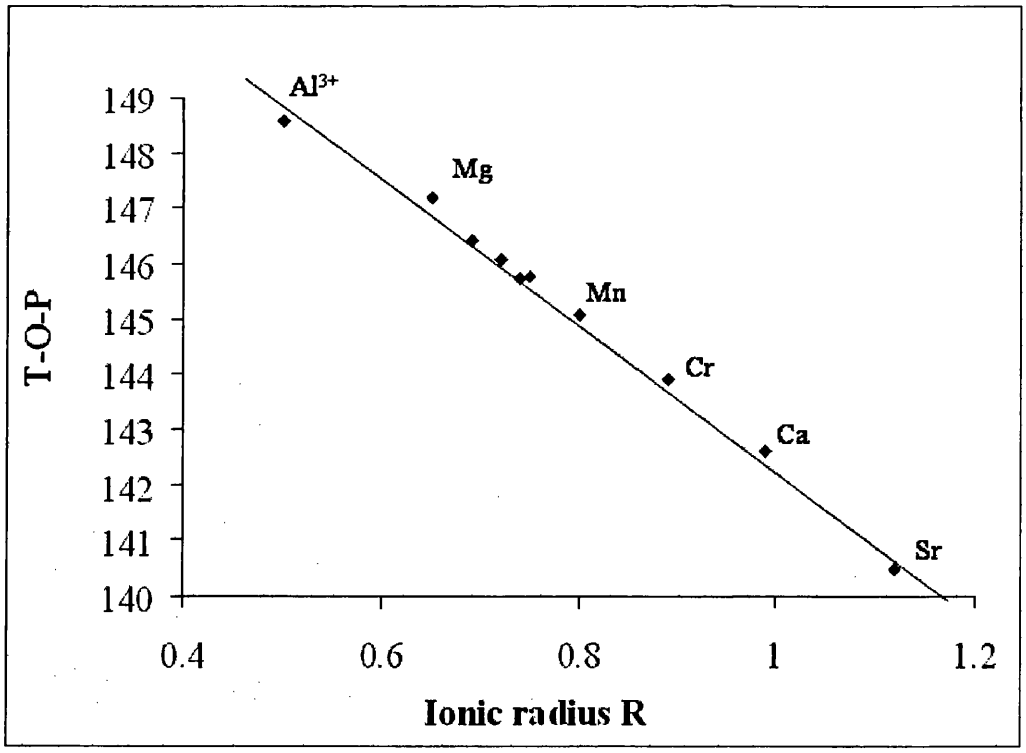

Figure 4.5: *Calculated T-O-P angle (in degrees) in Me^{2+}-doped AlPO-34 as a function of the ionic radius R of the Me dopant (from reference 8). R is given in Å.*

The effect of trivalent metal dopants on the T-O-P angles is less pronounced than that of the divalent metal dopants; results are collected in Table 4.4.

Table 4.4: *Calculated value of the T-O-P angles (in degrees) in the Me^{3+}AlPO-34 frameworks. Me-O-P is the average of the four angles on the oxygens that are nearest neighbour to the dopant, while the column T-O-P indicates the value of the angle averaged over the whole structure. The column indicated as Al-O-P refers to the angle around all oxygen ions in the structure, that are not nearest neighbour to the dopant.*

Me	Me-O-P	T-O-P	Al-O-P
B	151.34	150.13	149.89
Cr	144.95	147.99	148.60
Mn	138.74	147.54	149.30
Fe	144.58	148.72	149.55
Co	141.44	147.53	148.75
Ga	144.90	148.99	149.81
Al	148.59	148.59	148.59

From Table 4.4, we see that the average value of the calculated Me-O-P angle, for the four nearest neighbour oxygens of the metal dopant, is lower than the original Al-O-P angle in the pure AlPO framework. The largest difference, of ~10°, is shown by the Mn^{3+} dopant, which is also the ion whose environment is most distorted (with the exception of B^{3+}). The oxygens next to the Mn dopant are therefore the framework atoms that sustain the largest structural strain upon doping of the framework. The Me-O-P angles in Co, Fe and Cr-doped materials are instead less distorted. On examining T-O-P values, we find that these values are close to the original Al-O-P values. We conclude therefore that the effect of a trivalent metal dopant on the Me-O-P bond angle is less pronounced than that observed in divalent metal dopants; this feature is due to the smaller size of trivalent metal dopants, and to the absence of the charge compensating proton, which causes further distortion around the Me-O_H-P

bond angles in divalent metal-doped AlPO frameworks (see Table 4.3). Moving away from the dopant, the angles appear to be only marginally affected, and the value of the Al-O-P angles in the defective AlPO, averaged over the whole structure, remains close to its value in the undoped framework. Therefore the Me^{3+} dopants examined here cause only a short-ranged structural strain, which is appreciable only around the metal dopant itself.

4.2 Electronic properties of the metal dopants in AlPO-34

Having examined the local environment of divalent and trivalent metal dopants in AlPO frameworks, in this section we shall describe the electronic properties of the dopants.

Information on the electronic distribution of atoms in the solid can be obtained from the Mulliken population analysis. We are interested in analyzing the electronic distribution around the dopant. Net charges of the metal dopants and of the four neighbouring oxygens atoms and the overlap population between the metals and the neighboring oxygen atoms enable us to acquire a detailed atomic description of the nature of bonding between the metal dopant and the oxygens.

In Tables 4.5 and 4.6, we report results from a Mulliken population analysis of the electronic distribution for divalent and trivalent metal dopants respectively.

Table 4.5: *Mulliken population analysis of the electronic distribution around the Me^{2+} dopants in Me-(H)-AlPO-34. The symbol Q refers to the net ionic charges on the metal dopant and oxygens; $Q(O_{1-3})$ is the average net charge of the three unprotonated oxygens that are nearest neighbour to the Metal dopant; $Q(O_H)$ refers to the charge of the protonated oxygen; q_b denotes the bond population, in $|e|$.*

Me	Q(Me)	$Q(O_{1-3})$	$Q(O_H)$	$Q(O_{1-4})$	$q_b(Me\text{-}O_{1-4})$
Mg	1.67	-1.26	-1.03	-1.20	0.05
Ca	1.78	-1.25	-1.01	-1.19	0.00
Cr	1.60	-1.22	-0.98	-1.17	0.05
Mn	1.54	-1.21	-0.99	-1.16	0.05
Fe	1.62	-1.24	-1.01	-1.18	0.06
Co	1.61	-1.24	-1.01	-1.18	0.07
Ni	1.85	-1.32	-1.03	-1.24	-0.01
Zn	1.42	-1.20	-0.98	-1.15	0.09
Sr	1.84	-1.25	-1.01	-1.19	-0.02

Table 4.6: *Mulliken population analysis of the electronic distribution of Me^{3+} substitutional ions in AlPO-34.*

Me	$Q(O_{1-4})$	Q(Me)	$q_b(Me\text{-}O_{1-4})$
B	-1.13	1.57	0.22
Cr	-1.24	2.15	0.08
Mn	-1.24	2.17	0.09
Fe	-1.26	2.23	0.10
Co	-1.26	2.20	0.10
Ga	-1.29	2.33	0.11
Al	-1.26	2.20	0.14

From Tables 4.5 and 4.6, we note that the net charges of the Me^{2+} and Me^{3+} dopants are close to their formal values, and the values of the overlap population q_b(Me-O) are low, which suggests that the nature of bonding between the Me dopants and the neighbouring oxygen atoms is ionic in nature. The same situation is observed for the original metal ion Al, which is found to be of ionic nature in AlPOs.[16,17] Again, the

behaviour of B^{3+} differs (see Table 4.6), with a lower net ionic charge and a higher overlap population, suggesting that B^{3+} bonds covalently to the neighbouring oxygens. This result is not surprising as B^{3+} is a very small ion and is more electronegative compared to Al^{3+} and the other dopants. From results given in Table 4.5, we also note that the overlap population q_b (Me-O_{1-4}) values calculated for the Ni and Sr ions are negative; these negative values indicate a strong repulsion, and suggest an instability of the Ni and Sr ions in the tetrahedral coordination.

To support the finding of the ionic nature of the bonding between the metal dopants and neighbouring oxygens atoms, in Figures 4.6 and 4.7 we show the difference electron density maps (obtained as the difference between the electron density in the solid and the superposition of isolated formal ions) for the Me-O bond in the metal-doped AlPO-34 framework.

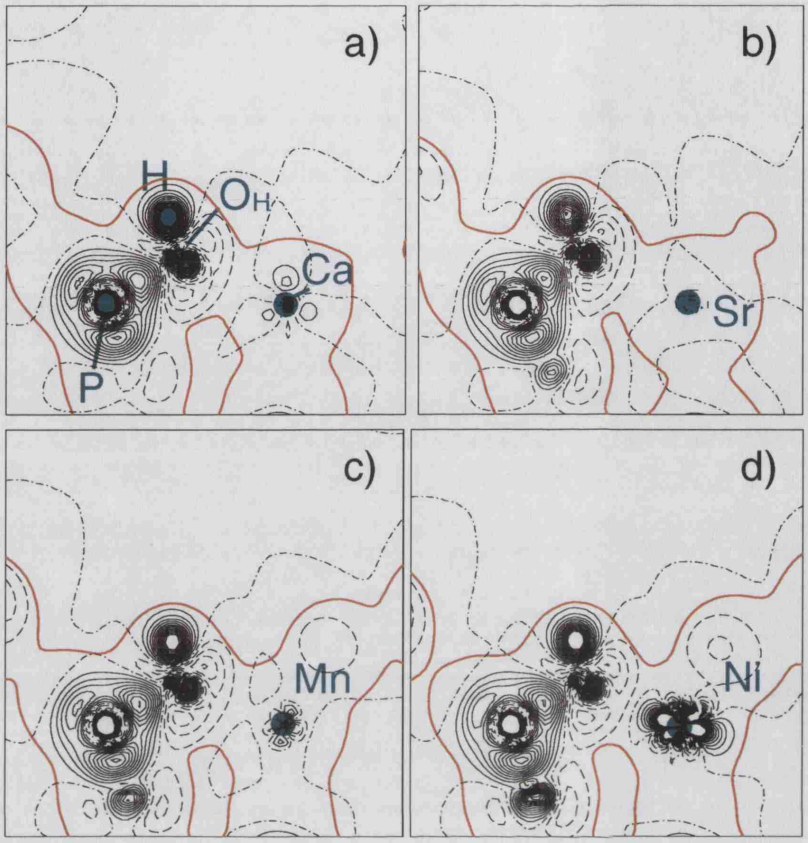

Figure 4.6: *Difference electron density maps, plotted in a plane containing one a) Ca-O(H)-P, b) Sr-O(H)-P, c) Mn-O(H)-P, and d) Ni-O(H)-P unit in AlPO-34. Continuous and dashed lines correspond to positive and negative densities, plotted between -0.1 and 0.1 a.u. ($|e|.bohr^{-3}$) at linear steps of 0.01 au. The red line is the total electron density level of 0.01 a.u., and indicates the framework size.*

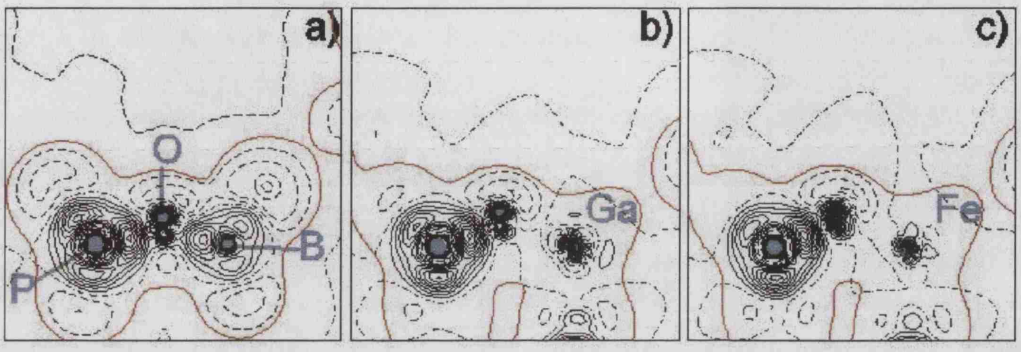

Figure 4.7: *Difference electron density maps (solid minus isolated formal ions), plotted in a plane containing one B-O-P (a), Ga-O-P (b) or Fe-O-P (c) unit in AlPO-34.*

The difference electron density maps give us information about the electronic rearrangement in the bonds between the metal dopant and its four neighboring oxygens in the solid. The maps are drawn in a plane containing the metal dopant, one of its oxygen neighbours oxygen bonded to the charge compensating proton for the 2+ dopants and the next nearest phosphorus ion bonded to the oxygen of the figure. From the electron density plots we clearly see an electronic redistribution in the covalent P-O bonds, but only minor features around the metal dopants. We can therefore describe the bonding between the metal dopant and the oxygens as being ionic, while the bonding between phosphorus and oxygen is covalent. For the B^{3+}-doped AlPO frameworks (see Figure 4.7), we find instead a significant electronic redistribution around B, which enforces our initial suggestion that the bonding of B^{3+} in the AlPO framework is covalent in nature.

For the original AlPO-34 framework, experimental evidence shows that Al is capable of increasing reversibly its coordination number when Lewis bases such as water and ammonia are present in the cages.[18,19] Furthermore, TGA data on doped AlPO materials show that the hydrophilicity of the framework increases when dopant ions are incorporated,[20] a result that is consistent with the ionic nature of the Me-O bonding found in our calculations. Ionic bonds are in fact non-directional and more flexible than covalent bonds towards changes of the coordination number. During adsorption processes, the dopant ions can act as Lewis acid centres, able to increase their coordination in the presence of Lewis bases. The Lewis acidity of the metal dopants will be discussed more in depth in section 6.3.

4.3 Conclusions

In this chapter we have studied the local environment and electronic properties of divalent and trivalent metal dopants in AlPO-34. From the results of our calculations and comparison with experiment, we conclude the following:

- The local environment of divalent metal dopants is a distorted tetrahedron, due mainly to the presence of the acid proton. The Me-O_H bond of the dopant to the protonated oxygen is ~0.15 Å longer than the other three Me-O bonds. The local environment of trivalent Co and Mn dopants is instead Jahn-Teller distorted. Cr^{3+}, Fe^{3+} and closed shell 3+ dopants have a more symmetric coordination.
- The deviation of the calculated T-O-P angles between the doped and the undoped AlPO structure provides a way of estimating the range of the structural distortion around the metal dopant. The structural strain caused by metal dopants is short-ranged, and does not propagate to undoped regions of the host AlPO framework.

- The nature of bonding between the metal dopants and the neighbouring oxygens is ionic in nature; the ionicity of the Me-O bonds may explains the Lewis acidity of the Me ions, which are able to increase their coordination number in presence of Lewis bases.

References:

1 M. Hartmann, L. Kevan, *Chem. Rev.*, **1999**, *99*. 635

2 G. Sankar, D. Gleeson, J. M. Thomas and A. D.Smith, *J. Syn. Rad.*, **2001**, *8*, 625

3 G. Sankar, J. M Thomas, C. R. A. Catlow, *Top. Catal.*, **2000**, *10*, 255

4 P. A. Barett, G. Sankar, C. R. A. Catlow, and J. M. Thomas, *J. Phys. Chem.*, **1996**, *100*, 8977

5 Y. Xu, J.W. Couves, R. H. Jones, C. R. A. Catlow, G.N. Greaves, J. Chen, J.M. Thomas. *J. Phys. Chem. Sol*, **1991**, *10*, 1229

6 N. N. Tusar, A. Tuel, I. Arcone, V. Kaucic, *Prog. Zeolites Microporous Materials.*, **1997**, *105*, 501

7 N. Thong, D. Schwarzenbach, *Acta Cryst. A.*, **1979**, *35*, 658

8 D. R. Lide [ed], *CRC Handbook of Chemistry and Physics*, 75th Ed, CRC Press, Boca Raton, **1994**

9 J. B. Nicholas, *Top. Catal.*, **1997**, *4*, 157

10 J. Sauer, in *Modelling of structure and reactivity in Zeolites,* P.183, C. R. A. Catlow (Ed), Academic Press, London, **1992**

11 A. Goiffon, G. Bayle, R. Astier, J. C. Jumas, M. Maurin, E. Philippot, *Rev.Chem. Miner.*, **1983**, *20*, 338

12 F. Corà, G. Sankar, C. R. A. Catlow, J. M. Thomas, *Chem. Commun.*, **2002**, 734

13 C. Zenonos, G. Sankar, F. Corà, D. W. Lewis, Q. A. Pankhurst, C. R. A. Catlow, J. M.Thomas, *Phys. Chem. Chem. Phys.*, **2002**, *4*, 5421

14 F. Corà, C. R. A. Catlow, B. Civalleri, R. Orlando, *J. Phys. Chem B.*, **2003**, *107*, 11866.

15 D. Müller, E. Jahn, G. Ladwig, U. Haubenreisser, *Chem. Phys. Lett.* **1984**, *109*, 332

16 F. Corà, C. R. A. Catlow, *J. Phys. Chem B.*, **2001**, *105,* 10278

17 F. Corà, C. R. A. Catlow, A. D'Ercole. *J. Mol. Catal A.*, **2001**, *166*, 87

18 A. Tuel, S. Caldarelli, A. Meden, L. B. McCusker, C. Baerlocher, A. Ristic, N. Rajic, G. Mali, V. Kaucic, *J. Phys. Chem. B.*, **2000**, *104*, 5697

19 M. P. J. Peeters, L. J. M. Van de Ven, J. W. de Haan, J. H. C. Van Hooff, *J. Phys. Chem.*, **1993**, *97*, 8254

20 J. Jänchen, M. P. J. Peeters, J. H. M. C. Van Wolput, J. P. Wolthuizen, J. H. C. Van Hooff, *J. Chem. Soc. Faraday. Trans.*, **1994**, *90*, 1033

Chapter 5 Metal dopants incorporation in AlPO catalysts: energetics and site ordering

In this chapter, we investigate the effects controlling the energetics and stability of metal dopants incorporation in AlPO frameworks. Using *ab initio* QM calculations, we calculate the energy required for substituting a range of di- and tri-valent metal dopants at the Al framework sites of AlPO-34. We will correlate these values with the ionic size of the metal dopants. The metal dopants investigated include all alkali earth and transition metals investigated in Chapter 4. Subsequently, using methods based on interatomic potentials, we investigate site ordering of trivalent metal dopants in two AlPO frameworks, namely AlPO-41 (AFO) and DAF-1 (DFO).

5.1 Introduction

In the previous chapter, we found that the incorporation of 2+ and 3+ metal dopants in the Al sites of AlPO-34 causes a noticeable structural strain in the doped region; the bond distance between metal dopants and their neighbouring oxygen atoms R (Me-O) increases, and the Me-O-P bond angles decrease (see Figure 4.4). The extent of the structural strain caused by the dopant incorporation increases linearly with the metal size. Therefore, we expect that the size of the dopants will play a major rôle in influencing the stability of metal incorporation in AlPO frameworks, and hence control the level at which these dopants can be present in the frameworks of AlPOs. The concentration of metal active sites in these materials can modify the catalytic activity of the doped AlPO frameworks.[1] However, increasing the concentration of

metal dopants can decrease the stability of the AlPO frameworks. Understanding the factors affecting the ease of replacement of different divalent and trivalent ions in the framework of AlPOs, and the stability of the doped materials, is a topic of fundamental and practical interest.

The feasibility of the incorporation of dopants depends critically on the *thermodynamic stability* of the doped AlPO frameworks, a property that can be examined theoretically by calculating the substitution energy of the dopants in the AlPO framework. Therefore, in order to gain an insight into this topic, we have calculated the replacement energies of divalent and trivalent metal dopants for the Al framework sites in the AlPO-34, using *ab-initio* QM calculations.

5.2 Substitutional energy of dopant ions in AlPO-34 framework

From our periodic QM calculations (see section 3.3.3) we obtain the calculated energies of the pure and doped AlPO-34 frameworks. These energies can be combined to calculate the substitution energy of the dopant in the AlPO-34 framework. Since the synthesis of MeAlPO frameworks is performed in an aqueous medium, by hydrothermal methods,[2,3] the replacement reaction can be represented as:

$$\text{Al (AlPO-34)} + \text{Me}_{aq} \longrightarrow \text{Me(AlPO-34)} + \text{Al}_{aq} \qquad (5.1)$$

We have taken as suitable states for the +2 and +3 ions outside the framework their hexa-aqua complexes. This is a crude approximation for the solvated metal ions, as only the first solvation sphere of the 2+ and 3+ ions is included; nonetheless, it represents a suitably simple computational model of the solvated ions. The replacement energies of the dopants are calculated according to the following equations:

$$AlPO\text{-}34 + [Me(H_2O)_6]^{2+} \xrightarrow{\Delta E_{II}} Me^{2+}HAlPO\text{-}34 + [Al(H_2O)_5(OH)]^{2+} \quad (5.2)$$

$$AlPO\text{-}34 + [Me(H_2O)_6]^{3+} \xrightarrow{\Delta E_{III}} Me^{3+}AlPO\text{-}34 + [Al(H_2O)_6]^{3+} \quad (5.3)$$

The replacement energies ΔE_{II} and ΔE_{III} indicate the ease of inclusion of Me^{2+} and Me^{3+} ions in the AlPO-34 framework, and are calculated according to the following equations:

$$\Delta E_{II} = E(Me^{2+}HAlPO\text{-}34) + E[Al(H_2O)_5(OH)]^{2+} - E(AlPO\text{-}34) - E[Me(H_2O)_6]^{2+} \quad (5.4)$$

$$\Delta E_{III} = E(Me^{3+}AlPO\text{-}34) + E[Al(H_2O)_6]^{3+} - E(AlPO\text{-}34) - E[Me(H_2O)_6]^{3+} \quad (5.5)$$

To obtain the replacement energies according to equations (5.4) and (5.5), we need to calculate in a consistent way the energies corresponding to the aqueous complexes $[Me(H_2O)_6]^{3+}$, $[Me(H_2O)_6]^{2+}$, $[Al(H_2O)_5(OH)]^{2+}$ and $[Al(H_2O)_6]^{3+}$ and the energies of the perfect and defective solids, *i.e.* AlPO-34 and MeAlPO-34.

The *ab-initio* QM calculations on pure and defective AlPO-34 frameworks are described section 3.3.3. In the following section we concentrate instead on describing the procedure used for our molecular systems and the results obtained from these calculations.

5.2.1 Molecular calculations of hydrated ions

The geometries of all the molecular systems have been optimised at the HF level of theory using the Gaussian 98,[4] and CRYSTAL programs.[5] We first optimised all the molecular structures using Gaussian 98, then for consistency with the solid-state results the final structures have been re-optimised using the latest version of the

CRYSTAL code. We have employed the same basis set for the Al^{3+}, Me^{2+} and Me^{3+} ions in molecular and solid state calculations of pure and doped AlPO-34 framework (see Appendix 1). The water molecules are described with a standard 6-31G* basis set.[6] No symmetry constraints were imposed on any of the molecules investigated. In the optimised structures, the hexa-aqua complexes are stable in an octahedral symmetry with point group T_h (High symmetry). The only exceptions are the optimised structures of $[Mn(H_2O)_6]^{3+}$, $[Co(H_2O)_6]^{3+}$ and $[Cr(H_2O)_6]^{2+}$ which have a lower symmetry configuration (point group D_{2h}) due to Jahn-Teller distortions, in this configuration the metal ion forms long bond distances with the two axial oxygens and short bond distances with the four equatorial oxygens. These results are in agreement with previous work by Akesson *et al.*[7] The optimised configurations of the hexa-aqua complexes are illustrated in Figure 5.1.

For the complexes of open-shell transition metal ions, we have optimised all possible spin states compatible with the number of *d* electrons. Our calculations found that all the transition metal ions studied in this work are as expected, stable in the high spin state (see Table 5.1). We attribute these results to the relatively low ligand field splitting of the Me-d levels caused by the water ligands.

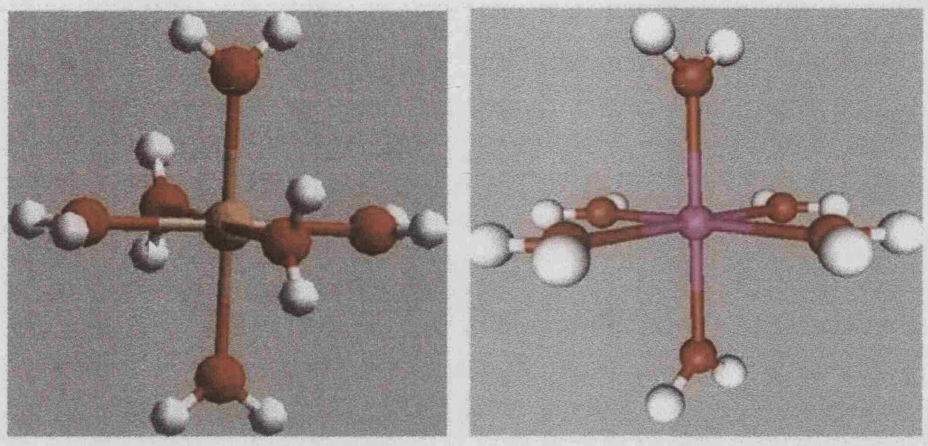

Higher symmetry configuration: T_h *Lower symmetry configuration D_{2h}*

A **B**

Figure 5.1: *Optimised geometry of the hexa-aqua complexes $[Me(H_2O)_6]^{n+}$.* **A***: T_h symmetry with all the Me-O bond distances are equal,* ***B****: lower symmetry configuration adopted by the $[Cr(H_2O)_6]^{2+}$, $[Co(H_2O)_6]^{3+}$ and $[Mn(H_2O)_6]^{3+}$ molecular ions.*

Table 5.1: *Relative stability of spin states of transition metal ions in hexa-aqua complexes:*

	High Spin (HS)	Medium Spin (MS)	Low Spin (LS)
Cr^{2+}	0	2.54	4.73
Cr^{3+}	0	-	3.60
Mn^{2+}	0	2.80	4.70
Mn^{3+}	0	2.15	4.71
Fe^{2+}	0	2.69	3.58
Fe^{3+}	0	3.48	5.06
Co^{2+}	0	-	2.50
Co^{3+}	0	2.67	2.77

The convergence of calculations for the systems containing transition metal ions with open shell electronic configuration, such as cobalt, iron, manganese, nickel and chromium, has proved to be particularly difficult to obtain. We employed the level shifting option, available in the Gaussian and CRYSTAL codes; [4,5] the latter option increases the energy difference between the occupied and the virtual orbitals, 'forcing' the electrons to stay in the occupied orbitals. We also started our optimisation using a lower convergence criterion (10^{-4} Ha) for the energy, to achieve an initial optimised geometry, followed by a new optimisation using the default convergence criterion of the Gaussian program (10^{-6} Ha). We then re-optimised the geometries using the CRYSTAL program using the default convergence criterion of 10^{-6} Ha.

All the geometry optimisations of the molecular systems have been followed by frequency calculations, to ensure that the structures obtained are true minima on the potential energy surface. No imaginary frequencies are present. The results of our calculations are compared in Table 5.2 with previous computational[7, 8, 9] and experimental studies.[10,11,12,13,14,15]

Table 5.2: *Calculated and experimental Me-O distances for hexahydrated molecular ions $[Me(H_2O)_6]^{n+}$. For Co^{3+}, the symbols 'l' and 'h' indicate low and high spin states, respectively.*

	R (Me-O)/ Å		
Me	**This work**	**Other theoretical works**	**Exp**
Al^{3+}	1.918	1.935[8]	1.900[10]
Mg^{2+}	2.082	-	-
Ca^{2+}	2.392	2.393[7]	2.240[11]
Ga^{3+}	1.988	1.998[9]	1.954[12]
Cr^{2+}	2.290	2.225[7]	2.167[13]

Cr^{3+}	2.032	2.025[7]	1.960[14]
Mn^{2+}	2.239	2.233[7]	2.175[13]
Mn^{3+}	2.063	2.042[7]	1.991[14]
Fe^{2+}	2.145	2.185[7]	2.126[13]
Fe^{3+}	2.060	2.052[7]	1.995[15]
Co^{2+}	2.136	2.143[7]	2.092[13]
Co^{3+}_{l}	1.928	1.933[7]	1.873[14]
Co^{3+}_{h}	2.020		
Ni^{2+}	2.086	2.108[7]	2.056[13]
Zn^{2+}	2.127	2.123[7]	2.092[13]
Sr^{2+}	2.611	2.581[7]	2.640[11]

While there is good agreement with the previous computational studies, the comparison with experimental results[10-15] is less satisfactory, and indicates the inadequacy of gas-phase-like $[Me(H_2O)_6]^{n+}$ complexes in representing 2+ and 3+ ions either solvated or in a crystalline matrix. For Co^{3+} and Mn^{3+}, in particular, which are both disproportionate in aqueous solutions, we compare the calculated Me-O distances with those obtained from X-ray diffraction data of a crystalline structure of Cesium Alum salts $[CsMe^{3+}(SO_4)_2 \cdot 12\ H_2O]$, in which Co^{3+} and Mn^{3+} are found as a hexa-hydrated unit, with an almost regular octahedral coordination.[14] The experimental values of the Me-O bond distances are shorter than the calculated ones by as much as 0.07 Å, which is far greater than expected from the quality of the calculations performed. This large difference is due to the long-range effects present in the aqueous solutions and in the crystalline matrix, but not in the isolated hexa-aqua complexes. Both in the water solutions and in the Alum salts, the strong hydrogen-bonds which link the first to the second hydration sphere polarize the water molecules and shorten the Me-O bonds.[16] Moreover, the steric pressure exerted on the $[Me(H_2O)_6]^{n+}$ core from the crystalline matrix, shortens the Me-O bond distance

with respect to the isolated complex. We can, however, assume that these 'long-range' forces affect systematically ions with the same charge (*i.e.* all the Me^{3+} and Me^{2+} ions examined here), and the error introduced will cancel out when considering energy differences, such as those of equations (5.3) and (5.4) needed to calculate ΔE_{II} and ΔE_{III} .

Based on assumptions from the experimental work on Alum Salts, Akesson *et al*[7] assumed in their study that Co^{3+} in the hexa-aqua complex is stable in the low spin state, $t^6_{2g}\, e^0_g$; we have instead investigated both the low and high spin states for Co^{3+}, and found the high spin state $t^4_{2g}\, e^2_g$ to be more stable by 2.77 eV (see Table 5.1). In Table 5.2 we report the calculated Co-O bond distances for both spin states, and we find that the difference in the Me-O distance between the two spin states is correlated with their ionic radius: the Co^{3+} in high spin is larger than Co^{3+} in low spin.

5.2.2 Replacement energies

Once we have achieved a description of both solid–state and molecular forms of the dopant ions, we have calculated their replacement energies ΔE_{II} and ΔE_{III} in the framework of AlPO-34, according to equations (5.4) and (5.5). Results are summarised in Table 5.3, while Figures 5.2 and 5.3 presents a plot of the calculated values of ΔE_{II} and ΔE_{III} for the different dopant ions examined, as a function of the Me-O bond distance in the optimised MeAlPO-34 structure.

Table 5.3: *Calculated replacement energies ΔE_{II} and ΔE_{III} (in eV) of a framework Al with Me^{2+} and Me^{3+} dopants, according to equations 5.4 and 5.5.*

Me	Mg	Ca	Ga	Cr	Mn	Fe	Co	Ni	Zn	Sr
ΔE_{II}	3.07	4.35	-	3.58	3.66	3.51	3.39	3.95	3.04	5.00
ΔE_{III}	-	-	0.38	2.26	1.03	0.98	0.84	-	-	-

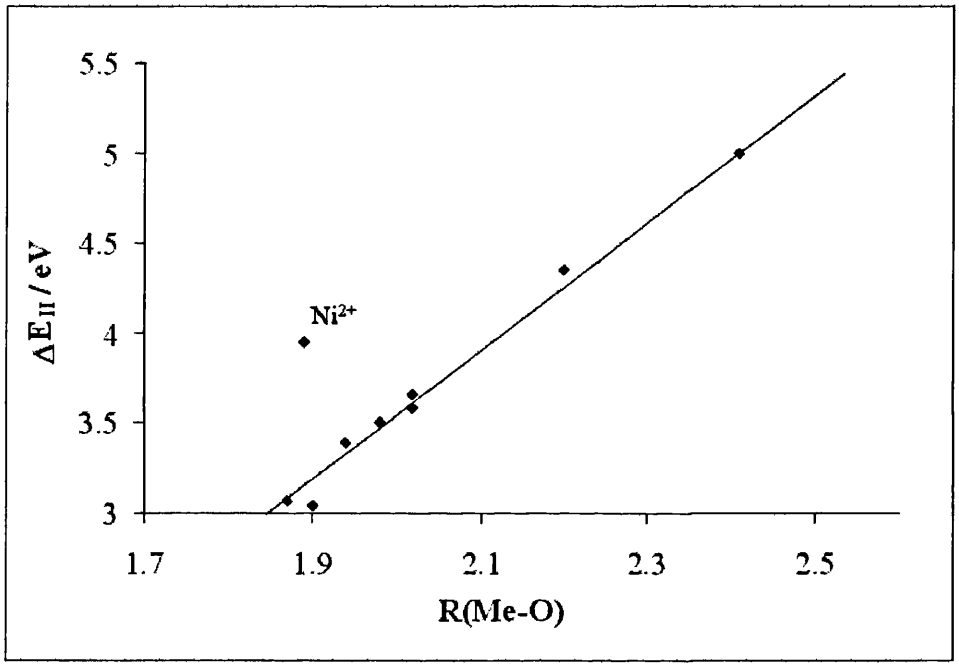

Figure 5.2: *Calculated replacement energy ΔE_{II} (in eV) for the 2+ dopants examined, as a function of the metal – oxygen bond distance, R(Me-O), in Å. The average bond distance employed here excludes the bond between the protonated oxygen and the metal.*

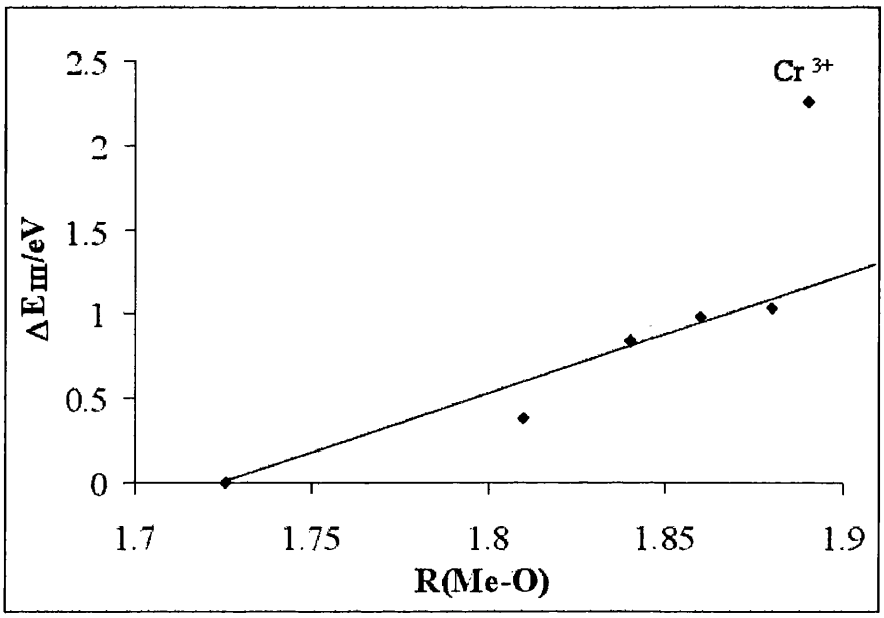

Figure 5.3: *Calculated replacement energy ΔE_{III} (in eV) for the 3+ dopant ions examined, as a function of the average metal –oxygen bond distance, R (Me-O) in Å.*

We clearly see from Figures 5.2 and 5.3, that the replacement energy increases linearly as a function of the Me-O bond distance; the larger the size of the metal dopant, the more energetically unstable its inclusion in the AlPO framework. The only exception to the linearity of ΔE_{II} and ΔE_{III} as a function of the ionic size are Ni^{2+}, and Cr^{3+}. The replacement energy of Ni^{2+} is ~ 0.9 eV higher than expected from its ionic radius; for Cr^{3+} the replacement energy is higher by ~ 1.20 eV than the expected value. The latter result is due to the instability of Ni^{2+} and Cr^{3+} ions in tetrahedral coordination. The crystal field stabilization energy of octahedral and tetrahedral Ni^{2+} and Cr^{3+} have been estimated for oxides with the spinel structure;[17] the resulting values are 1.23 eV and 2.33 eV for octahedral Ni^{2+} and Cr^{3+} ions, and 0.37 eV and 0.69 eV for tetrahedral $Ni^{2+}$and Cr^{3+}, which yields a difference of 0.86 eV in energy between the values for octahedral and tetrahedral coordination for Ni^{2+} and a difference 1.64 eV for Cr^{3+}. The value of 0.86 eV calculated for Ni is close to

the energy difference of ~ 0.9 eV, required in our calculations for bringing the replacement energy ΔE_{II} of Ni^{2+} in AlPO-34 in line with the trend observed for the other Me^{2+} dopants. For Cr^{3+} the difference of 1.64 eV in energy between octahedral and tetrahedral Cr^{3+} has the same order of magnitude as the energy difference of ~ 1.20 eV required in our calculations for bringing the replacement energy ΔE_{III} of Cr^{3+} in AlPO-34 in line with the trend observed for the other Me^{3+} dopants.

Our calculations predict therefore a marked preference of Ni^{2+} and Cr^{3+} for octahedral coordination in the AlPO-34 framework; we expect the substitution of these two dopants in the tetrahedral sites to be unstable, and difficult to achieve experimentally. This finding is consistent with experimental evidence, which shows that the amount of nickel that can be incorporated into the AlPO framework is relatively low compared to that which can be achieved for other divalent metal ions,[1] and supports the idea that Cr^{3+}, if present in AlPO frameworks, is not tetrahedrally but rather octahedrally coordinated with two extra water ligands, as originally suggested by Chen and Sheldon.[18]

From the relatively large values of ΔE_{II} and ΔE_{III}, we deduce a general *thermodynamic instability* of the doped AlPO framework, a result supported by experimental evidence, which shows that MeAlPOs are unstable upon high metal doping. From the linear relationship between the size of the metal dopant and the structural distortion it causes in the AlPO framework, discussed in section 4.1, we attribute the increasing value of ΔE_{II} and ΔE_{III} as a function of the Me-O bond distance shown in Figures 5.2 and 5.3 to the larger distortion of the framework required to accommodate the larger dopant ions (see Figure 4.4). We have seen in Chapter 4 that larger metal dopants cause a structural strain in the doped region; the bond distances between the metal dopants and the four neighbouring oxygen atoms

increase linearly with the size of the metal dopant, while the Me-O-P bond angles showed a clear correlation with the ionic size of the dopant. We therefore conclude that the *thermodynamic instability* of doped AlPO frameworks is due to the structural strain caused by the presence of the large dopants.

In the light of the results above, which emphasize the rôle of the dopant size upon the stability of MeAlPO frameworks, in the following section we extend our study, to investigate the influence of the dopant size upon its incorporation in AlPO frameworks.

5.3 Site ordering of trivalent metal dopants in AlPOs- size effects

Most microporous AlPO frameworks have a complex structure, with several non symmetry-equivalent T sites. The incorporation of dopants into such frameworks can occur in either *ordered* or *disordered* fashion. The former case, in which the dopant shows a marked preference for a specific T site of the structure, should be preferred for applications in catalysis; all active centres would in fact be located in the same crystalline environment, thus enhancing the selectivity of the catalyst. If instead the replacement of metal dopants is disordered, and the dopants are incorporated in different T sites, they will be in different environments, a feature that can contribute to decreasing the selectivity of the AlPO catalyst. Understanding the factors that promote site ordering is a problem of practical interest.

The use of experimental methods to investigate this topic is very difficult, as metals dopants are only present in few percent. This feature makes it difficult for the experimental characterization techniques to identify the exact sites of the

Chapter 5 Metal dopants incorporation in AlPO catalysts: energetics and site ordering

In this chapter, we investigate the effects controlling the energetics and stability of metal dopants incorporation in AlPO frameworks. Using *ab initio* QM calculations, we calculate the energy required for substituting a range of di- and tri-valent metal dopants at the Al framework sites of AlPO-34. We will correlate these values with the ionic size of the metal dopants. The metal dopants investigated include all alkali earth and transition metals investigated in Chapter 4. Subsequently, using methods based on interatomic potentials, we investigate site ordering of trivalent metal dopants in two AlPO frameworks, namely AlPO-41 (AFO) and DAF-1 (DFO).

5.1 Introduction

In the previous chapter, we found that the incorporation of 2+ and 3+ metal dopants in the Al sites of AlPO-34 causes a noticeable structural strain in the doped region; the bond distance between metal dopants and their neighbouring oxygen atoms R (Me-O) increases, and the Me-O-P bond angles decrease (see Figure 4.4). The extent of the structural strain caused by the dopant incorporation increases linearly with the metal size. Therefore, we expect that the size of the dopants will play a major rôle in influencing the stability of metal incorporation in AlPO frameworks, and hence control the level at which these dopants can be present in the frameworks of AlPOs. The concentration of metal active sites in these materials can modify the catalytic activity of the doped AlPO frameworks.[1] However, increasing the concentration of

metal dopants can decrease the stability of the AlPO frameworks. Understanding the factors affecting the ease of replacement of different divalent and trivalent ions in the framework of AlPOs, and the stability of the doped materials, is a topic of fundamental and practical interest.

The feasibility of the incorporation of dopants depends critically on the *thermodynamic stability* of the doped AlPO frameworks, a property that can be examined theoretically by calculating the substitution energy of the dopants in the AlPO framework. Therefore, in order to gain an insight into this topic, we have calculated the replacement energies of divalent and trivalent metal dopants for the Al framework sites in the AlPO-34, using *ab-initio* QM calculations.

5.2 Substitutional energy of dopant ions in AlPO-34 framework

From our periodic QM calculations (see section 3.3.3) we obtain the calculated energies of the pure and doped AlPO-34 frameworks. These energies can be combined to calculate the substitution energy of the dopant in the AlPO-34 framework. Since the synthesis of MeAlPO frameworks is performed in an aqueous medium, by hydrothermal methods,[2,3] the replacement reaction can be represented as:

$$\text{Al (AlPO-34)} + \text{Me}_{aq} \longrightarrow \text{Me(AlPO-34)} + \text{Al}_{aq} \qquad (5.1)$$

We have taken as suitable states for the +2 and +3 ions outside the framework their hexa-aqua complexes. This is a crude approximation for the solvated metal ions, as only the first solvation sphere of the 2+ and 3+ ions is included; nonetheless, it represents a suitably simple computational model of the solvated ions. The replacement energies of the dopants are calculated according to the following equations:

$$AlPO\text{-}34 + [Me(H_2O)_6]^{2+} \xrightarrow{\Delta E_{II}} Me^{2+}HAlPO\text{-}34 + [Al(H_2O)_5(OH)]^{2+} \quad (5.2)$$

$$AlPO\text{-}34 + [Me(H_2O)_6]^{3+} \xrightarrow{\Delta E_{III}} Me^{3+}AlPO\text{-}34 + [Al(H_2O)_6]^{3+} \quad (5.3)$$

The replacement energies ΔE_{II} and ΔE_{III} indicate the ease of inclusion of Me^{2+} and Me^{3+} ions in the AlPO-34 framework, and are calculated according to the following equations:

$$\Delta E_{II} = E(Me^{2+}HAlPO\text{-}34) + E[Al(H_2O)_5(OH)]^{2+} - E(AlPO\text{-}34) - E[Me(H_2O)_6]^{2+} \quad (5.4)$$

$$\Delta E_{III} = E(Me^{3+}AlPO\text{-}34) + E[Al(H_2O)_6]^{3+} - E(AlPO\text{-}34) - E[Me(H_2O)_6]^{3+} \quad (5.5)$$

To obtain the replacement energies according to equations (5.4) and (5.5), we need to calculate in a consistent way the energies corresponding to the aqueous complexes $[Me(H_2O)_6]^{3+}$, $[Me(H_2O)_6]^{2+}$, $[Al(H_2O)_5(OH)]^{2+}$ and $[Al(H_2O)_6]^{3+}$ and the energies of the perfect and defective solids, *i.e.* AlPO-34 and MeAlPO-34.

The *ab-initio* QM calculations on pure and defective AlPO-34 frameworks are described section 3.3.3. In the following section we concentrate instead on describing the procedure used for our molecular systems and the results obtained from these calculations.

5.2.1 Molecular calculations of hydrated ions

The geometries of all the molecular systems have been optimised at the HF level of theory using the Gaussian 98,[4] and CRYSTAL programs.[5] We first optimised all the molecular structures using Gaussian 98, then for consistency with the solid-state results the final structures have been re-optimised using the latest version of the

CRYSTAL code. We have employed the same basis set for the Al^{3+}, Me^{2+} and Me^{3+} ions in molecular and solid state calculations of pure and doped AlPO-34 framework (see Appendix 1). The water molecules are described with a standard 6-31G* basis set.[6] No symmetry constraints were imposed on any of the molecules investigated. In the optimised structures, the hexa-aqua complexes are stable in an octahedral symmetry with point group T_h (High symmetry). The only exceptions are the optimised structures of $[Mn(H_2O)_6]^{3+}$, $[Co(H_2O)_6]^{3+}$ and $[Cr(H_2O)_6]^{2+}$ which have a lower symmetry configuration (point group D_{2h}) due to Jahn-Teller distortions, in this configuration the metal ion forms long bond distances with the two axial oxygens and short bond distances with the four equatorial oxygens. These results are in agreement with previous work by Akesson *et al.*[7] The optimised configurations of the hexa-aqua complexes are illustrated in Figure 5.1.

For the complexes of open-shell transition metal ions, we have optimised all possible spin states compatible with the number of *d* electrons. Our calculations found that all the transition metal ions studied in this work are as expected, stable in the high spin state (see Table 5.1). We attribute these results to the relatively low ligand field splitting of the Me-d levels caused by the water ligands.

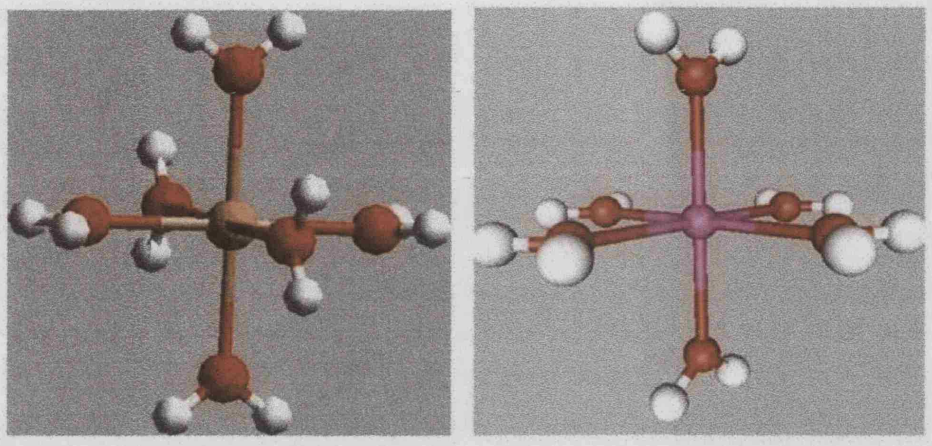

Higher symmetry configuration: T_h *Lower symmetry configuration D_{2h}*

A **B**

Figure 5.1: *Optimised geometry of the hexa-aqua complexes $[Me(H_2O)_6]^{n+}$.* **A***: T_h symmetry with all the Me-O bond distances are equal,* ***B****: lower symmetry configuration adopted by the $[Cr(H_2O)_6]^{2+}$, $[Co(H_2O)_6]^{3+}$ and $[Mn(H_2O)_6]^{3+}$ molecular ions.*

Table 5.1: *Relative stability of spin states of transition metal ions in hexa-aqua complexes:*

	High Spin (HS)	Medium Spin (MS)	Low Spin (LS)
Cr^{2+}	0	2.54	4.73
Cr^{3+}	0	-	3.60
Mn^{2+}	0	2.80	4.70
Mn^{3+}	0	2.15	4.71
Fe^{2+}	0	2.69	3.58
Fe^{3+}	0	3.48	5.06
Co^{2+}	0	-	2.50
Co^{3+}	0	2.67	2.77

The convergence of calculations for the systems containing transition metal ions with open shell electronic configuration, such as cobalt, iron, manganese, nickel and chromium, has proved to be particularly difficult to obtain. We employed the level shifting option, available in the Gaussian and CRYSTAL codes; [4,5] the latter option increases the energy difference between the occupied and the virtual orbitals, 'forcing' the electrons to stay in the occupied orbitals. We also started our optimisation using a lower convergence criterion (10^{-4} Ha) for the energy, to achieve an initial optimised geometry, followed by a new optimisation using the default convergence criterion of the Gaussian program (10^{-6} Ha). We then re-optimised the geometries using the CRYSTAL program using the default convergence criterion of 10^{-6} Ha.

All the geometry optimisations of the molecular systems have been followed by frequency calculations, to ensure that the structures obtained are true minima on the potential energy surface. No imaginary frequencies are present. The results of our calculations are compared in Table 5.2 with previous computational[7, 8, 9] and experimental studies.[10,11,12,13,14,15]

Table 5.2: *Calculated and experimental Me-O distances for hexahydrated molecular ions [Me $(H_2O)_6]^{n+}$. For Co^{3+}, the symbols 'l' and 'h' indicate low and high spin states, respectively.*

R (Me-O)/ Å			
Me	**This work**	**Other theoretical works**	**Exp**
Al^{3+}	1.918	1.935[8]	1.900[10]
Mg^{2+}	2.082	-	-
Ca^{2+}	2.392	2.393[7]	2.240[11]
Ga^{3+}	1.988	1.998[9]	1.954[12]
Cr^{2+}	2.290	2.225[7]	2.167[13]

Cr^{3+}	2.032	2.025[7]	1.960[14]
Mn^{2+}	2.239	2.233[7]	2.175[13]
Mn^{3+}	2.063	2.042[7]	1.991[14]
Fe^{2+}	2.145	2.185[7]	2.126[13]
Fe^{3+}	2.060	2.052[7]	1.995[15]
Co^{2+}	2.136	2.143[7]	2.092[13]
Co^{3+}_{l}	1.928	1.933[7]	1.873[14]
Co^{3+}_{h}	2.020		
Ni^{2+}	2.086	2.108[7]	2.056[13]
Zn^{2+}	2.127	2.123[7]	2.092[13]
Sr^{2+}	2.611	2.581[7]	2.640[11]

While there is good agreement with the previous computational studies, the comparison with experimental results[10-15] is less satisfactory, and indicates the inadequacy of gas-phase-like $[Me(H_2O)_6]^{n+}$ complexes in representing 2+ and 3+ ions either solvated or in a crystalline matrix. For Co^{3+} and Mn^{3+}, in particular, which are both disproportionate in aqueous solutions, we compare the calculated Me-O distances with those obtained from X-ray diffraction data of a crystalline structure of Cesium Alum salts $[CsMe^{3+}(SO_4)_2 \cdot 12\ H_2O]$, in which Co^{3+} and Mn^{3+} are found as a hexa-hydrated unit, with an almost regular octahedral coordination.[14] The experimental values of the Me-O bond distances are shorter than the calculated ones by as much as 0.07 Å, which is far greater than expected from the quality of the calculations performed. This large difference is due to the long-range effects present in the aqueous solutions and in the crystalline matrix, but not in the isolated hexa-aqua complexes. Both in the water solutions and in the Alum salts, the strong hydrogen-bonds which link the first to the second hydration sphere polarize the water molecules and shorten the Me-O bonds.[16] Moreover, the steric pressure exerted on the $[Me(H_2O)_6]^{n+}$ core from the crystalline matrix, shortens the Me-O bond distance

with respect to the isolated complex. We can, however, assume that these 'long-range' forces affect systematically ions with the same charge (*i.e.* all the Me^{3+} and Me^{2+} ions examined here), and the error introduced will cancel out when considering energy differences, such as those of equations (5.3) and (5.4) needed to calculate ΔE_{II} and ΔE_{III} .

Based on assumptions from the experimental work on Alum Salts, Akesson *et al*[7] assumed in their study that Co^{3+} in the hexa-aqua complex is stable in the low spin state, $t^6_{2g}\, e^0_g$; we have instead investigated both the low and high spin states for Co^{3+}, and found the high spin state $t^4_{2g}\, e^2_g$ to be more stable by 2.77 eV (see Table 5.1). In Table 5.2 we report the calculated Co-O bond distances for both spin states, and we find that the difference in the Me-O distance between the two spin states is correlated with their ionic radius: the Co^{3+} in high spin is larger than Co^{3+} in low spin.

5.2.2 Replacement energies

Once we have achieved a description of both solid–state and molecular forms of the dopant ions, we have calculated their replacement energies ΔE_{II} and ΔE_{III} in the framework of AlPO-34, according to equations (5.4) and (5.5). Results are summarised in Table 5.3, while Figures 5.2 and 5.3 presents a plot of the calculated values of ΔE_{II} and ΔE_{III} for the different dopant ions examined, as a function of the Me-O bond distance in the optimised MeAlPO-34 structure.

Table 5.3: *Calculated replacement energies ΔE_{II} and ΔE_{III} (in eV) of a framework Al with Me^{2+} and Me^{3+} dopants, according to equations 5.4 and 5.5.*

Me	Mg	Ca	Ga	Cr	Mn	Fe	Co	Ni	Zn	Sr
ΔE_{II}	3.07	4.35	-	3.58	3.66	3.51	3.39	3.95	3.04	5.00
ΔE_{III}	-	-	0.38	2.26	1.03	0.98	0.84	-	-	-

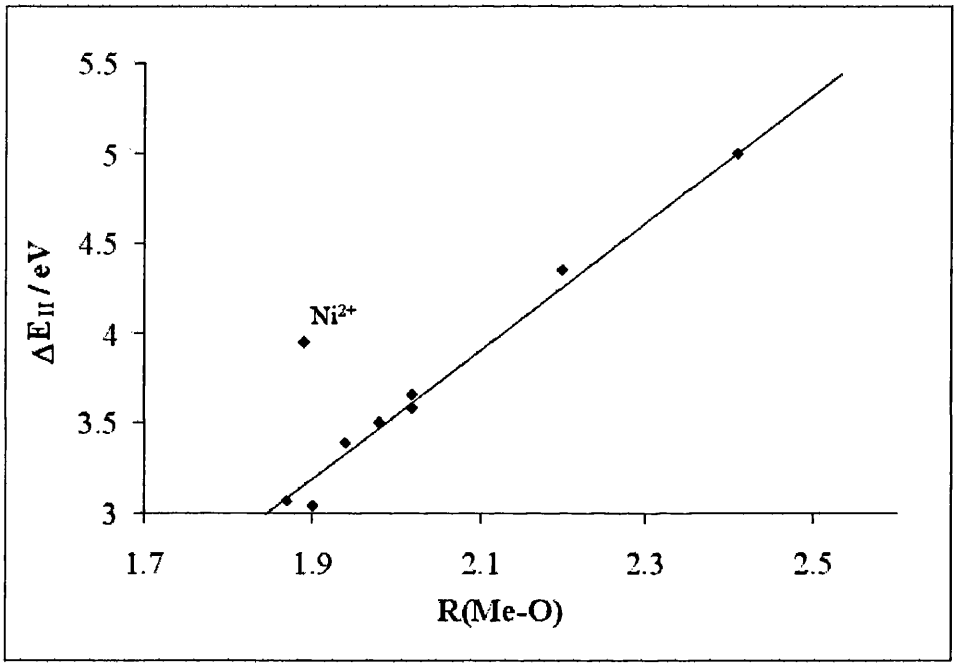

Figure 5.2: *Calculated replacement energy ΔE_{II} (in eV) for the 2+ dopants examined, as a function of the metal – oxygen bond distance, R(Me-O), in Å. The average bond distance employed here excludes the bond between the protonated oxygen and the metal.*

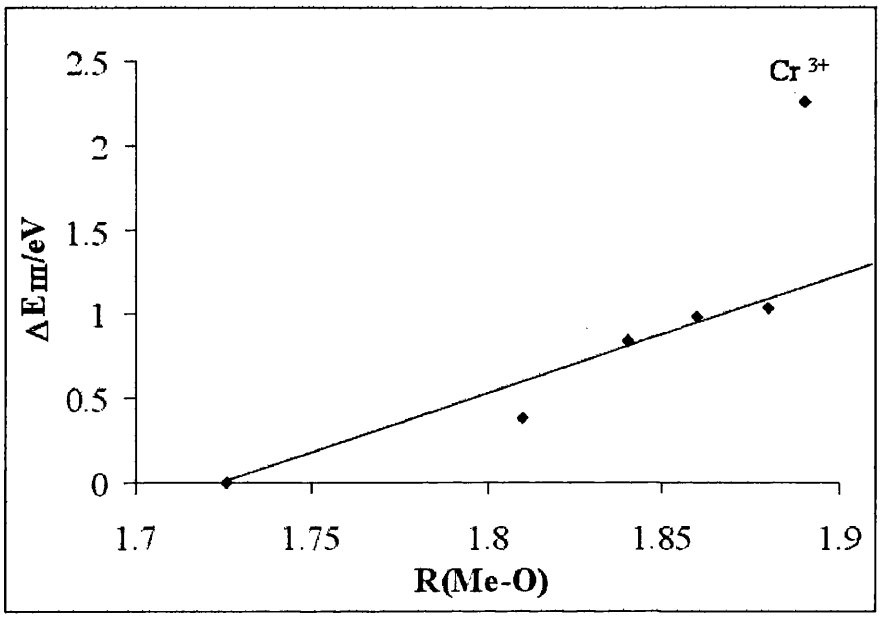

Figure 5.3: *Calculated replacement energy ΔE_{III} (in eV) for the 3+ dopant ions examined, as a function of the average metal –oxygen bond distance, R (Me-O) in Å.*

We clearly see from Figures 5.2 and 5.3, that the replacement energy increases linearly as a function of the Me-O bond distance; the larger the size of the metal dopant, the more energetically unstable its inclusion in the AlPO framework. The only exception to the linearity of ΔE_{II} and ΔE_{III} as a function of the ionic size are Ni^{2+}, and Cr^{3+}. The replacement energy of Ni^{2+} is ~ 0.9 eV higher than expected from its ionic radius; for Cr^{3+} the replacement energy is higher by ~ 1.20 eV than the expected value. The latter result is due to the instability of Ni^{2+} and Cr^{3+} ions in tetrahedral coordination. The crystal field stabilization energy of octahedral and tetrahedral Ni^{2+} and Cr^{3+} have been estimated for oxides with the spinel structure;[17] the resulting values are 1.23 eV and 2.33 eV for octahedral Ni^{2+} and Cr^{3+} ions, and 0.37 eV and 0.69 eV for tetrahedral $Ni^{2+}$and Cr^{3+}, which yields a difference of 0.86 eV in energy between the values for octahedral and tetrahedral coordination for Ni^{2+} and a difference 1.64 eV for Cr^{3+}. The value of 0.86 eV calculated for Ni is close to

the energy difference of ~ 0.9 eV, required in our calculations for bringing the replacement energy ΔE_{II} of Ni^{2+} in AlPO-34 in line with the trend observed for the other Me^{2+} dopants. For Cr^{3+} the difference of 1.64 eV in energy between octahedral and tetrahedral Cr^{3+} has the same order of magnitude as the energy difference of ~ 1.20 eV required in our calculations for bringing the replacement energy ΔE_{III} of Cr^{3+} in AlPO-34 in line with the trend observed for the other Me^{3+} dopants.

Our calculations predict therefore a marked preference of Ni^{2+} and Cr^{3+} for octahedral coordination in the AlPO-34 framework; we expect the substitution of these two dopants in the tetrahedral sites to be unstable, and difficult to achieve experimentally. This finding is consistent with experimental evidence, which shows that the amount of nickel that can be incorporated into the AlPO framework is relatively low compared to that which can be achieved for other divalent metal ions,[1] and supports the idea that Cr^{3+}, if present in AlPO frameworks, is not tetrahedrally but rather octahedrally coordinated with two extra water ligands, as originally suggested by Chen and Sheldon.[18]

From the relatively large values of ΔE_{II} and ΔE_{III}, we deduce a general *thermodynamic instability* of the doped AlPO framework, a result supported by experimental evidence, which shows that MeAlPOs are unstable upon high metal doping. From the linear relationship between the size of the metal dopant and the structural distortion it causes in the AlPO framework, discussed in section 4.1, we attribute the increasing value of ΔE_{II} and ΔE_{III} as a function of the Me-O bond distance shown in Figures 5.2 and 5.3 to the larger distortion of the framework required to accommodate the larger dopant ions (see Figure 4.4). We have seen in Chapter 4 that larger metal dopants cause a structural strain in the doped region; the bond distances between the metal dopants and the four neighbouring oxygen atoms

increase linearly with the size of the metal dopant, while the Me-O-P bond angles showed a clear correlation with the ionic size of the dopant. We therefore conclude that the *thermodynamic instability* of doped AlPO frameworks is due to the structural strain caused by the presence of the large dopants.

In the light of the results above, which emphasize the rôle of the dopant size upon the stability of MeAlPO frameworks, in the following section we extend our study, to investigate the influence of the dopant size upon its incorporation in AlPO frameworks.

5.3 Site ordering of trivalent metal dopants in AlPOs- size effects

Most microporous AlPO frameworks have a complex structure, with several non symmetry-equivalent T sites. The incorporation of dopants into such frameworks can occur in either *ordered* or *disordered* fashion. The former case, in which the dopant shows a marked preference for a specific T site of the structure, should be preferred for applications in catalysis; all active centres would in fact be located in the same crystalline environment, thus enhancing the selectivity of the catalyst. If instead the replacement of metal dopants is disordered, and the dopants are incorporated in different T sites, they will be in different environments, a feature that can contribute to decreasing the selectivity of the AlPO catalyst. Understanding the factors that promote site ordering is a problem of practical interest.

The use of experimental methods to investigate this topic is very difficult, as metals dopants are only present in few percent. This feature makes it difficult for the experimental characterization techniques to identify the exact sites of the

incorporated metal dopants. Computational techniques can contribute greatly in this area.

The driving force for ordering of the dopant can be calculated from the relative replacement energy of the dopant ion in the different T sites of the AlPO framework under investigation. A range of replacement energies comparable to the thermal energy will result in disordered distribution across T sites, while a range of replacement energies greater than the thermal energy indicates a strong thermodynamic driving force for the dopant towards an ordered incorporation in the framework.

Cormack *et al*[19] showed that the size of the cations has a major effect upon their site distribution in spinels, where octahedral and tetrahedral sites are available. All the framework sites in AlPOs are tetrahedrally coordinated and are differentiated only by the number of second or further shells of neighbours of the dopant. In such a case, the chemical interaction between nearest neighbour dopant and oxygen ions is largely equivalent in different polymorphic structures; the ease of inclusion of the dopant is related to *the topological features* of the host framework, and the ease with which it can adapt to the incorporation of ions of *variable size.*

In this section, we investigate trivalent substitutional ions (which replace a framework Al), and examine the effect of the dopant size upon its site distribution, in two different AlPO polymorphs, namely AlPO-41 (AFO)[20] and DAF-1 (DFO)[21], shown in Figure 5.4. These two frameworks have a number of topologically different T sites, incorporated into rings ranging in size from 4 to 12 tetrahedra, thus enabling us to examine the combined effect of *dopant size* and *framework topology* onto the dopant ordering.

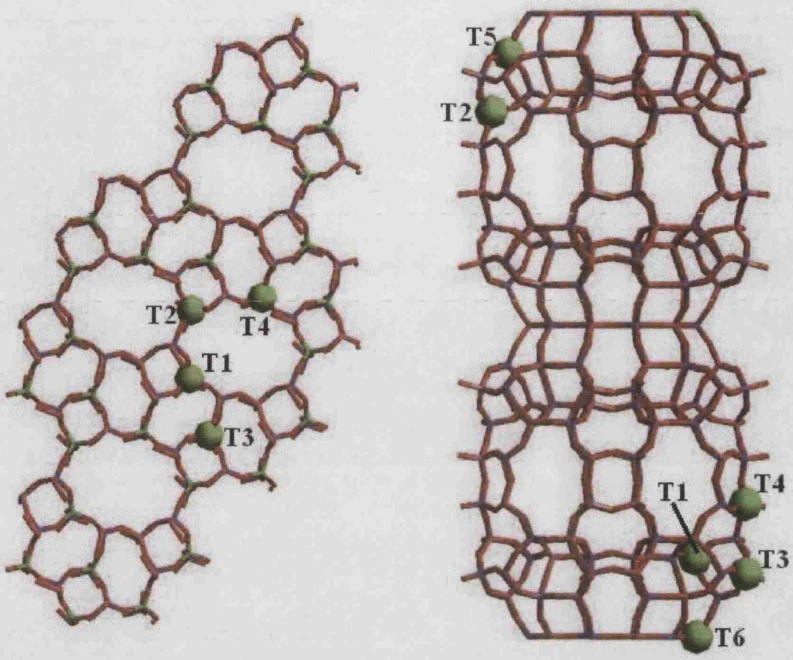

Figure 5.4: *Framework topology of AFO (left) and DFO (right) AlPO structures, with the topologically non-equivalent T sites labelled according to the Atlas of zeolite framework types.* [22]

5.3.1 Methodology

In these calculations we employed the GULP program and used the shell model potential of Gale and Henson,[23] to represent the undoped frameworks of AFO and DFO repectively. We have shown in section 3.2.2 that the potential of Gale and Henson is superior to other forcefields in terms of describing the geometries and energetics of AlPO polymorphs. The size of trivalent metal dopants considered in this study can be varied systematically by varying continuously the pre-exponential factor of the Buckingham potential, describing the Me-O interaction, according to the procedure we have described in section 3.2.1.

In our work we assumed the ionic radius of the framework Al^{3+} to be R_{Al}=0.51 Å,[24] and examined a range of ionic radii for the dopant ions of 0.35Å <R<0.90Å, which covers most of the 3+ ions available from the periodic table.

For each dopant size R, we located one substitutional dopant in each unit cell of the host framework, composed of 10 formula units in AFO, and 132 formula units in DFO; we examined the dopant incorporation in each topologically unique T site, T_n (4 in AFO and 6 in DFO). In the following discussion, sites are labelled as in the Atlas of zeolite framework types[22] (labels are also reported in Figure 5.4). For each combination of dopant size and T site, we have fully relaxed the structure to minimum energy, using P1 symmetry.

5.3.2 Results and discussions

We report in Figures 5.5 and 5.6 the relative energies of the doped frameworks and the equilibrium volume per atom against the ionic radius R of the metal dopant. The relative lattice energies (ΔE_n) are calculated, for each value of R, by taking the energy of the stable site T_i for the smallest ions (T1 both in AFO and DFO) as reference. The relative energy for site n is obtained as $\Delta E_n(R) = E_n(R) - E_1(R)$.

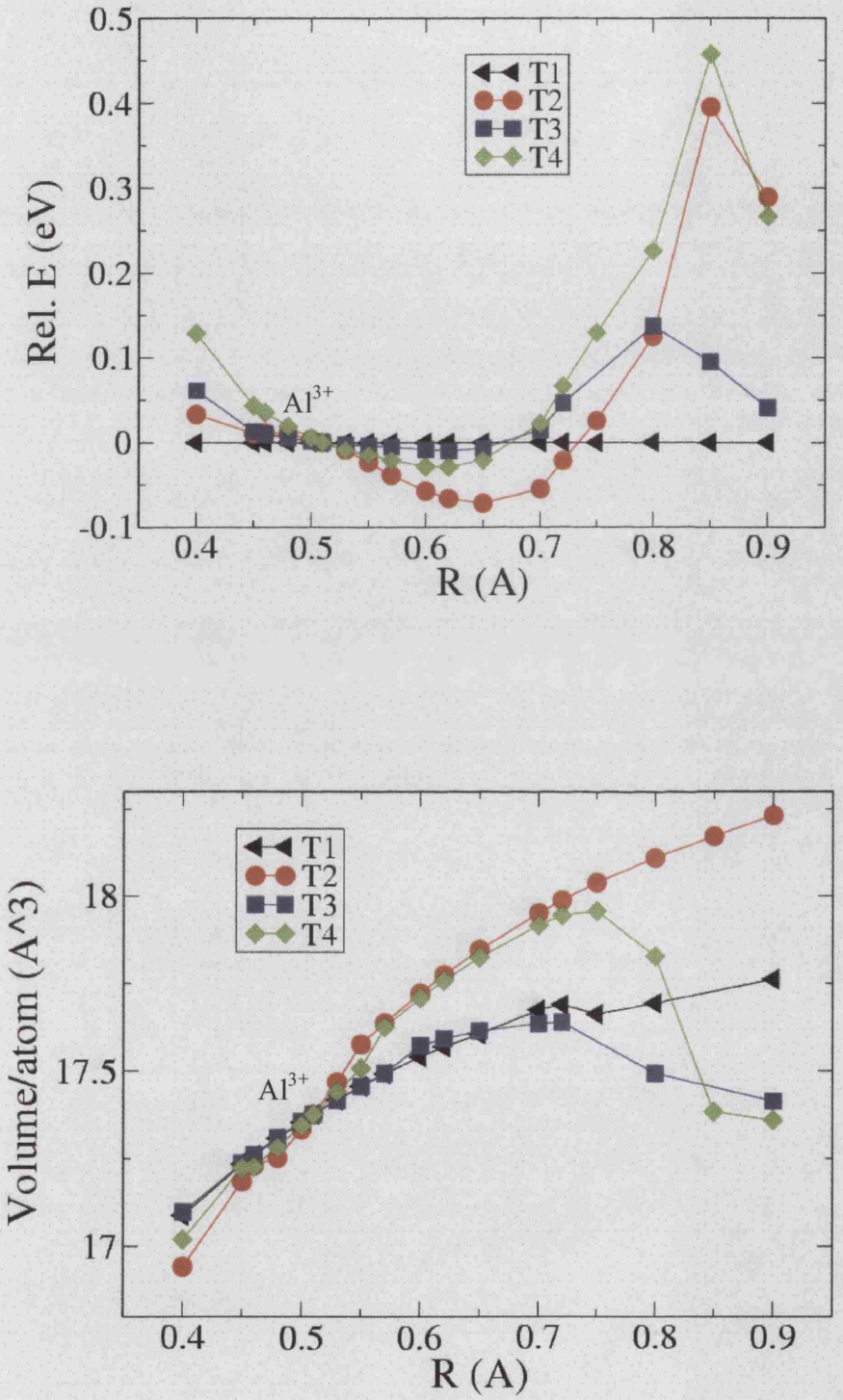

Figure 5.5: *Relative replacement energy ΔE_n (eV/dopant), and volume per atom: V_n ($Å^3$) for the doped AFO framework, as a function of the dopant radius R (Å).*

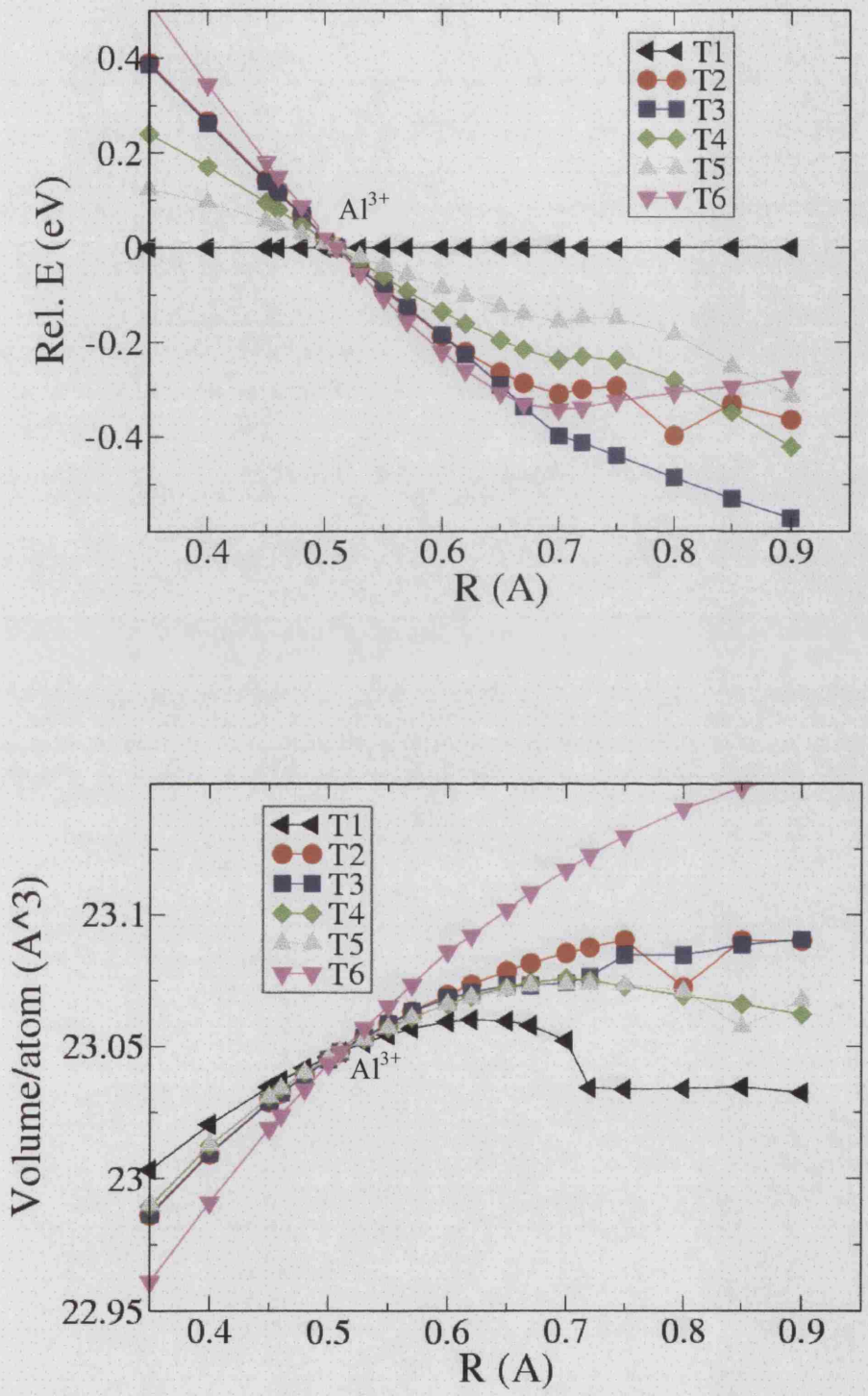

Figure 5. 6: *Relative replacement energy ΔE_n (eV/dopant), and volume per atom V_n ($Å^3$) for the doped DFO framework, as a function of the dopant radius R (Å).*

We see in Figures 5.5 and 5.6 that the relative lattice energies ΔE_n (R) are small for values of R similar to R_{Al} ($\Delta E_n(R_{Al})=0$ by necessity, as this is the undoped AlPO framework). The more the deviation of the ionic radius R from R_{Al}, the larger the energy dispersion of the ΔE_n values becomes. This result clearly indicates that a site-ordered inclusion in the framework is energetically favoured for dopant ions whose size is most different from that of the host Al^{3+} ion they replace. Ions of similar size to Al would instead favour a disordered inclusion into the AlPO framework.

To rationalise the behaviour shown in Figures 5.5 and 5.6, we examine the local environment of the dopant ion, and how it changes with the ionic size R.

In the AFO framework (see Figure 5.5), ions smaller than Al are stable in site T1, whereas dopant ions bigger than Al are energetically stable in site T2. The biggest change in the lattice energy and volume as a function of the ionic radius is seen for site T2, whereas for T1 (and T3) we see a small change in the energy and cell volume as the ionic size of the metal dopant varies.

We observe a similar behaviour for the DFO framework (see Figure 5.6), in which site T6 shows the biggest change in both energy and cell volume as the ionic size of the metal dopant increases; sites T6 and T3 are energetically stable for ions that are bigger than Al. The smallest change of the energy and cell volume is seen for site T1, which is stable for dopants that are smaller than Al.

This behaviour can be rationalised by partitioning the T sites available in the framework into two structural types:

1) Caged T sites, which include T1 and T3 in AFO; T1, T4 and T5 in DFO (see Figure 5.4). The AlPO framework forms a rigid structure around the site, with strong structural constraints. The framework structure around the 'caged' T sites is not free to relax upon doping; in particular its next-nearest neighbour P sites cannot readily

relax outwards following the dopant incorporation. The main relaxation movement around large dopants is therefore a bending of the Me-O-P angles around its nearest neighbour oxygens, which decrease on increasing R. Since the relaxation is local around the dopant, it causes only minor changes in the cell volume as a function of R, and the replacement of large ions is energetically unstable.

2) Free T sites: This is the case of T2 in AFO and T6 in DFO (see Figure 5.4), which are part of a large ring system, and hence are located in a more flexible framework region. The framework topology allows larger portions of the structure to relax around the dopant, which is reflected in the larger increase of the cell volume of the doped framework as a function of R. Since there are fewer constraints acting upon the metal dopant from the rest of the structure, replacement of large dopant ions is energetically favourable in the 'free' T sites.

The different structural behaviour is clearly illustrated in Figure 5.7, where we report the equilibrium value of the Me-O-P angle (averaged over the 4 oxygens that are nearest neighbour to the dopant) for sites T2 (free) and T1 (caged) in AFO. The value of the Me-O-P angle is smaller in the latter case, indicative of a more strained structure around the dopant.

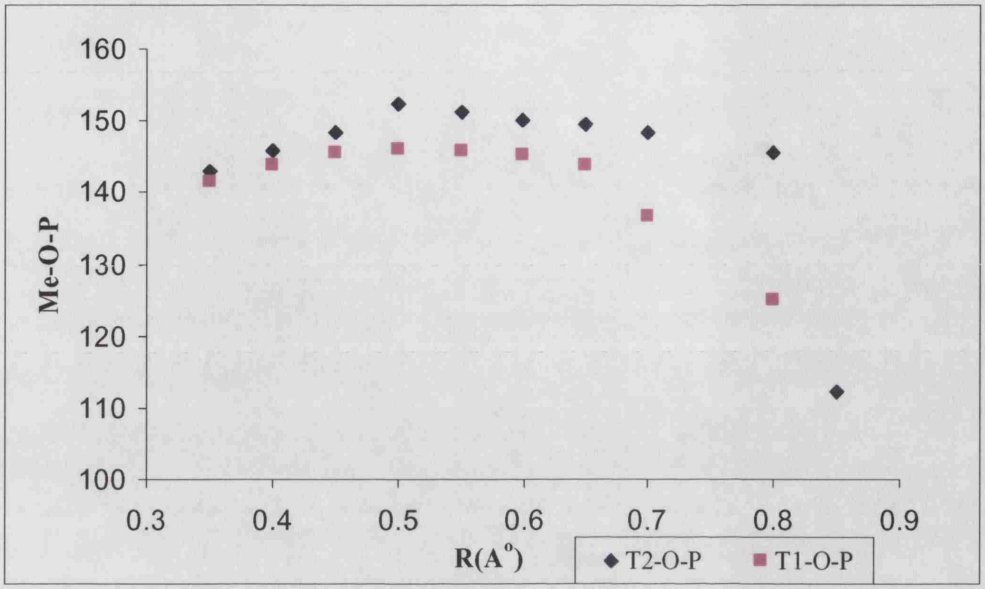

Figure 5.7: *Variation of the Me-O-P bond angle (averaged over the four oxygens that are nearest neighbour to the dopant M) as a function of the dopant radius R (Å), for sites T1 (caged) and T2 (free) in AFO.*

The structural freedom of the T sites is not unlimited: even if the substitution occurs in the more flexible T sites, on increasing the size of the metal dopant the structure becomes more and more rigid, until it swaps to a caged T site behaviour. This feature is illustrated by the progressive decrease of the Me-O-P angle around site T2 in Figure 5.7, which collapses for the largest dopant ions examined.

5.4 Conclusion

In this chapter we have demonstrated that the size of metal dopants has a major influence upon the thermodynamical stability of doped AlPO frameworks and the site ordering of the dopant in these frameworks. Bigger metal dopants prefer to substitute 'free' Al sites, located in unconstrained regions of the framework, whereas

small metal dopants are energetically stable when replacing Al sites situated in smaller cages. This site preference increases on increasing the size difference between host ion and dopant, and is explained via the topological features of the host AlPO framework. This prediction of the computational work is open for experimental verification.

References

1 M. Hartmann, L. Kevan, *Chem. Rev.*, **1999**, *99*, 635

2 B. M.Lok, C. A. Messina, R. L. Patton, R. T.Gajek, T. R Cannan, E. M. Flanigen. *J. Am. Chem. Soc.*, **1984**, *106*, 6092

3 J. S. Chen, J. M. Thomas, G. Sankar, *J. Chem. Soc- Faraday Trans.* **1994**, *90*, 3455.

4 M. J. Frisch, G. W. Trucks, H. B. Schlegel, G. E. Scuseria, M. A. Robb, J. R. Cheeseman, V. G. Zakrzewski, J. A. Montgomery, Jr., R. E. Stratmann, J. C. Burant, S. Dapprich, J. M. Millam, A. D. Daniels, K. N. Kudin, M. C. Strain, O. Farkas, J. Tomasi, V. Barone, M. Cossi, R. Cammi, B. Mennucci, C. Pomelli, C. Adamo, S. Clifford, J. Ochterski, G. A. Petersson, P. Y. Ayala, Q. Cui, K. Morokuma, D. K. Malick, A. D. Rabuck, K. Raghavachari, J. B. Foresman, J. Cioslowski, J. V. Ortiz, A. G. Baboul, B. B. Stefanov, G. Liu, A. Liashenko, P. Piskorz, I. Komaromi, R. Gomperts, R. L. Martin, D. J. Fox, T. Keith, M. A. Al-Laham, C. Y. Peng, A. Nanayakkara, M. Challacombe, P. M. W. Gill, B. Johnson, W. Chen, M. W. Wong, J. L. Andres, C. Gonzalez, M. Head-Gordon, E. S. Replogle, and J. A. Pople, Gaussian, Inc., Pittsburgh PA, 1998.GAUSSIAN 98 (Revision A, 6), **1998**

5 V. R.Saunders, R. Dovesi, C. Roetti, M. Causà, N. M.Harrison, R. Orlando, M.C. Zicovich-Wilson, K. Doll, B. Civalleri, *CRYSTAL 2003 User's Manual*, University of Torino, **2003**

6 W.J. Hehre, R. Ditchfield and J.A. Pople, *J. Chem. Phys.* **1972**,*56*, 2257; P.C. Hariharan and J.A. Pople, *Theoret. Chimica Acta*, **1973**, *28*, 213

7 R. Akesson, L. G. M. Pettersson, M. Sandstrom, U. Wahlgren, *J. Am. Chem. Soc.* **1994**, *116*, 8691

8 W. W. Rudolph, R. Manson, C. C. Pye, *Phys. Chem. Chem. Phys*, **2000**, *2*, 5030

9 W. W. Rudolph, C. C. Pye, G. Lrmer, *J. Raman. Spectosc.* **2002**, *33*, 177

10W. Bol, T. Welzen, *Chem. Phys. Lett.* **1977**, *49*, 189

11 Y. Marcus, *Chem. Rev.* **1988**, *88*, 1475

12 A. Muñoz-Páez, S. Diaz-Moreno, E. S. Marcos, J. M. Martinez, R. R. Pappalardo, I. Persson, M. Sandström, S. Pattanaik, P. Lindqvist-Reis, *J. Phys IV*, **1997**, *7*, C2-647.

13 F. A. Cotton, L. M. Daniels, C. A. Murillo, J. F. Quesada, *Inorg. Chem*, **1993**, *32*, 4861

14 J. K. Beattie, S. P. Best, B. W. Skelton, A. H. White, *J. Chem. Soc- Dalton Trans.* **1981**, *10*, 2105

15 S. P. Best, J. B. Forsyth, *J. Chem. Soc. Dalton. Trans.* **1990**, 3507

16 W. R. Wolfram, M. Roger, C. P. Cory, *Phys. Chem. Chem . Phys*, **2000**, *2*, 5030.

17 A. R. West, *Basic Solid State Chemistry*, Wiley; Chichester, **1988**.

18 J. D. Chen, R. A. Sheldon, *J. Catal.* **1995**, *153*, 1

19 A. N. Cormack, G. V. Lewis, S. C. Parker and C. R. A. Catlow, *J. Phys. Chem. Solids*, **1988**, *49*, 53.

20 Kirchner, R.M. and Bennett, J.M. *Zeolites*, **1994**, *14*, 523

21 P. A. Wright, R. H. Jones, S. Natarajan, R. G. Bell, J. Chen, M. B. Hursthouse, J. M. Thomas, *J. Chem. Soc, Chem. Commun*, **1993**, 1861.

22 Ch. Baerlocher, W.M. Meier, D.H. Olson, *Atlas of zeolite framework types, 5th ed.*, Elsevier, Amsterdam, **2001**.

23 J. D. Gale and N. J. Henson, *J. Chem. Soc. Faraday. Trans.*,**1994**, *90*, 3175

24 R.C. Weast, *CRC Handbook of Chemistry and Physics 59th ed.*, CRC Press, Palm Beach, **1978**.

Chapter 6 Catalytic properties of MeAlPO catalysts

In the previous two chapters we have investigated the electronic and structural properties of the doped AlPO frameworks, and the factors affecting their stability. In this chapter, we investigate the catalytic properties related to the metal dopants, namely the Brønsted and Lewis acidity and the redox potential of 2+ and 3+ transition metal ions. We shall investigate each of these topics in three separate sections.

6.1 Brønsted acidity of divalent metal doped AlPO frameworks

It is well established that among other factors, such as framework type and dopant concentration, the acidity of Me(H)AlPOs depends upon the *nature* of the divalent dopant incorporated. Indeed, the acid strength can be tuned by controlling the type and concentration of dopants during the synthesis. This is one of the fascinating properties of MeAlPOs which make them open to further improvement and tailoring. Hence, defining a scale of relative acidity for the possible dopants, and correlating this property with the chemical composition, would provide a way of optimising the activity and/or selectivity of the catalysts. In this respect, many attempts have been made in literature to correlate experimentally the acid strength of MeAlPOs with different structural parameters related to the Me dopant, such as the ionic radius,[1] electronegativity,[2] or the Me-O-P bond angle.[1,3]

Based on the analysis of Temperature Programmed Desorption (TPD) of methanol measurements Hočevar *et al*,[4] for instance, reported a correlation between the acid

strength and the Me-O bond distance in the MeAlPO catalysts: the smaller the size of the metal dopant, the stronger the Brønsted acidity. They also concluded that the acid strength does not depend on the *type* of AlPO framework but is only dependant upon the *nature* of the metal incorporated. De las Pozas *et al*,[2] instead, assumed a correlation of the acidity of MeAlPOs with the electronic properties of the Metal dopant, such as its electronegativity. Nur and Hamdan, [1] on the other hand claimed that the acid strength increases with the ionic size of the metal dopants, and with the value of the Me-O-P bond angle.[1]

Although the experimental works highlighted above have succeeded in finding a correlation between the acidity of MeAlPOs and the atomic properties of the metal dopants, they have been confined to only a few types of dopants. Extending the comparison to a wider range of dopants is experimentally very challenging: as we have discussed in chapters 4 and 5, isomorphous substitutions of divalent ions are often energetically unstable and difficult to achieve; owing to a bigger ionic size of divalent metal dopants, compared to the ionic size of framework aluminium ions. During the synthesis of MeAlPOs, it is difficult to control the concentration level of the dopant ions incorporated in the framework, which may result in different concentrations of dopants in framework and extra-framework positions in the final product. Furthermore, other active defect centres may be created in the catalysts, and the interaction between the defect centres in the same region of the catalyst can alter their activity. The use of computer modelling to study the acidity of MeAlPOs can therefore provide new insights: in a modelling work, it is possible to control all those parameters that are not easily controlled experimentally and modelling allows the prediction of the acidity associated with a wide range of dopants, even of those that have not yet been successfully incorporated in experiments. Thus enabling us to

compare the acidity associated with each metal dopant in the same AlPO framework. The importance of each parameter discussed above on the acidity of the material can in this way be examined separately.

In this section, we use results from our *ab-initio* calculations on doped AlPOs to calculate the acid strength associated with nine different divalent metal dopants. These are Mg, Ca, Cr, Mn, Fe, Co, Ni, Zn and Sr. We have investigated the acid properties of divalent metal doped AlPOs by calculating the OH stretching frequency ν_{OH} of the Brønsted acid site for the equilibrium structure of each ion in the AlPO-34 framework.

In principle, the OH stretching frequency is not a direct measure of the acidity, as there is no fundamental correlation between this property and the heterolytic OH dissociation energy. However, it is often assumed to be an effective measure of the chemical strength of the OH bond, and thus reflects the acid strength of the hydroxyl group. A weaker OH bond, *i.e.* a more acidic hydroxyl group, is reflected by a lower stretching frequency.[5] In the following discussion we shall therefore assume that a lower value of ν_{OH} represents a more acid OH group. ν_{OH} is an observable that can also be obtained experimentally from IR spectroscopy measurements.

The values of ν_{OH} are calculated in this work at the HF level of theory, which is known systematically to overestimate the ν_{OH} values by ~12% compared to experiments; the correction for this systematic error is often effected by scaling the calculated HF values of frequencies by a factor of 0.89.[6] Our intention in this work is not to compare the calculated ν_{OH} values with experiment, but to compare the calculated values of ν_{OH} for the different dopant ions, in order to deduce a scale of relative acidic strength. We therefore use unscaled values of ν_{OH}.

The results of our systematic study allow us first to define a scale of relative acidity for metal dopants, and second to investigate if the results of our computational work support possible correlations between the acid strength and either the atomic properties of dopants, such as the electronegativity (E.N) and the ionic radius (r), or their local environment in the AlPO frameworks, such as the Me-O_H-P bond angles and Me-O_H bond distances, as proposed in the literature. The results are summarized in Table 6.1, and presented in Figure 6.1, where we report plots of the calculated ν_{OH} as a function of the parameters described above.

Table 6.1: *Local environment of divalent metal ions examined in AlPO-34, atomic properties of the metal dopants, and calculated stretching frequencies. R refers to the calculated bond distances (in Å), Me-O_H-P is the bond angle between protonated oxygen and its two neighbouring ions. r is the ionic radius of the dopant, taken from reference 7. E.N is the electronegativity[7] of the dopants, ν_{OH} is the calculated stretching frequency in cm^{-1}.*

Me	R(Me-O_{1-3})	R(Me-O_H)	R(O_H-H)	Me-O_H-P	r	E.N	ν_{OH}
Mg	1.876	2.084	0.955	132.4	0.66	1.31	4037
Ca	2.204	2.408	0.950	126.0	0.99	1.00	4140
Cr	2.024	2.356	0.948	127.5	0.89	1.66	4243
Mn	2.027	2.265	0.950	127.8	0.80	1.55	4194
Fe	1.982	2.191	0.950	129.0	0.74	1.83	4157
Co	1.943	2.141	0.950	129.3	0.72	1.88	4192
Ni	1.899	2.192	0.950	126.4	0.69	1.91	4201
Zn	1.907	2.189	0.950	131.3	0.74	1.65	4207
Sr	2.411	2.555	0.949	116.2	1.12	0.95	4195

Before investigating possible correlations between the acidity and properties of metal dopants, let us first consider the scale of acidity predicted in this work. Our calculations indicates that the acidity decreases in the order of MgAlPO >>CaAlPO>>FeAlPO>CoAlPO> SrAlPO> MnAlPO> ZnAlPO> NiAlPO> CrAlPO.

The Mg-doped AlPO framework has the strongest acid sites of all dopants examined; its calculated value of ν_{OH} is in fact more than 100 cm^{-1} lower compared to any other dopant; CrAlPO is instead predicted in our work to be the weakest acid.

Experimental evidence shows that MeAlPO solid acids with moderate acidity are the most selective for the conversion of methanol into light olefins.[8] In the light of the calculated values of ν_{OH}, we expect Cr, Ni, Zn and Mn dopants in AlPO-34 to yield the highest selectivity for light olefins, while MgAlPO will be more active at the expense of selectivity. Linshke *et al*[8] reported that MgAlPO-5 has the lowest catalytic activity for the conversion of methanol to light olefins, when compared with other MeAlPO-5 materials, (Me= Cr, Zr, Co, Ni). The low activity of MgAlPO, however, is due to the fast formation of coke precursor compounds on the inner walls of the catalyst in early stages of the chemical reaction, a process which suggests that Mg-doped AlPOs indeed have very strong acid sites. NiAlPO-5 has been found instead by these authors to give the best results for the catalytic formation of light olefins, because it has a higher density of Brønsted acid sites of moderate strength, and a negligible portion of Lewis sites. These results support our finding regarding strong acidity of MgAlPOs and moderate acidity of NiAlPOs.

Let us now compare our results with the work of Nur and Hamdan,[1] who examined the selective conversion of cyclohexanol over different MeAlPO-5 catalysts. The experimental work found that the acidity of MeAlPO-5 catalysts correlates with the ionic size of the Me dopant ions according to the following order: Mn>Zn>Co>Mg, *i.e.* the bigger the size of the metal dopant, the stronger its acidity. In addition the authors report that the T-O-P bond angle, measured by ^{31}P MAS NMR spectra, increases with the ionic size of the metal dopant and that the lattice parameter of the MeAlPO-5 catalysts decreases with increasing the dopant content. None of the above

results agrees with our calculations; in section 4.2.2, for example, we found, that the larger the size of the metal dopant, the smaller the Me-O-P angle, and Nur and Hamdan's result [1] concerning the volume per formula unit of the doped materials, *i.e.* that the volume decreases on incorporating large metal dopants in the framework, is at least counter-intuitive. We consider the discrepancy between our work and the results of reference 1 to be due to the interaction of dopant ions in the framework of the experimental catalysts. While our model of the solid accounts for the behaviour of isolated dopant ions, and applies to AlPO frameworks with a low content of dopant ions, the catalysts employed by Nur and Hamdan contained a large fraction (~10%) of low-valent ions. In such a case, the formation of clusters of dopant ions in a limited region of the framework is very likely; we consider that the interaction between defect centres can cause the different structural behaviour observed in reference 1, which will modify the catalytic activity of the solid.

Let us now investigate if there is any correlation between the calculated values of ν_{OH} and the atomic properties of the dopants, *i.e.* the Me electronegativity, ionic radius of the metal, Me-O-P bond angle, and the Me-O bond distance. Results are shown in Figure 6.1. We see that in general *no absolute* correlation exists between the calculated values of the stretching frequencies ν_{OH} with either the atomic or the local structural properties of the dopants.

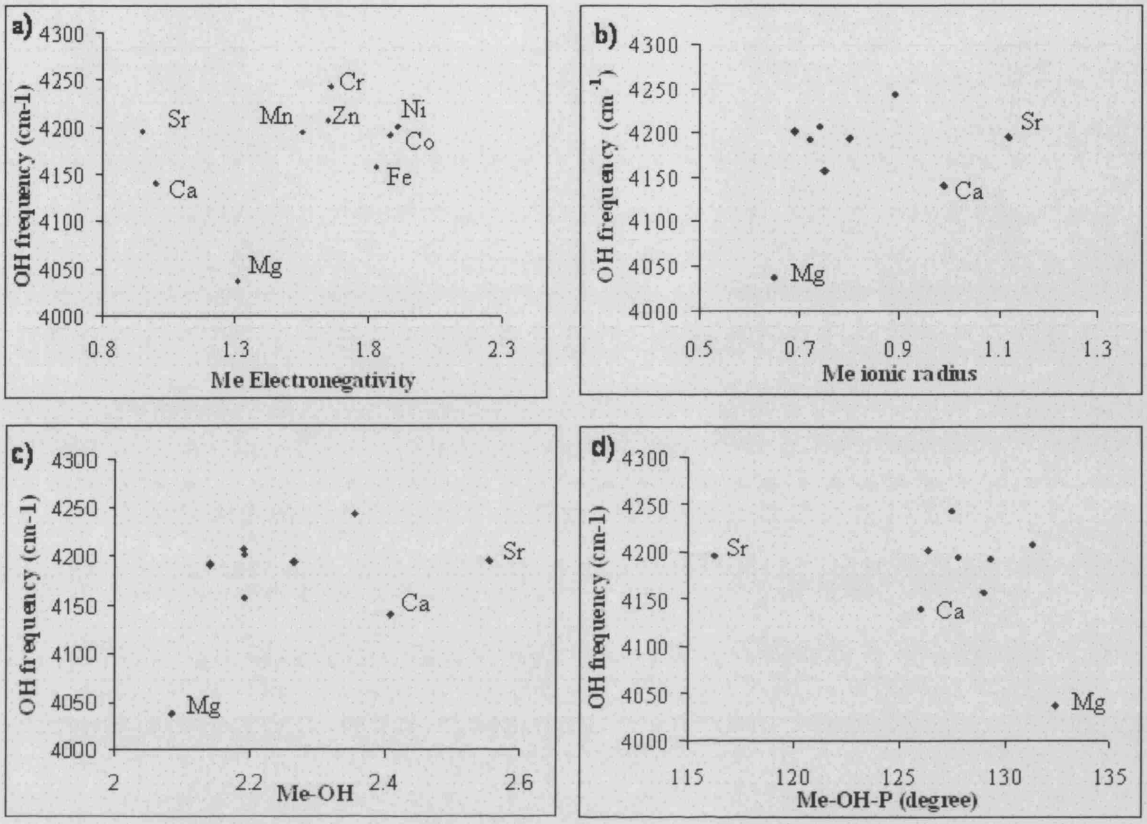

Figure 6.1: *Calculated ν_{OH} stretching frequencies (cm^{-1}) of the Brønsted acid site, as a function of a) electronegativity of the dopant[7], b) ionic radius of the dopan[7], c) calculated Me-O_H bond distance, and d) Me-O_H-P angle.*

Some correlations can be found between smaller groups of metal dopants, especially when we limit our attention to close shell ions such as Mg, Ca, and Sr, where we find that the calculated stretching frequencies of these ions correlate with their ionic size and the Me-O_H-P bond angle. In particular, ν_{OH} decreases on decreasing the size of the ion and on increasing the Me-O_H-P bond angle. Extending this comparative study to a wider range of low-valent dopant ions, however, shows that the correlation between acidity and atomic properties of the dopant is lost, and that the correlation

found within smaller groups of dopants is fortuitous, and not a law with general validity.

It is also of interest to note, in Figure 6.1a, that there is no correlation between acidity and electronegativity of the dopant. This result agrees with the molecular ionic character of MeAlPO frameworks. We have shown in section 4.3 that the Me-O bonds are ionic; in particular, the Me-O_H bond is long and very weak. Since there is no Me-O_H covalent bond, we expect the protonated oxygen to be only marginally affected by the electronegativity of the metal dopant. Hence the acidity of the OH group is not affected by the electronic properties of the metal dopant incorporated.

Our results do not support a simple correlation between the acid strength of doped AlPOs with either ionic radius, electronegativity or bond angles proposed in the literature[1-4] The real situation is more complex, and the acid properties of these materials seem to be *influenced* by a combination of both *electronic* and *structural* factors.

6.2 Lewis acidity of MeAlPO frameworks

Having investigated the Brønsted acidity of MeAlPO catalysts, we shall now examine the Lewis acidity of these materials. The nature and origin of Lewis acid centres in MeAlPO catalysts is still controversial.[9,10,11] While it is generally accepted that the Lewis acidity of MeAlPOs is related to the presence of the transition metal dopants in the framework, from evidence given by experimental temperature programmed desorption (TPD) and calorimetric data,[8,12] the atomic mechanism of the interaction of Lewis base molecules with the framework is still controversial.[13,14]

The question of whether Lewis acid centres contribute to the total acidity of the materials is still debated; while some authors argue that the total acidity of zeolites and MeAlPOs is correlated only with the total concentration of the Brønsted acid sites and does not depend on the concentration of Lewis acid centres,[15] others have shown that Lewis centres play a crucial rôle in influencing the total acidity of these materials. In fact, the enhanced acid character of some transition metal doped AlPOs is interpreted in terms of an equilibrium established between Brønsted and Lewis sites[10,11]:

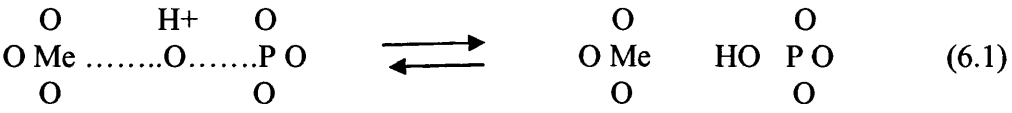

(6.1)

The ionic nature of bonding between transition metal dopants and the neighbouring oxygens, predicted in our work, implies that the Me-O bonds are more flexible than covalent bonds towards changes of the coordination number. Transition metal dopants can therefore act as Lewis acid centres, able to increase their coordination in the presence of Lewis bases, and enhance the acidity of the doped AlPO frameworks. This feature agrees, in principle, with the description of the equilibrium that may occur between the Brønsted and Lewis sites in AlPO frameworks described by equation 6.1.

The extent of the interaction between transition metal centres and Lewis base molecules varies for each transition metal; for example Ni^{2+} doped AlPOs have been shown to exhibit less Lewis acidity than the Co and Mn doped AlPO counterparts.[9] The reasons for the differences in the Lewis acid behaviour between transition metal dopants are not yet understood experimentally. Therefore, understanding the factors influencing the Lewis acidity of transition metal dopants is a topic of practical

importance, and one in which computational modelling of transition metal doped AlPO frameworks can give useful insights.

The aim of the study presented in this section is, therefore, to examine the possible origin of the Lewis acidity in MeAlPOs and the factors controlling such a property. For this purpose, we shall use the results of our QM calculations, in particular those concerning the electronic properties of transition metal dopants (see section 4.2) and we shall examine their calculated electronic distributions, including the orientation of the empty *d* atomic orbitals (AOs) on the metal site, which can be responsible for the Lewis acidity.

In transition metal doped materials, the half filled/or unpopulated *d* AOs are the natural candidates for Lewis acid sites in AlPO frameworks. To investigate this property, we have calculated the spin electron density of each transition metal dopant in their equilibrium structure; the result is plotted in Figure 6.2 for the divalent dopants, and in Figure 6.3 for the trivalent dopants. The plane of the figures is chosen to contain the transition metal ion, one of its neighbouring oxygen ions (for divalent metal dopants, we chose the protonated oxygen O_H), and the next-nearest phosphorus ion bonded to the oxygen ion previously described. In each plot, the continuous and dashed black and green lines are the isodensity levels calculated from the spin density.

The interstitial space within the microporous framework is not all accessible to adsorbed molecules: the Pauli repulsion caused by the overlap between the electronic density of the adsorbed molecule and of the framework atoms, makes the adsorption process energetically unfavourable when the molecules become too close to the framework atoms. How close the adsorbed molecule can approach the framework

and its active site depends upon the radial extent of the electronic density of the MeAlPO host framework. To include this feature, we have calculated the total electronic density of the doped MeAlPO-34 frameworks; in Figures 6.2 and 6.3 we plot in red the isodensity level of 0.01 a.u., which represents an "effective" framework size, beyond which adsorbed molecules cannot approach the framework ions.

Our calculations on transition metal doped AlPO-34 systems have been performed at the UHF level of theory (see section 3.3.3). To investigate whether the calculated spin electron density property is influenced by different Hamiltonians, we have repeated the calculation for the Ni^{2+} doped AlPO-34, this time using the DFT-B3LYP Hamiltonian.[16] Our results show no significant difference between the spin electron densities of the Ni^{2+} dopant, calculated with both Hamiltonians (see Figure 6.2 e and f).

When examining the Lewis acidity of open shell ions in a high spin state, it is important to differentiate between ions with less than half filled *d* AOs, *i.e* those with electronic configuration d^3-d^4, such as Cr^{3+} ($3d^3$), Cr^{2+} ($3d^4$), Mn^{3+}($3d^4$), and ions with *d* AOs that are at least half filled, *i.e.*, those ions with the electronic configuration d^5-d^8, for example Mn^{2+} ($3d^5$), Co^{3+}($3d^6$) and Ni^{2+} ($3d^8$). In the former case, the spin density represents the distribution of the half filled *d* AOs of the metal dopant, which is the least Lewis active, while the other *d* orbitals are empty and are the most Lewis active. In contrast, in the second case, the electronic spin density represents the Lewis active half empty *d* orbitals, while the remaining levels are completely occupied and are Lewis inactive.

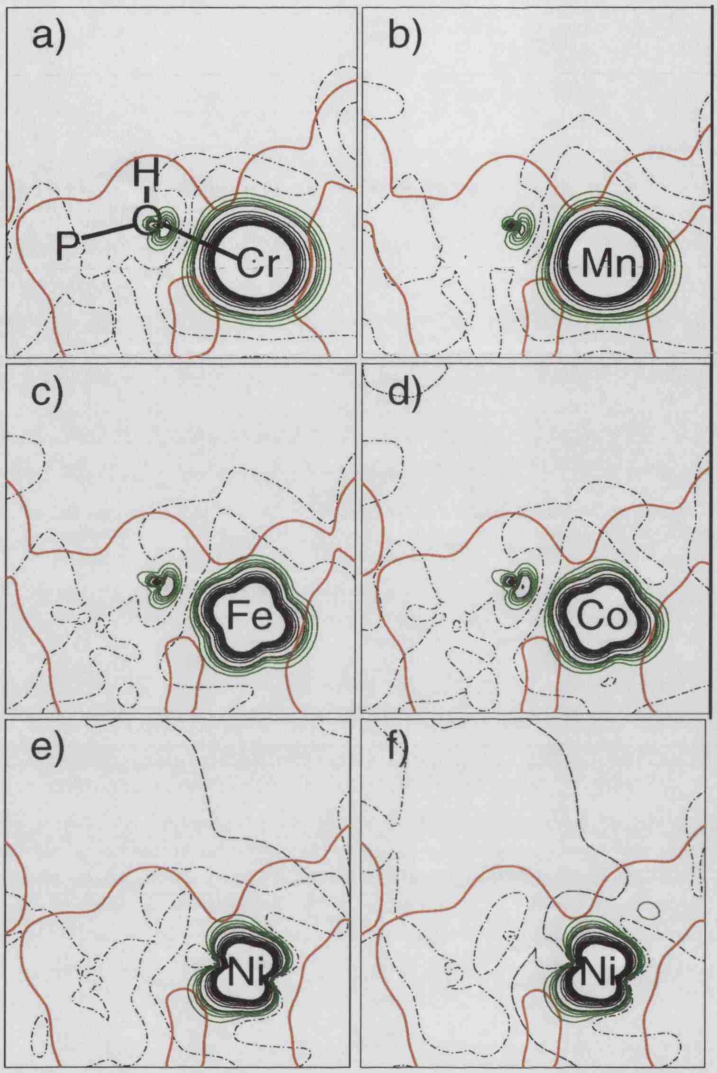

Figure 6.2: *Spin electron density maps for divalent transition metal doped AlPO-34, plotted in a plane containing one a) Cr-O(H)-P, b) Mn-O(H)-P, c) Fe-O(H)-P, d)Co-O(H)-P unit and e) Ni-O(H)-P. Plots a-e correspond to the UHF solution, while plot f) refers to the solution for Ni^{2+}, calculated with the B3LYP Hamiltonian. Continuous and dashed black and green lines are the isodensity levels calculated from the spin density; the black lines correspond to the spin levels between - 0.1 and 0.1 a.u ($|e|.bohr^{-3}$) at steps of 0.01, the green lines correspond to spin levels between 0 and 0.005 a.u. at steps of 0.001. The red line is the total electron density level of 0.01 a.u., and indicates the framework size.*

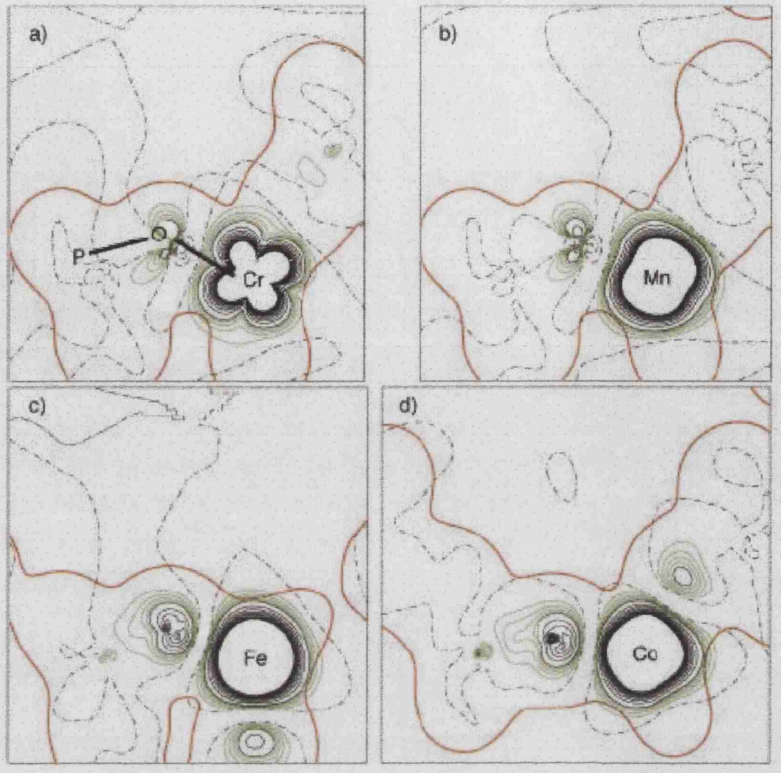

Figure 6.3: *Spin electronic density maps for trivalent transition metal dopants in AlPO-34. Symbols and units are as in Figure 6.2. The metal dopants are Cr^{3+}(a), Mn^{3+}(b), Fe^{3+}(c), and Co^{3+}(d).*

We clearly see in Figures 6.2 and 6.3 that the half-filled orbitals are well localised on the transition metal ions, with only minor contributions on the framework oxygen and phosphorus ions, in accordance with the ionic description of the Me-O bonding discussed earlier. Furthermore, the orientation of the spin density differs according to the electronic configuration of the dopant ion. As a result, the extent of spin density that spills outside the Pauli repulsion area (red line) varies considerably among the dopants examined. In particular, for the Ni^{2+} ion the Lewis-active orbitals are oriented along the framework; a molecule inside the microporous cages of a Ni-doped AlPO will therefore encounter Pauli repulsion from the framework before having an effective interaction with the Lewis active orbitals of the Ni ion. This is

not the case, instead, for Mn, Fe, and Co dopant ions, whose spin density spills outside the Pauli repulsion area. Lewis base molecules in Fe, Co, and Mn- doped materials can therefore undergo an appreciable chemical interaction with the Lewis acid center before being repelled by the framework. Our finding concerning the lack of Lewis acidity of Ni doped AlPO frameworks, is supported by experimental evidence. Lischke *et al* [8] reported that NiAlPO-5 has a lower concentration of Lewis acid sites than most other MeAlPOs (Me: Cr, Co, Mg, Mn, Co).

We further see from the calculated electron density of the divalent transition metal dopants (see Figure 6.2), that the spin density spills more effectively outside the Pauli repulsion area on the side of the framework opposite the proton. The interaction of Lewis basic molecules with the Lewis active centre appears therefore to be more effective when the Lewis base molecule can approach the metal centre from the side opposite the protonated oxygen; interaction of the adsorbed molecule with the Lewis acid centre on the same side as the Brønsted acid proton will be prevented, as the latter will hinder the Lewis-type acid/base interaction of transition metal ion. The Lewis base molecule would in this case interact instead with the Brønsted acid proton. We refer to this structural requirement as an *attack from behind* of the Lewis basic molecules to the transition metal dopant. This suggestion from our computational results is indirectly confirmed by experimental work on Co^{2+}-doped AlPOs, [13,14] in which the authors found that an effective Lewis interaction between the framework Co^{2+} and acetonitrile can only take place when the Co-O_H bond of Co^{2+} with the Brønsted acid OH group is broken. This structural property of Lewis-type interactions can differentiate the Lewis acidity of different AlPO frameworks, as illustrated in Figure 6.4.

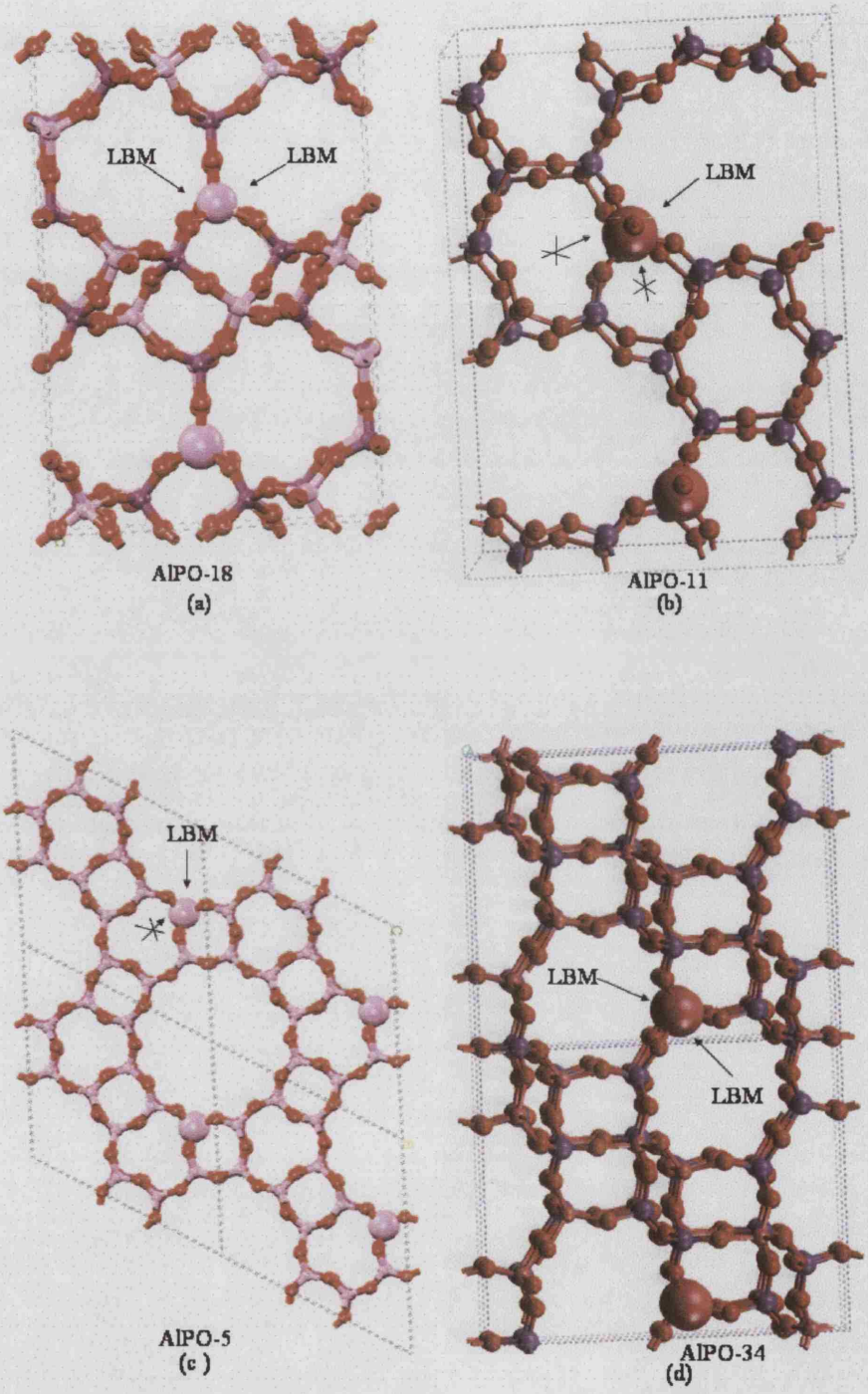

Figure 6.4: *Structural environment of the cationic framework sites in different framework topologies: a) AlPO-18, b) AlPO-11, c) AlPO-5, and d) AlPO-34. The two dimensional open space in AlPO-34 and AlPO-18 allows "attack from behind" of the framework ions by a Lewis base molecule (LBM). The one dimensional character of AlPO-5 and AlPO-11 prevents such form of attack.*

We expect low-valent transition metal dopants to be more Lewis active when they are located in open regions of framework, where the space behind the dopant and the protonated oxygen is not protected by other ions of the framework. The structures are instead expected to be less Lewis active when the dopant and the protonated oxygen cannot be approached from behind by adsorbate molecules, which can be the case when the transition metal dopant is situated in one-dimensional channels made of 'double-wall' building units like those found in AlPO5 and AlPO-11 (see Figure 6.4 b and c). These results may explain why, experimentally, the Lewis acid behaviour of CoAlPO-5 towards the adsorption of acetonitrile was found similar to that of Co-AlPO-11,[12] but different from that of CoAlPO-18 (see Figure 6.3 a). [13,14] We leave open for further experimental verifications this prediction of the computational work.

In chapter 7, we shall investigate direct interaction of Lewis acid centres in AlPO frameworks with water, as a representative Lewis base molecule in order to extend the ideas discussed above.

6.3 Redox properties of MeAlPO-34 catalysts

Another important application of transition metal doped AlPOs in heterogeneous catalysis consists in partial oxidation reactions, which exploits the redox chemistry of the doped frameworks.

Among other factors that can affect the redox catalytic activity, such as reaction conditions, temperature, solvent effects, type of oxidant and host framework used,[17] the ability of the transition metal dopant to switch between its variable oxidation states plays an essential rôle. Understanding how the redox potential of transition

metals in AlPO frameworks influences the catalytic properties of these systems is a topic of both practical and fundamental interest, and it is the aim of the study presented in this section.

Combining the energetic information obtained from our QM calculations for the Me^{3+} and Me^{2+} dopants, we can evaluate the redox energy for the Me^{2+}/Me^{3+} couples in the MeAlPO catalysts. The reference redox reaction between 2+ and 3+ oxidation states of the dopant ion is represented by equation 6.2, in which we use hydrogen as reductant.

$$Me^{3+}AlPO\text{-}34 + \tfrac{1}{2} H_2 \xrightarrow{\Delta E} Me^{2+}\text{-(H)- HAlPO-34} \qquad (6.2)$$

The corresponding redox energy $\Delta E(Me^{3+}/Me^{2+})$ is given by:

$$\Delta E\,(Me^{3+}/Me^{2+}) = E\,(Me^{2+}\text{-(H)-AlPO-34})\text{-}[1/2\,E(H_2) + E(Me^{3+}AlPO\text{-}34)] \quad (6.3)$$

The energy of H_2 molecule has been obtained by optimizing the latter at the HF level of theory with the CRYSTAL program.

The calculated redox potentials for the transition metal ions investigated are reported in Table 6.2.

Table 6.2 *Redox energies ΔE (in eV) for the transition metal ions examined in AlPO-34.*

	Cr^{3+}/Cr^{2+}	Mn^{3+}/Mn^{2+}	Co^{3+}/Co^{2+}	Fe^{3+}/Fe^{2+}
$\Delta E\,(Me^{3+}/Me^{2+})$ eV	-0.61	-2.67	-1.07	0.94

The results in table 6.2 clearly indicate that, among the transition metal ions investigated, Fe is most stable in the 3+ oxidation state, while Mn is the most stable as 2+ ion. Cr and Co, instead, have intermediate behaviour and can switch more

easily between the two oxidation states. The redox behaviour of the Co^{3+}/Co^{2+} couple had been previously investigated in AlPO-34 in a computational study that employed a different Hamiltonian (DFT-GGA, as opposed to the HF of the present work), code and computational settings.[18] It is reassuring to note that the calculated reaction energy for the Co^{3+}/Co^{2+} redox couple is consistent in the two cases: -1.18 eV in reference 18 and -1.07 eV here, which indicates the validity of the computational results obtained.

When correlating the redox energies reported in Table 6.2 with the activity of different MeAlPO catalysts, we need to consider the mechanistic steps involved in the catalytic cycle. Results will, in general, differ for each reaction examined; however, the scale of redox strength proposed in Table 6.2, when coupled with experimental data on the catalytic activity of different Me^{3+}/Me^{2+} dopant ions in the same AlPO framework, can help us identify the mechanistic details of the catalytic reaction.

As a general rule, each redox catalytic process will involve at least two elementary steps, which we can identify with the reduction of the Me^{3+} dopant to Me^{2+}, and with its reoxidation from the 2+ to the 3+ oxidation state. The relative performance of the different Me^{3+}/Me^{2+} dopants examined here will depend on which elementary step is rate determining for the catalytic reaction and at the experimental conditions examined. Framework type, temperature, partial pressures of reagents and products, can each influence the relative rates of the two elementary steps involving the Me dopant, and hence also the relative activity of Fe, Co, Mn and Cr-AlPO catalysts.

If we assume that the rate determining step in the catalytic cycle involves the reduction of the Me^{3+} to Me^{2+} state, our calculations would predict the relative

activity to decrease in the order of **Mn-AlPO>Co-AlPO>Cr-AlPO>Fe-AlPO**. An example of this behaviour has been reported by Thomas *et al.* [19] For the regioselective oxidation of linear alkanes by molecular oxygen, MnAlPO and CoAlPO are found to be superior to the inorganic catalysts which use sacrificial oxidants. The author reported that during course of the partial oxidation, the transition metal ions are reduced to their 2+ state.

If instead the rate determining step involves the reoxidation of the Me^{2+} dopant ion to Me^{3+}, we would expect a reverse order of activity, *i.e.* **Fe-AlPO>Cr-AlPO>Co-AlPO>Mn-AlPO**. Thomas *et al*[19] have reported that Fe-AlPOs show a remarkably high catalytic activity for the selective oxidation of cyclohexane in air (403K and 15 bar of dry air); the results of the catalytic activity of Fe-AlPOs are superior in this case to those of the Co and Mn–substituted analogues. The authors attributed this result to the fact that only a small proportion of Co^{2+} and Mn^{3+} ions that are isomorphously incorporated into the AlPO-36, AlPO-11 and AlPO-5 structures are convertible into the +3 oxidation state by O_2 or dry air,[20] in contrast to the situation with the Fe^{2+} and Fe^{3+} states.[21] This behaviour, which was not properly understood in the experimental work, is in agreement with our results: fewer Mn^{2+} and Co^{2+} ions can be oxidized by molecular oxygen because these ions are more stable than Fe in the +2 oxidation state. Oxidizing Mn^{2+} and Co^{2+} dopant ions in the AlPO framework is energetically unfavorable, and will therefore be difficult to achieve, in particular for the Mn active centre; whereas the oxidation of Fe^{2+} to Fe^{3+} is energetically favourable.

If we assume that the catalytic cycle involves a reduction of the Me^{3+} and its subsequent re-oxidation with a similar rate, the catalytic activity will be related to the ability of the metal ion to switch between its different oxidation states. In this case

we expect Cr to have the highest catalytic activity as its Me^{3+}/Me^{2+} redox potential has the lowest absolute value in our scale of calculated redox energies (see Table 6.2). Experimental results by Luna *et al*,[22] concerning the study of the redox catalytic activity of different metal dopants in the AlPO-VFI framework, for the oxidation of cyclohexane under mild conditions, show that CrAPO has the highest activity, and MnAPO the lowest.

Comparing the relative activity of different metal dopants in the oxidation of cyclohexane from the works of Thomas *et al*[19] and Luna *et al*,[22] suggests that the cyclohexane oxidation proceeds via different mechanisms in small and large pore AlPO catalysts. The AlPO-VFI structure has larger pore size than the AlPO-34 examined here and also of the catalysts used in the work of Thomas *et al.*[19] In a small-pore material, the cyclohexane molecule can only penetrate with difficulty into the micropores of the catalysts, and is always in close contact with the walls of the structure. Upon contact of the hydrocarbon with the Me^{3+} active center, one of the terminal hydrogens is extracted to yield Me^{2+} in the framework and an organic radical that will subsequently react with molecular oxygen. In the constrained environment of a small-pore catalyst, the contact between organic reagent and active site is much more effective than in a large pore material; this step will be fast (not rate-determining) in the former case, while in large-pore catalysts it can differentiate the redox activity of the Me^{3+} dopants. In the small pore catalysts, the rate determining step appears instead to be associated with the migration of the organic radical away from the active site, and the subsequent reoxidation of the Me^{2+} ion with molecular oxygen. The catalytic activity in small-pore catalysts is differentiated by the latter step. The experimental results, coupled with our calculated redox energies, suggest that the reoxidation of the Me^{2+} centre is important also in the large

pore VFI-type catalysts. The scale of the experimental activity is in fact consistent with a mechanism in which oxidation of Me^{2+} and the hydrogen abstraction from the cyclohexane have comparable rates. The highest activity in the cyclohexane oxidation is therefore given by Fe (the easiest to oxidise to 3+) in small-pore catalysts, and by Cr (the easiest to switch between 2+ and 3+) in large-pore materials.

6.4 Conclusion

Using *ab-intio* calculations, we have studied three catalytic properties of MeAlPO catalysts, namely the Brønsted acidity, Lewis acidity and redox potential associated with different dopant ions. From our results we conclude the following points:

- The acid strength is due to a complex combination of the structural and electronic features of the dopant ion, and does not show appreciable correlation with the local environment or electronic properties of the metal dopant in the framework.
- The Lewis acidity of transition metals doped AlPOs is a feature that requires the presence of electron acceptor empty *d* orbitals on the dopant. *Attack from behind* of Lewis basic molecules to 2+ dopant ions is favoured, and is expected to yield stronger Lewis acidity for polymorphs with single wall framework structure, rather than double 4 and 6 member rings.
- The calculated redox energies of the Me^{3+}/Me^{2+} couples indicate that, among the transition metal ions investigated, Fe is the most stable in the 3+ oxidation state, while Mn is the most stable as 2+ ion. Cr and Co, instead, have intermediate behaviour and can switch more easily between the two oxidation states. These results contribute to elucidate the mechanistic details of catalytic processes occurring in MeAlPOs.

References:

1 H. Nur, H. Hamdan, *Matt. Res. Bull*, **2001**, *36*, 315

2 C. de las Pozas, R. lopez-Cordero, J. A. Gonzales-Morales, N. Travieso, R. Roque-Malherbe, *J. Mol. Catal*, **1993**, *83*, 145

3 J. A. Rabo, G. J. Gajda, *Catal. Rev. Sci. Eng.* **1989**, *31*, 385

4 S. Hočevar, J. Batista, V. Kaučič, *J. Catal*, **1993**, *139*, 351

5 H. Van Bekkum, E. M. Fanigen, P. A. Jacobs, J. C. Jansen, *Introduction to Zeolites Science and Practice*, Elsevier, Amesterdam, **2001**, PP 467-519

6 A. P. Scott, L. Radom, *J. Phys. Chem.* **1996**, *100*, 16502

7 D. R.Lide [ed], *CRC Handbook of Chemistry and Physics*, 75th Ed, CRC Press, Boca Raton, **1994**

8 G. Lischke, B. Parlitz, U. Lohse, E. Schreier, R. Fricke., *App. Catal A. General* , **1998**, *166*, 351

9 H. G. Karge, V, Dondur, *J. Phys. Chem*, **1990**, *94*, 765

10 U. Lohse, R. Bertram, K. Jancke, I. Kurzawski, B. Parlitz, E. Löffler, E. Schreier, *J. Chem. Soc., Faraday Trans.* **1995**, *91*, 1163.

11 U. Lohse, A. Brückner, E. Schreier, R.Bertram, J. Jänchen, R. Fricke, *Microporous Mater.* **1996**, *7*, 139.

12 J. Jänchen, M. P. J. Peeters, J. H. M. C. Van Wolput, J. P. Wolthuizen, J. H. C. Van Hooff, *J. Chem. Soc-Faraday. Trans*, **1994**, *90*, 1033.

13 J. Chen, T. Thomas, G. Sankar, *J. Chem. Soc, Faraday Trans.* **1994**, *90*, 3455

14 P. A. Barrett, G. Sankar, R. H. Jones, C. R. A.Catlow, J. M. Thomas, *J. Phys. Chem. B*, **1997**, *101*, 9555

15 J. M. Thomas, *Angew Chem-Int.* **1999**, *29*, 3

16 A. D. Becke, *J. Chem. Phys.* **1993**, *98*, 548.

17 I. W. C. E. Arends, R. A. Sheldon, M. Wallau, U. Schuchardt, *Angew. Chem. Int. Eng.* **1997**, *36*, 1144

18 F.Corà, C. R. A. Catlow, A. D'Ercole. *J. Mol. Catal. A.* **2001**, *166*, 87

19 J. M. Thomas, *Angew. Chem. Int. Ed.* **1994**, *33*, 913

20 P. A. Barrett, G. Sankar, C. R. A.Catlow, J. M. Thomas, *J. Phys. Chem.* **1996**, *100*, 8977

21 R. Raja, G. Sankar, J. M. Thomas, *J. Am. Chem. Soc.* **1999**, *121*, 11926

22 F. J. Luna, S. E. Ukawa, M. Wallau, U. Schuchardt, *J. Mol. Catal. A: Chem* **1997**, *117*, 405

Chapter 7 Water adsorption in MeAlPO catalysts

In the previous chapters we have investigated the electronic and structural features, and the catalytic properties of a range of 2+ and 3+ dopant ions in AlPO-34. In this chapter we extend the work to investigate *hydration*, and the effect of water molecules on properties of the transition metal dopants, and on the framework stability. To achieve this goal we need to examine the interaction of water molecules with all the possible adsorption sites in metal-doped AlPO-34 frameworks. The metal dopants investigated are Mg^{2+}, $Cr^{2+/3+}$, $Mn^{2+/3+}$, $Fe^{2+/3+}$, $Co^{2+/3+}$, Ni^{2+} and Zn^{2+}. Hydration of the undoped AlPO-34 is also examined, for comparison.

7.1 Introduction

Given the potential applications of MeAlPO frameworks as solid acid and/or redox catalysts, the *hydrophilic* character of pure and metal doped AlPO catalysts is a topic that deserves special attention. As we have discussed in section 1.1.4, water plays an important rôle in catalysis, and is often one of the products generated *in situ* during the catalytic cycle. For instance, the condensation of methanol to olefins or gasoline (the MTO and MTG processes, respectively) catalysed by acid SAPOs[1,2] occurs via elimination of water (see equation 1.1 in section 1.1.4); similarly, in the oxidation of hydrocarbons catalysed by AlPOs doped with transition metal ions (Fe, Co, Mn), water is generated as a side product.

Understanding the details of the water interaction with pure and doped AlPO frameworks is a requisite towards characterising the catalytic behaviour of these heterogeneous catalysts, and is a topic that has recently received considerable

interest. Hydration has been examined computationally by Poulet *et al*[3], who demonstrated the hydrophilicity of undoped AlPO frameworks; in addition, a combination of NMR, Raman spectroscopy and structural modelling techniques[4] showed that the water-framework interaction causes a noticeable structural deformation in the host AlPO framework.

Water and methanol have been used as acidity probes for doped zeolites and AlPO catalysts in infrared and NMR studies. Much attention has been devoted to understand both experimentally [5, 6,7,8,9] and theoretically[10,11,12,13 ,14] the proton transfer mechanism from the doped framework to adsorbed water or methanol molecules. Computational works examined Al-doped zeolites and SAPOs, and studied whether or not protonation of water or methanol occurs, and the level of loading at which this happens. For instance Schwarz *et al*[10,11] have used first-principles molecular dynamics simulations to study the adsoption of water and methanol in zeolites; these authors found that water and methanol are not protonated at a coverage of one molecule per acid site, while at higher coverage (two water molecules or more) the proton detaches from the framework and is transferred to the admolecules. Termath *et al*[12] reported that deprotonation of the acid site in H-SAPO-34 is achieved by at least three water molecules per two nearby acid sites in the micropores of the solid; using molecular cluster models, Limtrakul *et al*[13] concluded instead that a coverage of at least four water molecules is required for the hydrogen transfer. These studies demonstrate that the amount of adsorbed molecules present in the zeolitic cages plays a crucial rôle in determining the acid properties of the framework.

The focus in the catalytic applications of doped AlPOs is currently shifting from the acidity of Si-doped materials (SAPOs) to the redox behaviour of transition metal-

doped frameworks (MeAlPOs). Accordingly, experimental studies of the hydration of MeAlPOs have recently been published, and several pieces of experimental information are available: thermogravimetric analysis (TGA) studies, for instance, revealed that the hydrophilicity of the AlPO framework increases upon doping.[15,16] This feature is directly linked to the presence of the dopant ions in the framework: trivalent metal dopants such as Fe, Mn and Cr, when incorporated in the AlPO framework, have been found to increase their coordination number from 4 to 5 or 6 in presence of water. Furthermore, the study of the H_2O sorption isotherms in pure AlPO-11 and its Si, Co^{2+} and Mn^{2+}-doped analogues, showed that the hydrophilicity increased in the doped framework, an effect explained by the authors as due to the generation of Brønsted acid OH groups, which interact favorably with the adsorbed water molecules.[5] While clearly demonstrating that doping modifies the framework hydrophilicity, these experimental studies lack the atomic-level detail concerning the effect of hydration on the region of the framework surrounding the dopant, which may modify both the structural and electronic features of the material. Modelling studies, which can provide this detail, are currently limited to investigating Al-doped zeolites and SAPOs, [10,12,13,14] with no work reported to date on transition metal-doped AlPOs. Hence the aim of this chapter is to bridge this gap and contribute to a better understanding on the topic of hydration in metal-doped AlPOs.

7.2 Methodology of work

AlPO-34 can reversibly adsorb up to 12 H_2O molecules per unit cell.[17,18] Fully water-absorbed systems have little relevance for catalysis, as AlPO catalysts are employed in dry atmosphere, and the presence of several water molecules per unit cell would leave no room for organic reagents to diffuse through the pores of the catalyst,

obstructing the active sites. During a catalytic cycle performed in dry atmosphere, we may expect only a limited number of water molecules to be present inside the cages of AlPO catalysts. We therefore consider two low levels of hydration of one and two water molecules per unit cell, which can provide an insight into the initial stages of hydration in the metal doped AlPO framework, as appropriate for the application of MeAlPOs in heterogeneous catalysis. As in previous work on SAPOs[12], only the first water molecule is allowed a direct interaction with the framework site; in the initial geometry for the systems with two water molecules, the second has always been positioned in a H-bonding configuration with the first molecule. This choice enables us to monitor how the direct interaction of the first admolecule with the framework varies when a second admolecule is present in the pores of AlPO-34.

The hydrophilic nature of AlPOs[18,19,20] suggests that the interaction of water with the framework is likely to display a complex potential energy surface (PES), characterised by the presence of several local minima, in which, for instance, water is H-bonded to different framework oxygens. To represent this complexity, we performed more geometry optimisations, for each adsorption site, using different initial geometries in which the water molecules are allowed to adopt different orientations. The computational cost of periodic *ab initio* QM calculations still makes a full statistical analysis of the PES prohibitive; comparing the different final structures obtained, however, enables us to estimate the importance of statistical (entropic) effects, and increases our confidence in locating the stable adsorption structures.

Once a starting geometry has been selected, to represent one or two water molecules interacting with a particular site of the framework, the structure has been geometry-optimised using the analytical evaluation of forces, available in the CRYSTAL

program.[21] No constraint is used during the optimisation, and all the calculations have been performed with P1 symmetry, as already performed for the anhydrous-frameworks (see section 3.3.3).

Experimental results show a small triclinic distortion of AlPO-34 and MnAlPO-34 structures upon hydration[19,20], which we have not considered here. The Al-O-P angles are very flexible, and can bend easily to accommodate the structural strain taking place in the framework upon hydration. This flexibility of the tetrahedral framework results in the structural relaxation caused by the water-framework interaction being adsorbed by bending the Al-O-P angles, so that the energetic cost linked to neglecting the triclinic distortion is likely to be very small.

As in the previous chapters, our calculations are performed with a periodic model of the solid. However, in the illustrations of the equilibrium hydration structures employed in this chapter, we show only the framework atoms in close contact with the water admolecules. A typical example is reported in Figure 7.1, where we define the nomenclature used subsequently in this chapter. M is the framework ion (Me or Al) where hydration occurs; as we shall see in the following sections, hydration of M often leads to a trigonal bipyramid environment. The framework oxygens that are nearest neighbours of M are then labelled as $O_{1\text{-}3}$ (the equatorial oxygens) and O_A (the axial oxygen); we also report the distance d_{123} of M from the plane defined by the three equatorial oxygens. For the low valent Me dopants, O_H is the protonated oxygen of the framework.

The atoms of the water molecule directly coordinated to M are indicated as O_{W1}, H_{11} and H_{12}; H_{11} is the hydrogen involved in the hydrogen bonding between water and an oxygen of the host framework, which we label O_F; in the presence of a second water

molecule, H_{11} represents the hydrogen involved in H-bonding with either the oxygen of the second water admolecule or of the host framework. Atoms of the second water molecule are indicated as O_{W2}, H_{21}, H_{22}; if a H-bonding interaction takes place between the second water molecule and the framework, we label as O_F the framework oxygen involved in this interaction, and P_F and Al_F its nearest neighbour P and Al ions.

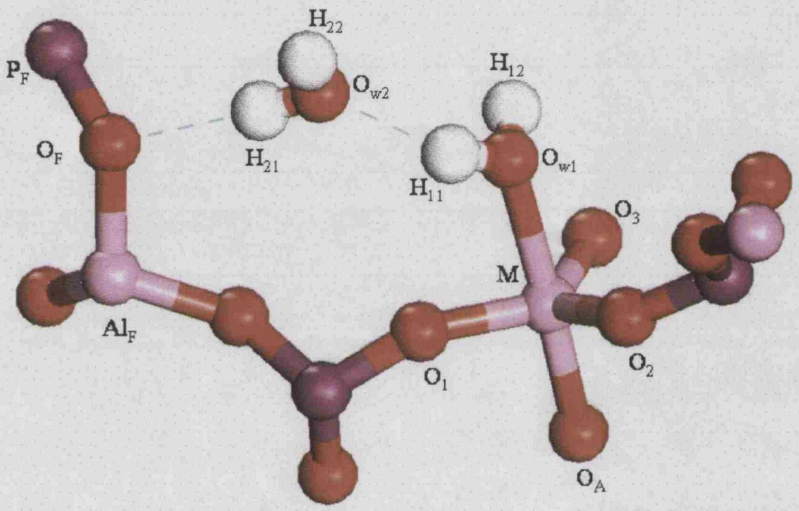

Figure 7.1: *Nomenclature scheme used for hydrated MeAlPO-34 frameworks.*

We have evaluated the adsorption energies ΔE^n_{ad} for n water molecules according to the following equation:

$$E^n_{ad} = [E(\text{Host-AlPO}) + E(H_2O)_n] - E(\text{Host-AlPO}\cdot nH_2O),\ n = 1,2 \quad \textbf{(7.1)}$$

where Host-AlPO is the dehydrated solid, which refers to either the perfect or the Me-doped system. Positive values of the adsorption energy indicate an energetically favourable hydration of the framework. To obtain the reference energy of the water

molecules, we have optimized the structures of one isolated water and of the water dimer in vacuum with the same basis set and Hamiltonian as the one used for the solid (see section 3.3.3). The equilibrium geometries (bond distances and angles) are reported in Table 7.1. The molecular calculations have been performed using the CRYSTAL program.

In the interaction of the framework with two water molecules, the reference energy of the water molecules is taken to be that of the gas-phase dimer, so that it includes the water-water hydrogen bonding effects in the gas-phase; this contribution is therefore not included in the water/ framework interaction.

Table 7.1: *Geometry of water molecule and dimer in the gas phase. Atoms are labeled using the same scheme described in Figure 1.7. Here and in the following of this chapter distances R are reported in Å.*

	H_2O	$(H_2O)_2$
$R(O_{w1}\text{-}H_1)$	0.944	0.948
$R(Ow_1\text{-}H_2)$	0.944	0.943
$(H_{11}\text{-}O_{w1}\text{-}H_{12})$	106.1	106.0
$R(H_{12}\text{-}O_{w2})$	-	2.034
$R(O_{w2}\text{-}H_{21})$	-	0.945
$R(O_{w2}\text{-}H_{22})$	-	0.945
$(H_{21}\text{-}O_{w2}\text{-}H_{22})$	-	106.4

7.3 Results and Discussion

In this section we describe the chemistry that follows hydration of metal doped AlPO-34 frameworks at coverages of one and two water molecules per unit cell, and examine the effect of hydration upon the stability and electronic properties of the doped material.

We shall examine the interaction of water with all the adsorption sites that may be responsible for the framework acidity (Brønsted and Lewis). In Me^{3+}-doped AlPO-34 two possible adsorption sites are represented by the metal dopant itself and by the aluminum framework sites, as shown in Figure 7.2a. In the Me^{2+}-(H)-doped AlPO-34 framework, in addition to the metal dopant and the framework aluminum, other adsorption sites for the basic water molecules are provided by the Brønsted acid OH group adjacent to the metal dopant (see Figure 7.2b). Furthermore, the adsorption of water on the divalent metal dopant can be achieved from two different directions with respect to the OH group, *i.e.* from the same side as the acid OH group, or from the side opposite to the acid proton.

We have shown in section 6.2 that the spilling outside the framework of the empty d-AOs of the metal dopant is oriented away from the OH group responsible for the Brønsted acidity. The attack of Lewis basic molecules on the transition metal dopant is therefore expected to be more favourable from the side opposite to the Brønsted acid site, an interaction that in section 6.2 we have termed as "*attack from behind*". By examining explicitly the interaction of a basic molecule with the Me^{2+}-OH site, we shall be able to prove if this suggestion is indeed correct.

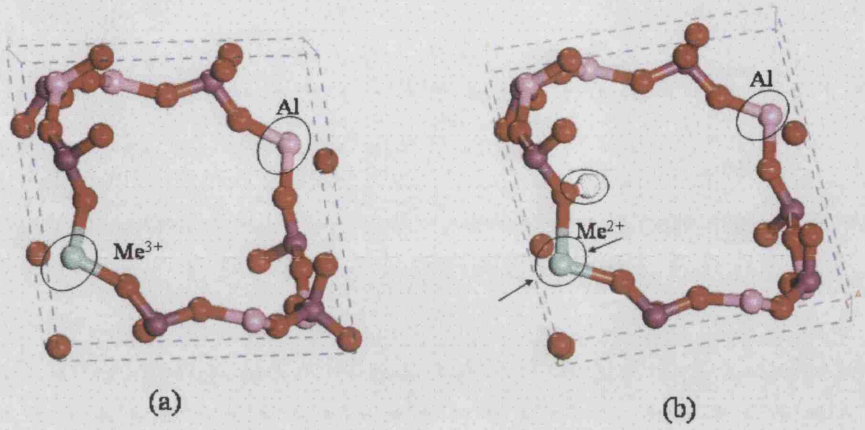

Figure 7.2: *Description of possible adsorption sites for water molecules in (a) Me^{3+} and (b) Me^{2+} doped AlPO-34 frameworks.*

In this section we shall first report results of the hydration of the undoped AlPO-34 framework, in which adsorption of water can only take place on the Al framework site. Second, we shall describe in detail the hydration of the Mn-doped AlPO-34 framework, chosen as a representative of the MeAlPO-34 materials; all the adsorption sites for the water admolecules listed above have been investigated. We shall also investigate the rôle of water loading upon the proton transfer in the H-Mn^{2+}AlPO-34 framework. Subsequently, we report the results on hydration of the other metal doped AlPO-34 frameworks, in which we shall highlight similarities and differences from MnAlPO-34, to investigate the effect of the dopant type on the hydration features.

7.3.1 Interaction of Water with Pure AlPO-34

Before considering the interaction of water with the doped MeAlPO-34 materials, we have investigated the hydration properties of the pure AlPO-34. To this purpose, we have optimised the geometry of the AlPO-34 framework in presence of 1 and 2 water molecules per cage, which represent the initial stages of hydration of the framework.[3] In both cases we find that in the equilibrium structure one framework Al is penta-coordinated, and interacts with the oxygen atom of one water molecule. In Table 7.2 we report the local environment of the Al^{3+} ion in the equilibrium geometry.

When one water molecule interacts with the framework Al^{3+} ion, it forms a long Al – O_W bond; the calculated bond distance is of 2.815Å, with an adsorption energy E_{ad} of 0.27 eV. When two water molecules are present, only one binds directly to the Al^{3+}, and the coordination number of Al is still 5 (see Figure 7.1).

Table 7.2: *Local environment of the hydrated Al^{3+} ion in pure AlPO-34, in the presence of one and two water molecules. The corresponding adsorption energies are given in eV. The local environment of a dehydrated Al^{3+} ion in the pure AlPO-34 framework is also included for comparison.*

	AlPO-34	AlPO-34. $1H_2O$	AlPO-34. $2H_2O$
$R(Al\text{-}O_1)$	1.712	1.737	1.755
$R(Al\text{-}O_2)$	1.723	1.741	1.760
$R(Al\text{-}O_3)$	1.729	1.746	1.765
$R(Al\text{-}O_A)$	1.733	1.763	1.824
d_{123}	-	0.438	0.205
$R(Al\text{-}O_{w1})$	-	2.815	2.117
$R(O_{w1}\text{-}H_{11})$	-	0.945	0.946
$R(O_{w1}\text{-}H_{12})$	-	0.945	0.959
$H_{12}\text{-}O_{w1}\text{-}H_{11}$	-	106.4	107.7
$R(H_{11}\text{-}O_{w2})$	-	-	1.829
$R(O_{w2}\text{-}H_{21})$	-	-	0.947
$R(O_{w2}\text{-}H_{22})$	-	-	0.946
$H_{22}\text{-}O_{w2}\text{-}H_{21}$	-	-	106.2

$R(H_{21}\text{-}O_F)$	-	-	2.698
$R(O_F\text{-}Al_F)$	-	-	1.740
$R(O_F\text{-}P_F)$	-	-	1.521
$Al_F\text{-}O_F\text{-}P_F$	-	-	147.0
E_{ad} (eV)	-	0.27	0.39

The presence of the second water molecule makes the first a much stronger base: $R(Al\text{-}O_{w1})$ shortens by as much as 0.70 Å, from 2.815 to 2.117 Å, while E_{ad} increases to 0.39 eV. The second water admolecule is oriented in such a way that one of its hydrogens points towards one framework oxygen. This orientation is clearly dictated by electrostatic forces, as the $H_{21}....O_F$ equilibrium distance of 2.698Å is too long to define this as a hydrogen bond.

While Al in the dehydrated material has a tetrahedral coordination, hydrated Al adopts a trigonal bipyramidal environment, in which the O_{w1} atom of the admolecule is one of the apices. This coordination environment breaks the symmetry equivalence of the four Al-O bonds in the anhydrous framework and creates two sets of three equatorial ($O_{1\text{-}3}$) and one axial (O_A) oxygen ions. Since the $Al\text{-}O_A$ bond within the framework is stronger than the Lewis interaction with the oxygen atom of the admolecule, O_{w1}, the Al environment is distorted: the $Al\text{-}O_A$ bond is shorter than the $Al\text{-}O_{w1}$, and Al is displaced off the equatorial plane (defined by the three equatorial oxygens) towards O_A. On increasing the strength of the $Al\text{-}O_w$ interaction, the Al ion moves closer to the equatorial plane, making the bipyramidal environment more symmetric. Measuring the distance d_{123} of Al from the equatorial plane provides therefore an additional way to evaluate the effectiveness of the Al-admolecule interaction. In the equilibrium structure we find d_{123} = 0.438 Å in the monohydrated system, and d_{123} = 0.205 Å in the di-hydrated, clearly showing the increased binding of Al with the first water when a second admolecule is present. For comparison, in an

undistorted AlO_4 tetrahedron with Al-O bond distances R = 1.73 Å, d_{123} would be 1.00Å.

The bond distances between Al and the equatorial oxygens increase by 0.02 Å upon the interaction with one H_2O molecule, and by 0.04 Å with the dimer. The bond distance R(Al-O_A) between the aluminium ion and the apical oxygen atom opposite the adsorbed water molecule, in presence of two admolecules is 0.06 Å longer than the bond between the aluminum ion and the three equatorial oxygens O_{1-3}.

To investigate the bonding of Al^{3+} with the admolecules and framework oxygens, in Table 7.3 we report the results of a Mulliken population analysis, performed on the equilibrium electronic density of hydrated AlPO-34. The values for isolated monomer,dimer and anhydrous AlPO-34 framework are also included for comparison.

Table 7.3: *Mulliken population analysis in the hydrated AlPO-34 framework. The values for isolated monomer, dimer and anhydrous AlPO-34 framework are also included for comparison.*

	$Q(O_{w1})$	Q(Al)	$Q(O_A)$	$Q(O_1)$	q_b(Al-O_w)	q_b(Al-O_A)	q_b(Al-O_1)
Isolated monomer	-0.67	-	-	-	-	-	-
Isolated dimer	-0.71	-	-	-	-	-	-
Pure AlPO-34	-	2.18	-1.26	-1.26	-	0.139	0.139
Adsorbed monomer	-0.68	2.21	-1.26	-1.25	0.008	0.132	0.136
Adsorbed dimer	-0.75	2.19	-1.24	-1.25	0.056	0.114	0.128

The overlap population value q_b(Al-O_w) increases from 0.008 |e| in the monohydrated framework to 0.056 |e| in the dihydrated. The former value is very

small, which reflects the weak interaction of one water molecule with the framework Al^{3+} ion, and shows no effective bonding between Al and the water molecule. The increase in $q_b(Al\text{-}O_w)$ when the second water molecule is present highlights the effect played by the second water molecule in activating the adsorption of the first. The weakening of the $Al\text{-}O_A$ bond is also confirmed by the population analysis: its bond population value decreases from 0.139 |e| in the dehydrated system, to 0.132|e| in the monohydrated and 0.114 |e| in the dihydrated. The effect of hydration is less pronounced on the three equatorial oxygens.

The adsorption of water on the Al^{3+} ion is energetically favourable, a result that confirms the hydrophilicity of the AlPO framework reported in the literature. [3,4, 18-20] The results described above indicate clearly that framework Al ions have a hydrophilic character, even in undoped AlPO frameworks. This property is in agreement with the ionic nature of the bonding of the Al ions in AlPOs,[22] discussed section 1.3.

7.3.2 Adsorption of water in Mn^{2+} doped AlPO-34 framework

In this section we shall discuss the adsorption of water on the three possible adsorption sites in Mn^{2+}-AlPO-34, namely the Brønsted acid site, the Mn^{2+} metal dopant, and a framework Al ion (see Figure 7.2b).

7.3.2.1 Adsoption of water on the Brønsted acid proton

To examine the interaction of water with the Brønsted acid, the geometry optimisation has been started by positioning the first water admolecule with its oxygen atom pointing towards the framework OH group. The coordination environment around the Mn^{2+}-OH site, in the equilibrium structures for the

dehydrated catalyst and in the presence of one and two water admolecules, is reported in Table 7.4. The stable equilibrium structures are also shown in Figure 7.3.

Table 7.4: *Local environment of the active site in H-Mn^{2+}-AlPO-34, for the dehydrated material, and in the presence of one and two water molecules, together with the calculated adsorption energies (eV).*

	Mn^{2+} AlPO-34	Mn^{2+}AlPO-34·1H_2O	Mn^{2+}AlPO-34· 2H_2O
R(Mn-O_1)	2.017	2.013	2.016
R(Mn-O_2)	2.025	2.037	2.062
R(Mn-O_3)	2.040	2.076	2.066
R(Mn-O_H)	2.265	2.247	2.229
R(O_H-H)	0.950	0.988	1.008
R(H-O_{w1})	-	1.585	1.496
R(O_{w1}-H_{11})	-	0.946	0.955
R(O_{w1}-H_{12})	-	0.948	0.947
H_{12}-O_{w1}-H_{11}	-	108.9	109.4
R(H_{11}-O_{w2})	-	-	1.897
R(O_{w2}-H_{21})	-	-	0.950
R(O_{w2}-H_{22})	-	-	0.944
H_{22}-O_{w2}-H_{21}	-	-	107.6
R(H_{21}-O_F)	-	-	2.030
R(O_F-P_F)	1.497	1.496	1.505
E_{ad} (eV)	-	0.93	1.19

At a coverage of one, the water molecule is adsorbed on the Brønsted acid site via a strong OH---O_{w1} hydrogen bond, whose length is of 1.585Å (see Figure 7.3a); a weaker hydrogen bonding interaction is also present between one H of the admolecule and a framework oxygen adjacent to the metal dopant. The length of this second (H_{11}-O_F) bond is of 2.466 Å. Several geometric parameters are modified upon the adsorption of water: the interaction between the acid proton and the basic water molecule lengthens the framework O_H-H bond by 0.038Å, from 0.950Å in the anhydrous to 0.988Å in the monohydrated system. We also see that upon interaction with the doped framework, the bond angle (H_{11}-O-H_{12}) in the water admolecule increases from 106.1° in the gas phase to 108.9°. The Mn-O bond lengths also vary

upon adsorption. In the anhydrous Mn^{2+}AlPO-34 system, the four bond distances of Mn^{2+} with its nearest neighbour framework oxygens show a large dispersion, with the Mn-O_H bond to the protonated oxygen (O_H) being 0.22-0.25Å longer than the three bonds to the non protonated ones (O_{1-3}). As we have discussed in section 4.1.1, this difference is due to the chemical inequivalence of the oxygens. The interaction of water with the Brønsted OH group weakens the association of the proton with the framework O_H ion, and reduces the difference among the four oxygens. As a result, upon hydration, the four Mn-O bond distances become more similar by shortening R(Mn-O_H) and lengthening R(Mn-O_{1-3}). The calculated value of the adsorption energy is 0.93 eV, much higher than in the undoped AlPO-34 discussed earlier.

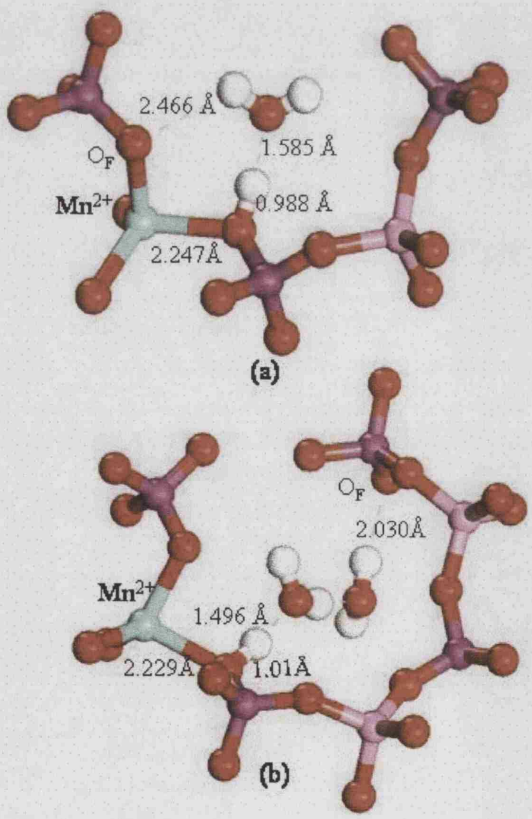

Figure 7.3: *Local environment of one and two water molecules adsorbed on the OH Brønsted acid site of H-Mn^{2+}AlPO-34.*

The water-framework bond distances obtained here are different from those obtained for hydrated H-SAPO-34[23] and Al-doped zeolites.[24,25] The Mn^{2+} dopant has much larger effective size (its ionic radius is R_{Mn}^{2+} = 0.80 Å) than Si^{4+} (0.41 Å) and Al^{3+}(0.50Å); the Mn-O_{1-3} bond-distances, calculated here as ~ 2.03 Å, compare to 1.57 Å for the Si-O_{1-3} in SAPO-34 and 1.69 Å for the Al-O_{1-3} in Al-doped Chabasite, calculated using the same Hamiltonian and setting as employed in this work.[26] The longer distance between the two framework oxygens that are nearest neighbour to the dopant prevents the water from effectively bridging these two ions, as can occur in SAPOs and Al-doped zeolites. As a result, in Mn^{2+}-AlPO-34 the equilibrium distance R(H-O_{w1}) between the framework proton and the oxygen of the admolecule, 1.585 Å, is shorter than those found with HF calculations in Al-doped zeolites: 1.77 Å [24] and 1.684 Å [25]. The distance R(H_{11}-O_F) between one hydrogen atom of the admolecule and the second framework oxygen nearest neighbour to the dopant is instead much longer in MnAlPO (2.466Å) than in SAPO and Al-doped zeolite catalysts. The adsorption energy of one water molecule on the Mn^{2+}-OH site calculated as 0.93 eV is higher than that calculated at the HF level of theory for Al-doped zeolites: 0.55 eV[24] and 0.83 eV.[25]

At a coverage of two water molecules per acid site, shown in Figure 7.3b, we observe a stronger hydrogen bonding interaction between the Brønsted acid proton and the first adsorbed water; the H---O_{w1} equilibrium bond distance is now of 1.496Å. The second admolecule is H-bonded to the first, and there is an additional hydrogen bonding between the second water molecule and one framework oxygen; the H_{21}-O_F bond distance is now of 2.030Å, *i.e.* much shorter than the value R(H_{11}-O_F)= 2.698Å observed for the undoped AlPO-34, and indicative of a more efficient water-framework interaction, not only for the water molecule directly adsorbed on

the acid site, but also for the second admolecule. This network of H-bonding makes the water-framework interaction more effective, further shortening $R(Mn^{2+}\text{-}O_H)$ to 2.229Å, lengthening $R(O_H\text{-}H)$ to 1.008 Å, and increasing the bond angle of the first admolecule ($H_{11}\text{-}O_{w1}\text{-}H_{12}$) to 109.4°. The calculated adsorption energy for the water dimer is 1.19 eV.

The hydrogen bonding interaction between the second water molecule and the framework oxygen O_F distorts the local environment also of O_F: the $P\text{-}O_F$ elongates from 1.497 Å to 1.505 Å. The latter result suggests that also the hydrogen bonding between the second water molecule and the framework oxygen is of a strong nature. Hydration, therefore, does affect the geometry of the framework not only in the close neighbourhood of the dopant, but extends to a region of the framework that is up to 9Å away from the dopant.

For comparison, one of the geometry optimisations performed resulted in an adsorption structure in which the second water molecule has no H-bonding interaction with the framework, and the shortest $H_{21}\text{-}O_F$ is longer than 3Å (see Figure 7.4); the latter configuration has a calculated energy which is 0.125 eV higher than that described in Table 7.4, which indicates the strength of the H-bonding interaction between the second water molecule and the framework.

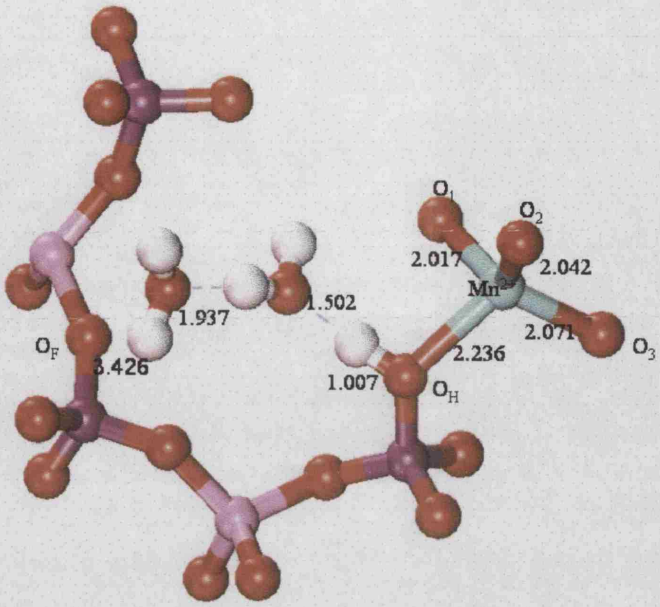

Figure 7.4: *Local environment of two water molecules adsorbed on the OH Brønsted acid site of H-Mn^{2+}AlPO34. The second water has no hydrogen bonding with the framework. All bond distances are given in Å*

7.3.2.2 Framework deprotonation

The results described in the previous section clearly indicate that the effect of water loading on the interaction with the framework is pronounced: an adsorbed water dimer is a much stronger base than a single admolecule. This difference may affect not only the ability of H_2O to coordinate to the Brønsted acid group of the doped framework, but also the protonation state of the system, and induce a hydrogen transfer from the framework to the admolecule. The effect of water coverage on the protonated site is documented in the literature for Al-doped zeolites and SAPOs,[10-14, 24] but not for the transition metal-doped frameworks. We have therefore investigated the proton transfer process from the framework to the adsorbed water molecules in Mn^{2+}-AlPO-34 at both water coverages, to analyse similarities and differences between SAPOs and MnAlPOs.

To study the case of a single water admolecule, we have defined a starting system $[Mn^{2+}\text{-AlPO-34}]^{-}\cdot [H_3O]^{+}$ in which the framework is deprotonated, and an hydronium ion H_3O^{+} located in the centre of the chabazite cage. During the course of geometry optimizations, however, one proton of the hydronium ion binds back to one of the framework oxygens adjacent the dopant. A similar behaviour has been observed in Al-doped zeolites.[24,27,28] The final equilibrium geometry is composed of one neutral water molecule, adsorbed on a framework Brønsted acid site, and is comparable to that described earlier using a neutral admolecule as starting point (see Figure 7.3a). This result indicates that the hydrogen transfer is not achievable at a coverage of one molecule in Mn^{2+}-doped AlPO-34, as was also the case for H-SAPO-34 previously discussed in the literature.[11,12,23] Since H-transfer from H_3O^{+} to the framework occurs during a geometry optimization, our calculations suggest that in MnAlPO-34 this process has no activation barrier and the protonated H_3O^{+} admolecule is not a local minimum in the potential energy surface.

To investigate the effect of water loading on the H-transfer process, we have repeated the above procedure, but this time starting from a protonated water dimer, $H_5O_2^{+}$, inside the cages of a deprotonated Mn^{2+}AlPO-34 framework. This protonation state of the system is now stable during the whole geometry optimization procedure, and in the course of the optimisation steps we have observed no hydrogen transfer between the water admolecules and the anionic framework. In the equilibrium configuration, whose details are reported in Table 7.5, we note the formation of a strong hydrogen-bonding network, comprising four short O---H interactions, that links the protonated water dimer with the Mn-AlPO framework.

Table 7. 5: *Local environment of $H_2O_5^+$ inside the anionic cage of Mn^{2+}AlPO-34, and deprotonation energy, E_{dep}, in eV.*

	$MnAlPO\text{-}34^-\cdot H_5O_2^+$
$R(M\text{-}O_1)$	2.024
$R(M\text{-}O_2)$	2.079
$R(M\text{-}O_3)$	2.118
$R(M\text{-}O_4)$	2.128
$R(O_3\text{-}H_{11})$	1.600
$R(O_4\text{-}H_{12})$	1.741
$R(O_{w1}\text{-}H_{11})$	0.988
$R(O_{w1}\text{-}H_{12})$	0.979
$R(O_{w1}\text{-}H_{13})$	0.987
$(H_{11}\text{-}O_{w1}\text{-}H_{12})$	104.0
$(H_{11}\text{-}O_{w2}\text{-}H_{13})$	113.5
$(H_{12}\text{-}O_{w2}\text{-}H_{13})$	113.9
$R(H_{13}\text{-}O_{w2})$	1.595
$R(O_{w2}\text{-}H_{21})$	0.954
$R(O_{w2}\text{-}H_{22})$	0.945
$(H_{21}\text{-}O_{W2}\text{-}H_{22})$	108.2
$R(H_{21}\text{-}O_F)$	1.983
$R(P\text{-}O_F)$	1.507
E_{dep} (eV)	0.00087

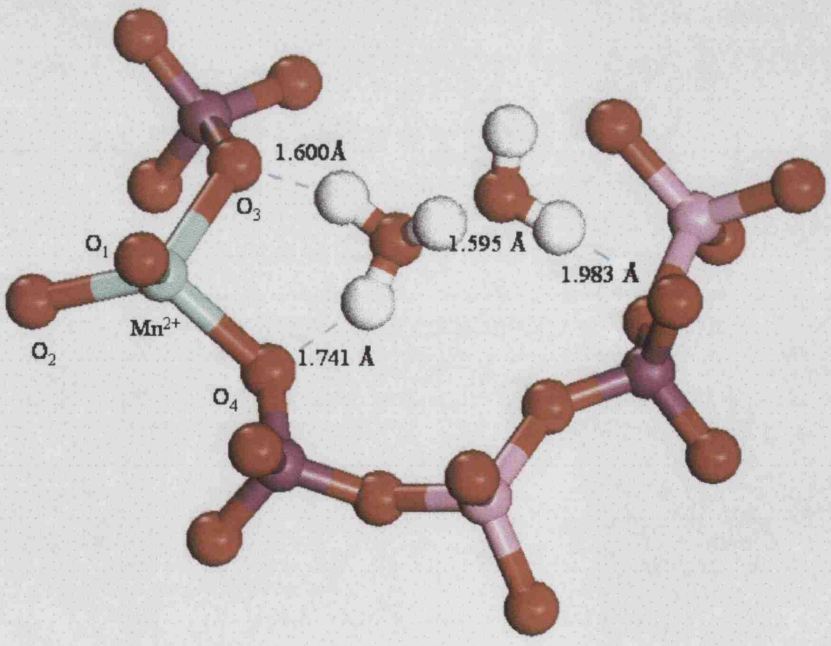

Figure 7. 5: *Local environment of a protonated water dimer $H_5O_2^+$, in the anionic Mn^{2+}AlPO-34 framework*

The H-bonding network has the following components:

- Two hydrogens of the H_3O^+ ion interact strongly with two framework oxygen atoms, both adjacent to the Mn^{2+} dopant ion. The bond distances $R(O_3\text{-}H_{11})$ and $R(O_4\text{-}H_{12})$ are equal to 1.600Å and 1.741Å respectively.
- The third interaction of the H-bonding network occurs between the third hydrogen of the protonated water molecule H_{13}, and the oxygen of the second water molecule, O_{w2}. The bond distance R $(H_{13}\text{-}O_{w2})$ is equal to 1.595 Å, and is 0.3 Å shorter than the calculated value for the $R(H_{12}\text{-}O_{w2})$ H-bond distance in the non-protonated water dimer adsorbed on the Mn-OH acid site. We also note that the water-water distance in the protonated dimer, $R(H_{13}\text{-}O_{w2})$, is the shortest of all the systems we have investigated. This very strong H bonding interaction between the second water molecule and the hydronium ion H_3O^+ stabilizes the $H_2O_5^+$ molecule inside the anionic $[Mn^{2+}AlPO\text{-}34]^-$ framework.
- The fourth interaction of the H-bonding network occurs between the hydrogen of the second water molecule and a framework oxygen, which is seven T-O bonds away from Mn^{2+}. Also this H-bonding interaction is of a strong nature; the bond distance $R(H_{21}\text{-}O_F)$ is 1.983Å , which again is the shortest value of $H_{21}\text{-}O_F$ among all the adsorption geometries studied in MnAlPO-34.

The deprotonation energy E_{dep} calculated according to the following equation

$$\text{Mn-(H)-AlPO-34}\cdot 2\,H_2O \xrightarrow{E_{dep}} \text{MnAlPO-34}^- \cdot H_5O_2^+ \qquad \textbf{(7. 2)}$$

is of 0.00087 eV, indicating a negligible energy difference between the two configurations. This result has the practical consequence that at non zero temperatures the protonation state of the system is a dynamical process, involving an equilibrium between different protonation states of the hydrated Mn^{2+}AlPO-34

system. The hydrogen bonding network linking the protonated water molecule with the framework and the second admolecule, and the second water molecule itself with one of the framework oxygen atoms plays therefore a crucial rôle in promoting the proton transfer from the framework to the admolecule.

Let us now investigate the environment of the Mn^{2+} dopant in the deprotonated framework. When no framework oxygen is directly bonded to the proton, the local environment of the Mn^{2+} dopant is more symmetrical than when the acid proton is attached to one framework oxygen. However, two oxygens that are nearest neighbour of Mn^{2+} are now perturbed by hydrogen bonding to the H_3O^+ admolecule. In this new geometry, the local environment of the dopant consists of two short and two long bonds; the latter involve the oxygens O_3 and O_4 that are hydrogen bonded to the H_3O^+ molecule (see Table 7.5). The difference between long and short bonds is now of ~ 0.05 Å compared to ~ 0.20 Å when the proton was directly bonded to one framework oxygen.

The adsorption geometry of the water dimer in the Mn^{2+}AlPO-34 system discussed above is consistent with previous ab-initio results on deprotonated Al-doped zeolites and SAPO-34 systems.[23] For instance Shah *et al*,[14] reported that in the case of methanol adsorption in the zeolitic cage of Chabazite-structured SSZ-13, the basic methanol attracts the acid proton to form a methoxionium ion, which is stable in the zeolite cage, and adopts a similar geometry to that found here for the $H_2O_5^+$ ion in Mn-AlPO-34. The calculated hydrogen bonding distance between two hydrogens of the methoxionium ion and the two framework oxygens are reported to be 1.54Å and 1.43Å for the SSZ-13 system. These distances are shorter than the $R(O_3\text{-}H_{11})$ and $R(O_4\text{-}H_{12})$ calculated here as 1.600 and 1.741 Å, see Table 7.5. Again, we explain the

different bond distances with the larger size of Mn^{2+} compared to the Al^{3+} ions in the Al-doped zeolites. [14,24]

Let us now examine in more detail the local environment of the Mn^{2+} dopant in the structures in which the proton is bonded to the AlPO framework; these data are reported in Table 7.4. We note that there is a clear correlation between several structural parameters, namely $R(O_H\text{-}H)$, $R(H\text{-}O_{w1})$, $R(Mn\text{-}O_H)$, $R(Mn\text{-}O_{1\text{-}3})$, $H_{11}O_{w1}H_{12}$ and the calculated values of the adsoption energies. On increasing the strength of the water-framework interaction (E_{ad}), the $R(O_H\text{-}H)$ bond distance elongates, while the H-bond distance $R(H\text{-}O_{w1})$ decreases. At the same time, weakening the $H\text{-}O_H$ association, hydration makes the Mn^{2+} crystalline environment more symmetric by shortening the $Mn^{2+}\text{-}O_H$ bond and elongating the $Mn\text{-}O_{123}$ ones. Upon adsorption, the $H_{11}O_{w1}H_{12}$ angle of the water admolecule increases. All the changes above reach extreme values when the framework deprotonates (see Table 7.5), and the framework oxygens are only differentiated by their H-bonding interaction with the adsorbed hydronium ion.

Although the local environment of Mn^{2+} changes significantly when water is adsorbed on the acid site, our calculations indicate that this structural modification has no effect upon the electronic state of the Mn^{2+} dopant, which remains stable in its high spin electronic configuration.

Our calculations show that protonation of the adsorbed water molecule in Mn^{2+}AlPO-34 occurs only in the presence of a second water molecule. The process is framework-assisted, and requires an H-bonding interaction of the second water admolecule to the framework to stabilize the protonated hydronium ion. The

framework oxygen involved in the latter interaction, O_F, is located four oxygens away from the metal dopant. The framework involvement in the H-bonding with the second admolecule agrees with studies of H-SAPO-34 based on periodic models of the solid, reported in the literature,[12] but not with results on H-SAPOs obtained with isolated clusters.[13] It has therefore practical implications for the computational study of the framework deprotonation: when choosing a cluster-model representation of the active site, we need to ensure that the cluster extends far enough from the Brønsted OH group to enable a description of the H_{21}-O_F interaction. The model chosen in reference 13, for instance, consisted of only three framework T sites, and is clearly not extended enough to account for the interaction of the second admolecule with the framework. This limited-size effect causes a disagreement of the calculated results with those obtained with periodic models of the solid or with embedded-cluster calculations.[25] The authors in reference 13 found in fact that framework deprotonation in H-SAPO occurs only when four water admolecules cluster around the active site. The limited model chosen, however, does not allow for the interaction of the second and subsequent admolecules with the framework, that we have shown to play an essential rôle in the hydrogen transfer process. Additional water admolecules are in this case required to provide an H-bonding network extensive enough to stabilize the framework deprotonation. In the true solid catalyst, this effect is provided by the framework itself; periodic models of the solid describe correctly the extended nature of the framework, and therefore do not suffer from this shortcoming.

7.3.2.3 Adsorption of water on the Mn^{2+} dopant

In this section, we report results concerning the interaction of water directly with the Mn^{2+} dopant, *i.e.* the Lewis-type acidity of the framework Mn ion.

In section 6.2 of this thesis, when examining the spin density map of divalent transition metal dopants, we have seen that the spin density of the Me-3*d* electrons is not symmetric with respect to the location of the Brønsted OH group, and is more extended in the direction opposite the O_H ion. We therefore predicted that an attack by a Lewis base molecule on the metal dopant is expected to be more effective from the region behind the proton. For convenience the spin density map of the Mn^{2+} dopant is shown again in Figure 7.6.

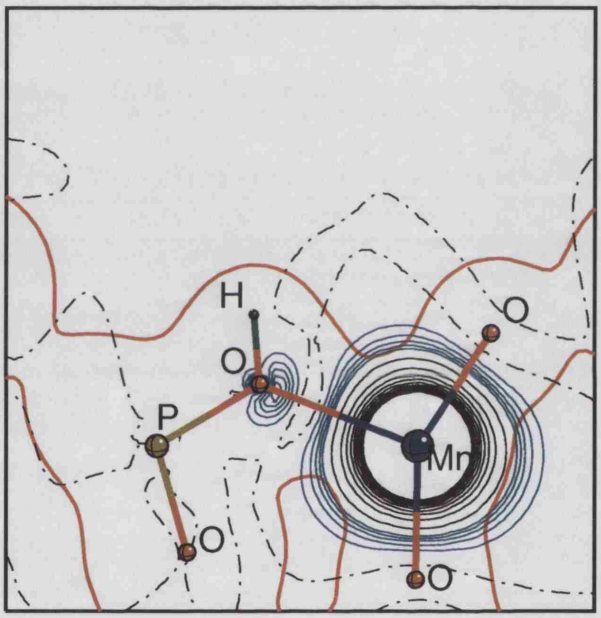

Figure 7.6: *Spin electron density map of H-Mn^{2+}AlPO-34 , plotted in a plane containing one Mn-O(H)-P unit.*

When the water molecules are initially adsorbed on the Mn^{2+} ion from the same side of the acid proton, our results show that after geometry optimisation the adsorbed water has migrated to the Brønsted acid proton. The equilibrium geometry is very similar to that described earlier in Table 7.4. This result is not surprising, since the strong hydrogen bonding interaction between the adsorbed water molecule and the acid site drives the oxygen atom of the admolecule towards the Brønsted acid group and away from Mn. We therefore conclude that when admolecules approach the

dopant from the same side as the OH group, the *substitutional Mn^{2+} ions are screened by the acid OH group from direct interaction with the adsorbed water.*

When, in the starting configuration, the water molecule is located next to the Mn^{2+} dopant, but on the opposite side of O_H, the metal interacts effectively with the admolecule. The local geometries around the Mn^{2+} active site, obtained after geometry optimisation, are reported in Table 7.6, while the structures are shown on Figure 7.7. The calculated adsorption energies are 0.838 eV and 1.173 eV for a water molecule and dimer respectively; in the latter case, this interaction is competitive with the adsorption on the Brønsted OH site.

Table 7.6: *Local environment of one and two adsorbed water molecules on the Mn^{2+} dopant, from behind the Brønsted acid proton, and calculated adsorption energies E^n_{ad}(eV).*

	Mn^{2+} AlPO-34	Mn^{2+} AlPO-34·1 H_2O	Mn^{2+}AlPO-34·2 H_2O
R(Mn-O_1)	2.017	2.030	2.025
R(Mn-O_2)	2.025	2.068	2.076
R(Mn-O_3)	2.040	2.071	2.089
R(Mn-O_H)	2.265	2.813	3.072
R(Mn-O_{w1})	-	2.291	2.222
R(O_H-H)	0.950	0.951	0.950
R(H-O_3)	-	2.329	2.288
R(O_{w1}-H_{11})	-	0.948	0.958
R(O_{w1}-H_{12})	-	0.948	0.947
H_{12}-O_{w1}-H_{11}	-	106.7	106.1
R(H_{11}-O_{w2})	-	-	1.862
R(O_{w2}-H_{21})	-	-	0.946
R(O_{w2}-H_{22})	-	-	0.945
H_{22}-O_{w2}-H_{21}	-	-	107.4
R(H_{21}-O_F)	-	-	2.308
R(O_F-Al_F)	-	-	1.769
R(O_F-P_F)	-	-	1.526
Al_F-O_F-P_F	-	-	142.9
E^n_{ad}		0.84	1.17

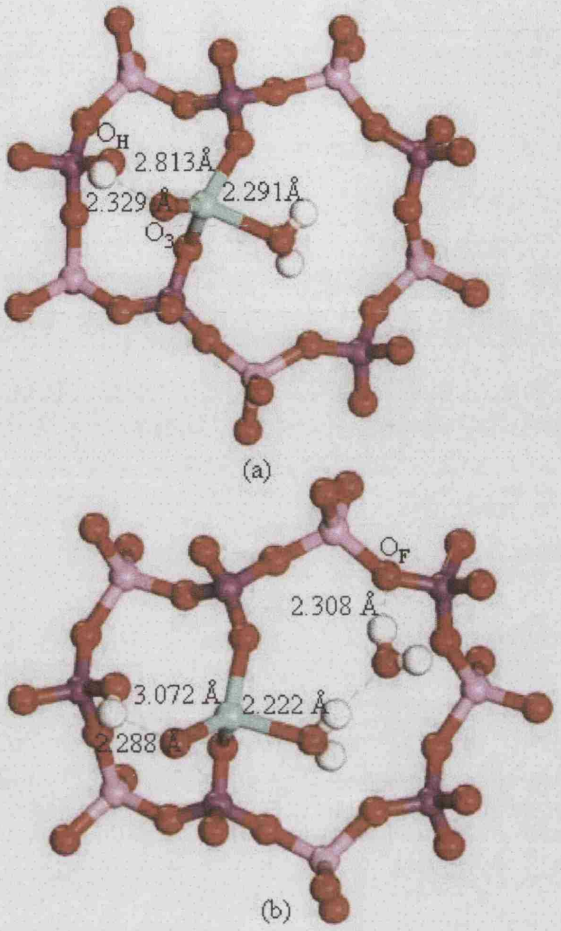

Figure 7.7: *Local environment of (a) one and (b) two water molecules adsorbed on the Mn^{2+} dopant, from behind the OH Brønsted acid site.*

The effect of H_2O adsorption on the local geometry of the Mn^{2+} site is dramatic; the bond between the metal dopant and the protonated oxygen elongates by as much as 0.81 Å, to 3.072 Å when the dimer is adsorbed. Attack from behind of the water causes therefore a weakening of the bond between the metal and the protonated oxygen, which in a true catalyst could lead to the irreversible breakage of that bond. In fact, in the equilibrium configuration, the framework OH group no longer interacts with Mn via the O_H ion, but forms a new H-bond via the Brønsted acid proton with another framework oxygen, adjacent to the Mn^{2+} dopant.

These results confirm the hypothesis formulated in section 6.2, concerning the Lewis acidity of a divalent metal-doped AlPO-34 framework. *Lewis and Brønsted acidity in the Mn^{2+}-AlPO-34 framework are mutually exclusive;* which interaction occurs between the water and Me-AlPO catalyst will depend on the accessibility of the active site and on the relative initial orientation of the water molecule approaching the Me^{2+} site with respect to the Me-OH group. Brønsted and Lewis acid/base interactions will therefore be controlled by kinetic, rather than thermodynamic effects.

7.3.2.4 Adsorption of water on the Al sites in Mn^{2+}AlPO-34

Let us now examine the adsorption of water on one of the framework Al ions in the H-Mn^{2+}AlPO-34 catalysts. In particular, we have chosen the framework Al that is located at the opposite end of the Mn^{II}-dopant in the chabazite cage. The 2+ dopant ion, charge-compensated by a Brønsted acid proton, creates an electrostatic dipole in the neighbouring region of the solid. The dipole has its negative end in the Mn^{2+} site, and its positive end on the proton; it is therefore oriented in a roughly perpendicular direction to the framework in the region containing the dopant, and points in the direction of the Al^{3+} ion at the opposite end of the chabasite cage. This feature is clearly shown in Figure 7.8, where we report the electrostatic potential, calculated as difference between undoped and Mn^{2+}-doped AlPO-34 frameworks, within the chabasite cage.

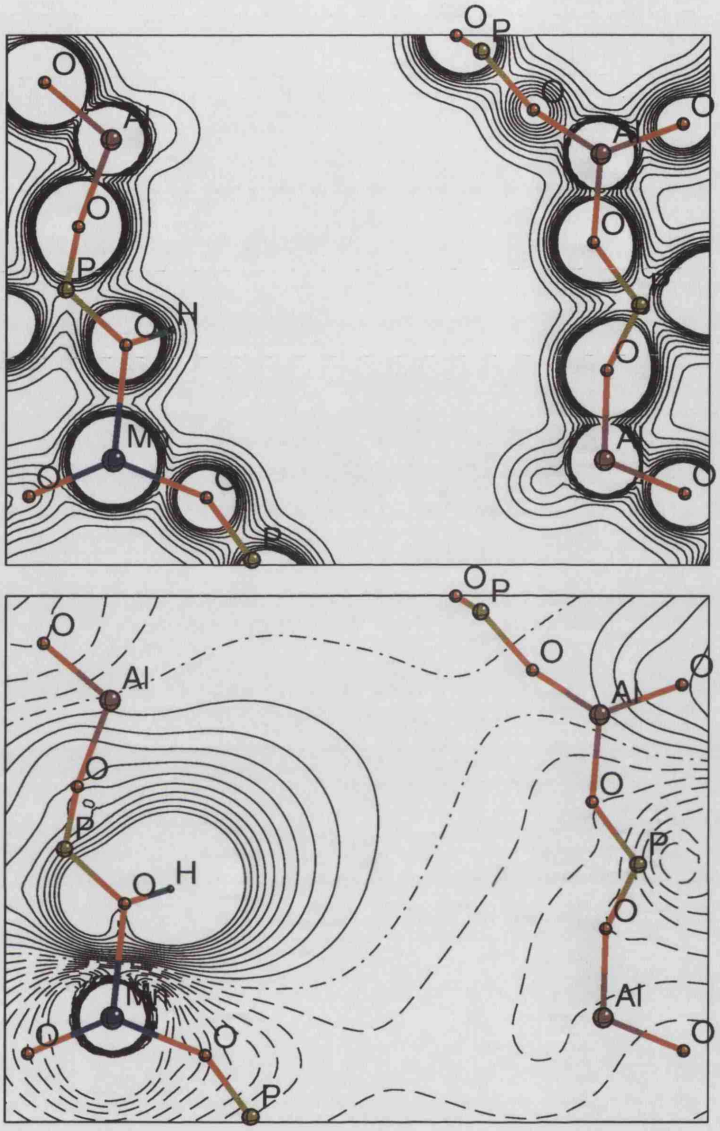

Figure 7.8: *Electrostatic potential, calculated as difference between undoped and Mn^{2+}-doped AlPO-34 frameworks, within a chabasitic cage.*

The framework Al ion on which the dipolar electric field is highest is therefore the one located in the same chabasite cage hosting the Mn^{2+} dopant ion, on the opposite side of the dopant. Since the Lewis interaction between framework Al and admolecule has an important electrostatic component, it is reasonable to assume that the latter Al ion is the one on which the effect of the Mn^{2+} dopant is highest.

We report in Table 7.7 the local environment of the Al ion, when one and two water molecules are adsorbed, together with the adsoption energies.

Table 7.7: *Local environment of dehydrated and hydrated Al^{3+} ion in Mn^{2+}- doped AlPO-34, and calculated adsorption energies E^n_{ad} (eV).*

	Mn^{2+}AlPO-34	Mn^{2+}AlPO-34·1H_2O	Mn^{2+}AlPO-34·2H_2O
R(Al-O_1)	1.724	1.735	1.739
R(Al-O_2)	1.734	1.750	1.761
R(Al-O_3)	1.744	1.758	1.774
R(Al-O_A)	1.789	1.862	1.909
d_{123}	-	0.267	0.161
R(Al-O_{w1})	-	2.311	2.095
R(O_{w1}-H_{11})	-	0.947	0.960
R(O_{w1}-H_{12})	-	0.947	0.947
H_{12}-O_{w1}-H_{11}	-	106.6	107.6
R(H_{11}-O_{w2})	-	-	1.836
R(O_{w2}-H_{21})	-	-	1.947
R(O_{w2}-H_{22})	-	-	1.946
H_{22}-O_{w2}-H_{21}	-	-	105.9
R(H_{21}-O_F)	-	-	2.496
R(O_F-Al_F)	-	-	1.748
R(O_F-P_F)	-	-	1.530
Al_F-O_F-P_F	-	-	137.3
E^n_{ad} (eV)	-	0.29	0.53

Our results indicate that the Al site opposite the Mn^{2+} dopant is readily hydrated, even when only one water molecule is present in the cages. The Al-O_w equilibrium distance is 2.311Å, while in the undoped AlPO-34 system we calculated R(Al-O_w) as 2.815Å. The presence of the low valent dopant, therefore, activates the framework towards hydration, *i.e.* it increases the hydrophilicity of the AlPO framework. For the monohydrated system the calculated adsorption energy is 0.29 eV, compared to 0.27 eV in the undoped AlPO-34.

The presence of a second adsorbed water molecule shortens the Al-O_w bond distance even further, to 2.095Å, with an increase of E_{ad} to 0.53 eV. The second water molecule forms a weaker hydrogen bond with a framework oxygen three bonds away

from the hydrated Al atom; this interaction, as we have seen in the previous sections, increases the basicity of the adsorbed water molecules.

In section 7.3.1 we have shown that in the undoped AlPO-34 the local structure of Al upon hydration is a trigonal bipyramid, in which the distance d_{123} of Al from the equatorial plane is inversely proportional to the strength of the Al---O_W interaction. Also in the Mn^{2+}-doped framework, the hydrated Al ion is located in a bipyramidal environment; the value of the parameter d_{123} is now calculated as d_{123} = 0.267Å for the monohydrated ion and 0.161Å for the di-hydrated. These values of d_{123} are approximately half the corresponding d_{123} values calculated for the undoped AlPO-34 framework. This result indicates that the structural effect of hydration is more pronounced in the Mn^{2+}-doped than in the undoped system, which is consistent with the higher hydration energy in the former case.

Although the adsorption of water on the Al site is less energetically favored than on the OH group and on the Mn^{2+} dopant, it is nonetheless higher than in the undoped material, thus indicating that the enhancement of the framework hydrophilicity upon doping is due not only to the presence of strong Brønsted (the OH group) and Lewis sites (the dopant ion itself), but also to an increased Lewis acidity of the host Al framework ions in the vicinity of the dopant.

Comparing the behaviour of all the adsorption sites examined in Mn^{2+}AlPO-34, we conclude that the stable adsorption site for water is the Brønsted acid group, (E_{ad}= 1.19 eV), closely followed by an attack from behind on the Mn^{2+} dopant (E_{ad}= 1.17 eV). However, the dopant activates also the framework Al ions towards hydration (the adsorption of a water dimer on Al in the doped system being more than 0.1 eV higher than in the undoped). Our results also suggest an increased framework

instability of the Mn-doped materials in wet conditions; direct interaction "from behind" of water with the Mn^{2+} ion causes a breaking of the framework along the Mn^{2+}-O_H bond that may be irreversible under operating conditions in a catalytic application.

7.3.3 Interaction of water molecules with the Mn^{3+}-doped AlPO-34 framework

In this section we shall discuss the adsorption of water on the two possible adsorption sites in Mn^{3+}-AlPO-34, namely the Mn^{3+} metal dopant and one of the framework Al ions.

7.3.3.1 Adsorption of water on the Mn^{3+} dopant

The local environment of the Mn^{3+} dopant in the presence of one and two adsorbed water molecules is reported in Table 7.8. In both cases the Mn^{3+} dopant readily increases its coordination number from 4 to 5 (see Figure 7.9).

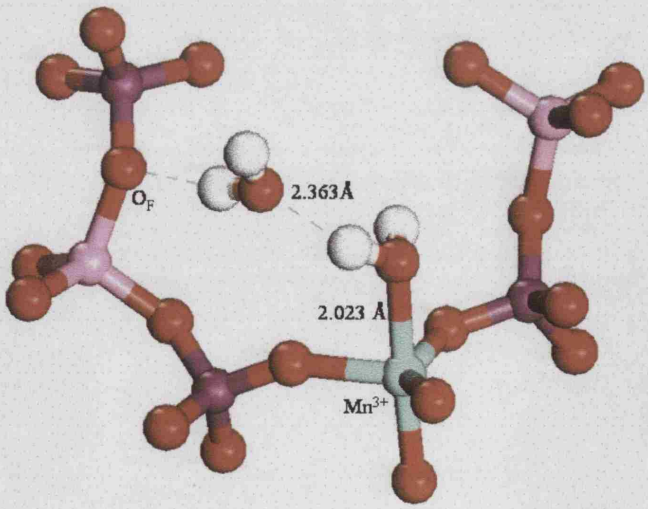

Figure 7.9: *Local environment of the hydrated Mn^{3+} dopant in the presence of two adsorbed water molecules.*

Table 7.8: *Local environment of the Mn^{3+} dopant in dehydrated and hydrated Mn^{3+}AlPO-34, calculated adsorption energies E^{n}_{ad} (eV).*

	Mn^{3+} AlPO-34	Mn^{3+}AlPO-34·1 H_2O	Mn^{3+} AlPO-34·2 H_2O
R(M-O_1)	1.865	1.877	1.888
R(M-O_2)	1.867	1.913	1.912
R(M-O_3)	1.907	1.929	1.947
R(M-O_A)	1.913	1.989	1.968
d_{123}	-	0.224	0.169
R(M-O_{w1})	-	2.066	2.023
R(O_{w1}-H_{11})	-	0.950	0.963
R(O_{w1}-H_{12})	-	0.950	0.949
H_{12}-O_{w1}-H_{11}	-	108.4	104.9
R(H_{11}-O_{w2})	-	-	1.842
R(O_{w2}-H_{21})	-	-	0.947
R(O_{w2}-H_{22})	-	-	0.944
H_{22}-O_{w2}-H_{21}	-	-	107.5
R(H_{21}-O_F)	-	-	2.363
R(O_F-Al_F)	-	-	1.524
R(O_F-P_F)	-	-	1.748
Al_F-O_F-P_F	-	-	142.3
E^{n}_{ad} (eV)	-	0.79	1.07

Our results show that even when only one water molecule is present in the Mn^{3+}AlPO-34 cage, the Mn^{3+} dopant is effectively bonded with the water admolecule; the Mn^{3+}-O_{w1} bond distance is of 2.066Å and is longer by ~ 0.1-0.2 Å than those with framework oxygens. Adsorption of water on the Mn^{3+} site affects its local geometry significantly; hydrated Mn^{3+} adopts a trigonal bipyramidal geometry, as in the case of the Al^{3+} ions in the pure and doped AlPO-34 frameworks. The calculated distance between the Mn^{3+} dopant and the equatorial plane (defined by the three equatorial oxygens O_{1-3}) d_{123} is of 0.224 Å. The latter value is approximately half the d_{123} value (d_{123} = 0.438 Å) calculated when the Al framework ion is hydrated with one water molecule in the pure AlPO-34 framework, a result which indicates that the Mn^{3+} dopant is a better Lewis acid than the Al^{3+} ion.

In the presence of the second water molecule, the interaction of the two water admolecules with the Mn^{3+} dopant is even stronger, as the bond distance between Mn and the first water admolecule decreases from 2.066Å to 2.023Å and the value of the parameter d_{123} decreases from 0.224 Å to 0.169 Å. The adsorption energy increases from 0.79 eV for the monohydrated to 1.07 eV for the dihydrated Mn^{3+}AlPO-34 system. These results are expected after the description of the previous sections; again, the presence of a second water molecule makes the first admolecule a much stronger Lewis base.

The d_{123} value (0.169 Å) calculated for the dihydrated Mn^{3+} dopant is ~ 0.04 Å shorter than the d_{123} value (0.205 Å) calculated for the dihydrated Al^{3+} ion in the pure AlPO-34. This result confirms that the Mn^{3+} dopant is indeed a better Lewis acid than the Al^{3+} ion, and increases the hydrophilicity of the doped framework.

Despite the higher charge of Mn^{3+} compared to Mn^{2+}, and a smaller bond distance between the water and Mn^{3+} when compared to that between the water and Mn^{2+}, the calculated adsorption energy E^n_{ad} of water on the Mn^{3+} ion (0.79 eV and 1.07 eV for the monohydrated and dihydrated system respectively) is lower than that on the Mn^{2+} ion (0.89 eV and 1.17eV for the monohydrated and dihydrated system respectively, see Table 7.6). One possible explanation for the lower adsorption energy on the Mn^{3+} dopant is the repulsion between water and framework at the shorter equilibrium distance. The Mn^{3+} dopant forms shorter bonds with its four neighbouring oxygens than Mn^{2+}. Repulsion between water oxygen and the oxygens adjacent to the 3+ metal dopant may make the water interaction less stable than that with the Mn^{2+} dopant. To investigate this matter we have examined the overlap population values between the oxygen of the water molecule and the framework oxygens adjacent to the metal dopant in the dihydrated system, $q_b(O_1\text{-}O_{w1})$, $q_b(O_2\text{-}O_{w1})$, and $q_b(O_3\text{-}O_{w1})$

respectively. The calculated values for the Mn^{3+}-doped framework are -0.014, -0.012 and -0.009 |e| respectively. The negative values of these overlap population values confirm that there is a short-range repulsion between the three framework oxygens and that of the water admolecule. For the Mn^{2+}-doped framework, the overlap population values are -0.001, -0.002, and 0.000 |e| respectively, which are less negative than those calculated for the Mn^{3+} doped system, indicative of a lower repulsion between the oxygen of the first water molecule and the framework.

An additional difference arises, in the case of the Mn^{2+} dopant, from the presence of the OH group in the framework. Upon attack from behind of the water admolecule on the Mn^{2+} dopant in Mn^{2+}-AlPO-34, an additional hydrogen bonding is formed between the Brønsted acid site and one framework oxygen adjacent to the metal dopant (O_3) (see Figure 7.7). The calculated H-bond distance between the acid proton and framework O_3, R(H-O_3) is 2.329Å and 2.288 Å for the monohydrated and dihydrated systems respectively. This additional hydrogen bonding interaction is not present for the Mn^{3+} doped AlPO-34 system. In Section 7.3.2.1, when describing the adsorption of water on the Bronsted acid in the Mn^{2+} doped AlPO-34 framework, we compared two geometries that differ for one H-bond. There we found that the geometry where the hydrogen bonding between the second water molecule and the framework oxygen is missing is unstable by 0.12 eV compared to the geometry in which the water- framework hydrogen bonding interaction is present. The adsorption energy of water on the Mn^{2+} is 0.10 eV higher than on the Mn^{3+} dopant. This energy difference is of the same order of magnitude as the 0.12 eV caused by one additional hydrogen bonding interaction such as the one involving the framework oxygen O_3 in the hydrated Mn^{2+}HAlPO-34 framework. We therefore conclude that the key factor that contributes to stabilising the adsoption of water on the Mn^{2+} dopant compared to

Mn^{3+} is the hydrogen bonding interaction between the Brønsted acid and the framework oxygen adjacent to the Mn^{2+} dopant. The repulsion between the oxygen of the water admolecule and the three framework oxygen adjacent to the dopant plays a minor part in the energy balance.

7.3.3.2 Redox potential of hydrated MnAlPO-34.

The ability of the Mn dopant to change its oxidation state plays a vital rôle in the redox activity of the Mn doped AlPO frameworks. The presence of water molecules, which as we have seen hydrate readily the Mn dopant, can alter the redox properties of the Mn active site, and hence its redox activity.

In section 6.3, we have calculated the redox energy of the Mn^{3+}/Mn^{2+} couple to be -2.67eV for the dehydrated MnAlPO-34 system. This value indicates that the Mn^{2+} dopant in the AlPO-34 framework is more stable than the Mn^{3+} dopant. The relative stability of the 2+ oxidation state can be modified by the interaction of water with the Mn dopant.

Since the calculated adsorption energy of water is higher on the Mn^{2+} dopant than on the Mn^{3+} dopant, *i.e.* $E^n_{ad}(Mn^{2+}) > E^n_{ad}(Mn^{3+})$, the presence of water stabilises even further the 2+ oxidation state of Mn, and makes the redox energy of the Mn^{3+}/Mn^{2+} couple more negative by an amount $\Delta E = E^n_{ad}(Mn^{2+}) - E^n_{ad}(Mn^{3+}) \sim 0.1$ eV. The ability of the Mn^{2+} dopant to switch into the 3+ state, therefore, decreases further when water is present in the cage of the microporous catalyst.

7.3.3.3 Adsorption of water on the Al sites in Mn^{3+}AlPO-34

In this section we investigate the adsorption of water on the Al sites of the Mn^{3+}-doped AlPO-34 framework. As for the Mn^{2+}-doped framework, we have chosen the framework Al that is located opposite to the Mn^{3+}-dopant in the chabasite cage.

In Table 7.9 we report the local environment of the Al ion, in the presence of one and two water molecules, together with the adsorption energies.

Table 7.9: *Local environment of dehydrated and hydrated Al^{3+} ions in Mn^{3+}-doped AlPO-34, and calculated adsorption energies E^n_{ad} (eV).*

	Mn^{3+} AlPO-34	Mn^{3+} AlPO-34·1 H_2O	Mn^{3+} AlPO-34·2H_2O
R(Al-O_1)	1.734	1.733	1.752
R(Al-O_2)	1.737	1.744	1.752
R(Al-O_3)	1.739	1.745	1.775
R(Al-O_A)	1.739	1.766	1.823
d_{123}	-	0.431	0.181
R(Al-O_{w1})	-	2.823	2.102
R(O_{w1}-H_{11})	-	0.945	0.957
R(O_{w1}-H_{12})	-	0.945	0.945
H_{12}-O_{w1}-H_{11}	-	106.4	106.4
R(H_{11}-O_{w2})	-	-	1.896
R(O_{w2}-H_{21})	-	-	0.947
R(O_{w2}-H_{22})	-	-	0.944
H_{22}-O_{w2}-H_{21}	-	-	107.2
R(H_{21}-O_F)	-	-	2.198
R(O_F-Al_F)	-	-	1.749
R(O_F-P_F)	-	-	1.524
Al_F-O_F-P_F	-	-	136.4
E^n_{ad} (eV)	-	0.27	0.46

Our results indicate that the Al site is hydrated in both water coverages. In the presence of one water molecule, the Al-O_w equilibrium distance is 2.823Å, which is comparable to that calculated in the pure AlPO-34 framework as 2.815Å, while in the Mn^{2+}AlPO-34 system we calculated R(Al-O_w) as 2.311Å. The calculated adsorption energy of 0.27 eV is equal to that in the pure AlPO-34. Unlike Mn^{2+}, therefore, the presence of the Mn^{3+} dopant does not significantly activate the framework Al^{3+} ions towards hydration. The presence of a second admolecule shortens the Al-O_w bond distance to 2.102Å, with an increase of E_{ad} to 0.46 eV. In both the mono- and di-hydrated systems the Al^{3+} ion adopts a trigonal bipyramid geometry. The value of the parameter d_{123} is calculated here as 0.431Å, and 0.181 Å

for the mono- and di-hydrated frameworks respectively. Again these values are comparable to those calculated in the pure AlPO-34 framework, which confirms that the Mn^{3+} dopant plays a minor part in activating neighbouring framework ions towards hydration compared to the Mn^{2+} dopant.

In the Mn^{3+} doped system, the second water molecule forms a weaker hydrogen bonding to a framework oxygen that is located five bonds away from the hydrated Al atom. In the Mn^{2+}-doped ALPO-34 system, the second water molecule was instead hydrogen bonded to a framework oxygen three bonds away from the hydrated Al ion. To understand the effect played by the interaction of the second water molecule with different framework oxygens, we have optimised the structure of the dehydrated Al^{3+} ion in Mn^{3+}AlPO-34, directing the second water molecule towards the framework oxygen three bonds away from the hydrated Al ion, *i.e.* the same that was hydrogen bonded in the Mn^{2+}-doped framework. The $R(H_{21}\text{-}O_F)$ distance is in this case calculated as 2.654 Å, and is longer compared to the 2.496 Å calculated when the O_F is five bonds away from the hydrated framework Al ion. The two equilibrium structures, however, differ in energy by only 0.02eV, and have identical bond distances between hydrated Al and nearest neighbour oxygens, indicating *that the hydrogen bonding interaction of the second water molecule with different framework oxygen atoms affects only marginally the energetics of the system.*

7.3.3.4 Basis set superposition error (BSSE) contributions.

Studies of adsorption energies performed with QM methods based on local basis sets may be affected by the so-called basis set superposition error (BSSE). This is related to the availability of a better basis set for the interacting systems (framework and water admolecules in our case) rather than for the isolated ones. We have therefore investigated the BSSE contribution to the adsorption energy for a water molecule and

dimer adsorbed on the Mn^{3+} dopant in the Mn^{3+}-doped AlPO-34 framework, and on the Al^{3+} ion in the pure AlPO-34 framework. These are the two adsorption geometries in which the M-O distance is shortest, and the BSSE is likely to be highest. In both cases we employed the calculated equilibrium geometry, and used the counterpoise method[29] to estimate the BSSE.

The BSSE contributions are calculated as follows: 0.14 eV for the framework Al ion in the presence of the basis set of the water dimer; 0.13 eV for the water molecules adsorbed on Al^{3+} in the presence of the basis set of the nearest eleven framework ions, *i.e.* those located at a distance of up to 3Å from the admolecules. The total BSSE correction for the adsorbed water dimer on Al^{3+} is therefore of 0.27 eV. In the case of one water molecule adsorbed on the Al^{3+} ion, the BSSE contributions are of 0.08 eV for the Al ion in the presence of the water basis set, and 0.07 eV for the water molecules in the presence of the basis set of the nearest framework ions. The total BSSE correction for the adsorbed water molecule is therefore of 0.15 eV, which is approximately half the BSSE value calculated for the dimer.

For water adsorbed on Mn^{3+}, the BSSE values are 0.16 eV for the Mn^{3+} dopant in the presence of the basis set for a water dimer, and 0.14 eV for the water admolecules, yielding a total BSSE of 0.30 eV. These values represent a fraction of 30% of the total adsorption energy in the Mn-doped framework. Correction for BSSE is therefore important, especially for the weakest adsorption site, *i.e.* the Al^{3+} ion of the doped and undoped AlPO-34 frameworks. However, the BSSE correction is roughly constant for the two sites discussed above. Since our main concern in this work is to compare the adsorption properties of the different adsorption sites available in the Mn doped AlPO-34 framework, the relative values of E^n_{ad} are not affected by adding a roughly constant BSSE to each adsorption site. No BSSE correction has been

therefore added to the values of the adsorption energies E_{ad} reported in this work. We believe that the comparisons performed concerning relative values of E_{ad} retain general validity.

Although the BSSE may appear large compared to the total adsorption energy E_{ad}, we consider this feature as "misleading". The adsorption process can in fact be decomposed into two semi-reactions: the first is a deformation of the structure of both the host AlPO framework and water admolecules from their equilibrium structure when isolated, to accommodate the water-framework interaction; the second is the interaction between the framework and water in their new geometry. This is illustrated in the following diagram.

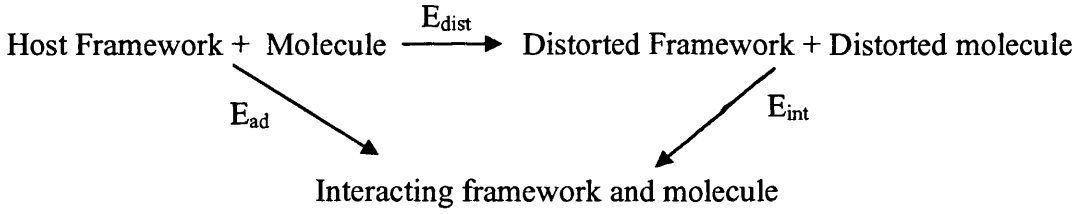

where E_{dist} is the distortion energy, which accounts for the deformation of the host framework plus the deformation of the admolecule itself; E_{int} is the interaction energy, which is a measure of the "effective" interaction of the deformed host framework and the deformed admolecule.

The three energy values are related by the following equation:

$$E_{ad} = E_{dist} + E_{int}$$

Since E_{int} is the actual interaction energy between water and host framework, we suggest that the BSSE should refer to the effective interaction energy E_{int} and not the adsorption energy E_{ad}.

In the hydrated Mn^{3+}AlPO-34 system, when two water molecules are adsorbed on the Mn^{3+} dopant, we have calculated a deformation energy of 1.02 eV, and an interaction energy of -2.10eV. The BSSE value of 0.30 eV calculated for this system accounts therefore for 14 % of the interaction energy E_{int}. In the pure AlPO-34 system, when two water molecules are adsorbed on the Al^{3+} ion, the calculated E_{dist} value is of 0.78 eV, while E_{int} is -1.17 eV; the BSSE value of 0.27 eV accounts here for 23 % of the total value of the interaction energy.

The BSSE affects the effective interaction energy by a value which is less than 25 %, which we consider to be acceptable. Higher fractions of the BSSE compared to E_{int} may in fact lead to geometry optimisation procedures in which the BSSE, and not the physical water-framework interaction, is optimised.

7.4 Hydration in other MeAlPO-34 catalysts

Having examined in detail the hydration of the Mn^{2+} and Mn^{3+} doped AlPO-34 framework, we shall now consider hydration in the other MeAlPO-34 materials, to understand the effect played by the *dopant type* on the water adsorption. The dopants investigated are the same discussed in chapters 4 and 5. For each dopant, only selected adsorption sites have been considered, which are a subset of those examined for MnAlPO-34. We recall that for the divalent metal dopants these are the Brønsted acid site, the metal dopant (the attack from behind configuration) and the Al dopant situated opposite to the metal dopant in the chabasite cage. For the trivalent metal dopants we report the result of water interaction with the metal dopant and the Al sites, respectively.

Results for each dopant are qualitatively similar to those described earlier for Mn; in this section we shall therefore highlight only trends and anomalies in the behavior of the other dopants.

7.4.1 Adsorption of water in divalent metal doped AlPO-34

7.4.1.1 Adsorption of water on the Brønsted acid site

The coordination environment around the Me^{2+}-OH site, for the dehydrated catalysts and in the presence of one and two water admolecules is reported in Table 7.10.

Table 7.10: *Bond distances, in Å, around the Brønsted acid site Me^{2+}-OH in anhydrous and hydrated Me^{2+}-doped AlPO-34 frameworks. n refers to the number of water molecules adsorbed.*

Me *n*	Me-O_1	Me-O_2	Me-O_3	Me-O_H	Me-H	O_H-H	H-O_{w1}	O_{w1}-H_{11}	H_{11}-O_{w2}
Mg									
0	1.8520	1.8709	1.9062	2.0837	2.4211	0.9551			
1	1.8573	1.8802	1.8910	2.0444	2.5264	0.9899	1.5945	0.9472	
2	1.8605	1.8862	1.9018	2.0414	2.5126	0.9978	1.5337	0.9536	1.9559
Cr									
0	1.9963	2.0295	2.0455	2.3562	2.8721	0.9478			
1	2.0015	2.0224	2.0802	2.3134	2.8022	0.9804	1.5859	0.9463	
2	1.9943	2.0699	2.0729	2.3043	2.7381	0.9955	1.5020	0.9553	1.9644
Mn									
0	2.0169	2.0254	2.0401	2.2654	2.8060	0.9498			
1	2.0126	2.0371	2.0764	2.2473	2.6841	0.9882	1.5853	0.9476	
2	2.0156	2.0622	2.0647	2.2293	2.6704	1.0077	1.4961	0.9553	1.8975
Fe									
0	1.9745	1.9812	1.9907	2.1907	2.7331	0.9495			
1	1.9780	1.9912	2.0058	2.1767	2.7461	0.9737	1.6561	0.9465	
2	1.9765	1.9993	2.0106	2.1731	2.7614	0.9870	1.5672	0.9539	1.9089
Co									
0	1.9382	1.9435	1.9486	2.1406	2.6686	0.9498			
1	1.9439	1.9503	1.9598	2.1200	2.6161	0.9789	1.6392	0.9509	
2	1.9493	1.9609	1.9614	2.0971	2.5996	0.9955	1.5468	0.9543	1.9276
Ni									
0	1.8971	1.8973	1.9016	2.1921	2.7486	0.9497			
1	1.8993	1.9144	1.9318	2.1576	2.6060	0.9878	1.5939	0.9469	
2	1.9005	1.9197	1.9356	2.1360	2.6030	1.0038	1.5176	0.9546	1.9332
Zn									
0	1.9041	1.9054	1.9126	2.1887	2.6839	0.9501			
1	1.9085	1.9147	1.9239	2.1384	2.6309	0.9798	1.6302	0.9502	
2	1.8987	1.9319	1.9431	2.1462	2.5857	0.9934	1.5448	0.9537	1.9559

As in the case of Mn^{2+}-doped AlPO-34, the environment around the Me^{2+}-OH site varies significantly upon adsorption of water on the Brønsted acid site. This is due to the formation of a hydrogen bond between the adsorbed water molecule and the acid site. Comparing the behaviour of the different ions we see that the closer is the oxygen of the water molecule to the acid proton, the longer the OH bond and the shorter the Me-O_H bond distance. For instance, in the case of Mg-doped AlPO-34 the OH bond distance increases by ~ 3 %, and the Me-O_H bond distance decreases by 2% upon adsorption of one water molecule. As the water coverage increases, the hydrogen bonding interaction between water admolecules and the Brønsted acid site becomes stronger; this is reflected in further lengthening of the OH bond and shortening of the Me-O_H and H-O_{w1} bond distances. The calculated adsorption energies are shown in Table 7.11, where we see that for all MeAlPO-34 systems investigated, the presence of a second water hydrogen bonded to the first makes the adsoption process more energetically favourable, as already discussed in the case of Mn^{2+}.

Table 7.11: *Adsorption energies (E^n_{ad}, in eV) of water on the OH site of Me^{2+}-doped AlPO-34.*

Me	Mg	Cr	Mn	Fe	Co	Ni	Zn
E^1_{ad}	0.79	0.94	0.93	0.72	0.76	0.90	0.74
E^2_{ad}	1.10	1.22	1.19	0.97	0.98	1.16	1.02

Comparing the adsorption energies given in Table 7.11, we note that the Fe^{2+}-doped AlPO-34 framework has the lowest adsorption energy in both the monohydrated and dihydrated AlPO-34 systems. Hydrated Co- and Zn-AlPO-34 frameworks have slightly higher adsorption energy than the Fe doped system, but considerably lower

than Cr, Mn, and Ni. To investigate the reasons why these three systems have lower adsorption energies, we shall examine in greater detail the equilibrium geometry of water. Results are highlighted in Figures 7.10, 7.11 and 7.12.

On examining the orientation of the acid proton in the dehydrated MeHAlPO-34 framework, we found that all the systems investigated, except Fe, Co and Zn-doped AlPO-34 framework, the proton points towards the centre of the eight membered ring of the chabasite framework (see Figure 7.10), and the OH group is *bent towards* the metal dopant, while in Fe-, Co- and Zn-doped AlPO-34 frameworks, the proton adopts a different orientation (see Figures 7.11 and 7.12). In Fe^{2+}-HAlPO-34 framework, the OH group points *away* from the Fe dopant, and is oriented towards one of the double six rings of the chabasite framework rather than a centre of the chabasite cage (see Figure 7.11). In the Co- and Zn-doped frameworks, the OH is *bent towards* the dopant, but the proton points outside the plane of the eight membered ring (see Figure 7.12). The exact factors affecting the orientation of the OH group are not yet clearly understood but are probably related to a combination of ionic size and electronic configuration of the dopant ion. This question is open for further experimental and theoretical investigation.

Upon adsorption of water on the Brønsted acid site, we found that the first water admolecule adapts to the original orientation of the Brønsted acid site in the anhydrous Me^{2+}HAlPO-34 framework described above, and that the second water molecule adapts to the orientation of the first water molecule, without modifying the orientation of the framework OH group. Depending on the stable orientation of the OH group we can therefore identify three different cases for adsorption, which we label as A, B, and C respectively as follows:

- ***Case A:*** The OH group points towards the centre of 8-membered rings. This case refers to the hydrated Mg, Cr, Mn, and Ni- doped AlPO-34, in which the adsorbed water molecule has qualitatively the same configuration explained in section 7.3.2.1 for the Mn^{2+}doped AlPO-34 system, (see Figure 7.10). Here the proton is very accessible since it is not obstructed by other framework atoms from direct interaction with a water molecule; hence the interaction of water with the acid site is effective and the adsorption energy is high (see Table 7.11). In addition, water *bridges* the metal dopant via two hydrogen bonds, which involve the Brønsted acid site (H) and the framework oxygen (O_F) adjacent to the dopant.

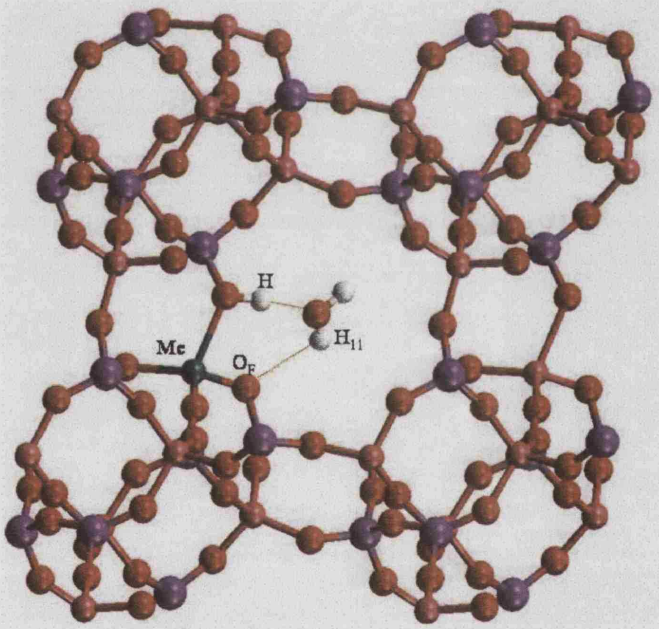

Case A: **Mg^{2+} -, Cr^{2+} -, Mn^{2+} -, Ni^{2+} - AlPO-34. 1 H2O**

Figure 7.10: *Adsorption geometry for a water admolecule on the Brønsted acid site in case A. The black dotted lines indicate hydrogen bonding interactions*

- ***Case B:*** The proton is in a region which is more protected by the framework ions, hence it is less accessible to water in the cage. This situation occurs in the Fe^{2+}-doped AlPO-34, which is illustrated in Figure 7.11. The water admolecule is in a region far from the metal dopant, as it adapts to the orientation of the OH

group which is bent away from the dopant. Here, the water admolecule does not *bridge* the dopant as seen in *case A*, instead it forms additional hydrogen bonding with the framework oxygen *five bonds away* from the metal dopant.

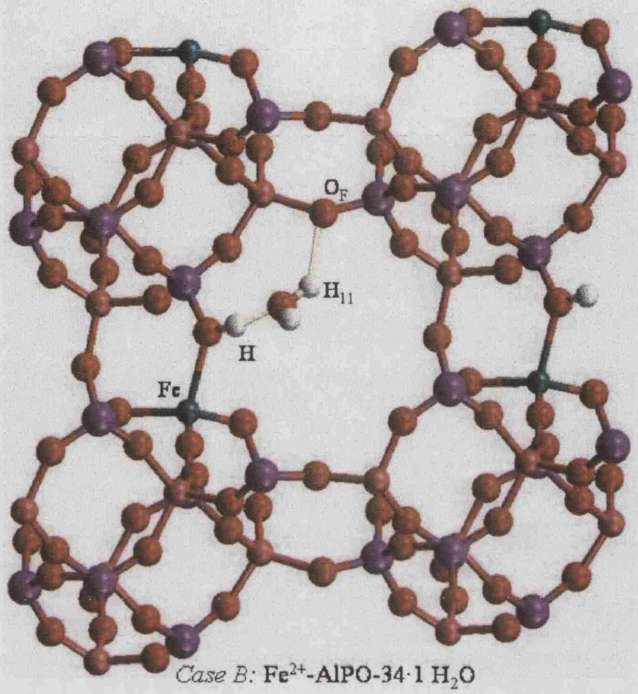

Figure 7.11: *Adsorption geometry for a water admolecule in case B.*

- ***Case C:*** The orientation of the OH group is intermediate between cases A and B, as found in the Co^{2+}- and Zn^{2+}- doped AlPO-34 (see Figure 7.12). The proton is not situated in a region of a framework which is too accessible nor it is too protected by the frameworks ions. Hence an intermediate behaviour in terms of the interaction with water is seen for these materials. Since the OH group is oriented towards the metal dopant, the water admolecule *bridges* the metal dopant in the same fashion seen in *case A*. The framework oxygen involved in the hydrogen bonding with water admolecule is different in this case.

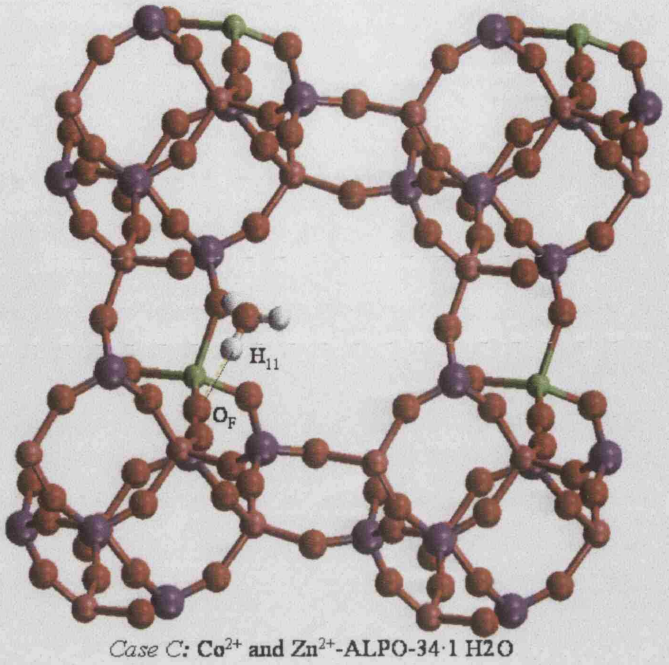

Figure 7.12: *Adsorption geometry for a water admolecule in case C*

The bond distances corresponding to the two hydrogen bonding interactions of water with the Brønsted acid site and framework oxygen O_F are reported in Table 7.12. In each case the bond with the Brønsted acid ($H\text{-}O_{w1}$) is shorter and stronger than the one involving the framework oxygen O_F.

Table 7.12: *Hydrogen bond distances between one water admolecule and the HMeAlPO-34 host framework.*

Case	Me	$H\text{-}O_{w1}$	$H_{11}\text{-}O_F$
(A)	**Mg**	1.594	2.639
	Cr	1.626	2.570
	Mn	1.585	2.466
	Ni	1.547	2.568
(B)	**Fe**	1.656	2.407
(C)	**Co**	1.639	2.314
	Zn	1.630	2.309

In the hydrated Fe^{2+}- doped AlPO-34 framework (*Case B*) (see Figure 7.11), the calculated hydrogen bond distance with the acid proton, $H\text{-}O_{w1}$=1.653Å, is the

longest of all the systems calculated, consistently with the less accessible orientation of the OH group in this material. The H_{11}-O_F is calculated to be 2.407 Å; this interaction with the framework oxygen causes the bonds angle of the water admolecule H_{11}-O_{w1}-H_{12} to increase from 106° in the isolated molecule to 108° in the adsorbed configuration.

In the hydrated Co- and Zn-AlPO-34 frameworks (*Case C*) (see Figure 7.12), the distance from the acid proton is calculated to be 1.639Å and 1.630 Å respectively. The distance between one of the hydrogen of water H_{11} and a framework oxygen adjacent to the metal dopant, H_{11}-O_F is instead 2.314Å and 2.308 Å for the Co- and Zn- doped AlPO-34 respectively. The equilibrium bond angle of the adsorbed water molecule H_{11}-O_{w1}-H_{12} is calculated to be 107.7° for both systems.

From data given in Table 7.12, we note that there is an inverse correlation between the two hydrogen bond distances H-O_{w1} and H_{11}-O_F; the longer the H-O_{w1} the shorter is the H_{11}-O_F. Shorter H_{11}-O_F indicates a strong hydrogen bonding interaction between water and the framework oxygen which appears to weaken the interaction between the water admolecule and the Brønsted acid site. Water tries to maximise its hydrogen bonding interaction with the acid proton, but in a situation where it is obstructed, as in the case of Fe^{2+}-doped AlPO-34 (*case B*), water therefore reacts by forming instead stronger interaction with the framework oxygen. Therefore, we conclude that *there is a competition between the two hydrogen bonding interactions, which influences the extent of water interaction with the Brønsted acid site.* This feature explains why the adsorption energies of water are higher in systems described in *case A* and lower in Fe, Co and ZnAlPO-34 frameworks.

7.4.1.2 Adsorption of water on the Me^{2+} dopant

Let us now investigate the direct interaction of a water dimer with the metal dopants, in the configuration from behind the acid site. The dopants considered here are Mg, Fe, Co, and Zn. As in the case of the Mn^{2+} dopant, we found that, the dimer interacts effectively with the metal dopant, which acts as a Lewis acid centre. This type of interaction leads to a breakage of the Me^{2+}–O_H bond for each dopant examined. The equilibrium geometry of the Fe^{2+}-doped AlPO-34 framework is given in Figure 7.13.

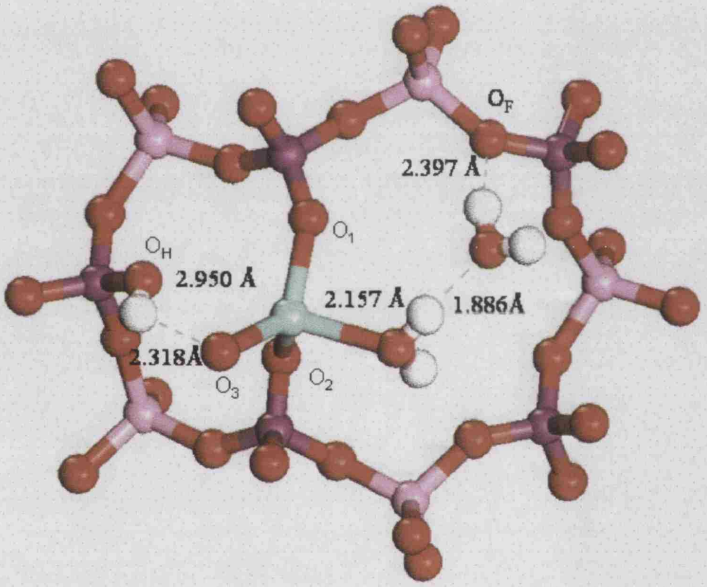

Figure 7.13: *Local environment of two water molecules adsorbed on the Fe^{2+} dopant, from behind the OH Brønsted acid site.*

The calculated adsorption energies in the presence of two water admolecules are given are in Table 7.13. In section 7.3.2.3 we have found that in the MnHAlPO-34 framework, the adsorption of a dimer molecule on the Lewis metal dopant and directly on the Brønsted acid site have comparable energies, the difference being of

~0.02 eV. To investigate if this is the case also for the other MeHAlPO-34 frameworks, we have calculated the difference in energy between these two adsorption sites in each MeAlPO-34 framework examined. The calculated values are summarised in Table 7.13.

Table 7.13: *Energy difference between adsorption of a water dimer on the Brønsted acid site and on the Lewis acid dopant.*

Me	Mg	Mn	Fe	Co	Zn
E_{ad}^{Me}	1.09	1.17	1.11	0.92	0.90
E_{ad}^{OH}	1.10	1.19	0.97	0.98	1.02
$E_{ad}^{OH} - E_{ad}^{Me}$	0.01	0.02	-0.14	0.06	0.12

From Table 7.13, we note that, for all the system investigated, except the Fe^{2+}-doped AlPO-34 framework, the energy difference between the adsorption of a dimer on the two acid sites, *i.e.* the Lewis active metal dopant and the Brønsted acid site is positive. This indicates that, for all those systems the adsorption of water on the acid proton is energetically favourable. For the Fe^{2+}-doped AlPO-34 framework, the energy difference calculated between the two acid adsorption sites is negative; indicating that the adsorption of water from behind on the Lewis active Fe^{2+} is 0.14 eV more stable that on the acid proton.

Similarly to the Mn^{2+}dopant, the energy difference calculated for the Mg- and Co-doped AlPO-34 framework is less than 0.1 eV, while this value is slightly larger for Zn-doped AlPO-34, calculated to be 0.12 eV respectively.

The results above suggest that in Mg-, Co-, and Mn-, doped AlPO-34, both the Lewis and Brønsted acid sites co-exist and are mutually exclusive. In the Zn-doped AlPO-34, the preference for water adsorption is shifted towards the Brønsted type of interaction, a process which is 0.12 eV more stable than the attack of water directly

on the Zn dopant. The Lewis type interaction of water with the dopant is instead energetically favourable in the case of Fe^{2+} dopant.

7.4.1.3 Adsorption of water on the Al^{3+} dopant

In this section, we investigate the interaction of water with framework Al in other divalent metal doped AlPO-34. For consistency with the Mn^{2+}-AlPO34 description (see Figure 7.1), we have chosen the Al ion which is situated in the opposite end of the metal dopant.

We have seen in section 7.4.1.1 that the orientation of the OH group is different in Me^{2+}-doped AlPO-34 systems, hence we expect the orientation of the electrostatic dipole created by the presence of the divalent metal dopant and the proton (as described in section 7.4.1.1) to be different depending on the orientation of the OH group. While in the Mg, Cr, Mn, Ni-doped AlPO-34 frameworks, the dipole points in the direction of the Al^{3+} framework ion at the opposite end of the chabasite cage, the orientation of the dipole may be different in the Fe, Co and Zn doped AlPO-34 sysytems. In this case, a different framework Al ion than the one studied here may be more activated by the dopant.

The local environment of the Al site, together with the adsorption energies E^{n}_{ad} (eV) are reported Table 7.14. In both water coverages examined, the Al framework ion interacts effectively with the adsorbed water molecules, maintaining the same structural features seen in the case of the hydrated Al site in the Mn^{2+} doped AlPO-34 material, *i.e.* the hydrated Al site adopts a trigonal bipyramidal geometry.

Table 7.14: *Local environment of dehydrated and hydrated Al^{3+} ion in Me^{2+}- doped AlPO-34, and calculated adsorption energies E^n_{ad} (eV).*

Me *n*	Al-O_1	Al-O_2	Al-O_3	Al-O_4	Al-Ow_1	d_{123}	H_w-O_F	E^n_{ad}
Mg								
0	1.7203	1.7235	1.7333	1.7710				
1	1.7324	1.7465	1.7493	1.8579	2.3252	0.270	2.6138	0.22
2	1.7360	1.7586	1.7662	1.9066	2.0977	0.158	2.5709	0.45
Cr								
0	1.7339	1.7439	1.7460	1.7815				
1	1.7448	1.7529	1.7650	1.8680	2.3580	0.268	2.7318	0.29
2	1.7561	1.7618	1.7793	1.8913	2.0828	0.162	2.6389	0.51
Mn								
0	1.7237	1.7337	1.7435	1.7892				
1	1.7348	1.7497	1.7579	1.8622	2.3110	0.267	2.6668	0.29
2	1.7392	1.7608	1.7737	1.9087	2.0952	0.161	2.4957	0.53
Fe								
0	1.7250	1.7341	1.7441	1.7851				
1	1.7360	1.7452	1.7542	1.8512	2.3625	0.283	2.6689	0.27
2	1.7417	1.7581	1.7734	1.9022	2.0968	0.164	2.5789	0.50
Co								
0	1.7217	1.7321	1.7406	1.7858				
1	1.7340	1.7473	1.7522	1.8544	2.3422	0.277	2.6508	0.25
2	1.7385	1.7583	1.7696	1.9055	2.1015	0.163	2.5299	0.48
Ni								
0	1.7210	1.7371	1.7407	1.7861				
1	1.7314	1.7527	1.7538	1.8542	2.3260	0.255	2.5758	0.28
2	1.7366	1.7654	1.7708	1.8963	2.0855	0.155	2.5301	0.52
Zn								
0	1.7247	1.7342	1.7396	1.7808				
1	1.7296	1.7358	1.7410	1.8107	2.8069	0.406	2.7451	0.28
2	1.7403	1.7586	1.7698	1.8954	2.1036	0.169	2.5780	0.48

From the data given in Table 7.14, we note that for Cr, Mn, and Ni-doped AlPO-34, the adsorption energy of water is higher compared to those calculated for Mg, Co, Zn and Fe doped AlPO-34. In the former systems the OH proton points towards the centre of the eight membered ring of the chabasite framewrok and the dipole moment points towards the Al located in the opposite end of the metal dopant; hence the Al framework ion is activated towards hydration by the presence by the divalent metal dopant whose influence is highlighted in the higher values of the adsorption energies and the shorter d_{123} parameter. We expected the hydration of the Al ion in the Mg doped AlPO-34 to have comparable adsorption energies to those calculated for the Cr, Mn and Ni doped systems, however hydration of Al in the Mg doped AlPO-34

was found to be the weakest of all the systems investigated, the exact reasons why this is the case are not well understood.

In the Co, Zn and Fe doped AlPO-34 frameworks, the orientation of the OH group is different from that in the Cr, Mn, and Ni doped AlPO-34, hence the Al ion is less activated by the dopant. This explains why the calculated adsorption energies for these systems are low.

The adsorption energies for the three adsorption sites, calculated for the MeAlPO-34 frameworks are summarised in Table 7.15. In each case, the adsorption of water in the doped AlPO-34 framework is energetically more favourable than in the pure AlPO-34 framework. The interaction of water with the Brønsted acid site or with the Lewis-active dopant is thermodynamically stable, with an adsorption energy of ~ 1 eV. The adsorption energies on the framework Al ion are of ~ 0.5 eV, which is higher by as much as 0.12 eV compared with the undoped AlPO framework. These results confirm that the presence of the divalent dopant increases the hydrophilicity of the framework.

Table 7.15: *Calculated adsorption energies E_{ad}^{n} (eV) (n is a number of water molecules= 1, 2) for water admolecules on the three adsorption sites available in Me^{2+} doped AlPO-34 framework.*

Adsorption site	OH		Me	Al	
Me	E_{ad}^{1}	E_{ad}^{2}	E_{ad}^{2}	E_{ad}^{1}	E_{ad}^{2}
Mg	0.79	1.10	1.09	0.22	0.45
Cr	0.86	1.22	-	0.29	0.51
Mn	0.93	1.19	1.17	0.29	0.53
Fe	0.72	0.94	1.11	0.27	0.50
Co	0.75	0.98	0.92	0.25	0.48
Ni	0.89	1.16	-	0.28	0.52
Zn	0.74	1.02	0.90	0.28	0.48
Undoped AlPO-34	-	-	-	0.27	0.39

7.4.2 Adsorption of water in trivalent metal doped AlPO-34 framework

7.4.2.1 Water adsorption on the Me^{3+} dopant

The local environment of the trivalent metal dopant in the presence of one and two adsorbed water molecules is reported in Table 7.16. In both cases, for all the MeAlPO-34 systems investigated, the Me^{3+} ion increases its coordination number from 4 to 5, and adopts a similar bipyramidal trigonal geometry as that described for the Mn^{3+} dopant in section 7.3.3.1.

Table 7.16: *Local environment of Me^{3+} in dehydrated and hydrated Me^{3+}AlPO-34, and calculated adsorption energy E^n_{ad} (eV).*

Me *n*	Me-O_1	Me-O_2	Me-O_3	Me-O_4	Me-Ow_1	H_{11}/H_{21}-O_F	d_{123}	E^n_{ad}
Cr								
0	1.8797	1.8825	1.8898	1.9130				
1	1.9054	1.9263	1.9379	1.9543	2.1151	2.535	0.209	0.98
2	1.9059	1.9253	1.9411	1.9517	2.0982	3.360	0.171	1.17
Mn								
0	1.8649	1.8668	1.9074	1.9131				
1	1.8770	1.9133	1.9291	1.9891	2.0664	2.526	0.224	0.79
2	1.8864	1.9149	1.9477	1.9678	2.0290	2.363	0.169	1.07
Fe								
0	1.8649	1.8654	1.8678	1.8808				
1	1.8856	1.8928	1.8995	1.9409	2.3046	2.760	0.295	0.51
2	1.8882	1.9059	1.9140	1.9591	2.1932	2.269	0.237	0.79
Co								
0	1.8325	1.8405	1.8507	1.8589				
1	1.8461	1.8691	1.8694	1.9260	2.2722	2.535	0.256	0.54
2	1.8457	1.8681	1.8739	1.9595	2.1984	3.360	0.198	0.69

From the data given in the Table 7.16, we note that at both water coverages of one and two molecules, the Me-O_{w1} bond distances are longer for hydrated Fe^{3+} and Co^{3+} ions compared to the ones calculated for hydrated Cr^{3+} and Mn^{3+} dopants. The adsorption energies of water calculated for the Fe^{3+} and Co^{3+} dopants are also lower. To understand why this is the case, we plot in Figure 7.14 the adsorption energy of a

dimer against the average bond distance between the metal dopant and the three equatorial oxygens (Me-O_{123}).

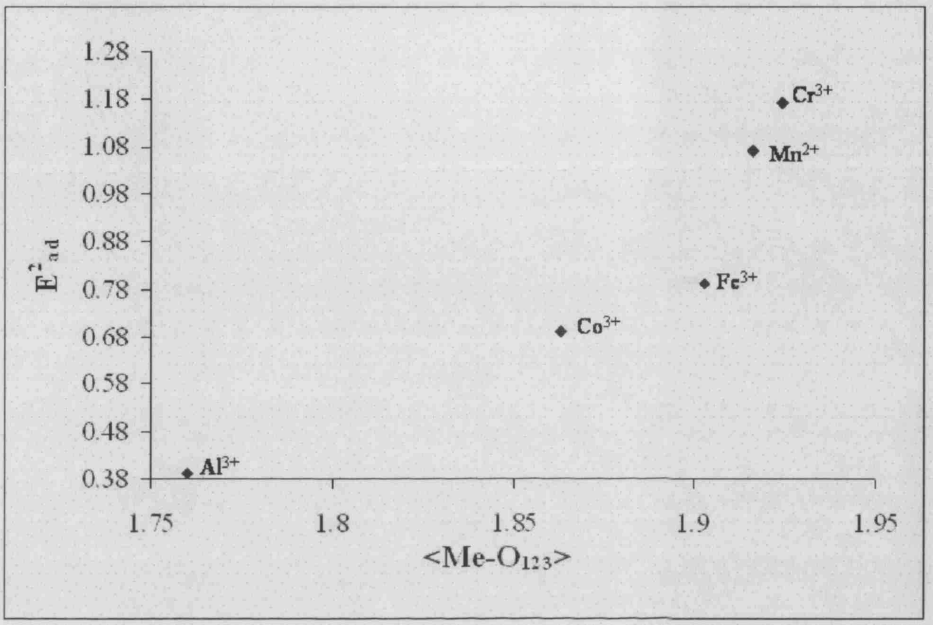

Figure 7.14: *Adsorption energy of a dimer (E^2_{ad}, eV) against the average bond distance between the metal dopant and the three equatorial oxygens <Me-O_{123}>, in Å.*

Figure 7.14 shows that there is a correlation between adsorption energy and average Me-O_{123} bond distance: the larger the <Me-O_{123}>, the higher the E^2_{ad}. Longer <Me-O_{123}> bond distances correspond to a more opened environment of the dopant, which makes the metal dopant more accessible to the water admolecules. Hence the adsorption energy of water on the metal dopant is high. Smaller metal dopants have shorter <Me-O_{123}> bond distances, hence they are less accessible and less Lewis acid compared to larger metal dopants. We have seen in section 6.2 that the Lewis acidity of transition metal dopants is influenced by the electronic orientation of the *d* (AO). The results of this section also indicate that the Lewis acidity is influenced by the ionic size of the dopant.

It is of interest to note that the Cr^{3+} dopant has the highest affinity for water. The adsorption energies are 0.98 eV and 1.17 eV for a mono- and di-hydrated system respectively. This result agrees with our finding discussed in Section 5.2, concerning the instability of the Cr^{3+} dopant in tetrahedral coordination, and agrees with experimental results which showed that the Cr^{3+} dopant when incorporated in AlPO frameworks is found to have higher coordination number than four with adsorbed water molecule.[30]

7.4.2.2 Adsorption of water molecule on the Al site

Let us now investigate the adsorption of water on the Al site in the Me^{3+}- doped AlPO-34. For all the Me^{3+}AlPO-34 systems investigated, the Al site is readily hydrated. The local environment of the mono- and di-hydrated Al site is similar to that described for the hydrated Al ion in the Mn- doped AlPO-34 framework. (See Table 7.17).

Table 7. 17: *Local environment of dehydrated and hydrated Al^{3+} ions in Me^{3+}-doped AlPO-34, and calculated adsorption energies E^{n}_{ad} (eV).*

Me *n*	Al-O_1	Al-O_2	R(Al-O_3)	R(Al-O_4)	R(Al-Ow_1)	d_{123}	H-O_F	E^{n}_{ad}
Cr								
0	1.7306	1.7331	1.7356	1.7381				
1	1.7496	1.7498	1.7658	1.7899	2.8271	0.441	2.9639	0.21
2	1.7671	1.7793	1.7940	1.8128	2.0299	0.147	2.1501	0.44
Mn								
0	1.7339	1.7369	1.7389	1.7393				
1	1.7335	1.7434	1.7454	1.7671	2.8298	0.431	3.1751	0.27
2	1.7514	1.7520	1.7748	1.8239	2.1030	0.181	2.1952	0.46
Fe								
0	1.7365	1.7394	1.7406	1.7415				
1	1.7418	1.7426	1.7489	1.7690	2.7196	0.412	2.7859	0.27
2	1.7587	1.7664	1.7697	1.8256	2.1135	0.207	2.4278	0.43
Co								
0	1.7226	1.7235	1.7301	1.7347				
1	1.7350	1.7434	1.7424	1.7589	2.6285	0.401	3.0012	0.30
2	1.7406	1.7542	1.7570	1.8361	2.1088	0.177	2.1881	0.39

We compare in Table 7.18 the adsorption energies calculated for the two adsorption sites in Me^{3+} AlPO-34 framework. The adsorption on the trivalent metal dopant is more energetically favourable than that on the Al framework site, for instance a water dimer adsorption energies on the Al site is of an order of ~ 0.45 eV, while the adsorption energies of the same species on trivalent metal dopants is of an order of ~ 1 eV.

Table 7.18 *Calculated adsorption energies E_{ad}^{n} (eV) for water admolecules on the the metal dopant and the Al framework sites in the Me^{3+} doped AlPO-34 framework.*

Adsorption site	Me^{3+}		Al	
Me	E_{ad}^{1}	E_{ad}^{2}	E_{ad}^{1}	E_{ad}^{2}
Cr	0.98	1.17	0.21	0.44
Mn	0.79	1.07	0.27	0.46
Fe	0.51	0.79	0.27	0.43
Co	0.54	0.87	0.30	0.46
Undoped AlPO-34	-	-	0.27	0.39

7.4.2.3 Effect of hydration on the redox potential

Let us now investigate how hydration can modify the redox potential of the Me^{3+}/Me^{2+} pair in the AlPO-34 frameworks; we have seen in section 7.3.3.2 that, in case of Mn doped AlPO-34, hydration stabilises the 2+ oxidation state of the Mn dopant by ~ 0.1 eV. This value was obtained by comparing the adsorption energy on the most stable adsorption site for water in the Mn^{2+}-and Mn^{3+}-doped systems. The same reasoning can be applied to the other redox-active dopants discussed here, *i.e.* Fe, Co, and Cr.

The calculated difference in the adsorption energy of water for the monohydrated and dihydrated Cr^{3+} and Cr^{2+} systems is -0.12 eV and 0.05 eV respectively; the presence of one water molecule stabilises the 3+ oxidation state of the Cr dopant by 0.12 eV, while the presence of a dimer instead stabilises the 2+ oxidation state by

0.05 eV. For Fe-doped AlPO-34, the difference in E^n_{ad} calculated for the monohydrated and dihydrated Fe^{3+} and Fe^{2+} dopants are 0.21 eV and 0.32 eV; in this case, the 2+ oxidation state is stabilised, and the presence of a water dimer stabilises further Fe^{2+} by ~ 0.1 eV compared when only one water admolecule is adsorbed. For the Co-doped AlPO-34 framework, the presence of one water admolecule stabilises the 2+ oxidation state by 0.22 eV, the dimer by 0.11 eV only.

With the exception of Cr in the presence of one admolecule, in all the cases studied above, hydration of the MeAlPO-34 framework stabilises the 2+ oxidation state of the dopant. In each case, the effect on the redox potential is loading dependent.

In the case of the Fe dopant we have seen in section 6.3 that the dopant is more stable in the 3+ oxidation state; the presence of water admolecules alters this property, as it stabilises the 2+ oxidation state of the dopant. We therefore conclude that water adsorption can affect the redox behaviour of metal dopants in the true catalytic cycle.

7.5 Conclusions

In this chapter we have presented an extensive study of the hydration in metal doped AlPO-34 frameworks. We conclude the following general points:

- Hydration in the pure AlPO frameworks is energetically favourable; the Al framework site is readily hydrated, increasing its coordination number from four to five.
- Upon interaction of water with the Brønsted acid site in Me^{2+} doped AlPO-34, water adapts to the original orientation of the OH group, the orientation of the OH group is different in each metal doped system.

- The hydrogen bonding interaction between the hydrogen of one water admolecule H_{11} and framework oxygen O_F competes with the interaction of water admolecule with the Brønsted acid site. The stronger the hydrogen bonding interaction H_{11}---O_F, the weaker is the interaction between the water and the Brønsted acid site. This situation is different when a dimer is present. The strong hydrogen bonding network between the OH---- dimer----O_F strengthens the interaction of water with the Brønsted acid site can lead to the deprotonation of the framework.
- Low valent Me ions incorporated in the framework of AlPO-34 display dual acid behaviour: both Brønsted and Lewis acid/base interactions can take place with water admolecules. Lewis and Brønsted acidity in the Me^{2+}AlPO-34 are mutually exclusive, which interaction occurs between water and framework in a true Me-AlPO catalysts depends on the accessibiltiy of the active site and on the relative initial orientation of the water molecule approaching the Me site with respect to the Me-OH group. Brønsted and Lewis acid/base interaction will therefore be controlled by kinetic, rather than thermodynamic effects.
- The presence of divalent metal dopants in AlPO frameworks activates the hydration of the Al framework situated in the opposite end of the dopant. This result is consistent with experimental evidence which shows that the hydrophilic character of AlPO frameworks increases with doping.
- For trivalent metal doped AlPO-34 frameworks, the metal dopant interacts effectively with the water admolecules; such an interaction is energetically favourable and is dependent upon the size of the metal dopant: the larger the metal dopant, the more it is accessible to water.

- Water adsorption can affect the redox behaviour of transition metal dopants in the true catalytic cycle.

References:

1 M. Stoecker, *Micropor. Mesopor. Mater.* **1999**, *29*, 3

2 M. Kang, T. Inui, *J. Mol. Catal. A: Chem.* **1999**, *140*, 55

3 G. Poulet, P. Sautet, A. Tuel, *J. Phys. Chem B*, **2002**, *106*, 8599.

4 P.-P Knops-Gerrits, H. Toufar, X. –Y. Li, P. Grobet, R. A. Schoonheydt, P. A. Jacobs, W. A. Goddard III. *J. Phys. Chem. A.* **2000**, *104*, 2410

5 P. S. Singh, P. N. Joshi, S. P. Mirajkar, B. S. Rao, and V. P. Shiralkar, *J. Phys. Chem. B*, **1999**, *103*, 5338.

6 Smith, A. K. Cheetham, R. E. Morris, L. Marchese, J. M. Thomas, P. A. Wright, J. Chen. *Science*, **1996**, *271*, 799

7 F. Salehirad, and M. W. Anderson, *J. Catal, 1998, 177,* 189

8 A. Buchholz, W. Wang, M. Xu, A. Arnold, M. Hunger, *Micropor. Mesopor. Mater, 2002*, 56, 267

9 A. Buchholz, W. Wang, M. Xu, A. Arnold, M. Hunger, *Micropor. Mesopor. Mater*, **2002**,*57*,157

10 E. Nusterer, P. E. Blöchl, K. Shwarz, *Chem, Phys. Lett*, **1996**, *253*, 448

11 K. Schwarz, E. Nusterer, P. E. Blöchl, *Catal. Tod*, **1999**, *50*, 501

12 V. Termath, F. Haase, J. Sauer, J. Hutter, and M. Parrinello, *J. Am. Chem. Soc*, **1998**, *120*, 8512

13 J. Limtrakul, P. Chuichay, S. Nokbin, *J. Mol. Stuct*, **2001**, *560*, 169

14 R. Shah, J. D. Gale, M.C. Payne, *J. Phys. Chem*, **1996**, *100*, 11688.

15 C. Zenonos, G. Sankar, F. Corà, D. W. Lewis, Q. A. Pankhurst, C. R. A. Catlow and J. M. Thomas, *Phys. Chem. Chem. Phys*, **2002**, *4*, 5421

16 J. D. Chen, R. A. Sheldon, *J. Catal.* **1995**, *153*, 1

17 S. Caldarelli, A. Meden, A. Tuel, *J. Phys. Chem. B.* **1999**, *103*, 5477

18 A. Tuel, S. Caldarelli, A. Meden, L. B. McCusker, C. Baerlocher, A. Ristic, N. Rajic, G. Mali, V. Kaucic, *J. Phys. Chem. B* **2000**, *104*, 5705.

19 N. Rajic, I. Arcon, V. Kaucic, A. Kodre, *Croat. Chem. Acta*, **1999**, *72*. 645.

20 N. Z. Logar, L. Golic, V. Caucic, *Croat. Chem. Acta*, **1999**, *72*, 187.

21 K. Doll, V. R. Saunders, N. M. Harrison, *J. Quantum Chem.* **2001**, *82* 1; B. Civalleri, Ph. D'Arco, R. Orlando, V. R. Saunders, R. Dovesi, *Chem. Phys. Lett.* **2001**, *348*, 131.

22 F. Corà, C. R. A. Catlow, A. D'Ercole. J. *Mol. Catal A*, **2001**, *166*, 87

23 Y. Jeanvoine, J. G. Ángyán, G. Kresse and J. Hafner. *J. Phys. Chem. B*, **1998**, *102*, 7307

24 M. Krossner, J. Sauer, *J. Phys. Chem.* **1996**, *100*, 6199.

25 S. P. Greatbanks, I. H. Hillier, N. A. Burton, and P. Sherwood, *J. Chem. Phys*, **1996**, *105*, 3770.

26 F. Corà, M. Alfredsson, C.M. Barker, R. G. Bell, M. Foster, I. Saadoune, A. Simperler, C. R. A. Catlow, *J. Sol. State. Chem*, **2003**, *176*, 496.

27 R. A. Van Santen, G. J. Kramer, *Chem. Rev*, **1995**, *95*, 637.

28 F. Haase, J. Sauer, *Microp. Mesop. Mater*, **2000**, *35-36*, 379.

29 S. F. Boys, F. Bernardi, *Mol. Phys.* **1970**, *19*, 553

30 J. D. Chen, R. A. Sheldon, *J. Catal.* **1995**, *153*, 1

Chapter 8 Conclusions and future work

8.1 Conclusions

In this thesis, we presented an extensive computational study of metal doped AlPO catalysts. We examined three main topics: the chemistry that follows doping divalent and trivalent metals in AlPO frameworks, and the factors affecting the stability of these materials, the acid and redox catalytic activity of the doped framework, and the interaction of active sites with water in the doped AlPO-34 catalysts.

The major conclusions can be summarised in the following points:

1. Structural and electronic features of the metal dopants

- The local environment of divalent metal dopants is a distorted tetrahedron, due to the presence of the acid proton. The Me-O_H bond of the dopant to the protonated oxygen is ~0.15 Å longer than the other three Me-O bonds. The local environment of trivalent Co^{3+} and Mn^{3+} dopants is instead Jahn-Teller distorted, while Cr^{3+}, Fe^{3+} and the closed shell 3+ dopants have a more symmetric coordination.
- The variation of the calculated T-O-P angles between the doped and the undoped AlPO structure provides a way of estimating the range of the structural distortion around the metal dopant. The structural strain caused by the size of most metal dopants is short-ranged, and does not propagate to undoped regions of the host AlPO framework.
- Analysis of the calculated electronic density suggests that the nature of bonding between the Me dopants and the neighbouring oxygens is ionic in nature; the

ionicity of the Me-O bonds explains the Lewis acidity of the Me ions, which are able to increase their coordination number in presence of Lewis bases.

2. The size factor

- The size of the metal dopants has a major influence upon the thermodynamical stability of doped AlPO frameworks and the site ordering of the dopants in these frameworks. Bigger metal dopants prefer to substitute 'free' Al sites, located in unconstrained regions of the framework, whereas small metal dopants are energetically stable when replacing Al sites situated in smaller cages. This site preference increases on increasing the size difference between host ion (Al^{3+}) and dopant, and is explained via the topological features of the host AlPO framework.

3. Catalytic properties of dopants

- The acid strength is due to a complex combination of the structural and electronic features of the dopant ion, and does not show appreciable correlation with the local environment or electronic properties of the metal dopant, either isolated or in the framework.
- The Lewis acidity of transition metals doped AlPOs is a feature that requires the presence of electron acceptor empty *d* orbitals on the dopant. *Attack from behind* of Lewis basic molecules to 2+ dopant ions is favoured, and is expected to yield stronger Lewis acidity for polymorphs with single wall framework structure, rather than double 4 and 6 member rings.
- The calculated redox energies of the Me^{2+}/Me^{3+} couples indicate that, among the transition metal ions investigated, Fe is the most stable in the 3+ oxidation state, while Mn is the most stable as 2+ ion. Cr and Co, instead, have intermediate behaviour and can switch more easily between the two oxidation states. These

results contribute to elucidate the mechanistic details of catalytic processes occurring in MeAlPOs.

4. Hydration of MeAlPOs

- Hydration in the pure AlPO frameworks is energetically favourable; the Al framework site is readily hydrated, increasing its coordination number from four to five.
- Upon interaction of water with the Brønsted acid site in Me^{2+} doped AlPO-34, water adapts to the original orientation of the OH group, which is different in each metal doped system.
- The hydrogen bonding interaction between one hydrogen of the water admolecule and a framework oxygen competes with the interaction of the water admolecule with the Brønsted acid site. The stronger the former hydrogen bonding interaction, the weaker the latter.
- When a water dimer is adsorbed, a strong hydrogen bonding between water and framework strengthens the interaction, and can lead to the deprotonation of the framework.
- Low valent Me ions incorporated in the framework of AlPO-34 display dual acid behaviour: both Brønsted and Lewis acid/base interactions can take place with water admolecules. Lewis and Brønsted acidity in Me^{2+}AlPO-34 are mutually exclusive; which interaction occurs between water and framework depends on the accessibiltiy of the active site and on the relative initial orientation of the water molecule approaching the Me site with respect to the Me-OH group. Brønsted and Lewis acid/base interaction will therefore be controlled by kinetic, rather than thermodynamic effects.

- The presence of divalent metal dopants in AlPO frameworks activates the hydration of the framework Al. This result is consistent with experimental evidence which shows that the hydrophilic character of AlPO frameworks increases with doping.
- For trivalent metal doped AlPO-34 frameworks, the metal dopant interacts effectively with the water admolecules; such an interaction is energetically favourable and is dependent upon the size of the metal dopant: the larger the metal dopant, the more it is accessible to water, and the higher the adsorption energy.
- Water adsorption can affect the redox behaviour of transition metal dopants; this effect is loading dependant.

The results of this work, therefore, gives us an insight at the atomic level on the structural, electronic, and catalytic properties associated with metal dopants in AlPO frameworks, and the way in which the active sites interact with base molecules such as water. This information is important for optimising the catalytic properties of MeAlPO catalysts, and helps us to understand many characteristics of MeAlPO catalysts that are of difficult characterisation from experimental works, such as the redox behaviour of transition metal dopants, the instability of doped AlPO frameworks when dopants are present at high concentrations, the Lewis acidity of transition metal dopants, and the structural instability of MeAlPO frameworks upon steaming.

8.2 Future work

Having investigated the topics mentioned above, and despite the numerous results achieved in this work, we feel that our study of doped AlPOs is only a start and there is still more work to be done to complete the study of AlPO materials.

Among the possible directions for future extensions, we mention the following topics:

- Derivation of a new interatomic potential for MeAlPOs
- The incorporation of metal dopants in the place of the phosphorus framework ion.
- The influence of the *host-framework type* upon the acid and redox activity of active centres in MeAlPOs.
- The influence of the dopant concentration upon the catalytic activity of these materials.
- Study of extra framework ions in the cavities of MeAlPO frameworks.
- Study of the direct interaction of active sites in MeAlPO catalysts with a number of Lewis base molecules such as methanol, acetonitrile and ammonia.
- Reaction mechanisms of important chemical processes, such as the selective oxidation of alkanes occurring in the cavities of transition metal doped AlPO frameworks.
- Use of molecular dynamics and/or high level QM Hamiltonians such as DFT and B3LYP when required.

"I do not know what I may appear to the world, but to myself I seem to have been only a boy playing on the sea-shore, and diverting myself in now and then finding a smoother pebble or a prettier shell than ordinary, whilst the great ocean of truth lay all undiscovered before me."

By Isaac Newton

Appendix 1: Basis set

In this appendix, we report the basis sets of all the elements employed in our molecular and periodic calculations. We have kept the same format used in CRYSTAL input files and we list the elements in the order of increasing atomic number.

H

```
1 3
0 0 3 0. 1.
   18.73113696   0.03349460434
    2.825394365  0.2347269535
    0.6401216923 0.8137573262
0 0 1 0. 1.
    0.1612777588 1.
0 2 1 0. 1.
    1.1  1.
```

B

```
5 4
0 0 6 2.0 1.0
  2.082E+03 1.850E-03
  3.123E+02 1.413E-02
  7.089E+01 6.927E-02
  1.985E+01 2.324E-01
  6.292E+00 4.702E-01
  2.129E+00 3.603E-01
0 1 2 0.0 1.0
  2.282E+00 -3.687E-01 2.312E-01
  4.652E-01 1.199E+00 8.668E-01
0 1 1 0.0 1.0
  1.243E-01 1.000E+00 1.000E+00
0 3 1 0.0 1.0
  0.8   1.0
```

O

```
8 4
0 0 6 2. 1.
    5484.671660     0.001831074430
     825.2349460    0.01395017220
     188.0469580    0.06844507810
      52.96450000   0.2327143360
      16.89757040   0.4701928980
```

```
      5.799635340    0.3585208530
0 1 3 8. 1.
     15.53961625    -0.1107775490  0.0708742682
      3.599933586   -0.1480262620  0.3397528390
      1.013761750    1.130767010   0.7271585770
0 1 1 0. 1.
      0.2742         1.            1.
0 3 1 0. 1.
      0.538          1.
```

Al

```
13  5
0  0  8  2.  1.
   70510.0       .0002226
   10080.0       .001900
    2131.0       .01110
     547.5       .05090
     163.1      0.1697
      54.48     0.3688
      19.05     0.3546
       5.402    0.04430
0 1 5 8. 1.
     139.6     -0.0112     0.0089
      32.53    -0.1136     0.0606
      10.23    -0.0711     0.1974
       3.810    0.5269     0.3186
       1.517    0.7675     0.2995
0 1 1 0. 1.
      0.576     1.          1.
0 1 1 0. 1.
      0.28      1.          1.
0 3 1 0. 1.
      0.52      1.
```

P

```
15 5
0 0  8  2.  1.
      202703.      0.0001
      22413.1      0.0013
      4625.08      0.0068
      1312.41      0.0275
      425.149      0.0951
      146.409      0.2667
      51.8363      0.4781
      18.5913      0.2971
0 1  5 8. 1.
     339.375    0.00089   0.00287
      94.9248  -0.03549   0.02778
      23.125   -0.153     0.172
```

```
      6.9753   0.355     0.4215
      2.275    0.9102    0.4109
0 1  2 0.  1.
      1.219   -0.3715    0.09158
      0.48105  1.271     0.9349
0 1  1 0.  1.
      0.135    1.        1.
0 3 1 0. 1.
      0.74583  1
```

Ca

```
20 6
0  0  8  2.  1.
 191300.    0.0002204
  26970.    0.001925
   5696.    0.01109
   1489.4   0.04995
    448.3   0.17014
    154.62  0.3685
     60.37  0.4034
     25.09  0.1452
0 1 6 8. 1.
    448.6   -0.00575  0.00847
    105.7   -0.0767   0.06027
     34.69  -0.1122   0.2124
     13.50   0.2537   0.3771
      5.820  0.688    0.401
      1.819  0.349    0.198
0 1 5 8. 1.
     20.75  -0.0020  -0.0365
      8.40  -0.1255  -0.0685
      3.597 -0.6960   0.1570
      1.408  1.029    1.482
      0.726  0.944    1.025
0 1 1 0. 1.
      0.453  1.       1.
0 1 1 0. 1.
      0.246  1.       1.
0 3 3 0. 1.
      3.922  0.139
      1.095  0.326
      0.380  0.427
```

Cr

```
24 8
0 0 8 2.0 1.0
  235200.0      0.00027
   35040.0      0.00211
    7806.0      0.01139
    2134.0      0.0486
```

669.2 0.1591
235.9 0.3555
90.52 0.4231
35.88 0.1482
0 1 6 8.0 1.0
735.0 -0.00473 0.00843
176.1 -0.0593 0.061
57.65 -0.1353 0.2304
21.84 0.2375 0.4743
8.987 0.6731 0.4606
3.460 0.2487 0.1696
0 1 4 8.0 1.0
33.84 0.011 -0.0279
11.72 -0.4207 -0.0812
5.414 -0.8673 0.2211
2.502 0.9675 1.033
0 1 1 0.0 1.0
1.159 1.0 1.0
0 1 1 0.0 1.0
0.5035 1.0 1.0
0 1 1 0.0 1.0
0.200 1.0 1.0
0 3 4 3.0 1.0
30.57 0.03077
8.403 0.1604
2.834 0.3907
1.002 0.4788
0 3 1 0.0 1.0
0.3538 1.0

Mn

25 8
0 0 8 2.0 1.0
292601.0 0.000227
42265.0 0.0019
8947.29 0.0111
2330.32 0.0501
702.047 0.1705
242.907 0.3691
94.955 0.4035
39.5777 0.1437
0 1 6 8.0 1.0
732.14 -0.0053 0.0086
175.551 -0.0673 0.0612
58.5093 -0.1293 0.2135
23.129 0.2535 0.4018
9.7536 0.6345 0.4012
3.4545 0.2714 0.2222
0 1 4 8.0 1.0
38.389 0.0157 -0.0311

```
      15.4367 -0.2535 -0.0969
       6.1781 -0.8648  0.2563
       2.8235  0.9337  1.6552
0 1 1 0.0 1.0
       1.2086  1.0     1.0
0 1 1 0.0 1.0
       0.4986  1.0     1.0
0  1  1  0.0  1.0
       0.20     1.0      1.0
0 3 4 5.0 1.0
       22.5929 0.0708
       6.1674  0.3044
       2.0638  0.5469
       0.7401  0.5102
0 3 1 0.0 1.0
       0.249   1.0
```

Fe

```
26 8
0 0 8 2.0  1.0
  315379.0      0.0002289
   45690.0      0.001908
    9677.3      0.011103
    2520.88       0.05015
    759.746       0.17040
    262.964       0.36925
    102.801       0.40334
    42.9733       0.14340
0 1 6 8.0 1.0
798.262 -0.00580 0.00850
191.162 -0.06822 0.06083
63.689 -0.13247 0.21125
25.362 0.25142 0.39446
10.734 0.64322 0.39802
3.794 0.27811 0.21568
0 1 4 8.0 1.0
48.144 0.017767 -0.022076
17.456 -0.25345 -0.088574
7.0031 -0.88634 0.21429
3.0599 0.964902 1.30386
0 1 1 0.0 1.0
     1.3389   1.0      1.0
0 1 1 0.0 1.0
     0.59123   1.0      1.0
0  1  1  0.0  1.0
       0.20     1.0      1.0
0 3 4 6.0 1.0
30.4989 0.059554
8.80205 0.25963
3.20567 0.51294
```

1.23864 0.57315
0 3 1 0.0 1.0
0.48038 1.0

Co

27 8
0 0 8 2.0 1.0
341701.0 0.0002298
48850.0 0.001932
10400.900 0.01111
2718.989 0.0496
819.661 0.1693
283.878 0.3664
111.017 0.4007
46.4756 0.1419
0 1 6 8.0 1.0
855.600 -0.0058 0.0088
206.499 -0.0683 0.062
69.091 -0.133 0.2163
27.288 0.2612 0.4095
11.587 0.6277 0.3934
4.209 0.2818 0.1757
0 1 4 8.0 1.0
51.600 0.0201 -0.023
18.896 -0.246 -0.0874
7.657 -0.7882 0.225
3.261 0.9383 1.295
0 1 1 0.0 1.0
1.415 1.0 1.0
0 1 1 0.0 1.0
0.636 1.0 1.0
0 1 1 0.0 1.0
0.200 1.0 1.0
0 3 4 6.0 1.0
33.59 0.0595
9.785 0.2559
3.6 0.4984
1.385 0.5666
0 3 1 0.0 1.0
0.522 1.0

Ni

28 7
0 0 8 2.0 1.0
367916.0 0.000227
52493.9 0.001929
11175.8 0.0111
2925.4 0.05

```
     882.875   0.1703
     305.538   0.369
     119.551   0.4035
      49.9247  0.1426
0 1 6 8.0 1.0
     924.525  -0.0052   0.0086
     223.044  -0.0679   0.0609
      74.4211 -0.1319   0.2135
      29.6211  0.2576   0.3944
      12.4721  0.6357   0.3973
       4.2461  0.2838   0.2586
0 1 4 8.0 1.0
      56.6581  0.0124  -0.018
      21.2063 -0.2218  -0.08
       8.4914 -0.8713   0.2089
       3.6152  1.0285   1.255
0 1 1 0.0 1.0
       1.5145  1.0      1.0
0 1 1 0.0 1.0
       0.6144  1.0      1.0
0 3 4 8.0 1.0
      41.0800  0.0405
      11.4130  0.2022
       3.8561  0.4338
       1.3302  0.4897
0 3 1 0.0 1.0
       0.411   1.0
```

Zn

```
30 8
0 0 8 2.0 1.0
  417016.5    0.00023
   60504.2    0.00192
   12907.9    0.01101
    3375.74   0.04978
    1018.11   0.16918
     352.55   0.36771
     138.19   0.40244
      57.851  0.14386
0 1 6 8.0 1.0
    1079.2   -0.00620   0.00889
     256.52  -0.07029   0.06384
      85.999 -0.13721   0.22039
      34.318  0.26987   0.40560
      14.348  0.59918   0.41370
       4.7769 0.32239   0.34974
0 1 4 8.0 1.0
      60.891  0.00679  -0.00895
      25.082 -0.08468  -0.03333
      10.620 -0.34709   0.08119
```

```
     4.3076 0.40633   0.56518
0 1 1 0.0 1.0
     1.6868  1.0 1.0
0 1 1 0.0 1.0
     0.62679 1.0 1.0
0 1 1 0.0 1.0
     0.15033 1.0 1.0
0 3 4 10.0 1.0
    57.345   0.02857
    16.082   0.15686
     5.3493  0.38663
     1.7548  0.47766
0 3 1 0.0 1.0
     0.51592 1.0
```

Ga

```
31 7
0 0 8 2.0 1.0
 444668.       0.00023
  64576.8      0.0019
  13935.2      0.0108
   3651.66     0.049
   1099.41     0.1672
    381.106    0.3643
    149.482    0.4028
     62.817    0.1477
0 1 6 8.0 1.0
   1155.65    -0.006    0.0088
    278.06    -0.07     0.063
     93.1902  -0.14     0.2196
     37.0948   0.2685   0.4083
     15.4816   0.6184   0.4154
      5.1517   0.3248   0.3536
0 1 4 8.0 1.0
    70.6212   0.0067  -0.0085
    27.1784  -0.0863  -0.035
    70.6212   0.0067  -0.0085
    27.1784  -0.0863  -0.035
    11.4394  -0.3455   0.0849
     4.6239   0.4086   0.5583
0 1 2 3.0 1.0
     1.850268  0.855486 1.061746
     0.71043   0.171938 0.272691
0 1 1 0.0 1.0
     0.3044     1.0      1.0
0 3 4 10.0 1.0
    67.4273   0.0259
    18.8367   0.1495
     6.3055   0.3805
     2.1298   0.4768
```

0 3 1 0. 1.0
0.67496 1.0

Sr

38 8
0 0 9 2. 1.
3.10952e+06 3.5e-05
422820 0.000318
83530.1 0.00209
19753.0 0.0112
5441.51 0.04785
1712.11 0.1572
604.84021 0.3531
233.819 0.4234
94.1737 0.1523
0 1 7 8.0 1.
7146.02 -0.000276 0.000858
1593.48 -0.00625 0.00867
458.627 -0.0587 0.0562
154.75 -0.1466 0.2194
59.5695 0.2419 0.4491
25.0685 0.7056 0.3948
10.5092 0.2262 0.0891
0 1 6 8.0 1.
176.264 0.000654 -0.0119
54.3686 -0.0369 -0.0786
20.6589 -0.3848 0.0943
8.4732 0.2977 1.0362
3.5246 1.1559 1.2501
1.3601 0.2195 0.2553
0 3 5 10.0 1.
335.491 0.00339
92.9774 0.0334
30.9923 0.1639
11.3976 0.3884
4.3462 0.4352
0 3 1 0.0 1.0
1.614 1.0
0 1 3 8.0 1.0005
3.738 -0.5932 -0.334
1.8387 -0.6031 0.6915
0.7484 2.0043 3.6737
0 1 1 0.0 1.
0.3224 1. 1.
0 1 1 0.0 1.
0.1332 1. 1.